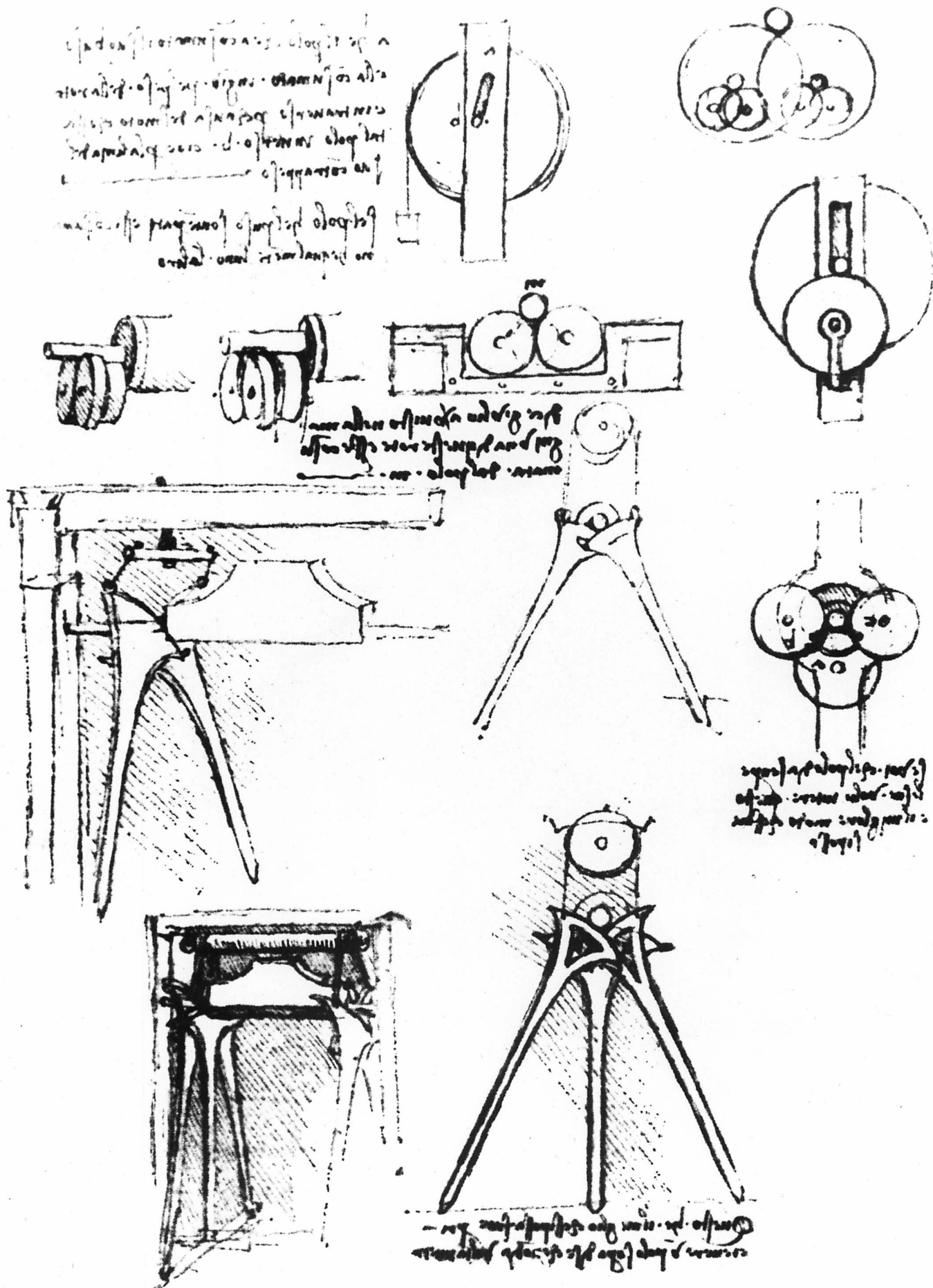RAPID SOLIDIFICATION OF TIN BASED ALLOYS

BY

MARK JOLLY
DARWIN COLLEGE
CAMBRIDGE

A dissertation submitted for the degree of
Doctor of Philosophy in the University of Cambridge

October, 1982.

Drawings from Leonardo da Vinci's Codex Madrid I. showing a two disc bearing (top) and a bearing to support a bell (bottom) (Reti 1971).

PREFACE

This dissertation, which is submitted for the degree of Doctor of Philosophy in the University of Cambridge, describes research carried out between October, 1978 and April, 1982 under the supervision of Prof. R.W.K. Honeycombe FRS., in the Department of Metallurgy and Materials Science, Cambridge and at the International Tin Research Institute, Alperton, London, with whom I was a C.A.S.E. student.

Except where due acknowledgement is made this work is, to the best of my knowledge, original and has been performed without collaboration. This dissertation does not exceed the regulation length.

I would like to thank:

Prof. R.W.K. Honeycombe F.R.S. for the provision of laboratory facilities in Cambridge and for his unfailing patience and guidance as a supervisor.

Dr. D.A. Robins for the provision of laboratory facilities at I.T.R.I. and further money at the cessation of my grant.

S.E.R.C. for financial support.

Dr. J.E. Field of the Cavendish Physics Laboratory for the provision of a high speed cine camera.

Dr. G.M. Lorimer of Manchester University for ion beam thinning one of my specimens.

Mr. B.C. Scott of I.T.R.I. for maintaining the S.E.M. and for his advice and support while I was at I.T.R.I.

Mr. B. Barber for his invaluable assistance with the photographic work especially the high speed cine.

Dr. I.M. Hutchings for his suggestions and advice on the high speed cine photography.

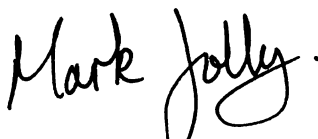Mr. R. Trumper for his enthusiastic help with the water modelling.

Mark Jolly.

October, 1982.

SUMMARY

Tin based alloys are used extensively in the production of plain bearings with a nominal composition of about 90%Sn - 7%Sb - 3%Cu. The amount of antimony that can be retained in solid solution by conventional production methods is limited to about 6% thus restricting the volume fraction of SbSn intermetallic that can subsequently be precipitated on ageing. In addition there is significant segregation in these alloys and copper is introduced to minimise this effect. There are also problems with grain growth and fatigue.

Rapid solidification is known to enable higher quantities of solute to be retained in solid solution in a number of alloy systems and in addition refine microstructures thereby improving the mechanical properties. The process of melt spinning has been used in this work to produce rapidly solidified alloys in the simple binary Sn-Sb system and the effect of process variables on the uniformity and dimensions of the product evaluated and observed using high speed cine and still photography.

The amount of Sb that can be retained in solid solution has been increased to between 15 and 20% from the equilibrium value of 3.8%. These super-saturated solutions were found to be unstable at room temperature and some precipitation occurred soon after solidification.

Consolidation to produce "bulk" rapidly solidified alloys was achieved by compaction and extrusion to produce rods of high integrity. Comparison with conventionally chill cast, extruded material and compacted, extruded alloy turnings show that microstructures obtained by each method are considerably different.

The mechanical properties of the alloys have been compared using tensile, compression, hardness and creep tests in the as-extruded and aged conditions and the results related to the difference in microstructure.

Rapid solidification is found to refine the microstructure of such tin alloys and reduce the segregation, considerable enhancement of strength and creep resistance of the alloys is also displayed.

Prolonged heating at high temperatures is found to have little effect on the properties of the compacted rapidly solidified alloys. The observation of a yield drop in compression tests in rapidly solidified Sn15%Sb is the first time such a phenomenon has been reported in these alloys.

CONTENTS

Units, Symbols and Abbreviations

Units.

S.I. units have been adopted throughout this thesis except where it has been more convenient to apply more commonly used units, for example the hour and the Ångström unit. Natural logarithms are denoted by "ln". Compositions are in weight % except where it is stated that atomic % is used.

Symbols.

A	melt puddle radius
A_o	initial cross sectional area
A_J, A_j	cross sectional area of jet
A_R	cross sectional area of ribbon
a	major lattice parameter, an index
a_o	average atomic distance
b	an index
C_D	discharge coefficient
C_p	specific heat capacity at constant pressure
c	minor lattice parameter, a constant
D, D_R	reservoir diameter
$\bar{D}$	average grain size
D_n	diffusion constant
d	dimension of length
$\bar{d}$	mean linear intercept
e	engineering strain
$\dot{e}$	strain rate
e_F	strain to failure
e_{TS}	strain to maximum load
F	force
f	a geometric factor
G_L	temperature gradient in liquid
g	acceleration due to gravity

H_v	Vicker's hardness
h	heat transfer coefficient, Miller index, height
I	nucleation rate
J	jet diameter
K	a constant
k	Miller index
L_F	latent heat of fusion
L_N	nozzle length
$1, \ell$	Miller index, dimension of length
$\bar{M}$	molecular weight
m	an index
Nu	Nusselt number
N_v	number of atoms per unit volume
n	an index
P	pressure, load
Q	a constant
Q_R, Q_J	volumetric flow rate
R	radius, correlation coefficient
$\underline{R}$	gas constant
Re	Reynolds number
R_F	solidification front growth rate
R_s	substrate microfinish
r	radius
s	dendrite spacing
T	temperature
T_B	substrate temperature
T_F	temperature of undercooling
T_ℓ	temperature of melt
T_m	melting point

T_s	starting temperature
t	time, splat thickness
U	cooling rate
V	volume
v_j	jet velocity
v_R/v_s	ribbon/substrate velocity
W	Weber number
w	ribbon width
x	volume fraction of solid
α	thermal diffusivity
β	an angle
γ	surface tension
ΔT_r	reduced undercooling
Θ	Bragg angle
λ	lamellar spacing
μ	viscosity
ν_p	melt puddle viscosity (a flow constant)
ρ	density, dislocation density
ρ_t	theoretical density
σ	engineering stress, standard deviation
σ_i, σ_o	initial stress, Peierls-Nabarro stress
σ_u, σ_{TS}	tensile strength
σ_y	yield point
τ	time period, shear stress
ϕ	nozzle diameter

Abbreviations

at.% or $^{at}/o$	atomic %
C.C	chill cast
C.T	chill cast turnings
Corr.	correlation coefficient
E.R	extrusion ratio
f.p.s.	frames per second
H.I.P.	hot isostatic pressing
R.A.	reduction of area
R.F.	radio frequency
R.S.	rapidly solidified ribbon
r.p.m.	revolutions per minute
S.A.	surface area
W.D.	work done

INTRODUCTION

Chapter 1 begins with an history and review of most of the methods available for rapid solidification. An attempt is made to summarise the effects of rapid solidification on the structure of metals and alloys by studying microstructural features such as grain size, lamellar spacing, dendrite spacing, microsegregation, supersaturation, production of new phases and the introduction of lattice defects. The history and properties of plain bearing alloys are briefly reviewed and the choice of the tin-antimony system is made as the model system for the present work.

Chapter 2 gives a detailed description of the melt spinning apparatus used in this research project and goes on to describe the effects which process parameters have on the product. Analysis of the data is carried out using a number of theories proposed by other workers. Some detailed observation is made of the flow observed in the metal system, and a model system using water, by high speed photographic techniques.

The structure and properties of the ribbon produced are discussed in chapter 3 and analysed by X-ray and metallographical methods.

Chapter 4 assesses the ease with which the ribbons may be consolidated and reviews the methods available. Extrusion is chosen and some preliminary results for the flow stresses of the material are presented and compared with the properties of chill cast alloys.

Chapter 5 is a detailed account of the microstructure obtained in the extruded rods of consolidated ribbon and chill cast turnings, and chill cast alloys. The effect of ageing is studied and the effect of an oxide dispersion introduced by the consolidation process is analysed.

Chapter 6 presents results of mechanical tests on all the alloys with the effect of ageing being considered. The results of these tests are combined with the results of chapter 5 to give a complete picture of the effect of rapid solidification on these tin alloys.

1.1. Introduction

Rapid extraction of heat from metals has long been used to produce non-equilibrium microstructures in order to improve their mechanical and physical properties.   Quenching of steels to induce the martensitic transformation is a prime example and has been performed by the blacksmith for centuries.   As the development of such desirable microstructures is crucial in the science of metallurgy many methods of achieving rapid cooling have been devised.

Cooling rates of 10^4 to 10^5 Ks^{-1} have been obtained by chill casting (Falkenhagen and Hofman, 1952; Hinesley and Morris, 1971) or atomisation (Jones, 1977) and of 10^5 Ks^{-1} in solid state quenching (Jones, 1977), while conventional commercial practices give cooling rates of $10^3 Ks^{-1}$ at best. Olsen and Hultgren (1950) produced quench rates of 9.7 x $10^4 Ks^{-1}$ by injecting molten alloys into iced brine.   Patterson (1979) suggests that this could be improved by injection into a low melting point liquid metal.

Duwez and his colleagues at Pasadena, used the idea of Falkenhagen and Hofman (1952), of quenching a liquid metal by conduction to a solid heat sink rather than convection in a liquid, and produced estimated quench rates in excess of $10^6 Ks^{-1}$ (Duwez et al, 1960a; Klement et al, 1960).   Since then many techniques of rapid solidification and quenching have been designed and it has been suggested that cooling rates of up to $10^{10} Ks^{-1}$ have been achieved in the thinnest sections of some specimens (Davies and Hull, 1974).

By imposing such enormous rates of heat extraction the scale of micro-structure of a metal or alloy can be changed drastically.   Grain size, dendrite cell size, volume fraction of defects, solid solubility and other structural features can be either severely reduced, as in the first

two, or greatly increased as in the last two. It is even possible to produce a featureless or amorphous microstructure if the composition of the alloy is correct and the cooling rate high enough (Klement et al 1960).

Many attempts have been made to review this field but the growth of the output of research papers is exponential (Masumoto, 1982. fig.1.1) and it is now easier for reviewers to take discrete areas of the subject. Early reviews by Anantharaman and Suryanarayana (1971), Jones and Suryanarayana (1973) on crystalline materials and Takayama (1976) on metallic glasses, give a good background but as the field is now so large a complete review is not available.

There have been four international conferences entitled "Rapidly Quenched Metals"; Brela, Yugoslavia (1970), Cambridge, Massachusetts, USA (1975), Brighton, U.K. (1978) and Sendai, Japan (1981). At the latest conference over 400 papers were presented. Other conferences related to rapid quenching have also been organised for example "Rapid Solidification Processing: Principles and Technologies" in 1978 and 1980 at Reston, USA. Numerous one day meetings are regularly held throughout the world keeping industry and academics in touch with each other.

1.2   Effect of Rapid Solidification on the Structure of Metals and Alloys

Equilibrium is the state of a system which implies that it is stable providing the conditions of the environment do not change. The system is at the position of lowest energy (stable equilibrium) or does not have enough energy to overcome an activation barrier to move to a lower energy (metastable equilibrium). Equilibrium can be described by the thermo-dynamics of the system and is relatively easily predictable for ideal conditions. The departure from ideal which occurs in experiment has led to the description of thermodynamics as the "science of the impossible" (Baker and Cahn , 1971).

Figure 1.1

Plot of Number of Papers Published on Rapid Solidification against
Year of Publication, showing the exponential growth rate of the
research in this subject.

(after Masumoto, 1981).
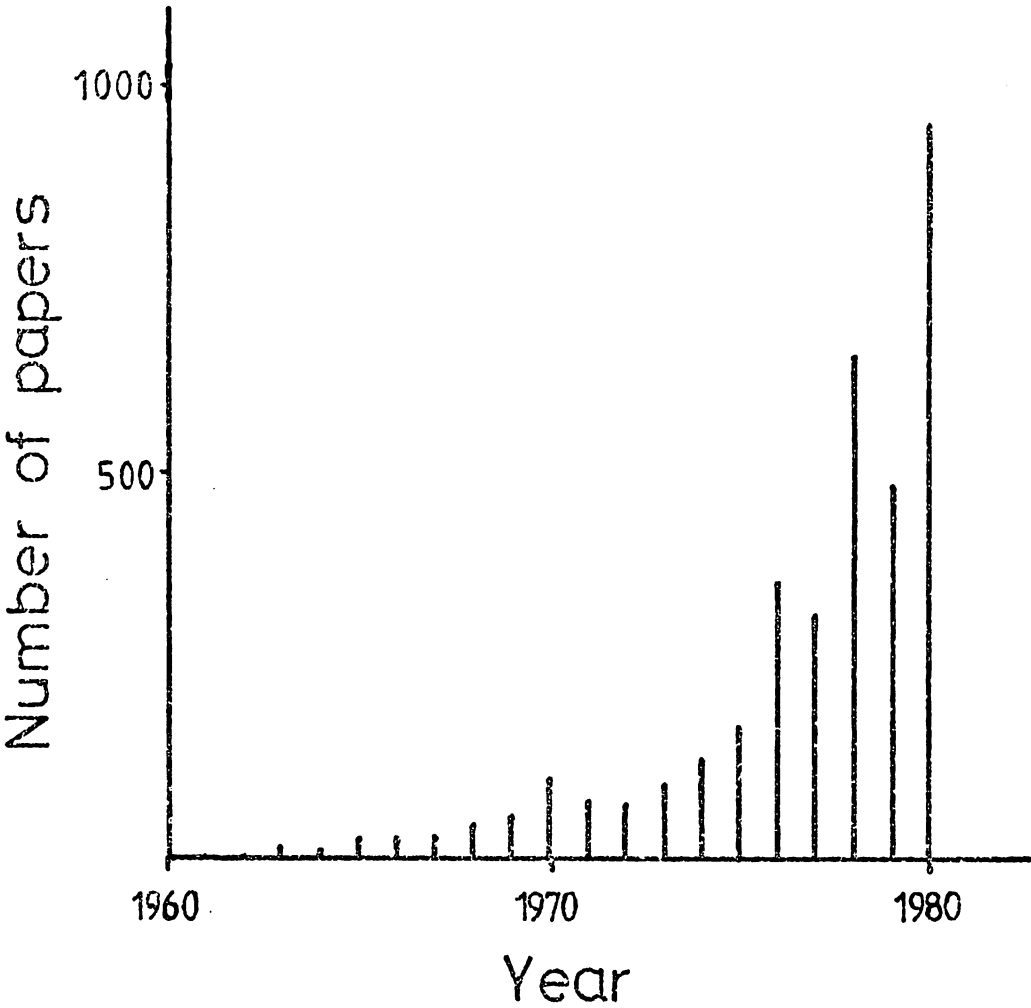
During solidification a system tries to move towards equilibrium but this is determined by the kinetics of the reaction. True equilibrium solidification structure can only be achieved if the cooling rate is infinitely slow so that each atom has adequate time and energy to adjust to the changing temperature. Rapid solidification forces a system into a state of, either non-equilibrium, which means that reactions continue to occur at ambient temperatures, or metastable equilibrium, in which reactions only occur if more energy is injected into the system, for example by annealing.

Honeycombe (1978) considers the effect of rapid solidification on five microstructural features of alloys which can change the properties of the material quenched:

(i) refinement of grain size

(ii) extension of solid solubility of alloy additions

(iii) change of segregation patterns

(iv) introduction of metastable phases

(v) introduction of high point-defect concentrations

In addition other workers have noted the effects on dendrite and lamellar spacings.

1.2.1 Grain size 'd'

It is well known that the grain size of a metal or alloy plays an important part in determining the mechanical and physical properties of the product. The relationship between tensile and yield strengths, σ, and grain size, d, in low carbon steels is given by

$$\sigma = \sigma_o + kd^{-\frac{1}{2}}$$ (1.1)

where σ_o is the Peierls-Nabarro stress and k is a constant which essentially measures the extent of dislocation pile ups. This is known as the Hall-Petch relationship (Hall, 1951; Petch, 1953). Examples where grain size is used to induce better properties in an alloy are in "controlled rolling", to produce small grain sizes for improving the strengths of many commercial

low alloy steels, and for good soft magnetic properties in Fe4%Si steel in which a large grain size is obtained.

By rapid solidification extremely small grain sizes can be achieved, these are usually of the order of a few micrometres (e.g. Midson et al, 1982,in Al-Cr). However grain sizes of 10nm have been observed in Al133 at. % Ge (Ramachandrarao et al, 1972) and of 100nm in pure Aluminium (Jones, 1973), but these were in electron transparent regions of the "splats" (∿100nm thick). The normal thickness of most rapidly solidified materials is of the order of tens of micrometres. Obviously as the thickness of the product varies, the cooling rate also changes and it is this variation which gives rise to the range of grain sizes often observed. A sigmoidal variation of grain size with cooling rate was obtained by Savitsky et al (1973) for niobium and vanadium. Boswell and Chadwick (1977) have attempted to describe a theory for the cooling rate dependence of grain size, as a measure of rate of heat extraction in rapidly quenched foils.

By assuming solidification is isothermal the fraction of solid present, x, at any time, t, is given by the Avrami equation

$$x = 1 - \exp\ ((-\pi I R_F^3 t^4)/3) \tag{1.2}$$

where I is the nucleation rate defined as

$$I = \left(\frac{D_n N_v}{a_o^2}\right) \exp \left\{-\frac{Q}{\Delta T_r^2 T_r^3}\right\} \tag{1.3}$$

and R_F is the solidification front growth rate defined by

$$R_F = \left(\frac{D_g f}{a_o}\right) \left(1 - \exp \left\{\frac{-L\Delta T_r}{\underline{R}T}\right\}\right) \tag{1.4}$$

$\Delta T_r = \dfrac{T_m - T_r}{T_m}$,the reduced undercooling where T_m is melting point and T_r the melt temperature.

L   = latent heat of fusion.

$\underline{R}$ = gas constant

N_v = number of atoms per unit volume

a_o = average atomic diameter

$D_n = D_g$ = bulk diffusion constant in liquid

f = geometric factor

Q = a constant

These equations can be used to construct Time-Temperature-Transformation (T.T.T) diagrams. Using the Johnson-Mehl equation

$$\bar{d} = (R_F/I)^{1/4}$$ (1.5)

which gives the frequency distribution for $\bar{d}$ for homogeneous nucleation, a plot of $\bar{d}$ vs. ΔT_r can be constructed. This shows that the average grain size for isothermal solidification passes through a minimum at approximately $\Delta T_r = 0.4$.

For non-isothermal cooling it can be assumed that the undercooling felt by an alloy is given by the intersection of the cooling curve with the T.T.T. curve, thus the largest undercooling possible is at the "nose" of the curve. This yields a result not significantly different from the isothermal case. By plotting calculated values of $\bar{d}$ versus cooling rate the relationship $d \propto U^{-3/4}$ is obtained where U is the cooling rate at the melting point in Ks^{-1}. Experimentally Boswell and Chadwick (1977) found that for <u>pure metals</u> these theories provided predictions very close to experimentally obtained values and in particular for pure aluminium $\bar{d}$ was found to be $1.75 \times 10^7 U^{-0.9}$. The theory is also successful in predicting critical cooling rate for metallic glasses but overestimates the minimum grain sizes in <u>alloys</u> by about an order of magnitude.

<u>1.2.2. Dendrite Spacing 's'</u>

As the grain size varies immensely with cooling rate it would seem reasonable to assume that the dendrite spacing would behave in a similar fashion. Matyja et al (1968) confirmed this with their work on Aluminium alloys with Si, Pd, Fe, Cu and Ni. They produced splats with dendrite

spacings of 0.1 - 0.15μm from which they estimated a cooling rate of 2 x $10^7 Ks^{-1}$

with a Nickel substrate.   Using the knowledge that the dendrite spacing is a

function of the degree of supercooling and the data of Predecki et al (1965)

and calculations of Ruhl (1967) they produced a plot of dendrite spacing

against cooling rate,from which the relationship

$$s \ U^a = c \tag{1.6}$$

where 'a' and 'c' are constants, was obtained and found to be valid over ten

orders of magnitude of U.   The index was found to be $\sim$0.32 which is close to

the theoretical value of $\frac{1}{3}$.   Other workers for example Suryanarayana and

Anantharaman (1970) and Ramachandrarao et al (1972) have confirmed this work in

Al alloys.   Both using the Al-Ge system, the former measured spacings of 530nm

and estimated U to be 2 x $10^6 Ks^{-1}$, the latter 25nm giving a cooling rate of

$10^{10} Ks^{-1}$.

Sarin and Grant (1972) extended the theory to cover Cu-Zr alloys.

Using quenching rates ranging from 10^0 to $10^8 Ks^{-1}$ they produced a similar plot

to Matyja et al,however 'a' was found to be $\sim$0.48.   Joly and Mehrabian (1974)

established that for some steels 'a' was 0.30 over the range from 10^{-1} to

$10^3 Ks^{-1}$.   Young and Kirkwood (1975) used steady state conditions of known

growth velocities and temperature gradients to validify the relationship

$sU^a = c$ and found that 'a' was again $\frac{1}{3}$ for Al-Cu alloys.   Jones (1978)

summarises the range of cooling rates from 10^{-6} to $10^9 Ks^{-1}$ with expected

dendrite spacings, he also includes a "limiting thickness value", calculated

from his own work (Jones, 1973) for which these cooling rates could be

expected to be obtained (fig.1.2).

<u>1.2.3. Lamellar Spacing'λ'</u>

The third structural feature that can be affected by the rate of

solidification is the lamellar spacing in eutectics . Burden and Jones (1970)

state that this feature should be used to measure the cooling rate in

Figure 1.2

Expected dendrite spacing(s) from various cooling rates (U)

Jones (1978)

Range of Cooling Rates (U) Ks^{-1}	Process	Characteristic Limiting thickness.	Expected Dendrite Spacing(s) *
$10^{-6} - 10^{-3}$	Large Sand Castings	>6m	5 to 0.5mm
$10^{-3} - 10^{\circ}$	Standard Castings Ingots & Strands	6 to 0.2m	500 to 50μm
$10^{\circ} - 10^{3}$	Thin strips and Die Casting. Normal Atomisation.	200 to 6mm	50 to 5μm
$10^{3} - 10^{6}$	Fine Powder Atomisation Melt Extraction.	6 to 0.2mm	5 to 0.5μm
$10^{6} - 10^{9}$	Spray Deposition, Melt Spinning, Electron Beam or Laser Glazing	200 to 6μm	0.5 to 0.05μm

*for Al-4.5% Cu alloy giving $U \sim 10^{5}/s^{3}$ (s in μm)

preference to the dendrite arm spacing, which at the time seemed open to

ambiguity in interpretation. They used the relationship between λ and

R_F the freezing velocity (R_F is related to cooling rate, U, and temperature

gradient in the liquid phase, G_L, by the expression $U=G_L R_F$)

$$\lambda R_F^{\,n} = A \tag{1.7}$$

where n and A are constants. They found n to be 0.5, which is what is

expected in theory, although other workers had found n to vary between 0.35

to 0.5. In splats of $Al-CuAl_2$ eutectic they found λ was 50nm and 200nm

for rough and polished copper substrates respectively. Davies and Hull (1974)

observed lamellar spacings of 8nm in Al-17.3% Cu from which they calculated

they had achieved a cooling rate of $10^{10}Ks^{-1}$.

1.2.4. Microsegregation

Microsegregation occurs at a particular temperature when a solid and

liquid phase have different compositions, for example typical hypo- or

hyper-eutectic alloys. (fig.1.3). For there to be a composition difference

diffusion of solute has to occur which requires a finite period of time.

In rapid solidification the period of freezing is so short that little,

if any, diffusion can take place, hence microsegregation is minimal. The

effect of freezing rate on segregation was studied by Olsen and Hultgren

(1950) in the range of cooling rates from 5.5×10^{-3} to $9.7 \times 10^{4}Ks^{-1}$ and

they found that the above statement was true. They also suggest that if

the cooling rate was infinitely slow as the temperature dropped solute atoms

would have time to diffuse back to the liquid to give the nominal composition

throughout the solid, a type of "autohomogenisation" process. They did not

however find such results and postulated that their cooling rates were not

slow enough. They proposed that the segregation was inversely proportional

to cooling rate. Baker and Cahn (1969, 1971) study the phenomenon of

solute trapping,in the Zn-Cd system, using thermodynamics and point out that

Figure 1.3

Example of an Hypoeutectic Alloy of A   (Schematic)
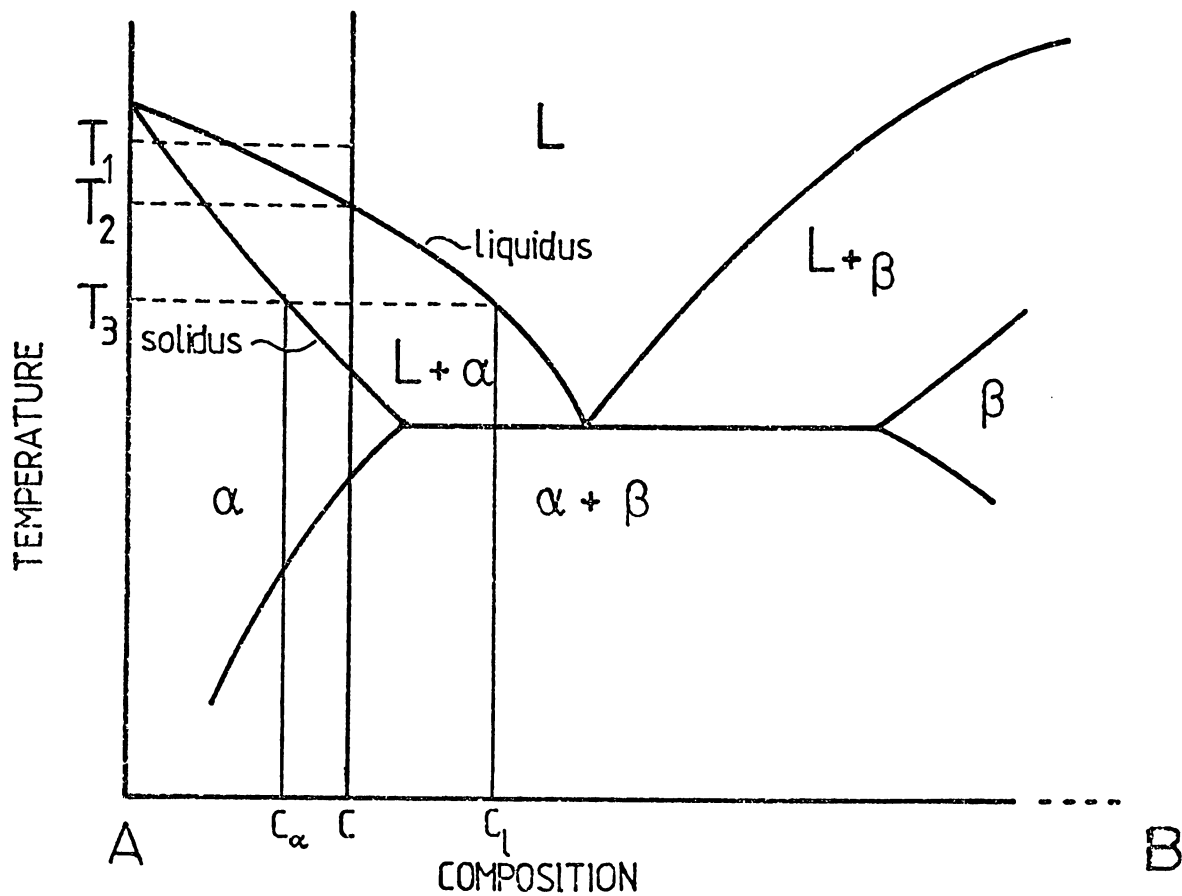
At T_1 :   homogeneous liquid of composition C.

T_2 :   nuclei of α form

T_3 :   composition of liquid follows liquidus = c_ℓ

composition of solid follows solidus   = c_α

therefore as solid is formed, the % 'A' in α

decreases and segregation occurs, the liquid

becomes enriched in B.

the four accepted theories of solidification (Borisov, 1962; Aptekar-
Kamenetskaya, 1962; Baralis, 1968 and Jindal-Tiller, 1968) which use
irreversible thermodynamical theory are somewhat contradictory in their
conclusions.   Masur and Flemmings (1982) use STEM analysis to determine
the solute redistribution in rapidly solidified Al-Cu ribbons.   With
point to point resolution of 25nm they found no evidence of solute trapping.

1.2.5. Supersaturation

However even after cooling at rates achieved by rapid solidification some
microstructural evidence of solute trapping has been observed (Jones, 1973)
if such is the case the estimation of the extension of solid solubility
becomes extremely dubious.   There is a limited number of metallic systems
which show complete solid solubility at equilibrium, they all obey the
Hume-Rothery rules:

   1)   the atomic size difference is no greater than 15%

   2)   atomic species should have equivalent electronegativities

   3)   metals of lower valency are more likely to dissolve in those of

higher valency. (Cottrell, 1975, p.192).

Several alloys do in fact obey these rules but do not form a complete
series of solid solutions.   It was while studying this phenomenon that Duwez
and his colleagues gave birth to the science of "splat quenching" (Grant
and Duwez, 1965; Duwez, 1967).Duwez et al (1960a) produced a continuous
series of solid solutions in Ag-Cu using their "gun-technique" (see section
1.3).   Since then solid solution extension has been observed in many alloys,
those with tin include: Ni (Klement, 1962), Co (Luo and Duwez, 1963), Sb (Varich
and Yakunin, 1968; Khera and Nayar, 1971); Kaczorowoski and Matyja, 1979),
Pb (Ramachandrarao et al, 1970; Patterson, 1979), Al (Kirin and Bonafacic,
1970; Tonejc et al, 1976) Bi (Laine et al, 1978). Supersaturation can be
observed metallographically and can be measured using X-ray techniques, for
as the solute atomic percentage increases so the lattice parameter changes,

the direction of change depending on whether the solute atom is larger or smaller than the solvent atom.

Midson and Jones (1982) attempt to predict the extent of solid-solubility extension obtainable using a kinetic approach. They conclude that the role of the cooling rate to produce diffusionless solidification is only to create the required supercooling before solidification occurs, and then to continue to cool until a temperature low enough to suppress solid state reactions is reached. As solidification involves the release of latent heat the necessary supercooling will therefore only be achieved if the relative rates of nucleation and growth allow it. Thus, from calculations of the necessary supercooling one cannot assume that diffusionless solidification _will_ take place, however such calculation can be a guide. For example, for tin using the Midson-Jones criterion $\Delta T_e = L_F/C$, where ΔT_e is the supercooling, L_F is the latent heat of fusion and C is the specific heat capacity, ΔT_e is 231K ($L_F = 59.4 \times 10^3 Jkg^{-1}$ C $= 0.257 \times 10^3$ $Jkg^{-1}K^{-1}$). Therefore as the melting point of tin is 505K totally diffusionless solidification when cooled to room temperature (300K) is impossible.

1.2.6. New phases; metastable intermetallics and glassy alloys.

As well as the extension of terminal solid solubility, rapid solidification can also induce new non-equilibrium metastable phases. Such phases were first reported by Duwez and his co-workers. A new intermetallic was observed in the Ag-Ge system (Duwez et al 1960b) and an amorphous phase reported in Au-Si (Klement et al, 1960). It has since been realised that many of the phases predicted by the Hume-Rothery rules but which had not been found can be produced by rapid solidification. Over the past twenty years many new phases both crystalline and amorphous have been reported, often they have been unpredicted but as more are observed the ability to predict has become better. For example it is accepted that in a binary system an amorphous phase is likely to be produced if there is a deep eutectic in the phase diagram.

Again many amorphous alloys commercially available contain a metalloid such as Boron, Silicon or Germanium at about 20 at. %.   If a system comprises two metals one each from the early and the late transition periods (e.g. Cu_x Zr_{100-x}) glasses are known to form relatively easily.

The main aim when producing a glassy alloy is to bypass the crystallisation temperature and thereby freeze in the liquid structure, similarly to inorganic glasses.   This is achieved by applying a rapid cooling rate and thus suppressing crystallisation until the viscosity of the melt becomes too high for diffusion, so that the atoms cannot rearrange themselves into a crystalline structure.   This point is commonly known as the "glass transition temperature", Tg (fig.1.4).   In general, alloys of tin do not produce amorphous structures so an in depth citation on glass formability is entirely unnecessary.   There is an excellent review by Takayama (1976) in which there is a reference to glassy Sn10%Cu being produced by vapour phase deposition (Ruhl, 1954).   Kamal and Pieri (1980) report an amorphous phase near the Sn-Sb-Ag peritectic point obtained by splat quenching.   The review above also gives information about the stability, structure and formation of metallic glasses. ·

However, there have been many reports of new metastable phases in tin alloys.   Kane et al (1966) report new phases in alloys with Ag, Al, Ca, Cu, Ga, Mg, Pb, Pd and Zn, these they designate γ phases and have a Valency Electron Concentration (V.E.C.) of between 3.4 and 3.9.   Alloys of Sn with Sb and Bi (V.E.C. > 4.0) do not form such phases.   The same group at MIT have since reported new phases in In, Cd (Srivastava et al 1968) Au (Giessen, 1968) Co, Ge, Ni, Pt and Tl (Giessen, 1969, Giessen and Vitek, 1972). Khera and Nayar (1971) studied the Sn-Sb system in detail and extended the solid solubility of Sb in Sn to 25.7^{at}/o from 3.8^{at}/o (fig. 1.5).   They also suggested a structural change such that the c parameter of the body centred tetragonal tin doubles in size on rapid solidification.   Neither this present

Figure 1.4

Figure 1.5

TIN-ANTIMONY PHASE DIAGRAM
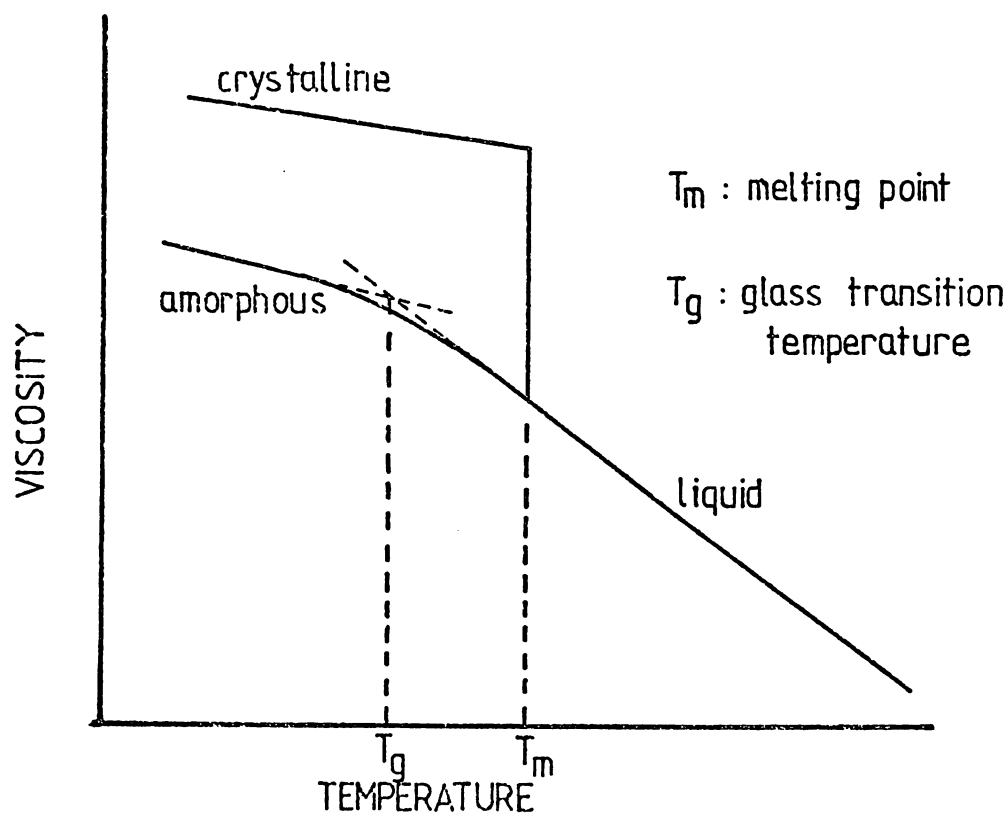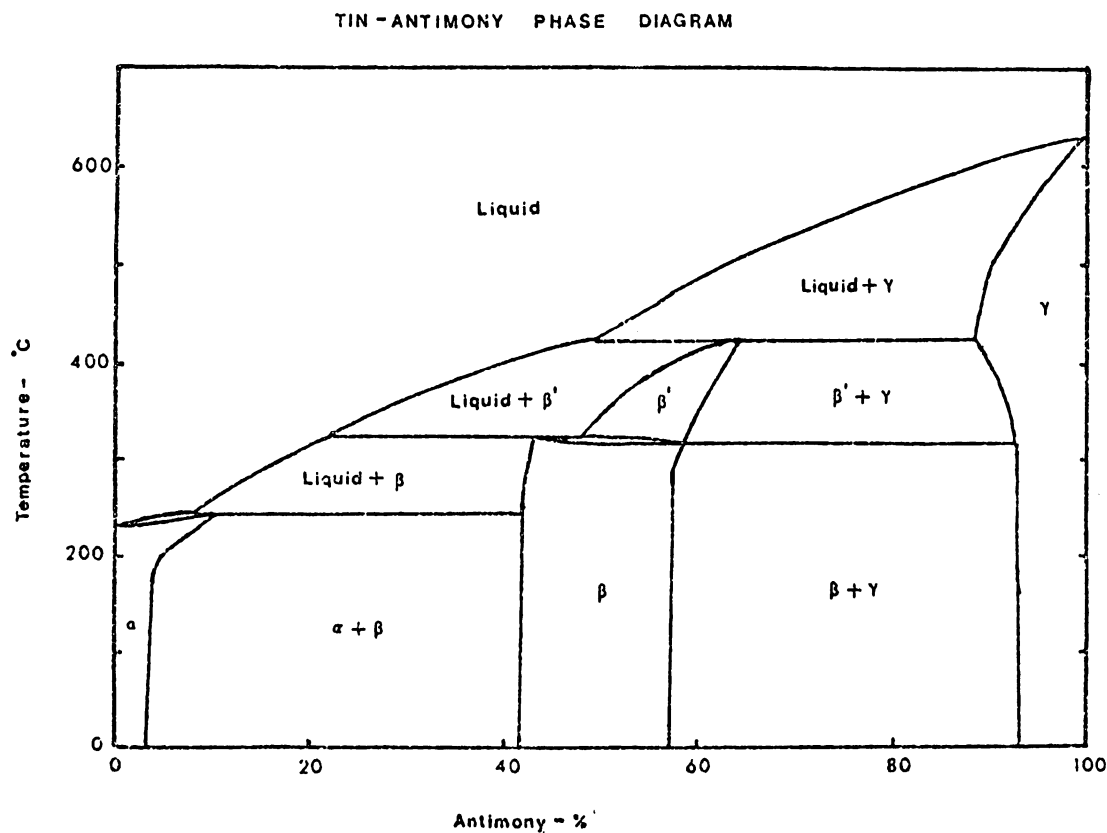
work nor the work of Kaczorowski and Matyja (1979) confirms this.

In order to account for kinetic effects of undercooling and to obtain a criterion for the formation of non-equilibrium phases, Dantzig and Davis (1977) adopt an unidimensional model of solidification. They identify a material property "the kinetic delay time parameter", τ, that can be calculated from the experimental conditions. The drawback of the analysis is that it only applies to systems with discrete melting points e.g. pure metals and eutectics.

1.2.7. Lattice Defects

One of the first observations made by Duwez was that splat quenching seemed to increase the vacancy concentration in pure metals and alloys thus solidified (Duwez and Willens, 1963). Very high densities of defects in the form of perfect vacancy loops with denuded zones in a region of approximately 0.1μm wide next to the grain boundaries were reported by Thomas and Willens (1964) in Aluminium. They also reported increases in vacancy concentrations with increasing melt superheat. Regular arrays of dislocation loops oriented in the <100> direction have been observed in Fe20%Cr25%Ni alloys (Wood and Honeycombe, 1974) although they do not seem to undergo metastable phase changes during rapid solidification.

Although high vacancy concentrations may be quenched into a metal by rapid solidification there is also an increased number of sinks such as grain boundaries which may negate the effect or at least lower it. In rapidly quenched equilibrium alloys solute clustering can be suppressed. In extended solid solutions clustering is bound to happen and will play a major part in affecting the mechanical properties.

"Clustering and high volume densities of heterogeneous nucleation sites afforded by grain boundaries or stacking faults restricts age-hardening, but dispersion-hardening is very effective and the fine distribution of second phases enhances plasticity, endurance and other

properties", states Jones (1977) referring to Aluminium alloys, but that statement can be held in general for any rapidly solidified crystalline alloy.

1.3. Techniques of Rapid Solidification

1.3.1. Introduction

The technique of rapid solidification is not yet 30 years old, only in 1952 did Falkenhagen and Hofmann (1952) manage to produce a cooling rate of $10^5 Ks^{-1}$ in Aluminium by casting into a chilled copper mould, a method still used in 1970 (Hinesley and Morris, 1970) to produce tensile specimens with a quench rate estimated at $2.5 \times 10^4 Ks^{-1}$. Although 1952 could be seen as the commencement of the art it was not until eight years later that the science really took off. Duwez et al (1960a) reported that a continuous series of solid solutions had been obtained in the normally binary eutectic system of Ag-Cu. This was reproduced in the psuedo-binary system GaSb-Ge and solid solution extension was achieved in the Ag-Ge system. Klement working with Duwez (Klement et al, 1960) then reported that in Au25%Si an amorphous phase had been obtained by rapid solidification. It was the results of Duwez and his co-workers which really started the scientific snowball rolling and since then a multitude of different techniques have been tried, some are still used, and some were never more than academically interesting.

Most of the techniques developed have satisfied the following three conditions:

    (i)   large substrate mass compared to specimen mass, the substrate having a high thermal conductivity as an efficient heat sink.

    (ii)   good thermal contact between the specimen and substrate during solidification and for as long as possible during subsequent solid state cooling.

    (iii) high specimen surface-to-volume ratio.

1.3.2. "Discontinuous Specimen" techniques.

1.3.2. a) Gun Technique

This was the original method used by Duwez and his co-workers. A

small droplet of molten metal was ejected onto the inside of a rotating

copper drum where it was kept in contact with the drum and spread out by

centripetal force.   The drum was modified (Duwez and Willens, 1963) to

become a "ski-slope" (fig.1.6).   The centripetal forces were created by

the motion of the specimen on the curved surface.   This was the most

common of the early rapid quenching techniques and the idea is very

simple.   "Splats", from which the name "Splat quenching" (Grant and

Duwez, 1965), are produced some 20mm x 10mm and about 20μm thick.

Measurement of physical and mechanical properties of the splats was not really

possible because of their convoluted profile and non uniform thickness.

However they were suitable for X-ray and transmission electron microscopy

studies.   Predecki et al (1965) completed an analysis involving velocity,

shape and size of the splats, the heat transfer coefficient (h) and cooling

rate obtained.   The original Duwez gun technique has been modified by many

workers, Willens and Buehler (1966) used a silver coated hearth as a

crucible to melt refractory alloys.   Davies and Hull (1972) put the apparatus

into an inert atmosphere in an attempt to improve the thermal contact between

the splats and substrate by reducing oxidation, and later reported that

cooling rates in the order of $10^{10}Ks^{-1}$ could be obtained in the thinnest

sections of the specimen (Davies and Hull 1974).

1.3.2. b) Piston and Anvil/Double Piston

In an attempt to produce foils of uniform thickness Pietrokowsky (1963)

developed the piston and anvil technique (fig.1.7) and Harbur et al (1969)

built a double piston apparatus and quenched Pb-Sn solders and Aluminium.

(fig.1.7).   Again a small quantity of material is melted either in a

crucible or by levitation melting (Booth and Charles, 1966) if reactive,

and then ejected or allowed to fall, between plates which are brought

together very rapidly, with either one or both plates moving.   This action

spreads the droplet to give a splat of reasonable uniformity of thickness.

Methods of Rapid Solidification

1.6 Gun Splat Technique

(after Duwez and Willens 1963)
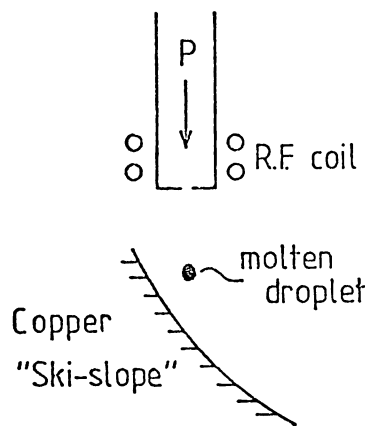
1.7 Double Piston/Piston and Anvil

(after Harbur et al, 1969)
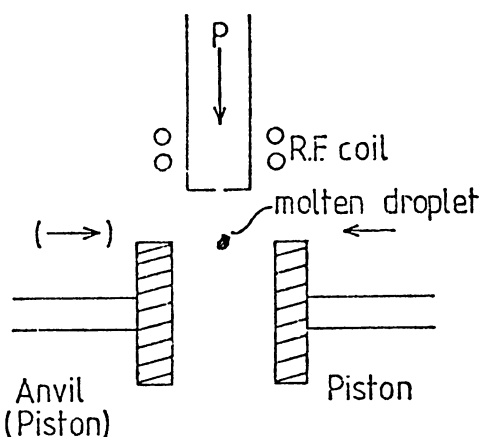
1.8 Rotating Copper Dish

(after Pond, 1958)
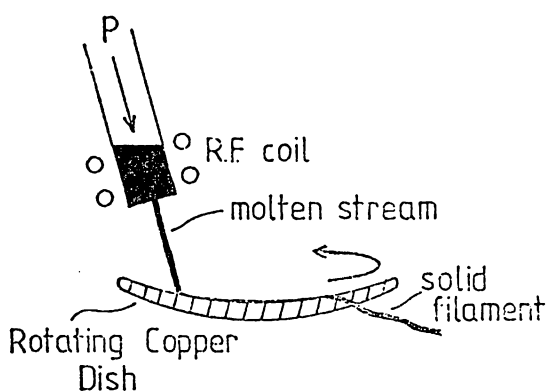
1.9 Rotating Copper Drum.

(after Pond Jr., and Maddin, 1969)
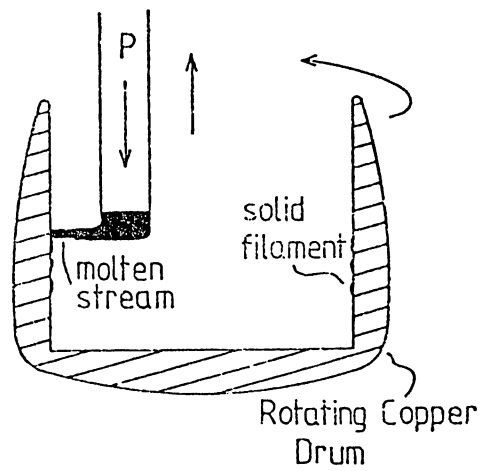
1.10 Double Roller

(after Chen and Miller, 1970)
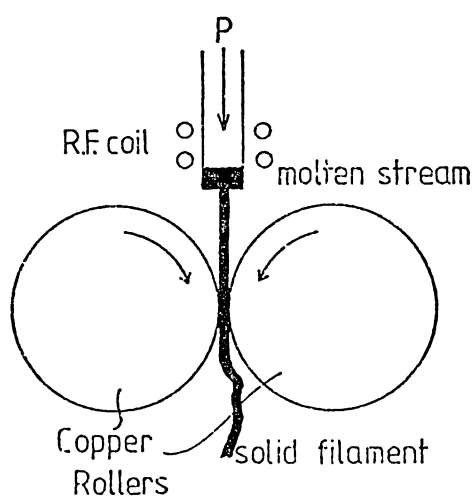
1.11 Belt and Roll

(after Sakata and Ishibashi, 1981)
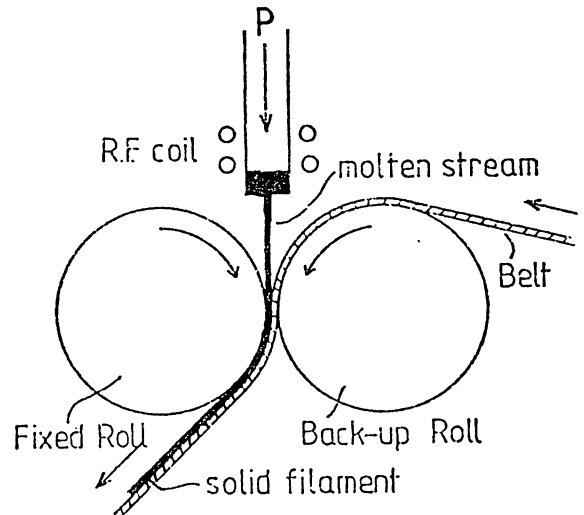
Although these splats are on the whole thicker than produced by the gun technique, ∿100μm rather than ∿20μm, there is heat extraction from both surfaces so the cooling rates are still in the order of $10^5 Ks^{-1}$. These specimens are more amenable to mechanical property testing but have to be thinned for transmission electron microscopy. As with the gun technique various groups of workers have adapted the basic idea to give them apparatus to quench, for example, in vacuo or at low pressures and in an inert atmosphere. Yoshimura and Somiya (1982) have developed a technique of melting materials with melting points up to 3000°C by using a Xenon arc-imaging furnace. Various types of control and propulsion of the pistons have also been tried. The main disadvantage of this method is that the pistons effectively forge the specimens thereby producing considerable plastic deformation.

1.3.2. c) Centrifuge and Rotary

This method is essentially the forerunner of what are now classed as atomisation techniques (see section 1.3.4). Proposed by Kumar and Sinha (1963) it involved ejection of molten metal through an orifice in a crucible by means of centripetal force. The droplets then impinged on a copper substrate surrounding the crucible. Kaufmann and Muller (1964) also used this method but it was not fully developed until Jones and Burden (1971) were aiming to produce splats in quantity. Cahn et al (1976) devised a similar method but the propulsion mechanism was a rotating vane which projected the molten droplets against a copper cylinder.

1.3.3. Continuous Filament Techniques

1.3.3.a) Free Jet Spinning/Melt Extrusion

This method was originated by Pond (1961) and involves ejection of molten liquid from a crucible with quenching being obtained by the surrounding fluid medium, originally a gas. This was described in detail by Kavesh (1978a) who used a liquid quenchant, typically refrigerated salt solution. He suggested quench rates of $10^4 Ks^{-1}$ are obtained. Ohnaka and Fukusako,(1978)

quenched liquid Pb in this fashion both into the atmosphere and into water
and commented on the stabilities of the jet.

1.3.3. b) Chill Block Melt Spinning.

This title covers a number of processes all using basically the same
principle to extract heat.   Rather than a fluid, a solid heat sink is used,
which being rotated, allows continuous filament to be produced.   The first
of such apparatus was really designed by Strange and Pim (1908) who
proposed that "thin sheets, foil, strips or ribbons of Zinc, Lead or other
metal or alloy" might be produced.   The principles they used were then redis-
covered by Pond (1958) who ejected molten metal onto the surface of a rotating
copper dish (fig.1.8) and Pond and Maddin (1969) who used a rotating copper
drum and ejected onto the inside surface (fig.1.9).   Thus a helical ribbon
of solid material was produced on the inside of the drum.   As with the first
splats produced, their studies were restricted to X-ray and electron microscopy
due to the dimensional variations, with a small number of electrical
resistivity measurements being made.   Their ribbons were 5-50μm thick and
0.2 to 1.5mm wide and they managed to produce a complete range of solid
solutions of Ag-Cu. Chen and Miller (1970) revised the original Pond (1958)
method but found it still introduced curvature into the product.   They
therefore developed the Double Roller Quench method (fig.1.10).   Babić
et al (1970a) independently also designed such a machine whereby liquid
metal is injected into the nip of two rotating chill rollers.   At first
continuous ribbon was difficult to produce.   Strips 7-15μm thick, 1-2mm
wide and 20-30mm long were reported (Babić et al, 1970b).   Lewis et al (1977)
and Davies et al (1978) suggested the quench rate was much slower than in
the subsequently developed melt spinning technique.   There were also
problems eliminating eccentricities of the wheels which mirrored themselves
in the dimensional variations of the product.   These were studied in detail
by Miyazawa et al (1982) and, Ishihara and Ikuta (1982).   However Leontić

et al (1978) continued to work on the method and produced a low temperature machine, and in the same paper suggested that a single roll and flexible belt might be more successful.   This idea was taken up by Sakata and Ishibachi (1982) (fig.1.11) who managed to design an apparatus which produced ribbon continuously with a thickness variation of only ±2μm in 30μm. Miyazawa and Szekely (1981) propose a mathematical model from which they conclude that there is only a narrow range of process parameter to give a stable operating mode, however their work only considered discrete melting alloys e.g. pure metals and eutectics, not those with a "mushy" region involving two phase casting. They also assumed a fixed geometry and roll dimensions but suggested their results could be extended.

Bedell (1975) redesigned the original Strange and Pim machine to produce a technique now known as Melt Spinning, a process in which the crucible movement and helical product shape were eliminated by casting onto the perimeter of a rotating copper disc (fig.1.12).   The centrifugal reaction throws the ribbon off the chill surface (fig.1.13) and thus the process can be completely continuous provided the wheel is kept clean and cool. The intimate contact needed for heat transfer is created by the ejection pressure.

Various workers have again adapted this principle to produce ribbons from multifarious alloys in many different environments. Leontić et al (1978) developed the process at liquid nitrogen temperatures to form Al6%Cr ribbons. Pavuna and Hainsworth (1980) also spun at low temperatures and low pressures using the water turbine principle to drive their wheel with a gas jet at 5000r.p.m. Liard et al (1978) used a high vacuum to produce difficult alloys such as $Mg_{70}Zn_{30}$ and $Gd_{67}Co_{33}$.   They also used inert gas atmospheres as many workers have done.   Helium has often been used to increase the cooling rate when the ribbon leaves the wheel, as it has a higher thermal conductivity than either air or a vacuum.

Figure 1.12

Melt Spinning of Tin Alloys (Schematic)
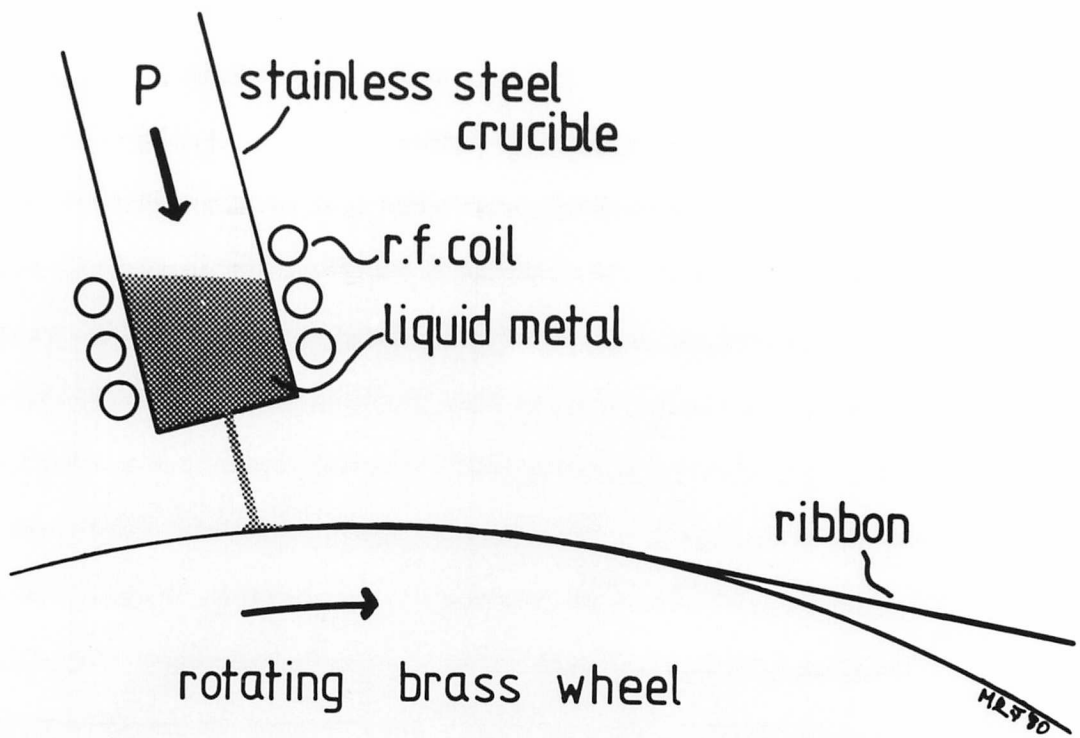
Figure 1.13

Melt Spinning of a Tin Alloy
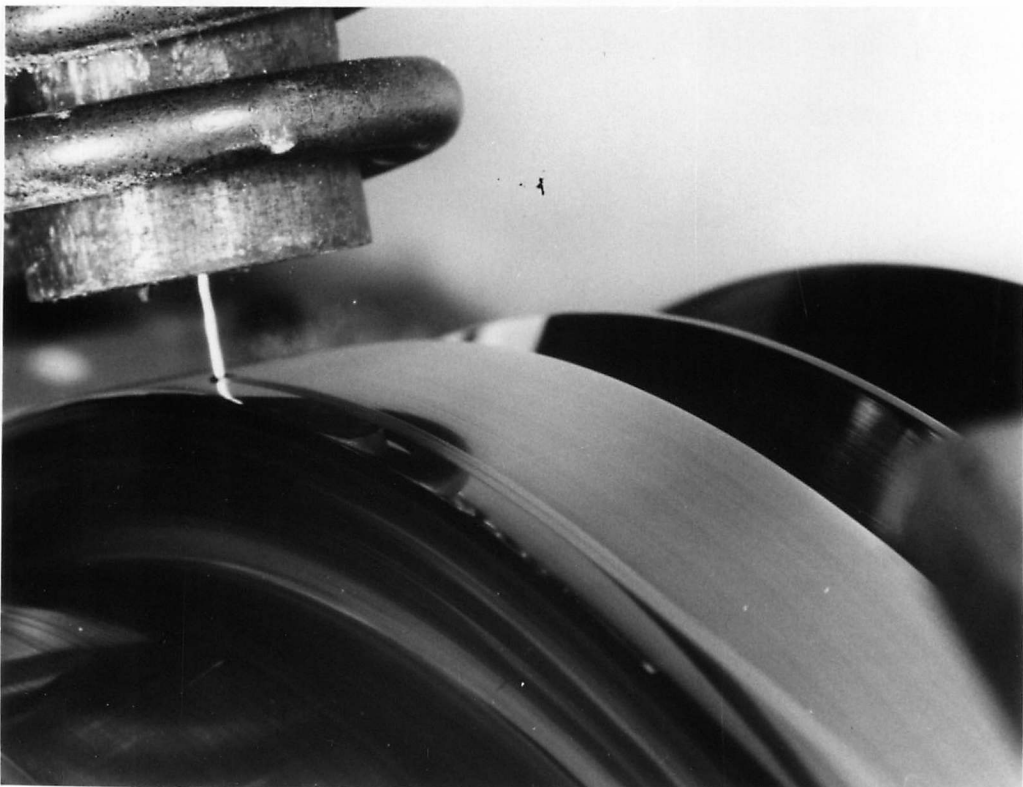
Figure 1.14

Coaxial Jet Melt Spinning (Liebermann,1981)
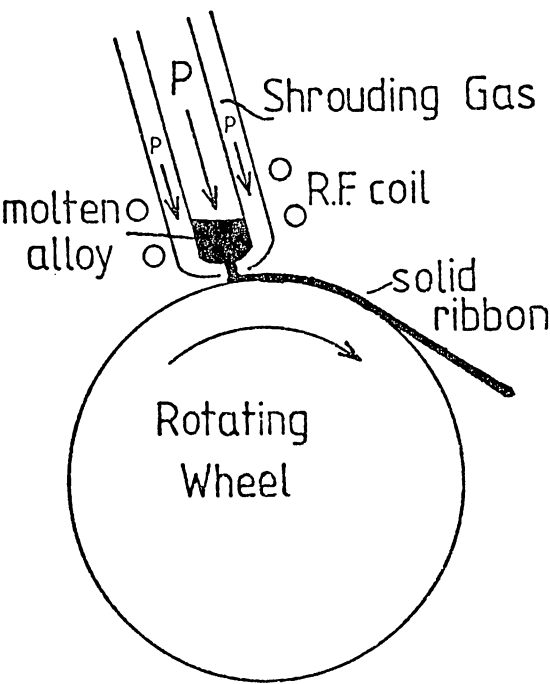
Figure 1.15

Quenching Stabilizer. (Pavuna, 1980)
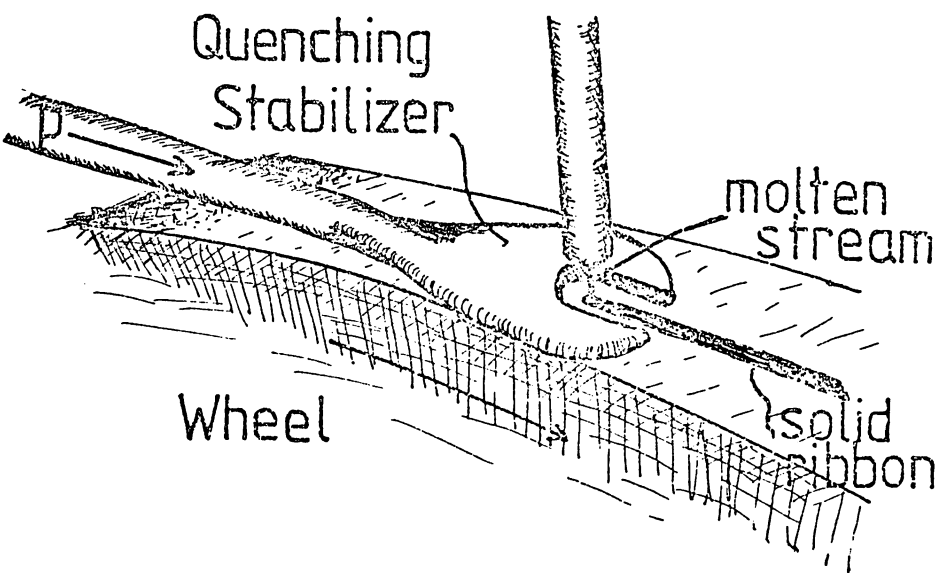
Cline and Anthony (1978) produced ribbon using a rectangular cross section nozzle instead of the usual round cross section, this they called "planar flow casting" (Narasiman, 1979). Essentially it was the same process but the nozzle was closer to the wheel to eliminate any contraction of the jet which might occur (Rayleigh 1879). Using this technique Liebermann (1979a) managed to produce amorphous ribbon 20mm wide. Melt spun amorphous alloys are now produced commercially up to 150mm wide for use in the electrical engineering industry for transformer cores.

Liebermann (1981) developed a process called Coaxial Jet Melt Spinning (C.J.M.S.) of ribbons (fig.1.14) to improve their quality. Pavuna (1980, 1981, 1982) also attempted to produce better quality ribbon by inventing a device called "the quenching stabilizer" by which a shroud of inert gas was introduced around the melt puddle region by a jaw shaped tube (fig.1.15).

Shimanuki et al (1982) managed to produce composite tapes by melt spinning a second ribbon onto an already cooled primary ribbon (fig.1.16). By such a process both amorphous/amorphous and amorphous/crystalline alloy tapes were produced.

Many workers have analysed the process and devised relationships between various parameters such as flow rate, jet velocity, substrate speed and melt jet impingement angle, and the product dimensions of width and thickness. Most notable are papers by Liebermann and Graham (1976), Liebermann (1978, 1979b,c, 1980a), Anthony and Cline (1978, 1979), Kavesh (1978) and Vincent et al (1982).

A technique for producing wire instead of ribbon was developed by Maringer and Mobley (1974) who proposed two methods both of which involved the principle of dragging a fine filament of molten material away from a melt surface using a rotating knife edge. Crucible Melt Extraction (fig.1.17) involved lowering the rotating copper knife edge onto the melt while in

Methods of Rapid Solidification

1.16 Compound Melt Spinning

(Shimanuki et al, 1981)

1.17 Crucible Melt Extraction

(Maringer and Mobley, 1974)
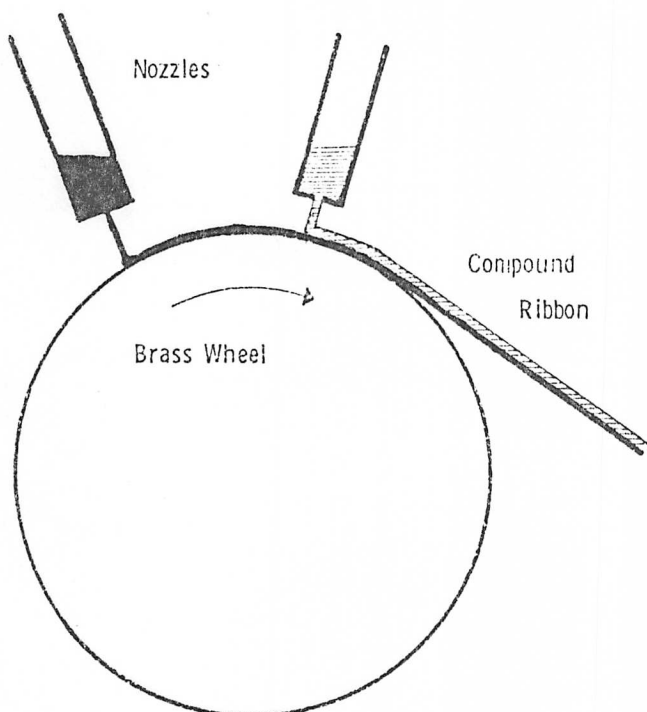
Double Nozzle Melt Spinning Method
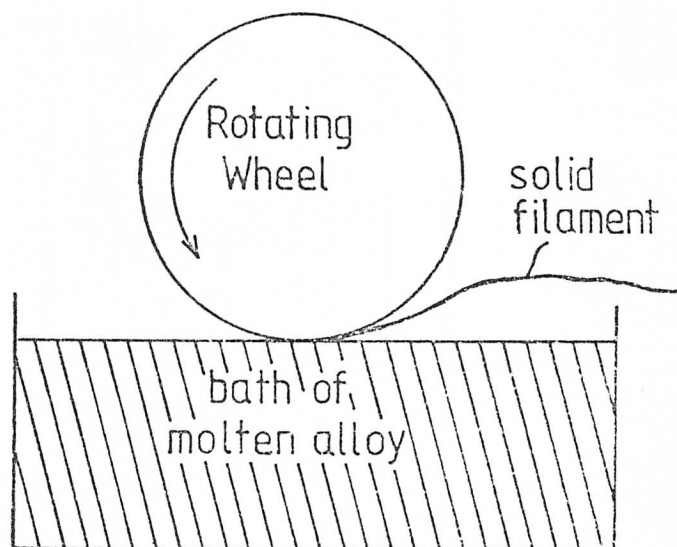
1.18 Pendant Drop Melt Extraction

(Maringer and Mobley, 1974)
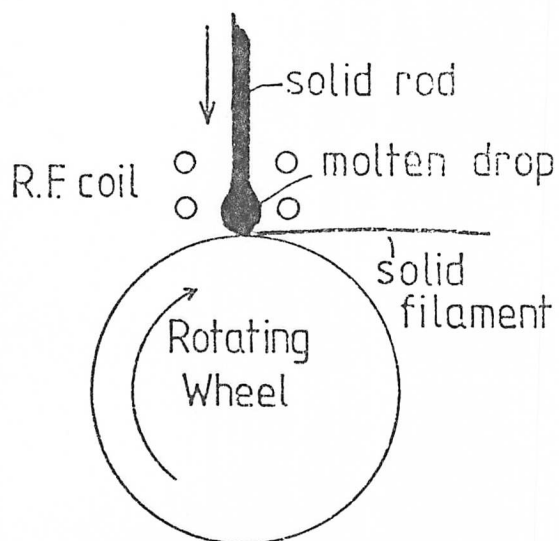
1.19 Cross section of Wire.

Produced by Melt Extraction on

a knife Edge. (Schematic).
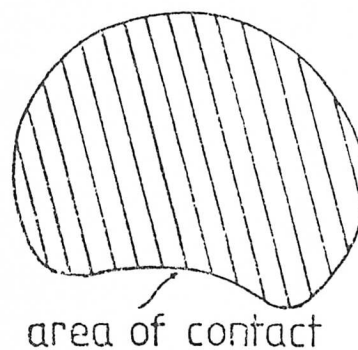
Pendant Drop Melt Extraction (fig.1.18) the stock material was lowered

through a heat source,to produce a droplet held in suspension by surface

tension,and then onto the knife edge.   Both methods were continuous and it

was also possible to produce tape rather than wire. The disadvantage of

both methods was that to obtain perfectly circular cross section wire

was extremely difficult, if not impossible, it was usually slightly

kidney shaped. (fig.1.19).   The original paper also described the effect

of feed rate and wheel speed on the shape and size of fibres produced.

The process has been revised and developed in the patents by Maringer

et al (1974, 1975), Stewart et al (1974) and, Mobley and Maringer (1975).

In 1980 workers at Osaka and Tohuku Universities, Japan, combined

the method of free jet spinning and rotating drum spinning in order to

produce circular cross section filament. Ohnaka et al (1981, 1982) and

Masumoto et al (1982) reported that using their "In-Rotating-Liquid

Spinning" method (fig.1.20) amorphous wire could be produced in many binary

and ternary systems.   The technique involved ejection of molten alloy

through a nozzle onto the surface of a revolving copper drum containing a

quench fluid,usually water.   The complex interactions of surface tensions

between the fluid molten alloy and drum gave a uniform circular cross

section product.   These studies also produced an analysis of the process

variables involved to give optimum conditions for production of continuous

filament.

1.3.4. Bulk Specimen Techniques.

The form of product obtained in all the techniques described so far

have had little or no use as engineering materials. Ribbon and tape has

been used in the electrical engineering industry for transformers and the

electronics industry as a screening material but the applications apply

only to amorphous alloys. In the last few years emphasis has been placed

on producing material, microcrystalline or amorphous, that can be used in

Figure 1.20

In-Rotating-Liquid-Spinning.

(Ohnaka et al, 1982)
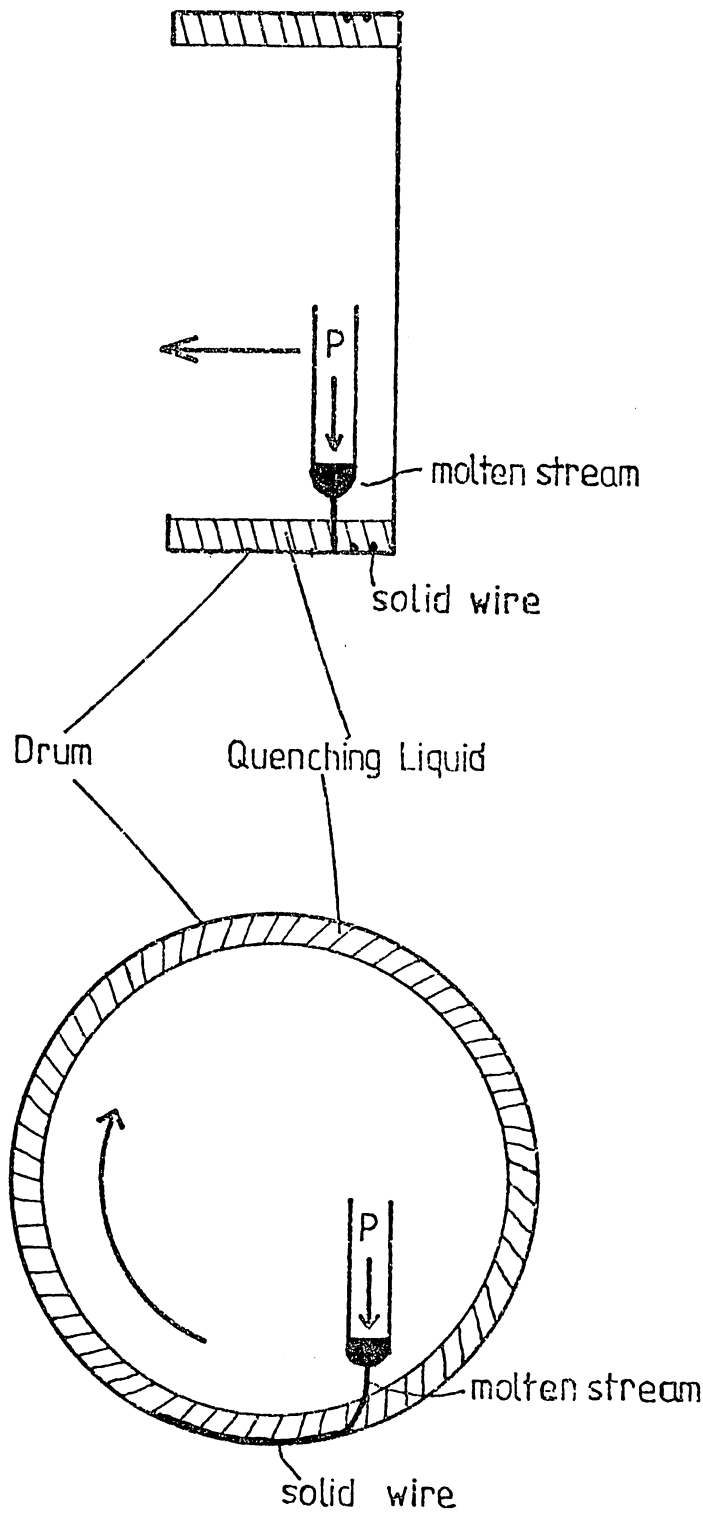
bulk form.   The most obvious way of doing this is to consolidate material

in particle form.   The original splats of Duwez were far too convoluted to

use as stock for Powder Metallurgy so other production methods had to be

produced.   These processes fall into two groups, those in which the

product has to be consolidated and those in which consolidation occurs

at the same time.

1.3.4. a) Serrated Wheel Techniques.

Maringer and Mobley (1978) suggest that instead of a smooth knife edge

or flat being used in their melt extraction process, a serrated wheel might

be used.   Described as Serrated Disc Melt Extraction (SDME) Maringer (1980)

then applied the idea to melt spinning.   Carbonara et al (1982) produced

both microcrystalline and amorphous flakes by serrated wheel melt spinning.

1.3.4. b) Roller Atomisation

This technique was developed by Ishii et al (1982) again to produce

power for subsequent compactium.   Atomised liquid particles of alloy were

propelled into the nip between two rotating rolls (c.f. double roller quenching).

1.3.4. c) Spraying Techniques

Moss et al (1964) redeveloped the gun technique to become essentially a

batch process.   Fine particles of prealloyed power were injected into a

plasma and impinged onto a copper substrate thus producing splats which

can be subsequently rolled or forged.   Thursfield and Jones (1971) used

"gas atomisation" as their melting method and again used a cooled copper

substrate to solidify the particles.   Kim and Jones (1982) studied the

effects of process variables on the structures obtained by such a process

in Al alloys.   Miura et al (1982) produced amorphous sheet $\sim 350\mu m$ thick

by "flame spraying", which consisted of introducing alloy power into an

oxyacetylene flame, propelled by an inert gas, and impelling the liquid

droplets at a water and cryogen cooled copper substrate.

A combination of gas atomisation and melt spinning was used by Savage

and Jones (1982) to rapidly solidify Al-Mn alloy powers prior to consolidation by extrusion.

1.3.5. Rapidly Solidified Layers.

To produce a rapidly solidified layer requires that an intense but short lived, localised source of power achieves rapid melting of a thin surface layer of bulk specimen which then acts as its own heat sink. This was first attempted by Mutsuzaki et al (1963) then Kaneko and Ikeuchi (1965), using electrodischarge machining. Hiller (1968) used electron beam melting to produce a refined microstructure and Jones (1969) used a laser to produce metastable layers.

The technique, known generally as "Laser Glazing" has been used to produce amorphous and microcrystalline layers. Some workers have coated substrates with prealloyed power and then "glazed" the surface with the result of a rapidly solidifed layer of different composition to the bulk material. It can be seen that these layers might be useful in wear and corrosion resistant applications.

1.4. Cooling Rates in Rapid Solidification

1.4.1. Introduction

The problem of measuring and assessing the cooling rate during rapid
solidification is one that has intrigued workers since the beginning of
the science.   Ruhl (1967) assumes two possible regimes of conduction
cooling and shows how the cooling rate varies in each regime by altering
conditions.

The initial state of the model for rapid solidification is shown in
figure 1.21.   The two extremes of conduction cooling evolve from whether the
controlling process is transfer of heat across the boundary (Newtonian)
or whether the interface has no effect but transfer is controlled by
conduction in the splat and the substrate (Ideal).   In the first case
the heat transfer coefficient, h, is low, in the latter h is high.

Assuming one dimensional heat flow then

$$\frac{\partial T}{\partial t} = \alpha \left(\frac{\partial^2 T}{\partial \ell^2} \right) \qquad \text{(Ficks 2nd Law)} \qquad (1.8)$$

where   T : temperature

        t : time

        ℓ : distance

        α : thermal diffusivity $= k/\rho Cp$

                k: thermal conductivity

                ρ: density

                Cp: specific heat capacity

By finite-difference methods, temperature profiles can be constructed
for different times (fig.1.22).   If the cooling is ideal then there will
be no temperature discontinuity at the interface however if h is low then
the temperature gradients in the substrate and splat can be ignored and
the interface becomes the controlling parameter and the cooling then follows
an exponential time law,

Ruhl's Analysis of Splat Quenching, (1967).

1.21 Initial State For Splat Cooling. (Schematic).

TEMPERATURE

T_S

time(t) = 0

T_B

spat → ← substrate

DISTANCE
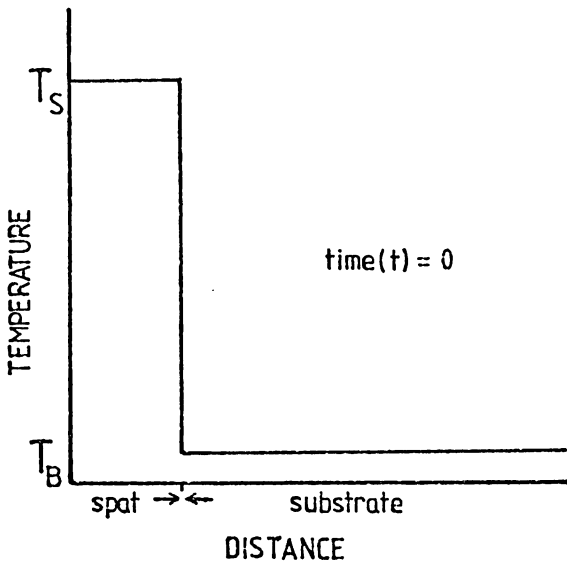
1.22 Temperature Profile for Ideal Cooling (Schematic)

T_S

t = 0

h→0

TEMPERATURE

$t_1 > 0$

$t_2 > t_1$

T_B

DISTANCE
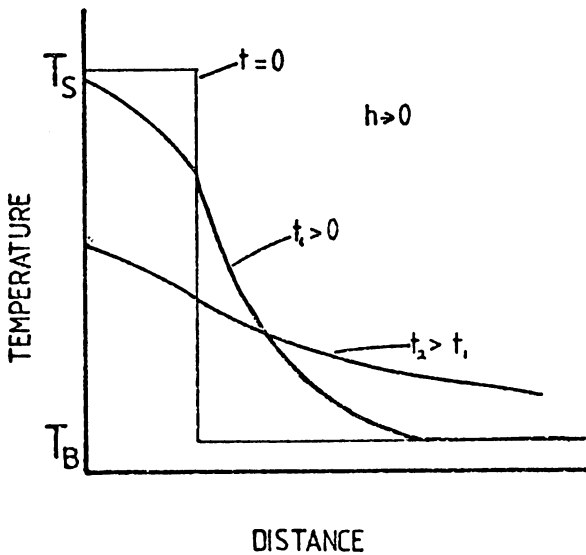
1.23 Temperature Profile for Newtonian Cooling (Schematic)

T_S

t = 0

$t_1 > 0$

h>>0

TEMPERATURE

$t_2 > t_1$

T_B

DISTANCE
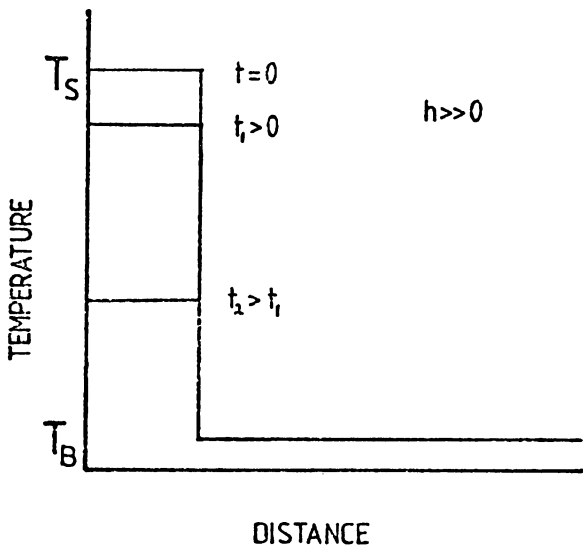
$$T = T_B + (T_s - T_B) \exp \left\{ - \frac{ht}{\rho C_p \ell} \right\} \qquad \text{(fig.1.23)} \qquad (1.9)$$

T_B : Substrate temperature, T_s = starting temperature

ℓ : position in frame of reference

The dimensionless group $h\ell/k$, where ℓ is splat thickness, h is the transfer coefficient and k thermal conductivity is known as the Nusselt Number (Nu), essentially if Nu > 30 cooling is ideal, when Nu < 0.015 cooling is Newtonian and intermediate cooling exists between these values. Cooling rates of $8 \times 10^9 Ks^{-1}$ could be obtained with Fe on a Copper substrate assuming ideal cooling and a splat thickness of 1.0μm, Ruhl (1967).

Figure 1.24 shows a summary of Ruhl's examination of ten variables of splat cooling for both ideal and Newtonian cooling.

From fig. 1.24 it can be seen that the splat thickness, heat transfer coefficient of the interface and instantaneous splat temperature have the greatest influence on the cooling rate and the former two determine the regime of cooling with the thermal conductivity. Even assuming Newtonian cooling with h =40kJ/m²sK, for pure tin a cooling rate of $2 \times 10^6 Ks^{-1}$ is achieved in a splat 20μm thick, at the melting point.

Ruhl's assumptions have been used by many workers when measuring cooling rates (see 1.4.2). However, Shingu and Ozaki (1975) insist that for a proper evaluation of rapid solidification in order to predict new structures, the rate of advancement of the solid-liquid interface must be taken into account. Their conclusions though do agree with the results of Ruhl's inasmuch as the solidification rate is strongly influenced by thickness, thermal contact resistance and the difference between initial temperature and freezing point of the solidifying material. Davies and Lewis (1976) suggest that although Shingu and Ozaki's theoretical assumptions are mainly correct they have not taken into account the viscosity changes which occur and their assumed value of 'h' is far too low and therefore the cooling is not close enough to "ideal" to be realistic.

Figure 1.24 Effects of Certain Variables on Cooling rate (U) (Ruhl, 1967)

For Fe splat on copper substrate.

Variable	Ideal	Newtonian
Time	Discontinuity at T_m which represents end of splat solidification.	After solidification cooling rate decreases more slowly than in ideal.
Splat Temperature.	Cooling rate does drop with decreasing temp. but not much effect until $T < 500°C$.	No cooling at melting point so rate drops to 0. Rate drops drastically at $T \sim 200°C$.
Position in splat.	Cooling rates vary considerably with highest rates near substrate.	By definition all temperatures within the splat are the same.
Initial splat temperature, T_s	As T_s increases U drops slightly. The effect is minor.	Little effect.
Solidification Range or Temperature.	Little effect.	Little effect but no period of zero cooling rate.
Initial Substrate Temperature, T_B	Little effect until T_s approaches T_B	Little effect in most cases except low melting point alloys.
Splat and Substrate Materials.	U depends on thermal properties of both materials but effect is small compared with t and h.	Differences occur due to L_F and T_m of splat materials. Substrate material in-consequential, but both influence Nu, thus criterion for Newtonian cooling is also affected.
Splat thickness. (ℓ)	$U \propto \ell^{-2}$ Also affects Nu.	$U \propto 1/\ell$
Interface heat transfer co-efficient (h)	No effect if in the ideal regime.	$U \propto h$

1.4.2. Measurement of Cooling Rate, U, during rapid solidification.

Very few researchers have actually attempted to measure the cooling rates in splat cooling directly. Thomas and Willens (1964) estimate U to be in the region of $10^6 Ks^{-1}$ by assuming solidification stopped the observed amount of spreading. Duwez (1966) obtained the same value by using high speed cine films at 1000 frames per second. Brown et al (1965) used an ingenious method to actually measure the cooling rates in the gas quenching of Titanium. Using a thermocouple attached to the solid specimen they showed that rates up to $8000Ks^{-1}$ could be measured. Problems obviously arise though if one is trying to measure the cooling rate through a liquid solid transition. Predecki et al (1965) used the thermo-electric voltage produced when the molten metallic droplets contacted a bimetallic substrate in the gun technique. Cooling rates of between 10^6 to $5 \times 10^8 Ks^{-1}$ were reported using a silver/nickel substrate. Relying on the same effect but this time using a piston and anvil apparatus to quench, cooling rates of 7×10^5 to $1.2 \times 10^6 Ks^{-1}$ for Pb and Al have been obtained using iron and aluminium plates as the intrinsic thermocouple. (Harbur et al, 1969). The Nusselt number was also calculated and for all the alloys and substrates used cooling was found to be in the intermediate regime using Ruhl's criterion. A calorimetric method was designed by Pond and Winter (1976) to measure the cooling rates obtained in melt spinning and melt extraction. By measuring the temperature rise of a bath of trichloroethane when the fibres were spun into it, the product temperature was calculated. From the wheel velocity and "arc of contact" length, the ribbon's "dwell time" on the wheel can be calculated. Assuming no significant quenching through the atmosphere before being quenched by the trichloroethane the quench rate is taken as the temperature difference between the molten metal and solid product divided by the dwell time. Values obtained were about $1 \times 10^6 Ks^{-1}$ for melt spinning and $5 \times 10^4 Ks^{-1}$ for melt extraction for Sn, Zn and Pb and consistent with those values

measured using microstructural features. This difference in cooling
rates between the two processes would seem to arise from the differing
thickness of product, the tape for melt extraction being 2 to 3 times
thicker than the melt spun material. The most recent attempt to make
a direct measurement of cooling rate is by Shohoji et al (1982). Using
the idea of pyrometry, black and white photographs were taken of the melt spinning
of Ni based superalloys at 1/2000s. By calibrating the film density against
a platinum standard of known temperature and spectral emissivity using wedge
pyrometry, a temperature profile of the melt puddle and subsequent solid
state quench can be obtained. These workers estimated a cooling rate of
$1.5 \times 10^5 Ks^{-1}$ for a 40μm tape. The method has two main drawbacks, firstly
if an oxide layer forms on the surface of the melt then the emissivity
changes therefore the calibration with clean platinum is incorrect, secondly
it cannot be used if the temperatures are below 600°C (Warrington, 1982, private
communication).

As has already been mentioned a common way of estimating the cooling rate
is by measuring some microstructural feature, usually in alloys the dendrite
spacing,s,(Matyja et al, 1968) although lamellar spacing,λ, (Chadwick, 1963;
Burden and Jones, 1970) and grain size,d, (Boswell and Chadwick, 1977)
have been used. The relationship between the cooling rate U and such
features can be approximated as follows.

Dendrite spacing $\qquad s \propto U^{-0.33}$

(Work done on Al alloys)

Lamellar spacing $\qquad \lambda \propto U^{-0.5}$

$(Al-GeAl_2)$

Grain size $\qquad d \propto U^{-0.9}$

(Aluminium)

These empirical relationships can really only be applied to the system
for which they were measured. As they are very close to theoretical

predicted values, they could be used as a guide for other systems however it must be remembered that they were mainly obtained by extrapolating from data obtained at low <u>directly measurable</u> cooling rates. Comparison with direct measurements made is favourable but do suggest a slight over-estimation of the cooling rates obtained. One of the best accounts of methods used to estimate cooling rates is given by Jones (1978).

1.5. Tin Bearings: History, Properties and Structure.

1.5.1. Brief History.

Whenever there is movement between two surfaces some form of bearing is created. It has been suggested that the earliest concept of a bearing is 5000 years old. Traces of lubricant, such as animal fats, have been found on very early examples of bearing surfaces the oldest case is an Egyptian charriot some 3400 years old. Leonardo da Vinci (da Vinci c.1498; Reti, 1971) made references to the design of bearings which are very similar to the concept patented by Babbitt (1839). Da Vinci also refers to "antifriction metal" being made of three parts copper and seven of tin.

This first notion of a plain bearing has changed little over the years, only the materials have changed from linings of iron, copper or bronze (Bierlein, 1975) to Tin, Lead or Aluminium based alloys.

1.5.2. Bearing Alloys of Tin

In 1839 Isaac Babbitt from USA patented a "mode of making boxes for axles and gudgeons" (Babbitt, 1839) in which he states the lining should be of "Britannia metal or pewter", and in particular the composition should be "50 parts of tin, five of antimony and one of copper" ($Sn9\%Sb2\%Cu$). Despite extensive research in bearings and bearing alloys the current commercial "Babbitt" or "White" metal is little different $Sn7-8\%Sb3-4\%Cu$ which is cast onto a variety of backing materials (e.g. Steels and Bronzes) often continuously. Approximately 7% of the total output of tin is used in the manufacture of pewter and bearing alloys (Robins, 1980) and as engineering requirements become more stringent other alloys are replacing it, because of their better fatigue resistance.

1.5.3. Properties required of a bearing material

Figure 1.25 is a schematic diagram of a typical Journal bearing. The shaft (journal) rotates in a sleeve (bearing) of slightly larger diameter and the remaining gap is filled with a lubricant. As can be seen from the

Figure 1.25

Diagram of a Plain or Journal Bearing showing
Eccentricity of the Oil Film on Loading and with
Rotation.
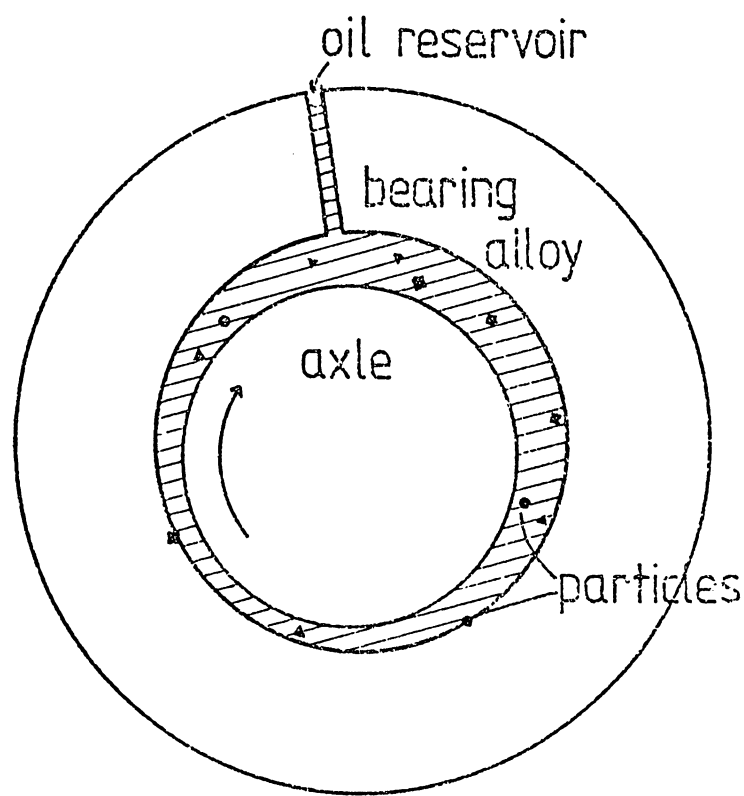
diagram the shaft runs eccentrically as a result of the load and its

rotation; the oil film is therefore unevenly distributed and thus can

often break down.   Should this happen the shaft and bearing must not weld

by friction or "seizing" will take place, for this reason it is advantageous

if the bearing has a low melting point or low melting point constituent,

and temporarily melts, this property is known as "compatability".

It can be seen that the main strengths required by the material used

in such a situation are compressive, and as the shaft is rotating and

stresses are cyclic, fatigue resistance is very important (Honeycombe, 1946).

These strengths have to be maintained often in temperatures in excess of

$100°C$ (>0.7 T_m for Babbitts) Good thermal conductivity is therefore important

to dissipate the heat generated by the friction at the surface and thermal

fatigue has to be avoided as such bearings are usually not run continuously.

In such conditions wear resistance is important but the bearing surface

should not be so hard that the shaft is worn. It should also have good

"embeddability", as oils often contain particles of detritus which have to

be accepted into the material of the sleeve without producing general

deformation of the surface. The ability to adsorb lubricant is highly desirable

and yet the material must be able to withstand the corrosive environment

without failing.

Although high strengths are needed for fatigue and load bearing the sleeve

must also be soft enough to "conform" to any irregularities in the shaft or

alignment while it is being "run in".

The performance of tin based bearing alloys has been compared with

other materials by Bierlein, (1975) fig.1.26.

1.5.4. The Microstructure of tin bearing alloys.

A typical tin based bearing alloy has the microstructure shown in

figure 1.27.   The three phases are primary needles of Cu_6Sn_5, secondary

cuboids of SbSn and a matrix of Sn rich solid solution often described as a

Figure 1.26

Comparison of The Properties of Bearing Materials (after Bierlein, 1975)

EMBEDDABILITY

RESISTANCE TO FATIGUE

RESISTANCE TO SCORING

RESISTANCE TO CORROSION

SILVER GRID

SILVER

TIN BASED BABBITT

LEAD BASED BABBITT

ALUMINIUM 20% TIN

COPPER — LEAD
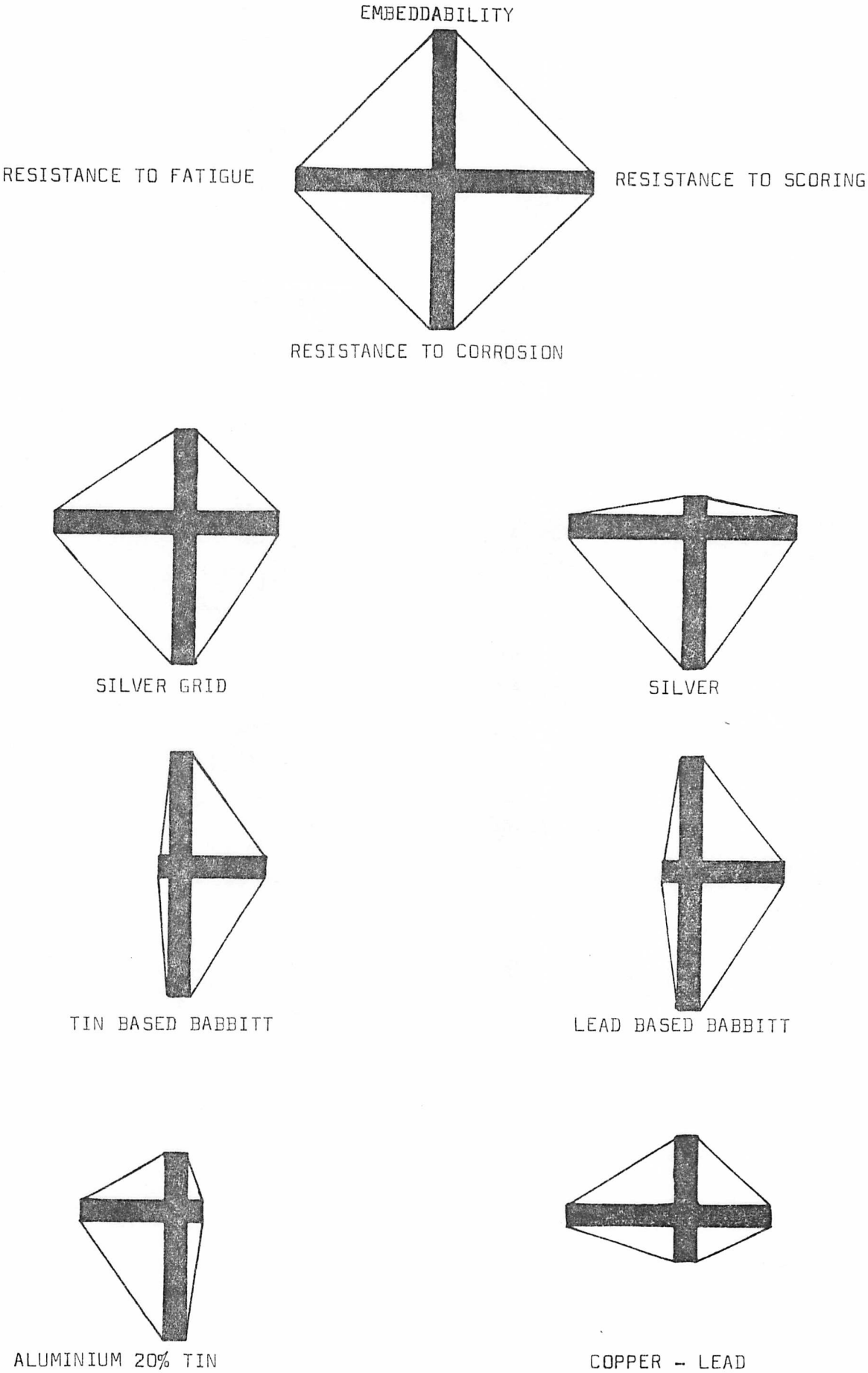
"psuedo-eutectic" (fig.1.28). The traditional requirements of a bearing alloy microstructure are that it should consist of <u>two</u> phases, hard load bearing particles in a soft matrix which is able to accept damage and channel the lubricant. This hypothesis has not been discredited and only one <u>single</u> phase material has been tried. Dayton (1938) used silver, which, apart from being extremely expensive had a tendency to seize at low loads after running for some time at high loads. Any developments in bearings would therefore seem to be dependent on the improvement of existing tin alloys as their performance is unrivalled excepted in the area of fatigue.

Figure 1.27

Micro-structure of a typical White Metal

Bearing Alloy of Composition Sn-9.5% Sb-4.5% Cu

100μm
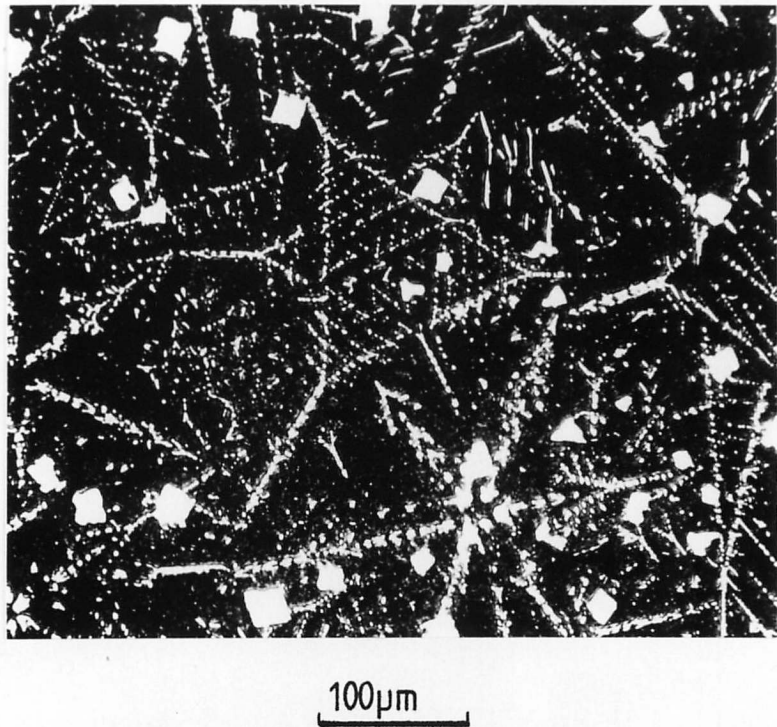
Figure 1.28

Phase Diagram of the Sn-Sb-Cu System (as cast).
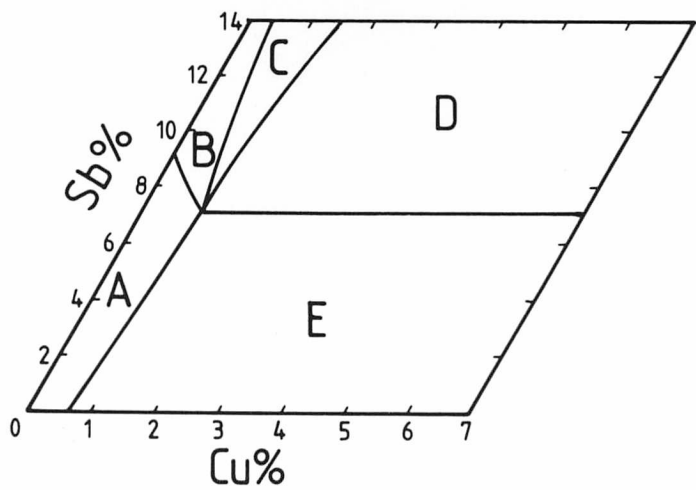
A: Matrix only

B: Matrix and Primary SbSn

C: Matrix, Primary SbSn and Secondary Cu_6Sn_5

D: Matrix, Primary Cu_6Sn_5 and Secondary SbSn

E: Matrix and Primary Cu_6Sn_5

1.6. Choice of Alloy system and Process

The microstructure of Babbitt metals is three phased rather than the required two phases. The addition of copper to the binary Sn-Sb system produces the primary needles of Cu_6Sn_5 which being denser than the liquid during solidification tend to sink while the lower density SbSn cuboids float. The two phases thus physically interact to produce an even distribution of intermetallics.

As can be seen from figure 1.26 tin based alloys perform well in all fields except fatigue and as loads in heavy duty engineering applications increase it is this property which must be improved without a detrimental effect on the others.

Rapid quenching from the melt, as has been shown in section 1.3, is known to increase terminal solid solubility in a large number of systems, and in addition to refine microstructures thereby improving mechanical properties. On ageing excess solute can be precipitated and thus give rise to further strengthening. Changes of intermetallic morphology might also occur as reactions which originally occurred in the liquid state now become solid state, thus introducing constraints on the growth direction.

Due to the rapidity of the solidification the need for copper additions in Babbitt metals may become redundant as segregation would be repressed, if indeed the SbSn is formed at all.

From these considerations the Sn-Sb binary system (fig.1. 5) was chosen as a logical initial starting point for the investigation of the effects of rapid solidification on tin alloys.

As has been seen in section 1.3 the number of available techniques for rapid solidification is fairly large. It was decided that the most convenient method to produce large quantities of easily handled product was melt spinning (1.3.3.b).

Chapter 2.   MELT SPINNING

2.1. Design of Melt Spinning Machine (figure 2.1)

2.1.1. The Wheel.

The main component of the melt spinning machine is a large disc of
material of high thermal conductivity. This is usually made of copper or a
copper based alloy although silver could be used at prohibitive cost.
Alloys of copper are rather better than pure copper as their wear resistance
is superior. It is not necessary to have a solid copper wheel for often it
is enough to heat shrink a copper rim of about 10mm depth onto a disc of
cheaper engineering material, for example steel. Such a hub need not be
solid but contain holes to reduce the inertial forces. However for long
production runs the larger the mass of the wheel and the higher the
conductivity the better. Other surfaces than copper, brass or silver have
been used for example, chromium plating to reduce wear.

The disc is usually driven by a variable speed electric motor either
directly, or via a belt and cog system. The speed should ideally be
tachometrically controlled, as the forces applied to the wheel during
spinning,especially when using multiple nozzles, can be enough to slow it
down. By contrast, Pavuna and Hainsworth (1980) use the water turbine
principle to drive their low temperature wheel with Argon as the propulsion
fluid.

In the present work the 230mm diameter wheel was driven by a 1hp motor
(750W) at speeds of up to 2700rpm giving circumferential velocities from 10
to 33ms^{-1}. The surface of the wheel had an 18mm wide flat used for melt
spinning and two knife edges for the purpose of melt extraction.

2.1.2. The Crucible.

The crucible performs two functions. The first is to contain the
solid and liquid material before ejection without either itself melting,
or reacting with the molten charge. The second is to direct the molten

Figure 2.1

The Melt Spinning Apparatus
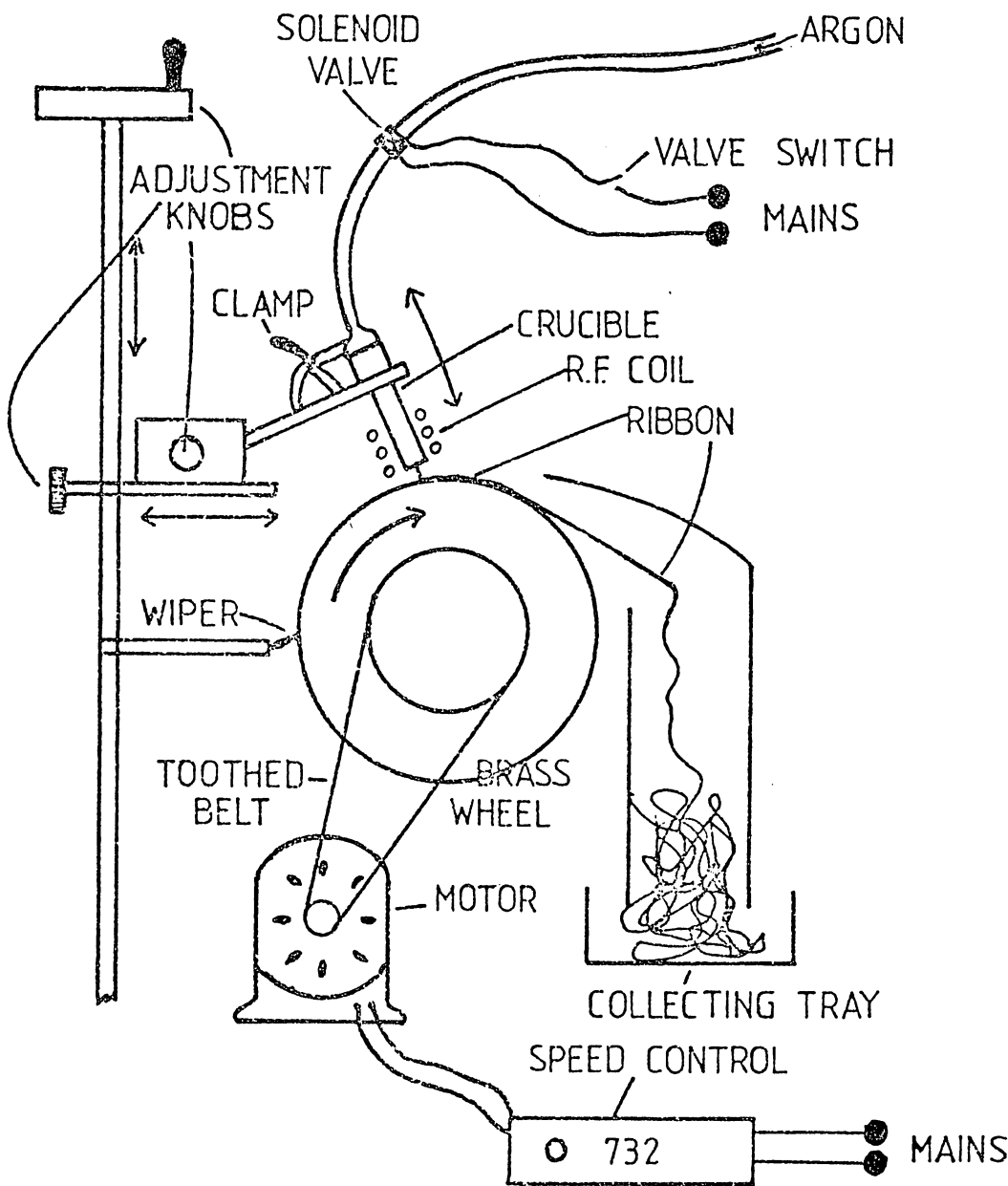
material at the angle, height and flow rate required to produce uniform, sound ribbon.

Early workers in the field (Duwez and Willens, 1963, Pond and Maddin, 1969) used silica or quartz crucibles. These perform adequately with respect to the first function but to produce an exactly circular orifice is exceedingly difficult, the wear resistance of these materials is not sufficiently high enough for them to be of commercial value. Initially in the present work the crucibles used were made of silica but problems with the flow from the nozzle led to other materials being used. Graphite was the first substitute its benefits being that it was cheap and extremely easy to machine and so almost any profile nozzle could be made. Wear was however a major problem, after a few runs the orifice was considerably enlarged (fig.2.2). The other problem encountered was lack of strength, when heated the graphite oxidised rapidly, more so at hot spots created by the Radio Frequency (R.F.) induction heating coil. The result was failure on application of the ejection pressure (fig.2.3). To supply the graphite crucible with more strength and to cut down on the amount of machining required a mild steel sheath was then used to support it, the result is shown in fig.2.4. The affinity of carbon for steel produced cast iron which melted under the conditions of R.F. heating. The final choice of material was stainless steel. Originally the crucible had interchangeable nozzle plates which screwed onto the bottom of the crucible tube but a problem was encountered with the high penetration of tin and consequently sealing the joint proved to be very difficult. The final design of crucible is shown in fig.2.5. and the results of this shape on the flow of the material is discussed in section 2.4.

Alignment of the crucible with respect to the wheel, thus giving control over angle of impingement and length of molten stream was achieved by mounting

Graphite Crucibles

2.2 Enlarged Crucible Orifice

10 mm

• original orifice size
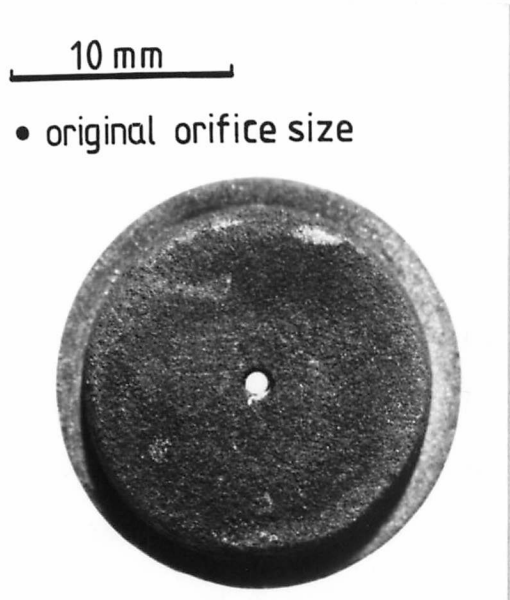
2.3a Failed Graphite Crucible

2.3b Failed Graphite Crucible

2.4 Mild Steel Sheath

the crucible and R.F. coil, as one unit on a Sindanyo block which was connected

to an axle between two helical gears. Two worm gears gave a step down ratio

of 180:1 and thus the angle could be changed by 2° for every revolution of

the adjustment knob (fig.2.6). Vertical, horizontal and lateral movement

was achieved by three simple sliding rod arrangements all controlled by

screw threads (fig.2.7). Flexible leads to the induction coil were

incorporated into the apparatus thus giving complete freedom of movement,

and accuracy by adjustment of the controls.

It was felt that these were necessary developments in the apparatus as

previously the only method of adjusting the process parameters of angle and

height was by bending the solid R.F. leads and moving a retort stand and

clamp (Patterson 1979).

2.1.3. Other Features

Gas ejection was achieved via an electrically operated solenoid valve

which proved necessary during the work using high speed cine photography

(section 2.5). Argon was used as the ejection gas at pressures of 25 to

210 kPa.

The wheel was cleaned every revolution by a soft cloth wiper which

had the added effect of helping to destroy the gas boundary layer on the

wheel (section 2.4). After every run the wheel was abraded with 1200 grade

emery paper and polished with "Brasso" metal polish to give a mirror surface

finish.

The product ribbon was channelled into a collecting tray by an

Aluminium tunnel. The whole apparatus can be seen in figure 2.8.

2.2. Process parameters and their effect on ribbon dimensions.

The process of melt spinning can be described by the following

parameters:

(i)   melt jet impingement angle with respect to substrate, β,

(ii)   ejection gas pressure, P or melt jet velocity, v_j

Details of Melt Spinning Apparatus (I)

2.5   Stainless Steel Crucible Design.
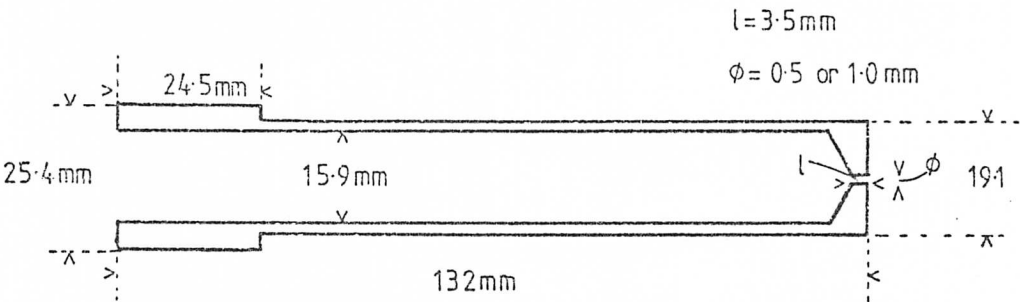
2.6   Diagram of Gear Box for Tilting Mechanism.
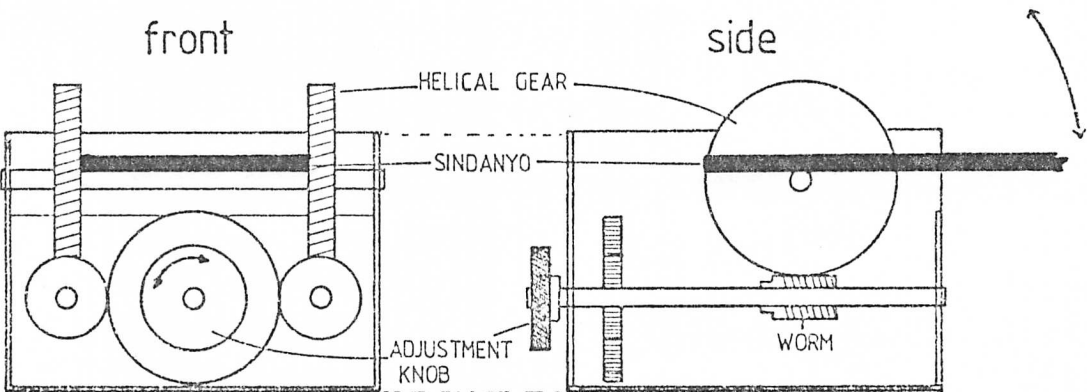
Details of Melt Spinning Apparatus (II)

2.7   Diagram of Alignment Mechanism.
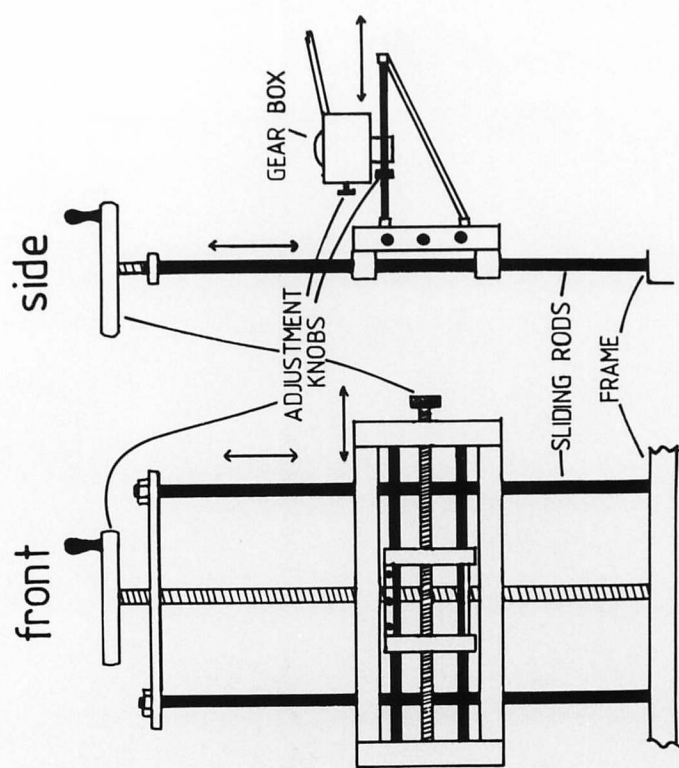
2.8   Photograph of Melt Spinning Machine.
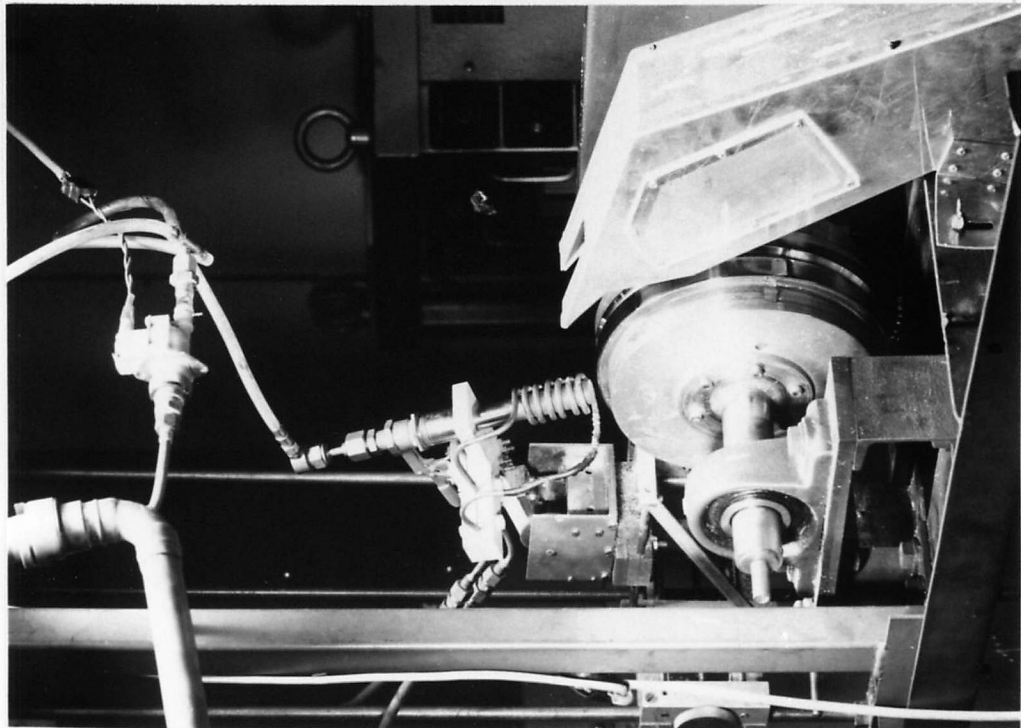
(iii)   crucible orifice diameter, ϕ

(iv)   substrate surface speed (ribbon production speed) $v_s (v_R)$

(v)   substrate microfinish, R_s

(vi)   substrate material

(vii)   melt temperature, T_ℓ

(viii) melt composition

(ix)   atmosphere

(Liebermann, 1979c)

Variation of any of these can change the ribbon dimensions of thickness, t, and width, w.

2.2.1. Empirical Analyses

Liebermann and Graham (1976) made the first detailed study of melt spinning parameters, although Williams and Jones (1975) had studied the effect of melt superheat and impact velocity on splat dimensions in the gun technique.   They found that as superheat and velocity increased the thickness decreased.

By applying Bernoullis equation for an inviscid incompressible fluid in a pipe,

$$P + \tfrac{1}{2} \rho v_j^2 + 2h\rho g = k \tag{2.1}$$

where P is the applied pressure, ρ is liquid density v_j is the velocity of liquid, h is any change in height of the fluid and k is a constant.

and using a mass balance, again assuming incompressibility,

$$A_R v_R = A_j v_j \tag{2.2}$$

where A_R, A_j are the cross sectional areas of the ribbon and liquid stream respectively and v_R and v_j their velocities,

and by assuming that

$$A_j = \frac{\pi \phi^2}{4} \tag{2.3}$$

Liebermann and Graham obtain the equation

$$A_R = \frac{\pi \phi^2 P^{\frac{1}{2}}}{\rho^{\frac{1}{2}} v_R 2^{3/2}} \tag{2.4a}$$

Figure 2.9

Plots of A_R against $\dfrac{\phi^2 \rho^{\frac{1}{2}}}{v_R}$ to measure the

Discharge Coefficient, C_D (Charter et al, 1980)

a) Sn
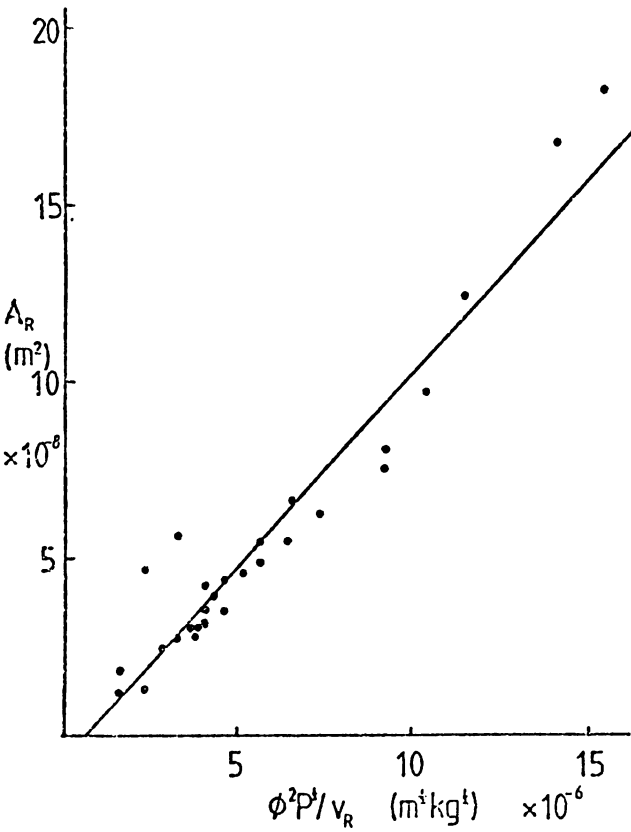
b) Sn 5% Sb
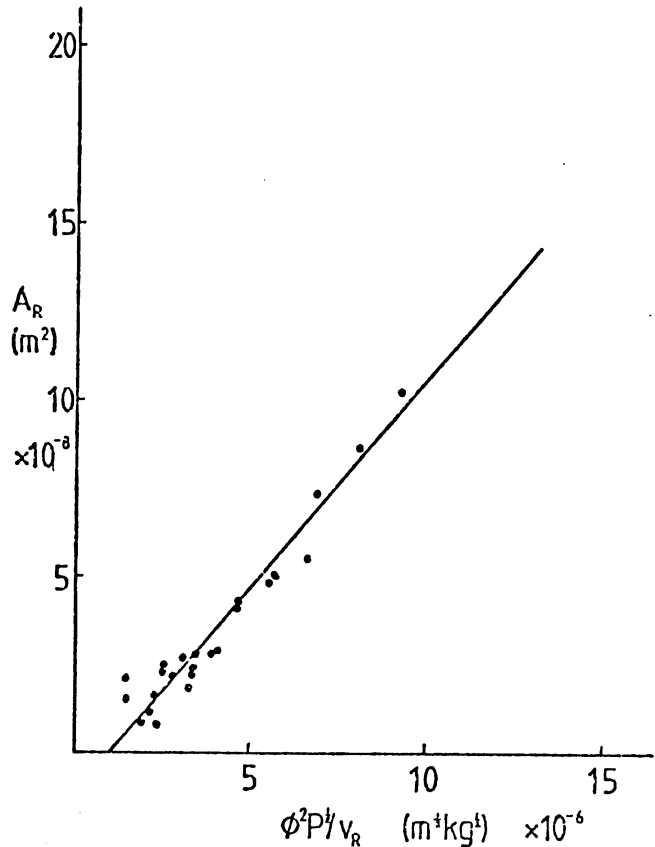
c) Sn 10% Sb
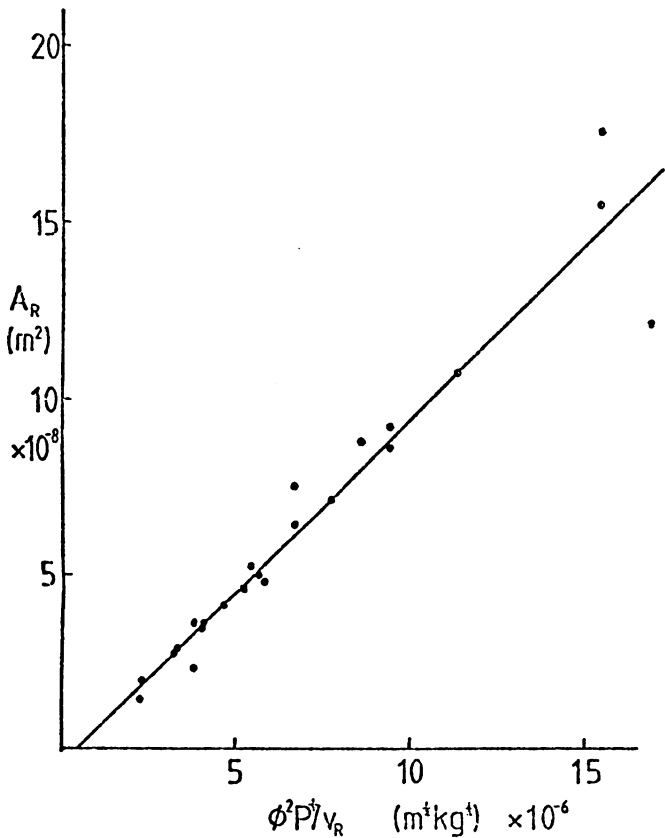
d) Sn 15% Sb
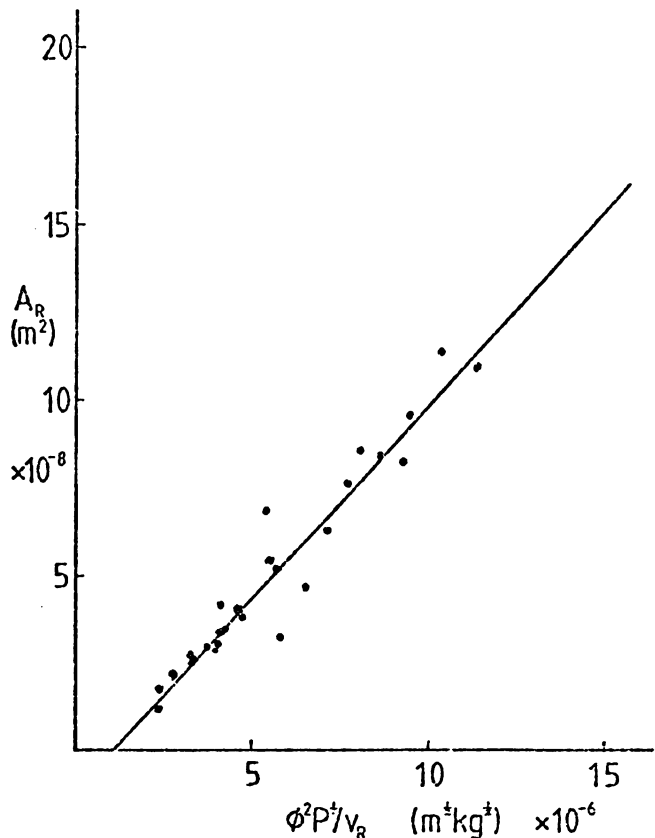
It has since been suggested (Charter et al, 1980) that the proportionality may not be unity if flow is not perfect (see section 2.4) and so a "discharge coefficient" C_D is introduced, so that

$$A_R = C_D\left(1.979 \ \frac{\phi^2}{v_R}\right)\left(\frac{P}{\rho}\right)^{\frac{1}{2}}$$ (2.4b)

From the results of the present work plots of A_R against $1.979 \text{x} \phi^2/v_R(P/\rho)^{\frac{1}{2}}$ were constructed for tin and tin-antimony alloys (fig.2.9). Figure 2.10 gives the values of C_D obtained for such plots.

Charter et al (1980) obtain values for C_D of 1.02 and 0.76 for Pb-Sn and Al (Mn,Fe) melts respectively. They suggest that the lower value of C_D, the poorer the castability of the alloy.

Neither Liebermann and Graham nor Charter et al. take into account the change in the flow rate that might occur throughout one run due to the change of head of molten metal. This may be a reasonable assumption with charges of 2/3 grammes as in their case but in this work charges were often in excess of 80 grammes. The original assumption ignoring the "hρg" quantity in the Bernoulli equation is therefore not valid and will give the random variations of C_D values. The drop in jet velocity at low ejection pressures can be 10% from start to finish of a run. Assuming the jet area and substrate velocity remain constant then the variation of ribbon cross section could be of the same order of magnitude.

The thickness of the ribbon produced can be assessed in two ways either by measuring with a micrometer thus giving the maximum thickness, t_m, or by measuring the width, w, and length, 1, of a known mass of ribbon, m, and using the density, ρ, to give an average thickness, $\bar{t}$, from the equation

$$\bar{t} = \frac{m}{1w\rho}$$ (2.5)

Figure 2.11 shows plots of $\bar{t}$ against v_R and as Liebermann and Graham state, they indicate that the ribbon thickness is primarily controlled by

Figure 2.10

Values of C_D for tin and tin-antimony alloys

Alloy	C_D	Corr.
Sn	0.85	0.96
Sn 5% Sb	0.90	0.96
Sn 10% Sb	0.75	0.97
Sn 15% Sb	0.84	0.96

Figure 2.11

Plots of thickness ($\bar{t}$) against substrate velocity (v_R)

at constant Ejection Pressure, for pure tin.
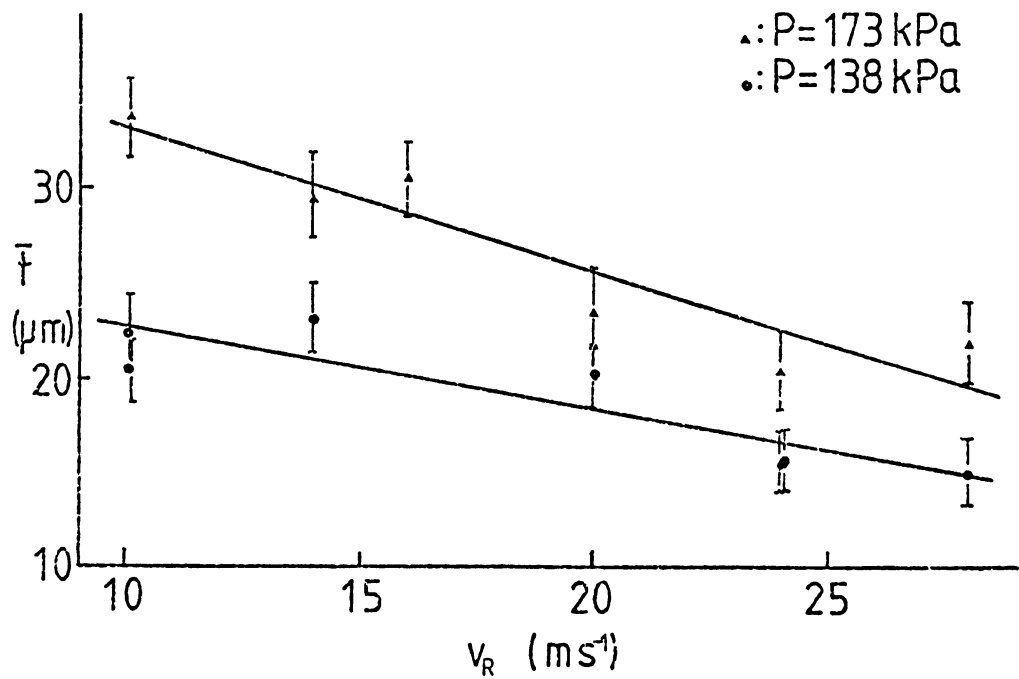
substrate speed such that

$$\bar{t} \propto \frac{1}{v_R} \qquad (2.6)$$

for a constant ejection pressure. Liebermann and Graham (1979) define an empirical relationship for $\bar{t}$ dependent on v_R, ϕ and P, for the $Fe_{40}Ni_{40}B_{20}$ system such that

$$\bar{t} = \frac{v_R}{(0.354 - 0.510\phi)v_R \quad -6.18 + 9.81\phi} + \frac{12.6P}{1.35v_R} \qquad (2.7)$$

where v_R is in ms^{-1}, ϕ in mm, P in kPa and $\bar{t}$ in μm.

Empirical equations such as the above can only be applied to the alloy system and apparatus configuration from which the relationship was derived and as such are very limited in their usefulness. In this work no such attempt is made to produce a relationship, for only one orifice diameter was used for the majority of runs.

To obtain a relationship for the width of the ribbon produced most workers assume a parameter called the "volumetric flow rate" Q which is given by

$$Q_R = v_R \, w \, \bar{t} \qquad (2.8)$$

Q can also be defined by

$$Q_j = A_j v_j \qquad (2.9)$$

$$= \frac{\pi\phi^2}{2^{3/2}} \left(\frac{P}{\rho}\right)^{\frac{1}{2}} \qquad (2.10)$$

As can be seen from figure 2.12 these two methods of calculating Q give comparable figures and the differences arise from casting instabilities and are measured by the discharge parameter C_D so that

$$Q_R = C_D \, Q_j \qquad (2.11)$$

The width of the ribbon can be related to the flow rate Q_R by the expression

$$w = w_o + \frac{Q_R}{v_p} \qquad \text{(Liebermann, 1979c)} \qquad (2.12)$$

where w_o and v_p are constants.

Figure 2.12

Values of Q_R and Q_j for Pure Tin.

v_R (ms^{-1})	P (kPa)	Q_j m^{3}s^{-1}	Q_R m^{3}s^{-1}
23.5	48	715	314
16	173	1352	880
14	173	1352	864
10	173	1352	970
28	173	1352	859
28	35	605	338
28	208	1481	878
20	208	1481	1096
20	138	1209	888
20	104	1047	852
20	35	605	940
20	208	1481	980
20	173	1352	919
20	69	855	567
28	69	855	1028
28	138	1205	768
28	104	1047	675
24	173	1352	956
10	138	1209	750
24	138	1209	690
24	138	1209	734
10	138	1209	810
10	35	605	352
28	35	605	522
20	104	1047	714
14	138	1209	928

Plots of w against Q_R are shown in figure 2.13 and the values obtained for the constants are shown in figure 2.14. The constant ν_ρ can be described as the "melt puddle viscosity", it has the same units as kinematic viscosity $(m^2 s^{-1})$. The values obtained for tin alloys are all lower than the value of $1.12 \times 10^{-3} \ m^2 s^{-1}$ obtained by Liebermann for $Fe_{40}Ni_{40}B_{20}$ which is not surprising as tin is much less viscous than such alloys, just above their melting points.

The randomness of the values obtained for w_o could possibly be accounted for by instabilities in casting. w_o should be a reflection of the size of orifice used and should therefore be the same in each of the alloys used.

Liebermann (1979c) derives the following equations for w and $\bar{t}$ founded on observation and theory which take into account orifice diameter, ϕ, surface tension γ, volumetric flow rate, Q_R, and impingement angle, β.

$$w = \phi \ \frac{Q - Q_{min}}{\nu_\rho} \left(1 - \frac{\beta}{2}\right) \tag{2.13}$$

where $Q_{min} = \frac{\pi}{4} \phi^2 \left(\frac{8\gamma}{\rho\phi}\right)^{\frac{1}{2}}$ (2.14)

and if $\bar{t} = \frac{Q}{v_R w}$ (2.8)

then

$$\bar{t} = \frac{Q \ \nu_\rho}{\phi \ \nu_\rho + (Q-Q_{min})(1-\beta/2)} \cdot \frac{1}{v_R} \tag{2.15}$$

These "semi-empirical" relationships seem to fit his data very well but when applied to this work the results are somewhat dubious. They also make various assumptions regarding the flow of the jet and ignore the possibilities of changing conditions throughout a run.

Figure 2.13

Plots of width (w) against volumetric flow rate (Q) for
tin-antimony alloys to give values of
w_o and ν_ρ
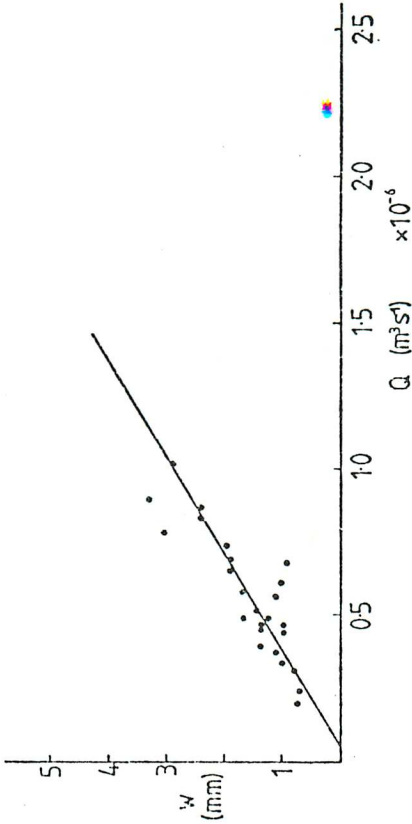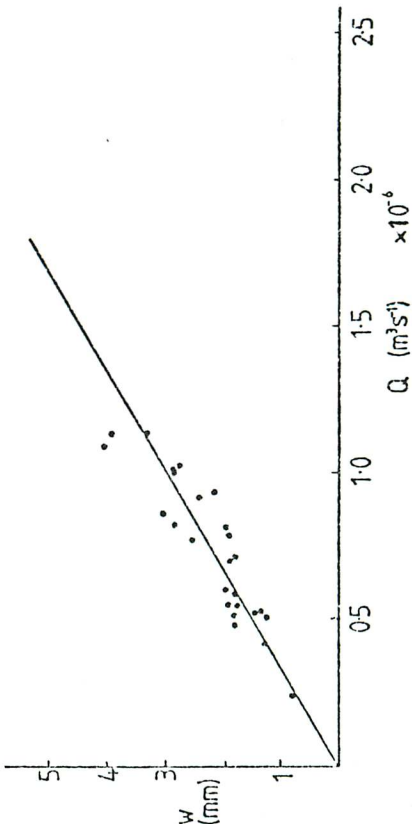
a) Tin
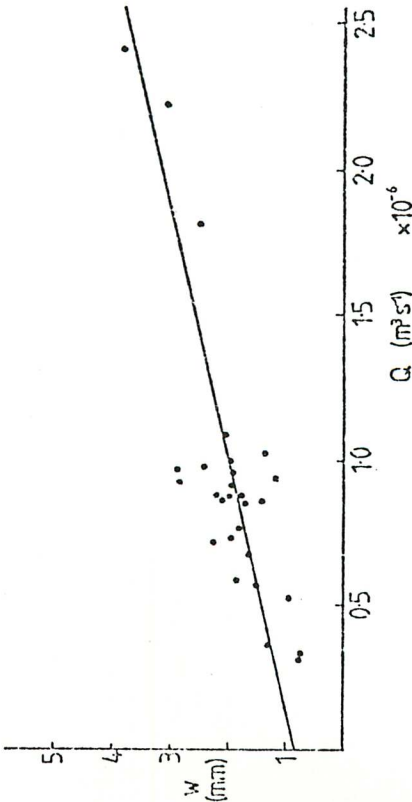
b) Sn 5% Sb
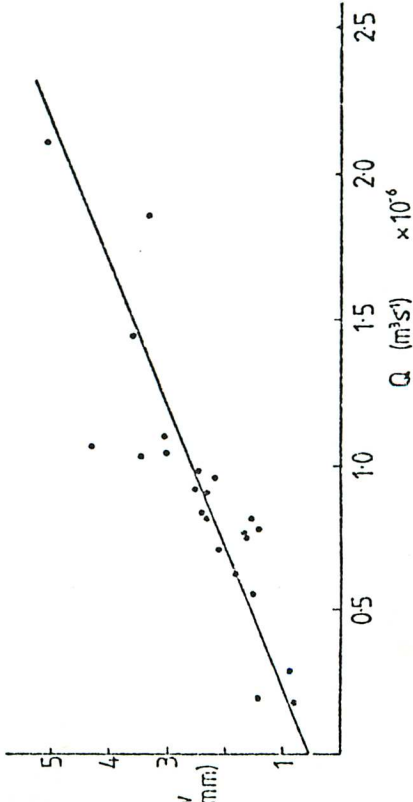
c) Sn 10% Sb

d) Sn 15% Sb

Figure 2.14

Values of w_o and ν_p from Liebermann's Analysis for width.

$$w = w_o + \frac{Q}{\nu_p} \qquad (2.12)$$

Alloy	w_o m x 10^{-3}	ν_p $m^2 s^{-1} x 10^{-3}$	Correlation Coefficient
Sn	0.86	0.864	0.79
Sn5%Sb	−0.15	0.330	0.86
Sn10%Sb	−0.54	0.485	0.86
Sn15%Sb	−0.05	0.343	0.89

2.2.2. Theoretical Analyses

The melt spinning process can be analysed by two methods; that of a transport dominated phenomenon, controlled by either a momentum or thermal boundary, or by an energy equilibrium situation which assumes a balance between the surface and viscous forces.

Kavesh (1978) assumes that thermal transport is the controlling process and states that for his analysis the following conditions must apply,

       (i)   no phase change (e.g. solidification)

       (ii)   initial temperature distribution is constant

       (iii) negligible cooling of top surface

       (iv) bottom surface temperature constant

       (v)   negligible viscous heating

       (vi) constant puddle thickness

       (vii) one dimensional heat flow

       (viii)negligible thermal contact resistance.

The first assumption is totally unreasonable for a microcrystalline alloy and the last two are not really correct. However he starts by assuming that the melt puddle is an ellipse of dimensions ℓ and w where $\ell \cdot w$ is constant. Workers have since questioned the validity of this assumption, Hillman and Hilzinger (1978) and Vincent et al (1981) suggest that ℓ/w is constant is a more viable criterion.

Kavesh arrives at the following expressions for w and $\bar{t}$

$$w = c_3 \left(\frac{Q^n}{v_R^{1-n}} \right) \qquad (2.16a)$$

and

$$\bar{t} = \frac{1}{c_4} \left(\frac{Q^{1-n}}{v_R^n} \right) \qquad (2.17a)$$

and predicts that n should be approximately 0.75 and c is dependent on jet angle.

In his energy balance analysis Kavesh assumes that the liquid puddle does not

"feel" the effect of the substrate velocity and therefore the width and length of puddle are independent of v_r. As

$$Q_R = v_R \, \bar{t} \, w \tag{2.8}$$

then

$$\bar{t} \propto \frac{1}{v_R} \tag{2.6}$$

Comparison of the two analyses shows that both arrive at a similar result for the relationship of $\bar{t}$ with v_R. However for the variation of w the analyses are very different.

Plots of $\ln(w\bar{t})$ against $\ln(Q_r v_R)$ and of $\ln(\bar{t}v_r)$ against $\ln(Q_R v_R)$ are shown in figure 2.15 for the alloys in the present work. An analysis using a three constant solution was also carried out such that

$$w = c_1 \left(\frac{Q^a}{v_R^{\,b}} \right) \tag{2.16b}$$

and

$$\bar{t} = \frac{1}{c_2} \left(\frac{Q^p}{v_R^{\,q}} \right) \tag{2.17b}$$

Figure 2.16 shows a summary of the results using both analyses.

Plots of observed values of w and $\bar{t}$ against calculated values of w and $\bar{t}$ are seen in figure 2.17. These show that the three constant analysis is only slightly superior to the two constant analysis. Kavesh analysed his own data for $Fe_{40}Ni_{40}P_{14}B_6$ and Liebermann's data for $Fe_{40}Ni_{40}B_{20}$ in the same fashion. Charter et al (1981) used the analysis for PbSn eutectic and Al(MnFe) systems. Vincent and Davies (1980) have also calculated values of n for various systems. Figure 2.18 summarises all these results.

Hillmann and Hilzingers' (1978) analyses assume that

$$t \propto \left(\frac{\ell}{v_R} \right)^m \tag{2.18}$$

ℓ is the puddle length and ℓ/v_R is a parameter called the dwell time, τ.

Figure 2.15

Plots of wV_R and $\bar{t}V_R$ against QV_R to find the constants, 'c' and 'n', in the Kavesh Analysis using 2 constants, for tin-antimony alloys.
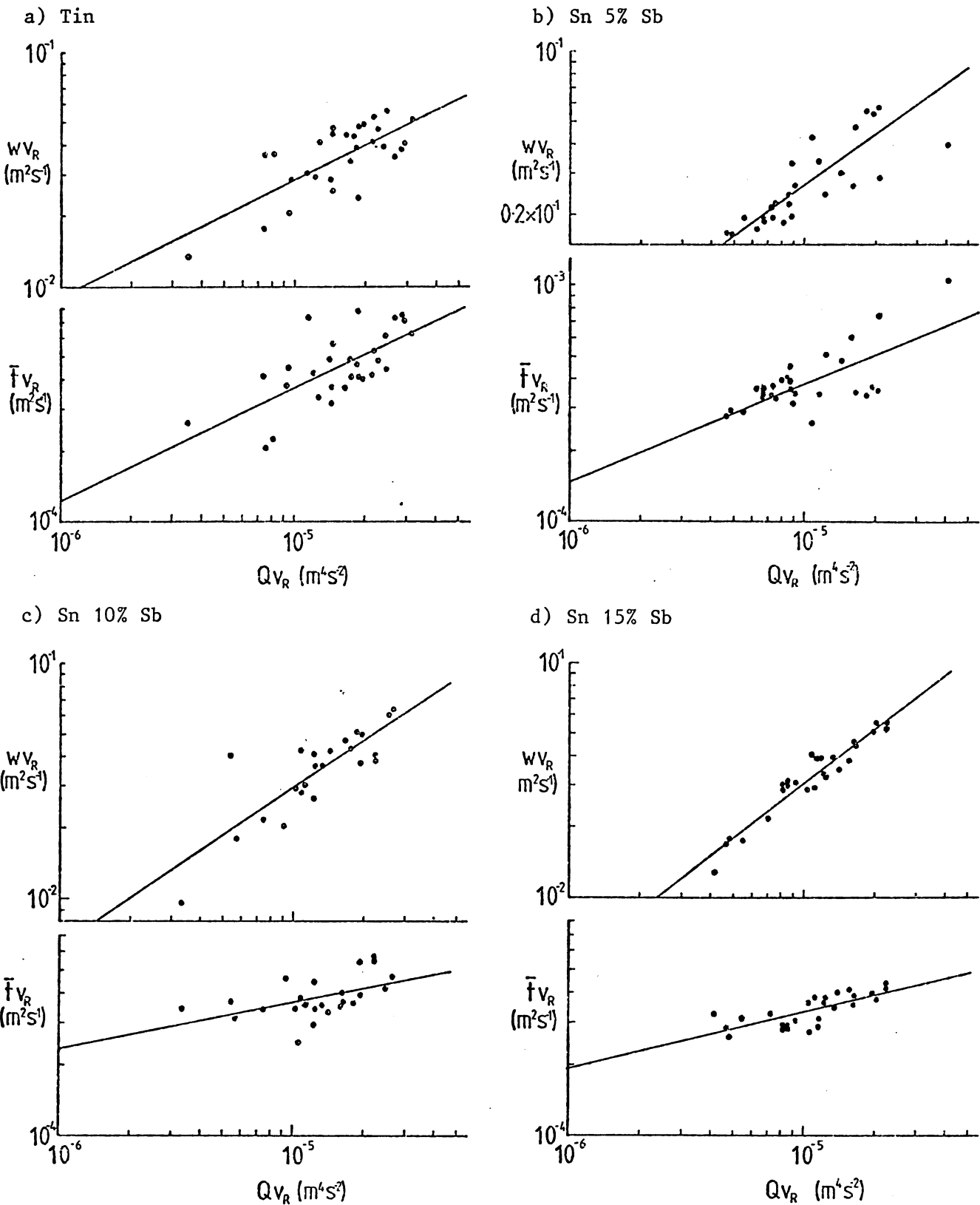
Figure 2.16

Summary of results of the Kavesh Analysis for the variation of $\bar{t}$ and w with Q_R and v_R during melt spinning, for tin and tin-antimony alloys.

2 constants

$$w = c_3 \left(\frac{Q^n}{v^{1-n}} \right) \qquad \bar{t} = \frac{1}{c_4} \left(\frac{Q^{1-m}}{v^m} \right)$$

$c_3 \sim c_4$

$m \sim n$

$1-m \sim 1-n$

width

Alloy	n	1-n	c_3	R
Sn	0.50	0.50	8.7	0.81
Sn5%Sb	0.72	0.28	103.5	0.90
Sn10%Sb	0.67	0.33	69.4	0.89
Sn15%Sb	0.77	0.23	208.5	0.96

thickness

1-n	m	c_4	R
0.47	0.53	11.8	0.78
0.41	0.59	23.6	0.91
0.19	0.81	292.9	0.82
0.24	0.76	200.3	0.93

3 constants

$$w = c_1 \left(\frac{Q^a}{v^b} \right) \qquad \bar{t} = \frac{1}{c_2} \left(\frac{Q^P}{v^q} \right)$$

$c_1 \sim c_2$

$a \sim q$
$b \sim p$
$b \sim (1-a)$
$p \sim (1-q)$

width

Alloy	a	b	c_1	R
Sn	0.53	0.58	18.11	0.83
Sn5%Sb	0.59	0.42	23.3	0.88
Sn10%Sb	0.65	0.20	35.8	0.89
Sn15%Sb	0.85	0.31	894.4	0.97

thickness

p	q	c_2	R
0.34	0.40	109.6	0.73
0.41	0.61	22.0	0.93
0.17	0.69	609.9	0.82
0.15	0.68	863.2	0.93

Figure 2.17a-d

Plots of observed width (w_{obs}) against calculated width (w_{calc}) for melt spinning of tin-antimony alloys using Kavesh Analysis for two and three constants.

Legend ———•——— : two constants ——•—— : three constants

a) Tin   b) Sn 5% Sb
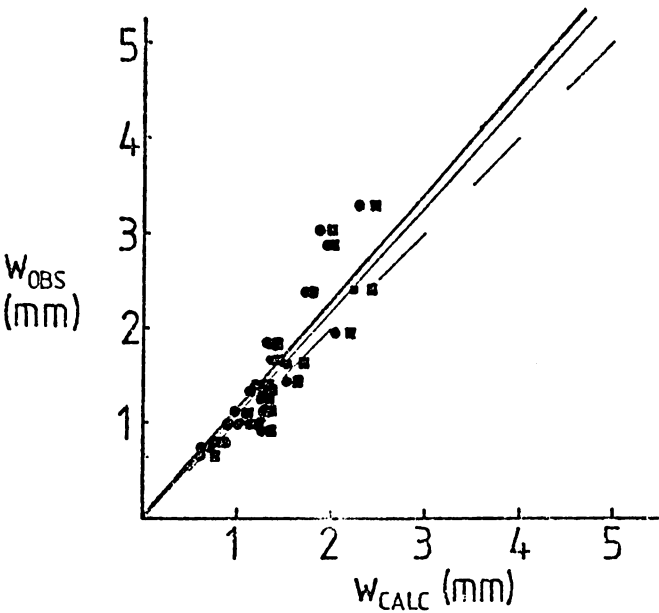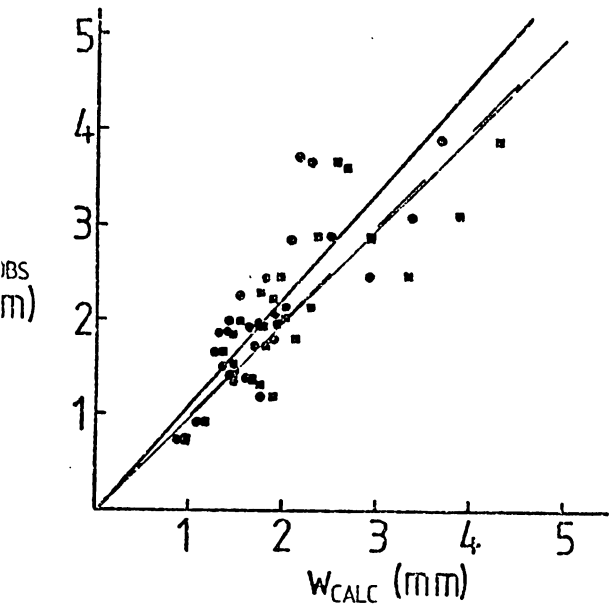
c) Sn 10% Sb   d) Sn 15% Sb
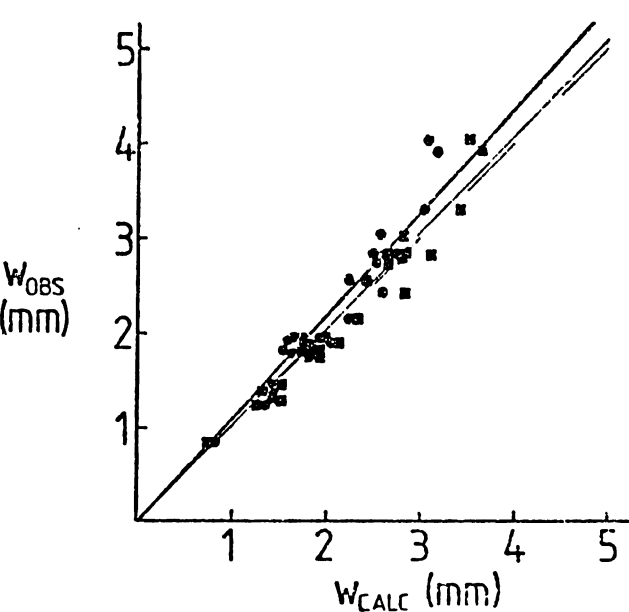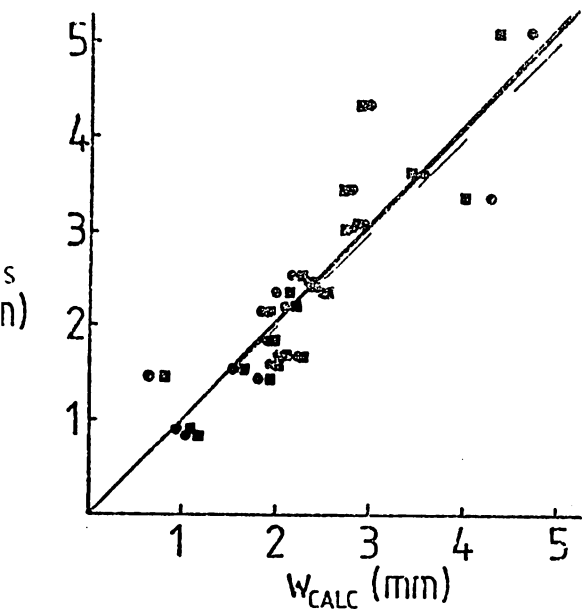
Figure 2.17e-h

Plots of observed thickness ($\bar{t}_{obs}$) against calculated thickness ($\bar{t}_{calc}$) for melt spinning of tin-antimony alloys using Kavesh analysis for two and three constants.

Legend ———⦿——— : two constants ———■———: three constants

e) Tin

f) Sn 5% Sb
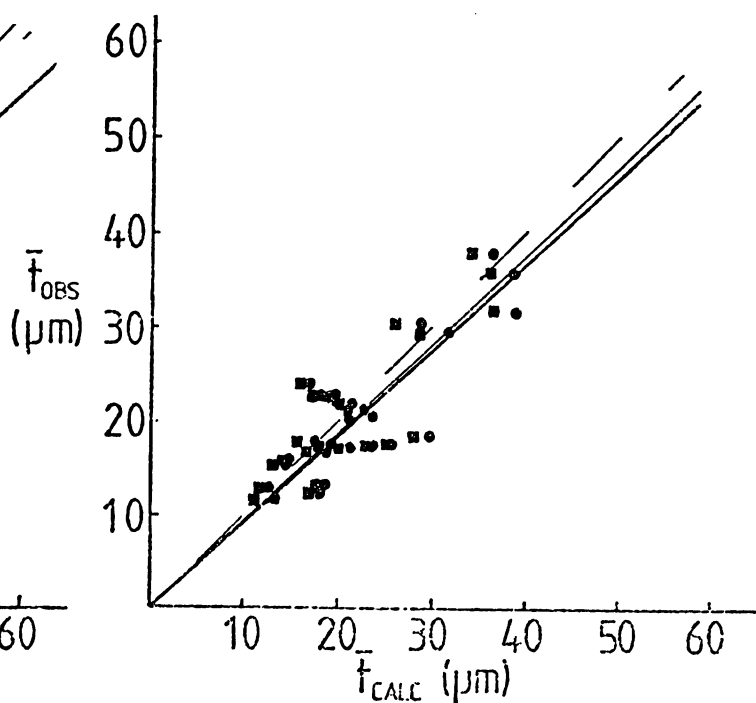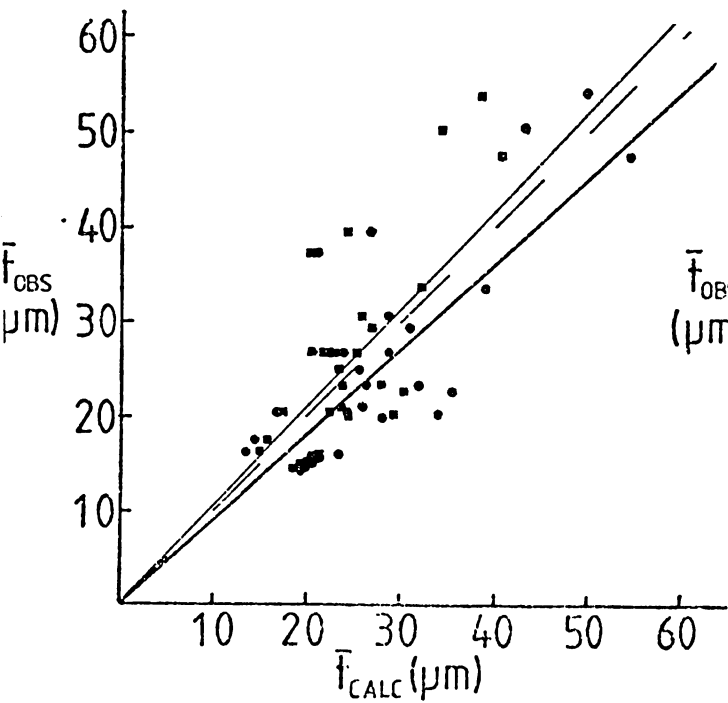
g) Sn 10% Sb

h) Sn 15% Sb
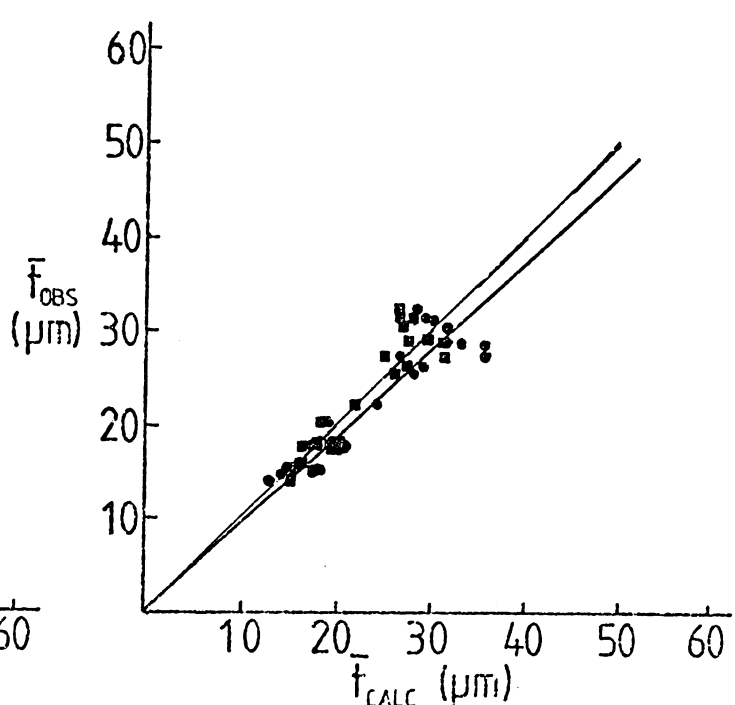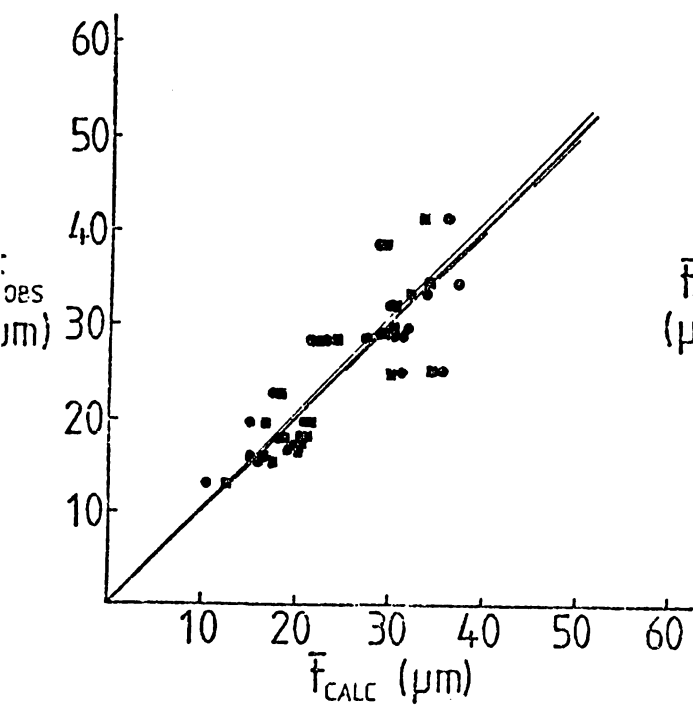
Figure 2.18

Summary of values of "n" using Kavesh's analysis.

Workers	Alloy	State	$\overline{w}$		$\overline{t}$	
			n	Corr	n	Corr
Kavesh	$Fe_{40}Ni_{40}P_{14}B_6$	amorphous	0.83	0.96	0.83	0.96
Liebermann	$Fe_{40}N_{40}B_{20}$	amorphous	0.87	0.93	0.87	0.89
Charter et al	PbSn	cryst.	0.81	0.99	0.81	0.80
	Al(Mn,Fe)	cryst.	0.93	0.94	0.75	0.80
Vincent et al	Various	cryst.	0.67-0.73			
The present work.	Sn alloys	cryst.	0.5 -0.7		0.58-0.81	

They propose that m varies from 0.5 for ideal cooling to 1.0 for Newtonian conditions. ℓ was measured by taking photographs and it was found that it varied as the inverse square root of the substrate velocity. i.e.

$$\ell \propto v_R^{-0.5}$$

Thus from equation 2.18 for ideal cooling

$$t \sim \ell^{1.5} \text{ or } t \sim v_R^{-0.75}$$

and for Newtonian cooling

$$t \sim v^{-1.5} \text{ or } t \sim \ell^3$$

Fitting their own data into the equations they obtain values of $t \sim v^{-0.8}$ and $t \sim \ell^{1.6}$. This suggests that the cooling is rather closer to ideal than Newtonian.

In this work no measurements were made of puddle length or width so no analysis was possible using this method. However Vincent et al (1982) also use an analysis which assumes

$$t \sim \tau^m \tag{2.19}$$

and from their work a value of m can be obtained.

Vincent et al do not agree with Kavesh and Hillmann and Hilzinger in the assumption of heat transfer control. They argue that momentum transfer is the key factor in the process. They also assume that the ribbon dimensions are related to the melt pool such that the ribbon width and pool width are equal and the thickness is related to the pool length as follows

$$t \propto \left(\frac{\ell}{v_R}\right)^m \tag{2.18}$$

They also assume ℓ/w is constant. From these assumptions it is easy to derive that

$$t \propto \frac{Q_R^{\,n}}{v_R^{\,2n}} \tag{2.20}$$

and

$$w \propto \frac{Q_R^{\,1-n}}{v_R^{\,1-2n}} \tag{2.21}$$

where $n = \dfrac{m}{1+m}$ (2.22)

Using these relationships plots of $\ln\left(\dfrac{wv_R}{Q}\right)$ vs. $\ln(v_R^2/Q)$ or $\ln(\bar{t})$ vs. $\ln(v_R^2/Q)$

have been constructed.   For pure tin the gradient was 0.29.

Thus the relationships become

$$t \propto \dfrac{Q^{0.29}}{v_R^{0.58}} \quad \text{and} \quad w \propto \dfrac{Q^{0.71}}{v_R^{0.42}}$$

All other tin-antimony alloys show similar values for n. (Figure 2.19),

it is interesting to note that as for the Kavesh analysis the correlation

coefficient increases with increasing antimony content.

Although the correlation for this analysis is lower than for the Kavesh

method the values of n obtained are much more consistent for the different

alloys.   Using equation 2.22 values of m can be found to vary between 0.37

and 0.41 this is much lower than expected and suggests that the assumption

$$t \propto \left(\dfrac{\ell}{v_R}\right)^m \tag{2.18}$$

is not quite correct.

In the end it is really only a matter of personal choice when choosing

between the different theories, all of them make assumptions which may not

necessarily be valid.   Certainly it would seem likely that the situation

would be different for a glassy alloy compared with a crystalline alloy.

Melt temperature and viscosity of the melt puddle are extremely important

parameters that are not really considered by any method, although Vincent

et al (1982) include the viscosity (μ) in their final expression for $\bar{t}$

$$\bar{t} \sim \left(\dfrac{\ell\mu}{v_R}\right)^{\frac{1}{2}} \tag{2.23}$$

and they also suggest that the viscosity changes during cooling could be

significant.   Observations of the melt puddle in this work have suggested that

the puddle changes shape depending on temperature, and thus presumably viscosity

and wheel/jet velocity ratio.

Figure 2.19

Summary of values of "n" using the analysis

of Vincent et al. for alloys in this study.

Alloy	n	intercept	K	Corr.
Sn	0.29	4.897	134	0.75
Sn5%Sb	0.27	5.269	194	0.80
Sn10%Sb	0.27	5.378	217	0.85
Sn15%Sb	0.29	5.021	152	0.90

where
$$t = K \left(\frac{Q_R^{\,n}}{v_R^{\,2n}} \right) \qquad (2.20)$$

and
$$w = K \left(\frac{Q_R^{\,1-n}}{v_R^{\,1-2n}} \right) \qquad (2.21)$$

A summary of all the analyses used in this work is given in figure 2.20, showing the correlation coefficients and the relevant constants for each alloy.

Figure 2.20.

Summary of Analyses used in this work.

<u>Charter et al (1980)</u>

$$\bar{wt} = C_D \times \left(\frac{\pi}{2^{3/2}}\right)\left(\frac{\phi^2}{v_R}\right) \left(\frac{P}{\rho}\right)^{\frac{1}{2}}$$

C_D in the present study varies between 0.84 and 0.90

Correlation coefficients from 0.96 to 0.97.

<u>Liebermann (1979a)</u>

$$w = w_o + \frac{Q_R}{v_p}$$

w_o varies from -0.54 to 0.86mm

v_p varies from 330 to 860mm^{2}s^{-1}

Correlation coefficients from 0.79 to 0.89.

<u>Kavesh (1978)</u>

$$w \propto \frac{Q_R^n}{v_R^{1-n}} \qquad\qquad t \propto \frac{Q_R^{1-n}}{v_R^n}$$

for w: n varies from 0.5 to 0.7   Correlation coeff. 0.73 to 0.97.

 t: n varies from 0.58 to 0.87 Correlation coeff. 0.67 to 0.95.

<u>Vincent et al (1982)</u>

$$w \propto \frac{Q_R^{1-n}}{v_R^{1-2n}} \qquad\qquad t \propto \frac{Q^n}{v_R^{2n}}$$

n varies from 0.27 to 0.29

Correlation coefficients vary from 0.75 to 0.90.

2.3. Production of Wide Ribbon

After initial experiments using a conventional single jet nozzle it was decided to try to increase the width of the ribbon by employing a multi-holed nozzle.   The reason was that this would make tensile tests on the ribbons easier (see section 3.6).

Wide ribbon is now produced commercially at least up to 150mm wide and has possibly been produced experimentally 400mm wide.   There have been several suggestsions about how this is achieved, including that of Planar Flow Casting (P.F.C.).   This process uses a slit nozzle and the crucible is a minimal distance away from the substrate surface.   Cline and Anthony (1978) discuss the stability of such a jet and the various nozzle shapes that could be used.   They describe the influence of the surface tension forces which determine that the substrate nozzle distance has to be small as a result of the "dog bone" mode of flow through such an orifice (fig.2.21).

The other suggested method is the use of a multihole nozzle.   Walter (1978,1979) uses a 5 holed nozzle in a "W" configuration to produce ribbon 2.5 times the width of his normal ribbon.   Liebermann (1979a) uses P.F.C. to produce 20mm wide $Fe_{40}Ni_{40}B_{20}$ tape.

Two multiholed nozzles were used in this work.   A 3 holed nozzle with ϕ of 0.5mm and the centre to centre spacing, d, of 1mm.   This produced tape only 4mm wide, which was no wider than a ribbon produced at high flow rate from a single nozzle, it was however about three times as thick.   To increase the width another 6 holes were added in the same straight line configuration. Again this only produced ribbon about 10mm wide and if the flow rate was excessive ridges were formed along the "free solidification" surface.   The next change was to increase the spacing between the holes to 1.5mm (fig.2.22). With this configuration ribbon up to about 14mm could be produced with a reasonable top surface finish. (fig.2.23).

Figure 2.21

Flow from a Slit Nozzle for the Planar Flow Casting

Process for the production of Wide Ribbon showing the

"Dog Bone" mode of flow.

rectangular section

"dog bone" section
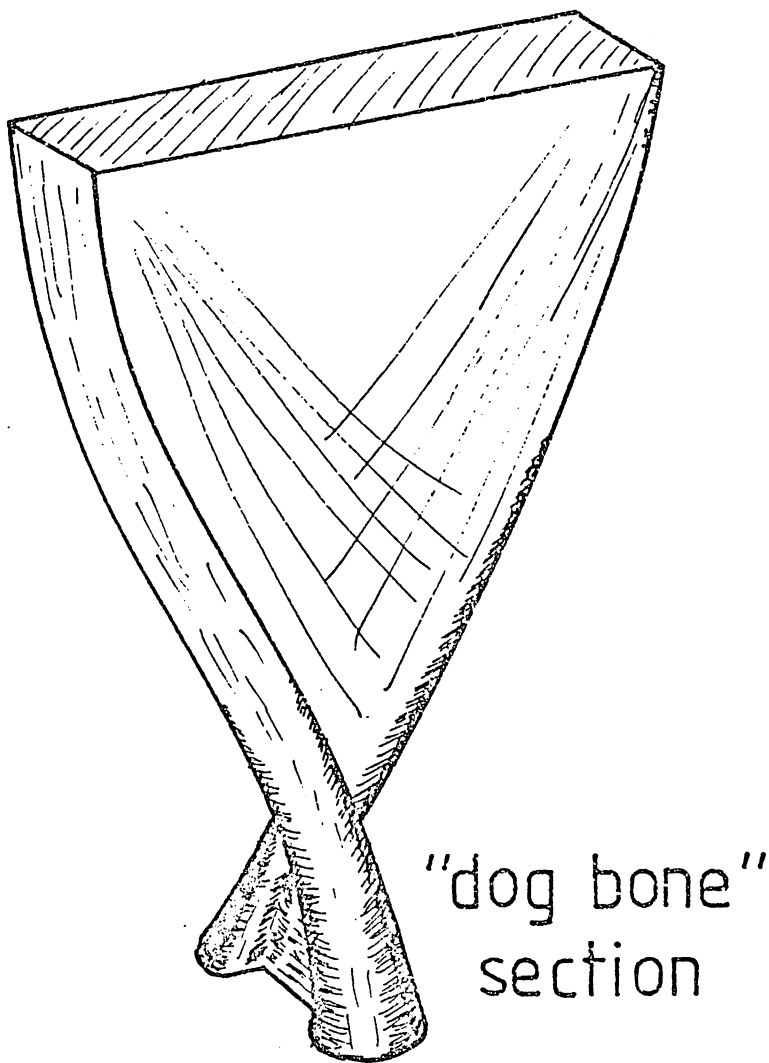
Figure 2.22

Nine Holed Nozzle for Wide Ribbon Production
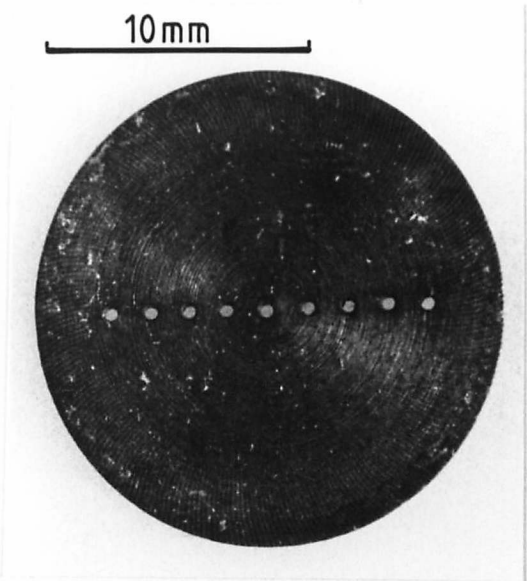
Figure 2.23

Free solidification surface of Wide Ribbon
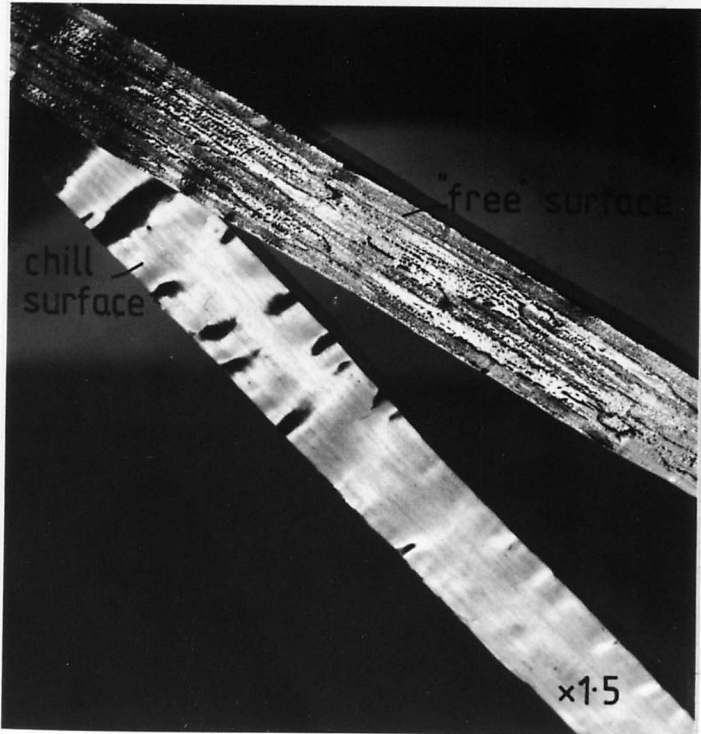
When producing wide ribbon the flow rate had to be high enough to ensure joining between the individual streams so that slits did not appear along the major axis of the ribbon. The interaction of the adjacent streams and the limiting controlling factors of thickness and width are discussed in the next two sections.

2.4. Jets and Flow from Nozzles

The stability of the Molten metal stream is of prime importance when considering the uniformity of the ribbon. If the jet is not stable then considerable fluctuation can occur in the length and width of the melt puddle thus changing the dimensions of the ribbon. In the extreme the stability of the melt puddle can break down completely and ribbon is no longer formed.

2.4.1. Minimum Volumetric Flow Rate

The minimum flow rate is defined as the volumetric flow rate below which flow will not occur due to surface tension forces and may be estimated as follows.

Consider a nozzle with the geometry as seen in figures 2.24.

The pressure at point p when a liquid with surface tension γ attains an hemispherical shape of radius $\phi/2$ is given by:

$$p = \frac{4\gamma}{\phi} \qquad (2.24)$$

(Gibbs-Thompson-Freundlich Equation, Christian(1975)182)

for flow to occur then the total pressure exerted, P_{total}, must therefore be:

$$P_{total} > \frac{4\gamma}{\phi}$$

as

$$P_{total} = P_{applied} + h\rho g \qquad (2.25)$$

then $\quad P_{applied} + h\rho g > \frac{4\gamma}{\phi}$

For total control over the process so that flow does not begin before a pressure of gas is applied then:

$$h\rho g < \frac{4\gamma}{\phi}$$

For the crucible used in this work with an included angle, β, of 120° the maximum charge can be calculated for tin, for various nozzle diameters. The result can be seen in figure 2.25, with the internal pressure at p also plotted on the ordinate for the condition

Figure 2.24

Nozzle Geometry and Limiting Condition

$$p = 4\gamma/\phi$$

limiting
condition
$(p = 4\gamma/\phi)$

molten
metal
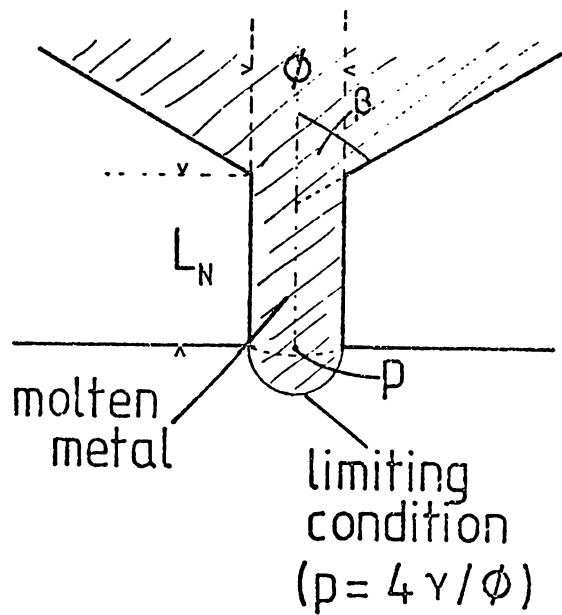
Figure 2.25

Plot of ϕ (mm) against limiting mass (g) of
batch for melt spinning crucible
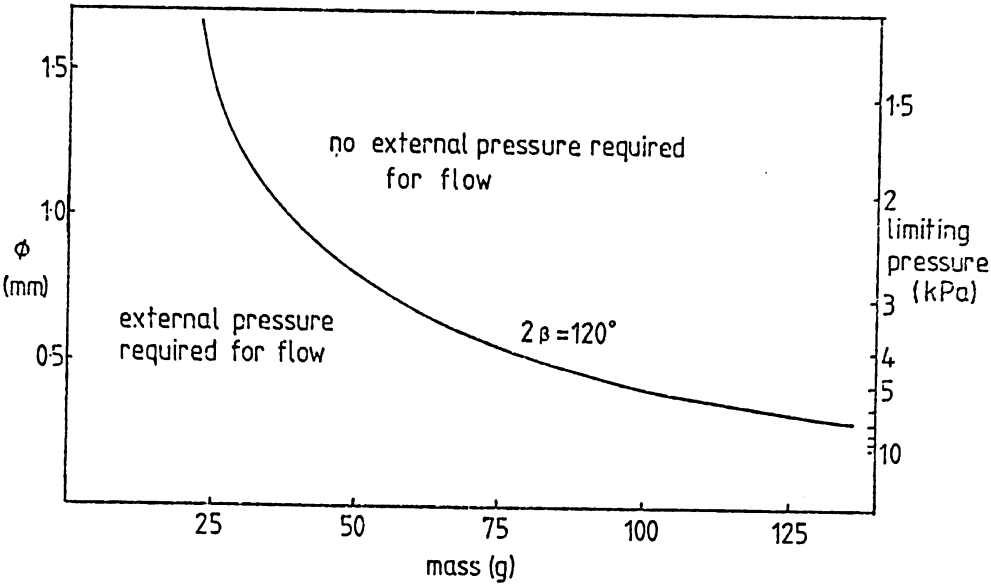
$$P = \frac{4\gamma}{\phi} \qquad (2.24)$$

Assuming $v^2 = \frac{2P_{total}}{\rho}$ (2.25a)

then $v_{min}^2 = \frac{8\gamma}{\phi\rho}$ (2.25b)

(from 2.9 and 2.14)

Thus for tin, the minimum velocity, v_{min}, of liquid for a nozzle of diameter 0.5mm, assuming γ to be 0.535 Nm^{-1}, is 1.08ms^{-1}.

The minimum volumetric flow rate given by

$$Q_{min} = v_{min} \frac{\pi\phi^2}{4} \qquad \text{(from 2.14)}$$

is therefore 0.212×10^{-6} $m^3 s^{-1}$.

2.4.2. Sources of Instability.

2.4.2. (1) Nozzle Geometry.

A moving fluid is described as turbulent when it is not 'streamlined', that is instead of the direction and velocity at any point in the stream being constant with time there are "eddy currents" and therefore considerable backward flow relative to the stream. The point at which a stream of liquid changes from streamlined to turbulent flow is given by a critical Reynolds Number. The Reynolds Number ($\bar{Re}$) is the ratio of intertial to viscous forces of a system and is a dimensionless group defined as:

$$\bar{Re} = \frac{\bar{v}\rho\ell}{\mu} \qquad (2.26)$$

where $\bar{v}$ is the average stream velocity, ρ and μ are the fluid density and static viscosity respectively and ℓ is a dimension of the stream cross section. For any two systems if they are geometrically similar then a similar Reynolds Number gives dynamical comparability. It has been found that if $Re > 2000$ then turbulent flow will probably exist (see Coulson and Richardson (1964) Chapter 9, and Batchelor (1967) Chapter 5).

For melt spinning the velocity in the stream, v_j, can be given as

$$v_j = \left(\frac{2P}{\rho}\right)^{\frac{1}{2}} \qquad \text{Liebermann (1979c)}$$

(2.25)

where P is the total pressure (usually taken as the ejection pressure).

The Reynolds Number is therefore given by

$$\bar{Re} = \frac{\phi}{\mu} (2P\rho)^{\frac{1}{2}}$$ (2.27)

where ϕ is the diameter of the nozzle orifice.

Assuming viscosity of 1.45×10^{-3} Pa.s for tin and a nozzle diameter 0.5mm then for the range of applied pressures in this work, 25-210kPa, the Reynolds Number is from 7700 to 19000 (v_j is from 3ms^{-1} to 7.54ms^{-1}).

This suggests therefore that flow in the molten tin jet is turbulent and could be streamlined only by reducing the pressure or the nozzle size.

However as there are other restrictions on the flow rate because of surface tension and the "head of charge" effect, a minimum nozzle diameter can be calculated,

as $$\bar{Re} = \frac{\bar{v}\phi\rho}{\mu}$$ (2.26)

and $$\bar{v}_{min} = \left(\frac{8\gamma}{\phi\rho}\right)^{\frac{1}{2}}$$ (2.25b) from 2.9 and 2.14)

then $$\bar{Re}_{min} = \frac{\sqrt{8\gamma\phi\rho}}{\mu}$$ (2.28)

for streamlined flow $\bar{Re}_{crit} < 2000$

therefore $$2000 > \frac{\sqrt{8\gamma\phi\rho}}{\mu}$$

assuming γ is 0.535Nm^{-1}, ρ is 7310kgm^{-3} and μ is 1.45×10^{-3} Pa.s.

then $$\phi_{crit} = 0.27 \times 10^{-3}m$$

Which suggests that for tin streamlined flow can be achieved if the nozzle orifice is less than 0.27mm in diameter assuming flow to be at the minimum possible rate. As soon as the flow rate is increased the Reynolds number would increase and so turbulent flow would result. It would therefore seem to be an impossible task to achieve streamlined flow in the melt spinning of tin due to its comparatively high surface tension x density/viscosity ratio, but it is known that laminar flow can exist when the Reynolds number is as

high as 25000 (Anthony and Cline, 1978).

However this is taking a very simplistic view of the flow and assuming the liquid immediately takes the shape of the orifice it is flowing through and assumes its diameter. The actual case is somewhat different as can be seen in figure 2.26 which shows the real situation. The fluid is flowing first through a region of contraction and then into what could be described as a sudden expansion, assuming the atmosphere to be a channel of infinite diameter. At the first change of diameter a phenomenon called "vena contracta" occurs in which the stream continues to decrease in diameter. After the enforced contraction the stream attempts to expand again to fill the width of the channel. This effect of vena contracta can be minimised by designing nozzles with a slowly decreasing diameter rather than a sudden constriction. Vena contracta can also be minimised by keeping the jet-substrate distance large enough for the jet to reach a stabilised diameter before contacting the substrate.

The minimum angle of convergence, β, to ensure non-turbulent flow, can also be calculated from the depth of nozzle and the diameter of the crucible reservoir (D_R) (Anthony and Cline, 1978) and is given by

$$\beta \geq \tan^{-1}\left[\frac{D_R}{2L_N}\right] \tag{2.29}$$

The nozzle length, L_N, also helps determine whether streamline flow takes place. For example, if the Reynolds Number is high, 2.5×10^4, then laminar flow persists for 25 to 40 diameters length past the change in diameter. Thus $L_N < 25\phi$ should increase the chance of continuing streamline flow.

Using the values of dimensions of the system in figure 2.5 the following information can be obtained from the above equations.

$$D_R = 15.9 \times 10^{-3} m. \qquad \phi = 0.5 \times 10^{-3} m$$

Figure 2.26

"Vena-Contracta". (Schematic)

molten
metal
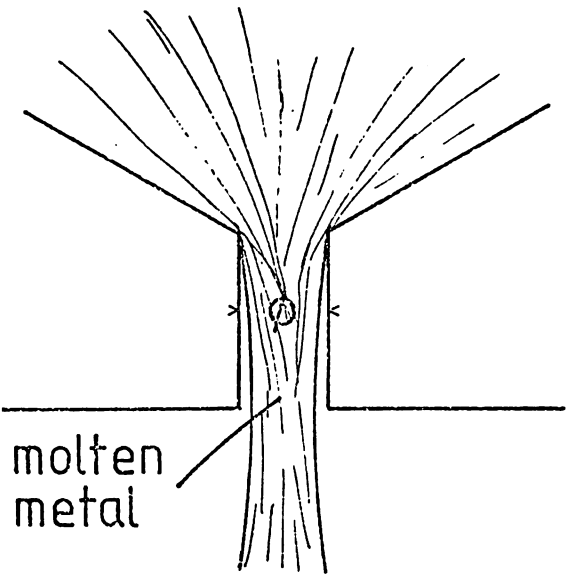
Figure 2.27 Table showing

$\dfrac{\text{Molecular Weight}}{\text{Viscosity}}$ $\dfrac{\overline{M}}{\mu}$ for various gases

Gas	He	H_2	Ne	Air	CO	Ar	CO_2	Kr	Xe
$\overline{M}/\mu$	2.06	2.30	6.49	15.8	16.0	18.1	29.7	34.1	58.1

$\overline{M}/\mu$ values X 10^2 m.mol.s.

$$Re_R \text{ (Reynolds No. of the reservoir)} = \frac{v_R \rho D_R}{\mu} \tag{2.26}$$

$$v_R = \frac{v_j A_j}{A_R} = \frac{v_j \phi^2}{D_R^2} \qquad \text{from conservation of mass} \tag{2.2}$$

$$\text{as } v_j = \left(\frac{2P}{\rho}\right)^{\frac{1}{2}} \tag{2.25}$$

$$\text{then } Re_R = \frac{\rho \phi^2}{\mu D_R} \left[\frac{2P}{\rho}\right]^{\frac{1}{2}} \tag{2.30}$$

Assuming an applied pressure of 200kPa then Re_R for the maximum pressure used is about 590.

The nozzle length must be kept to less than $25 \times 0.5 \times 10^{-3}$m for the streamline flow to persist despite the fact that the Re. number of the nozzle is about 19000.

The minimum angle of convergence is calculated, from equation 2.29, to be:

$$\beta > \tan^{-1} (0.636)$$

$$\beta \geq 32^{\circ}$$

It would seem therefore that by putting in these values for the system and those for liquid tin we obtain results that suggest the system produces turbulent flow through the nozzle. However by taking the geometry of the system into account it does appear as though streamlined flow could be created.

2.4.2 (2) Stream Instabilities.

(a) Capillary Waves

Once the stream has passed through the nozzle orifice, either stationary or travelling capillary waves can form on it. These can be initiated either at the opening itself or where the stream impinges on the substrate. The velocity, v_λ, of a travelling capillary wave of wavelength λ, is determined by a balance between the intertial and surface tension

forces such that

$$v_\lambda = \left[\frac{2\pi\gamma}{\lambda\rho}\right]^{\frac{1}{2}} \qquad \text{(Anthony and Cline, 1978)} \qquad (2.31)$$

where γ is the surface tension of the liquid and ρ the density.

By considering the effect of surface tension and pressure induced by a curved surface of a liquid, the wavelength of a spontaneously formed capillary wave can be given by

$$\lambda \geqq \pi\phi \qquad (2.32)$$

where ϕ is the stream diameter

If λ is smaller than this the waves will be damped by surface tension forces. (Anthony and Cline, 1978). For an orifice of 0.5×10^{-3}m only waves greater than 1.57×10^{-3}m will spontaneously form.

For pure tin assuming a wavelength of 1.6×10^{-3}m and taking γ as 0.535Nm^{-1} then v_λ is 0.54ms^{-1}. This velocity is considerably smaller than the velocities attained by the stream in this work which are typically greater than 3.0ms^{-1}, thus any capillary waves of this wavelength should be destroyed. However as $\lambda \to 0$, $v_\lambda \to \infty$ therefore smaller capillary waves may be stable if they can form.

(b) <u>Jet Break-up Length.</u>

The break-up length, ℓ_b, for an isothermal jet in a gaseous medium is given by

$$\ell_b = \phi \left[\sqrt{W} + 3W/Re\right] \ln (\phi/2\epsilon_0) \qquad (2.33)$$
$$\text{(Weber, 1931)}$$

where W is the Weber number defined as

$$W = \frac{\rho v_j^2 \phi}{\gamma} \qquad (2.34)$$

and ϵ_0 is an experimentally determined coefficient. Liebermann (1979b) has shown that in most practical cases $3W/Re \ll W$ and therefore

$$\ell_b = \sqrt{\rho/\gamma} \ (\phi^3/2 \quad v_j)\ln (\phi/2\epsilon_0) \qquad (2.35)$$

Since the distance between nozzle and substrate is only of the order of 10×10^{-3} m and this predicts much longer break-up lengths, then consideration of this phenomenon, as an instability, is unnecessary.

2.4.2. (3) Instabilities Introduced by the Substrate.

Any irregularity on the substrate surface or change in conditions, for example fluctuation of surface velocity or roughness, can influence the dimensions and uniformity of the ribbon. In the first case by changing the momentum transfer conditions and in the second the heat transfer conditions. It is therefore necessary to keep the surface clean of detritus by employing a wiper in the system and to periodically polish and/or regrind the wheel surface.

Another cause of instability of the melt puddle is the effect of the gas boundary layer surrounding the rotating wheel. As the gas is a fluid it is possible to produce conditions where either streamlined or turbulent flow exists in this layer, depending on its Reynold's number. The Reynold's number in such a case is given by

$$ Re = \left[\frac{v_R wP}{RT} \right] \left[\frac{\bar{M}}{\mu} \right] \qquad \text{(Liebermann, 1978) (2.36)} $$

where v_R is the gas velocity, w is the melt puddle width, P is the ambient gas pressure, $\underline{R}$ the gas constant, T the ambient temperature, $\bar{M}$ molecular weight of the gas and μ the static gas viscosity. Liebermann divides the expression into two groups as above, the first being process variables, the second physical constants of the casting atmosphere. Figure 2.27 shows a table of $\bar{M}/\mu$ for various gases, and thus gives the propensity of gases to create turbulent flow. The higher this figure, the higher the probability of creating a turbulent boundary layer at ambient pressure and temperature. It is suggested that it is this gas boundary layer effect which creates the defect which can be described as "fir tree edges". It can be seen from the relationship that the Re. number is directly proportional to the product of the melt puddle width, and therefore ribbon

width, and the velocity of the gas layer. Assuming the gas boundary layer velocity to be that of the substrate then a comparison can be made between the product $v_R w$ and the ribbon quality. In this work $v_R w$ ranges from about 10×10^{-3} to 60×10^{-3} $m^2 s^{-1}$. Therefore assuming constant temperature and pressure, $[v_R w P / \bar{R} T]$ ranges from 0.4 to 2.4 $m^{-1} mol^{-1} s^{-1}$. This gives Reynolds numbers of 632 to 3800 for wheel speeds of 10 and $28 ms^{-1}$ respectively, if cast in air with a $[\bar{M}/\mu]$ value of 15.8×10^2 m.mol.s. This suggests that at higher wheel speeds the gas layer becomes turbulent. Using the criterion that turbulent flow occurs if Re>2000 then the expression $w=2.923 \times 10^{-2}/v_R$ is obtained and thus a maximum value of w can be calculated for each velocity, above which turbulent flow occurs and the ribbon's edges become frayed.

If the value of $v_R w$ is plotted against v_R (figures 2.28) it can be seen that the majority of runs in the present work giving an edge defect, were for $v_R w$ values of greater than $2.923 \times 10^{-2} m^2 s^{-1}$. However as v_R increases the value of $v_R w$ at which serration begins increases as well, suggesting that R_{crit} is dependent on the velocity of the wheel.

Plotting $\ln (v_R w)_{crit}$ against $\ln(v_R)$ gives a straight line with a gradient of 0.56 and an intercept -4.79. (figure 2.29) and thus the relationship

$$(v_R w)_{crit} = 8.3 \times 10^{-3} . v_R^{0.56}$$

is found. Plotting this curve back on the graphs of $v_R w$ against v_R (fig.2.29) shows that most of the values of $v_R w$ which gave serrated ribbon lie above this line.

Values of Re_{crit} can now be calculated by substituting into equation 2.36 giving:

$$Re_{crit} = (8.3 \times 10^{-3} . v_R^{0.56}) \frac{P}{\bar{R}T} \left[\frac{\bar{M}}{\mu}\right]$$

giving values of Re_{crit} from 2062 to 3670 for velocities of 10 to $28 ms^{-1}$ respectively. This does not seem unrealistic as it has been noted before

Figure 2.28

Plots of $v_R w$ against v_R for Tin-Antimony alloys showing

increase of stability with increasing v_R
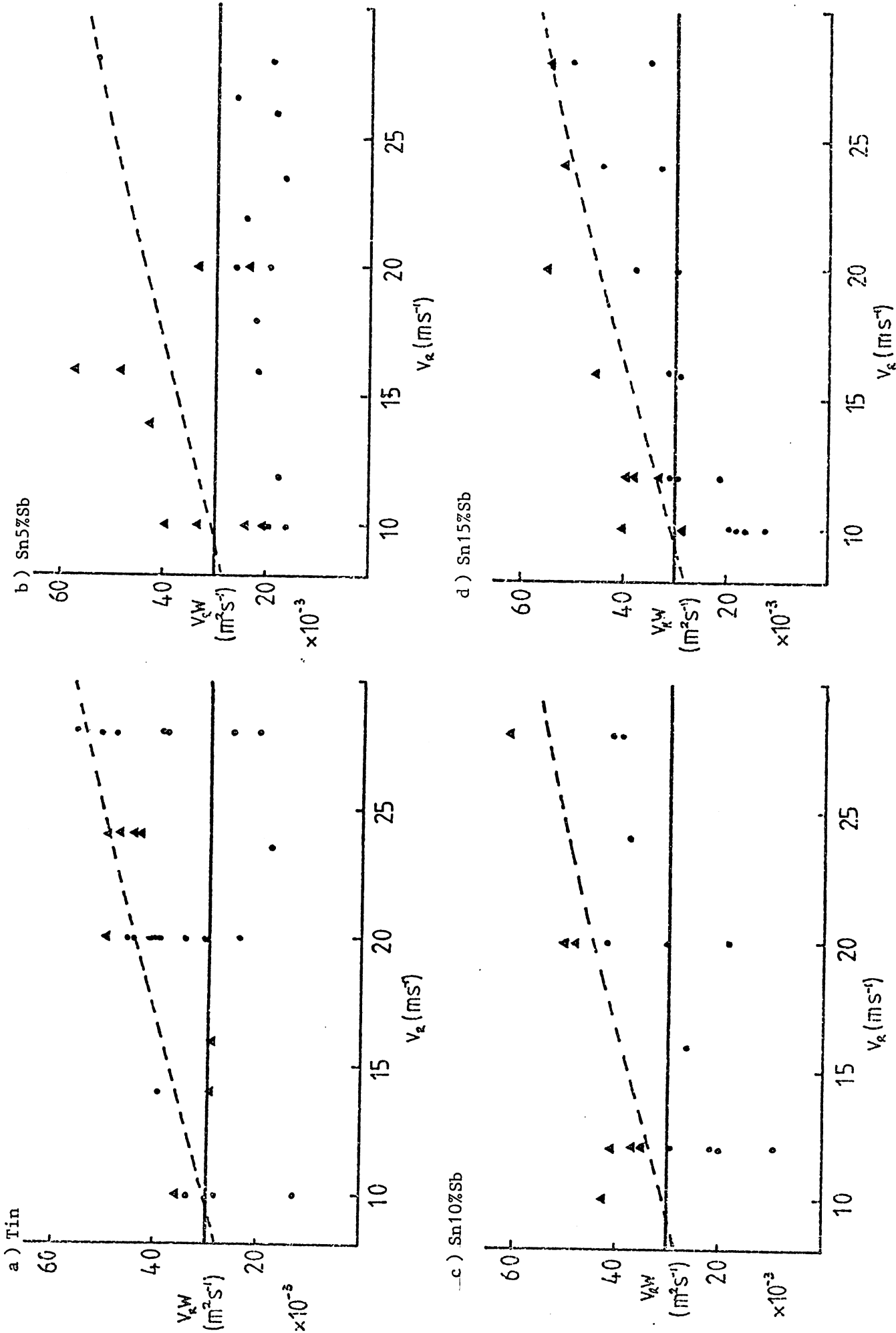
Figure 2.29   Plot of vw_{crit} against v from critical values

obtained in Figure 2.28.
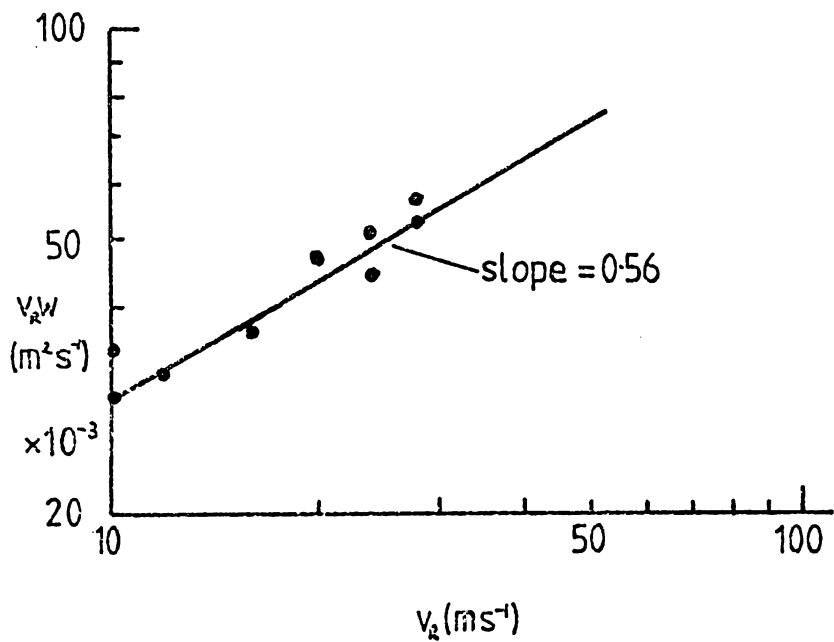
Figure 2.30

Values of Re_{crit} and w_{crit} for corresponding wheel surface velocities

using relationship.

$$Re_{crit} = (8.3 \times 10^{-3} v_R \ 0.56) \frac{P}{R\bar{T}} [\frac{\bar{M}}{\mu}]$$

v (ms^{-1})	Re_{crit}	w_{crit} (mm)
10	2026	3.01
12	2283	2.78
14	2489	2.60
16	2682	2.45
18	2865	2.32
20	3040	2.25
24	3366	2.05
28	3670	1.92

that streamline flow can be achieved in certain circumstances when Re is greater than 2000, which is a fairly arbitrary figure anyway. Using these values of Re_{crit}, then w_{crit} can be calculated for each velocity, above which the ribbon will be serrated (figure 2.30).

Other instabilities which the substrate could introduce but are difficult to quantify are those caused by vibration or non-alignment of the wheel. The effects which any instabilities of the melt puddle might have on the dimensions of the product ribbon are dealt with definitively by Anthony and Cline (1979).

2.4.2. (4) Instabilities created by the interaction of two or more parallel

streams (multi-jet melt spinning)

The aim of using multi-jet melt spinning is to produce wider ribbon than is possible using a single nozzle. The first consideration is to ensure that the adjacent melt pools interact enough to produce coherent ribbon but do not produce a ridged surface where there is an excess of liquid metal. This requires that the ratio between orifice size and spacing, as well as flow rate, is controlled.

Consider two parallel streams of liquid with centre line spacing of d and orifice diameters ϕ (figure 2.31). The optimum width, w, for each melt puddle is just greater than d (w > d). The flow rate, Q_h, for each hole is given by:

$$Q_h = twv_R \tag{2.8}$$

where v_R is the substrate velocity.

The optimum flow rate per hole is therefore

$$Q_{opt} > tdv_R$$

as

$$Q = \frac{\phi^2 \pi}{2^{3/2}} \left[\frac{P}{\rho}\right]^{\frac{1}{2}} \tag{2.10}$$

where P is ejection pressure and ρ is fluid density,

then

$$t_{opt} > \frac{\phi^2}{d\rho^{\frac{1}{2}}} \frac{\pi}{2^{3/2}} \left[\frac{P}{v_R^2}\right]^{\frac{1}{2}} \tag{2.37}$$

Figure 2.31

Multijet Spinning (Schematic)
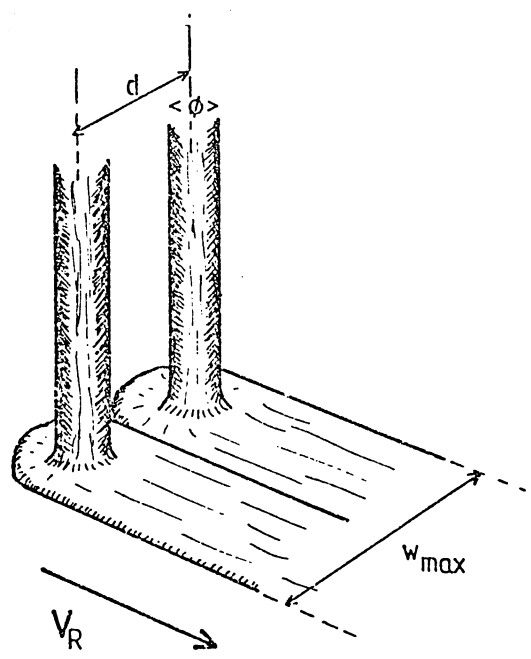
Figure 2.32   Plots of Optimum thickness (t_{opt}) against Velocity ($\mathbf{v}_R$)
at Constant Ejection Pressure (P) for Multijet Melt
Spinning of Tin.
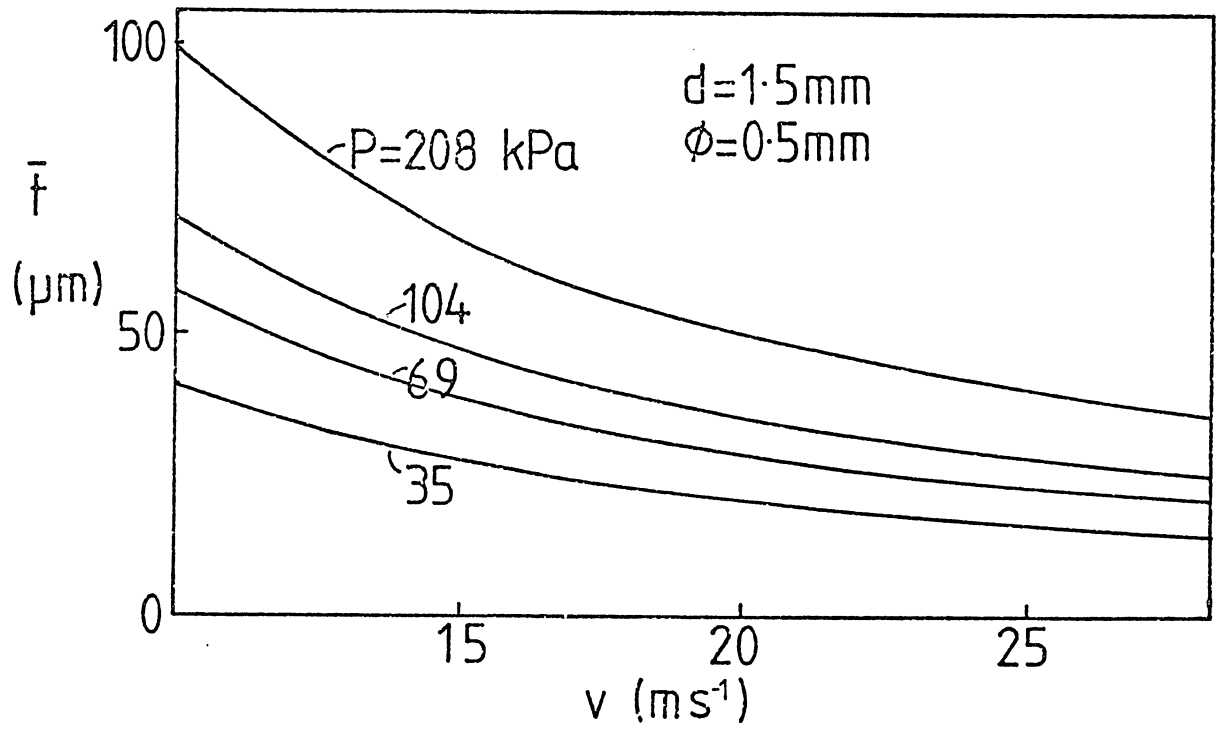
Assuming that ϕ takes the value 0.5mm and d is 1.5mm then

$$t_{opt} > 2.17 \times 10^{-6} \left[\frac{P}{v_R^2} \right]^{\frac{1}{2}}$$

A plot of t_{opt} against v_R for constant ejection pressure P results in the family of curves shown in figure 2.32. This could be used for any array of holes with the same ϕ^2/d ratio, for liquid tin.

The maximum width of a ribbon with no ridges is obviously just greater than n x d (where n is the number of holes). Therefore for a 9 holed array spaced by 1.5mm a ribbon of just greater than 13.5mm should be expected if the surface is to be acceptable.

2.5. Observations of the melt puddle during melt spinning.

2.5.1. Introduction.

The behaviour of the melt puddle during melt spinning was studied using two methods. Modelling of the process using a steady state water system and filming the actual process by high speed cine and still photography.

The early development of high speed photography from the days of Fox-Talbot in the 1830s to modern commercial high speed techniques is described by Lunn (1981).

A modern high speed cine camera makes use of a rotating prism to cause the image to move with the film and act as a shutter. This class of camera can produce speeds of up to 10000 frames per second (f.p.s.) which can be halved or quartered to give a maximum 40000 ¼ f.p.s. With such high film speeds, electronic speed control, synchronisation and timing circuits have become necessary and the modern high speed cine camera is a complicated piece of apparatus. Once the film has been exposed and processed it is then replayed at normal speeds, 25 f.p.s. or slowed down to 1 f.p.s. for proper analysis, obviously it is also possible to look at the individual frames.

Walter (1978) and Liebermann (1979) have both carried out some high speed cine photography of the melt spinning of amorphous alloys using single nozzle, multiple nozzles and planar flow casting. The speed they used was much slower, 1200 f.p.s., than in this study.

Various workers have used conventional cameras to take high speed stills of the process and Shohoji et al (1982) have even used the technique to measure the temperatures and cooling rates involved.

2.5.2. Water Modelling of Melt Spinning.

2.5.2. (1) Experimental arrangement

Using a constant head apparatus water was ejected from a perspex crucible through nozzles of one, two or three holes, 0.5 or 1.0mm in diameter. The liquid stream(s) impinged on a rotating copper wheel 9mm wide and 147mm in

diameter giving surface velocities of from 2 to 12ms^{-1}. The wheel surface

was sprayed with a PTFE coating and kept dry by continued wiping. The angle

of impingement, β, was varied from 0° to 20°. The head of water was varied between

0.25m and 0.795m.

The melt puddle was observed by taking photographs with 35mm SLR

camera, using Ilford Pan F film with a 75mm lens at f32, to give a

magnification of approximately 3x on the negative. Flash lighting was

used and estimated to give an exposure time of ∿ 1/1500s.

With this apparatus it was possible to observe the flow of

the stream(s) under steady state conditions.

2.5.2. (2) Flow Rates.

The flow rate, Q, was assessed by measuring the volume of water collected

in time, t, for various heads.

Using Bernoulli's equation we have seen that, in melt spinning, the jet

velocity, v_j, is given by:

$$v_j = \left[\frac{2P}{\rho}\right]^{\frac{1}{2}} \qquad (2.25)$$

and the flow rate Q is given as

$$Q = A_j v_j \qquad (2.9)$$

$$\text{where } A_j = \frac{\phi^2 \pi}{4} \qquad (2.3)$$

The pressure in this experiment was determined by the head of liquid, h, and given as

$$P = h\rho g \qquad (2.38)$$

$$\text{where } \rho \text{ is the liquid density.}$$

From these relationships it can be seen that
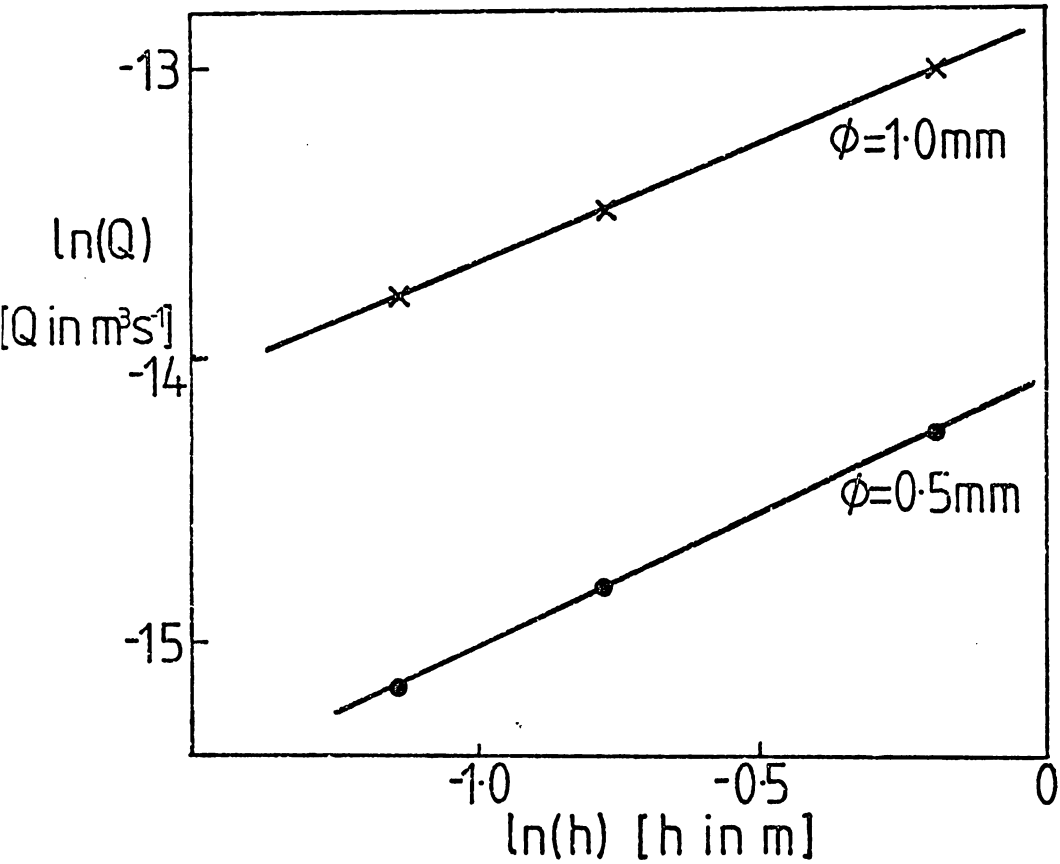
$$Q = \frac{\pi\phi^2}{2^{3/2}} (hg)^{\frac{1}{2}} \qquad (2.39)$$

$$\text{or } \ln(Q) \propto 0.5 \ln(h) \qquad (2.40)$$

However plots of lnQ vs. lnh (fig. 2.33) gave gradients of 0.74 and 0.84

for 1.0 and 0.5mm nozzles respectively. This would seem to suggest that as

Figure 2.33

Plot of ln (Q) against ln (h) for water modelling

with the results of Charter et al. a discharge coefficient, C_D, should
be added into the equation to account for "non-perfect" flow through the
nozzles.

The Reynolds number, Re, can be calculated for the system as follows:

$$Re = \frac{v_j \phi \rho}{\mu} \qquad (2.26)$$

as $\quad v_j = \left[\frac{2P}{\rho}\right]^{\frac{1}{2}} \qquad$ and $\quad P = h\rho g \qquad (2.25, 2.38)$

then $\qquad Re = \frac{\phi\rho(2hg)^{\frac{1}{2}}}{\mu} \qquad (2.41)$

Putting in values for ρ, μ and g of $1 \times 10^3 Kg.m^{-3}$, $1 \times 10^{-3} Pa.s$ and
$9.81 ms^{-2}$ respectively then

$$Re = 4.43 \, \phi h^{\frac{1}{2}} \times 10^6$$

or $\qquad Re_{\phi=0.5mm} = 2.21 \, h^{\frac{1}{2}} \times 10^3$

$$Re_{\phi=1.0mm} = 4.43 \, h^{\frac{1}{2}} \times 10^3$$

As the head of water ranged from 0.25 to 0.795m this gave Re numbers
from 1105 to 3950 with v_j varying between 1.1 to $2.69 ms^{-1}$. This means that,
although this system was geometrically similar to the experimental arrangement
for tin, because of the differences in jet velocity and fluid density the
systems differed in their dynamic characteristics. To obtain dynamical
similarity the water system would have had to be run with nozzles of greater
than 1.8mm diameter with a head of water greater than 1m. For a head of
0.25m then ϕ would have to have been greater than 3.6mm. The other dimensions
of the nozzle would then have to be changed to produce geometrical similarity.
This was not performed and so any comparisons really have to be restricted
to qualitative rather than quantitative observations. Such observations

can show changes in puddle form, the effect of wheel speed and angle on instabilities not dependent of the type of flow, and the interaction between adjacent melt puddles.

2.5.2. (3) Puddle Shape

Figure 2.34 shows the effect on the stream of increasing the substrate velocity, v_R, at constant jet velocity, v_j. As v_R increases the shape of the puddle changes from a broad flat form (A) with a ridged edge, to the "foot" like appearance (B) so often seen in the melt spinning of amorphous alloys (Walter, 1978) (figure 2.35).

As the jet velocity increases the phenomenon of "back flow" begins to play an important part. A ridge can build up around the puddle until it becomes unstable and breaks like a wave, thus creating a turbulent puddle (figure 2.36). Figure 2.37 shows a series of melt puddles obtained for low medium and high, jet and substrate velocities.

It would seem therefore that the ratio of jet to substrate velocities (v_j/v_R) must determine the shape of puddle obtained.

It was seen in section 2.4.2.(3) that the gas boundary layer related to the spinning wheel can be either turbulent or streamlined and that this flow affects the stability of the melt puddle. The Re number of the layer is defined as

$$Re_R = \frac{v_R w \ P_{amb}}{RT} \left[\frac{\bar{M}}{\mu} \right] \tag{2.36}$$

where v_R: substrate velocity, w: puddle width, P_{amb}: ambient gas pressure, R: gas constant, T: absolute ambient temperature, $\bar{M}$: molecular weight of atmosphere and μ: viscosity of the atmosphere

while
$$Re_j = \frac{v_j \phi \rho_\ell}{\mu_\ell} \tag{2.26}$$

where v_j: jet velocity, ϕ: jet diameter, ρ_ℓ: liquid density and μ_ℓ: liquid viscosity.

Figure 2.34   Water Modelling of Melt Spinning $(v_j = 1.1ms^{-1})$
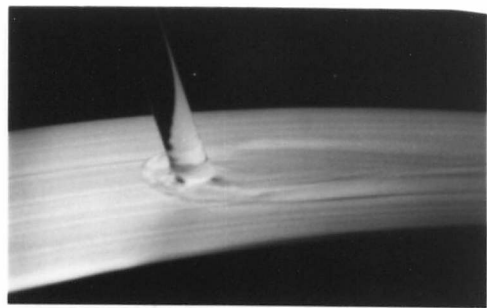
$v_R = 2.14ms^{-1}$

$v_R = 4.75ms^{-1}$

$v_R = 6.8ms^{-1}$

Figure 2.35

$v_R = 11.40ms^{-1}$

"Melt" Puddle Shapes

A

high v_j
low v_R

B

high v_R
low v_j
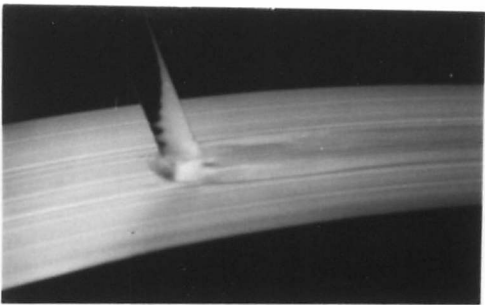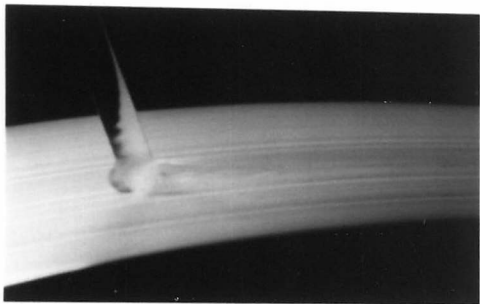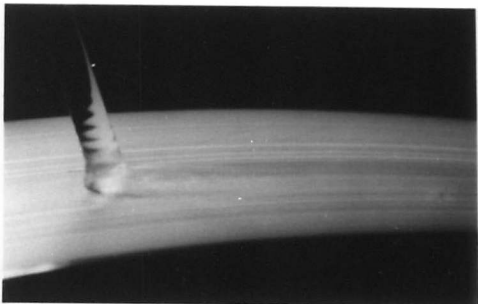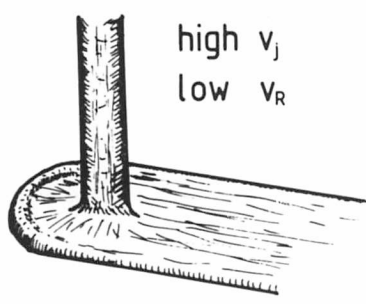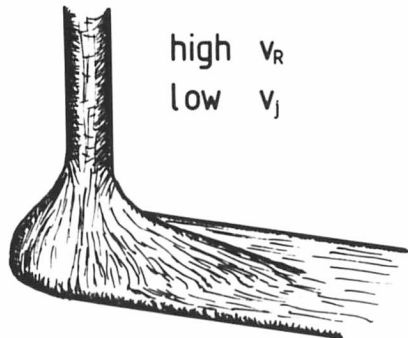
Figure 2.36

Photographs of Unstable "Melt" Puddles during Water Modelling
of Melt Spinning.
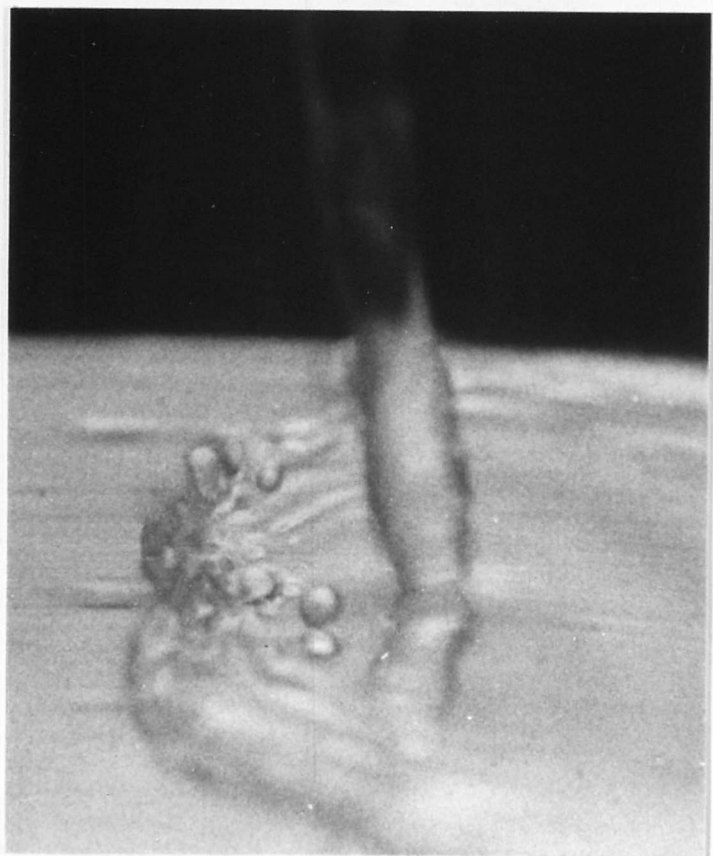
Figure 2.37

Melt Spinning with Water. (ϕ = 0.5mm)

v_j (ms^{-1})

2.63

2.21

1.6

v_R (ms^{-1})

2.14

6.80

11.40
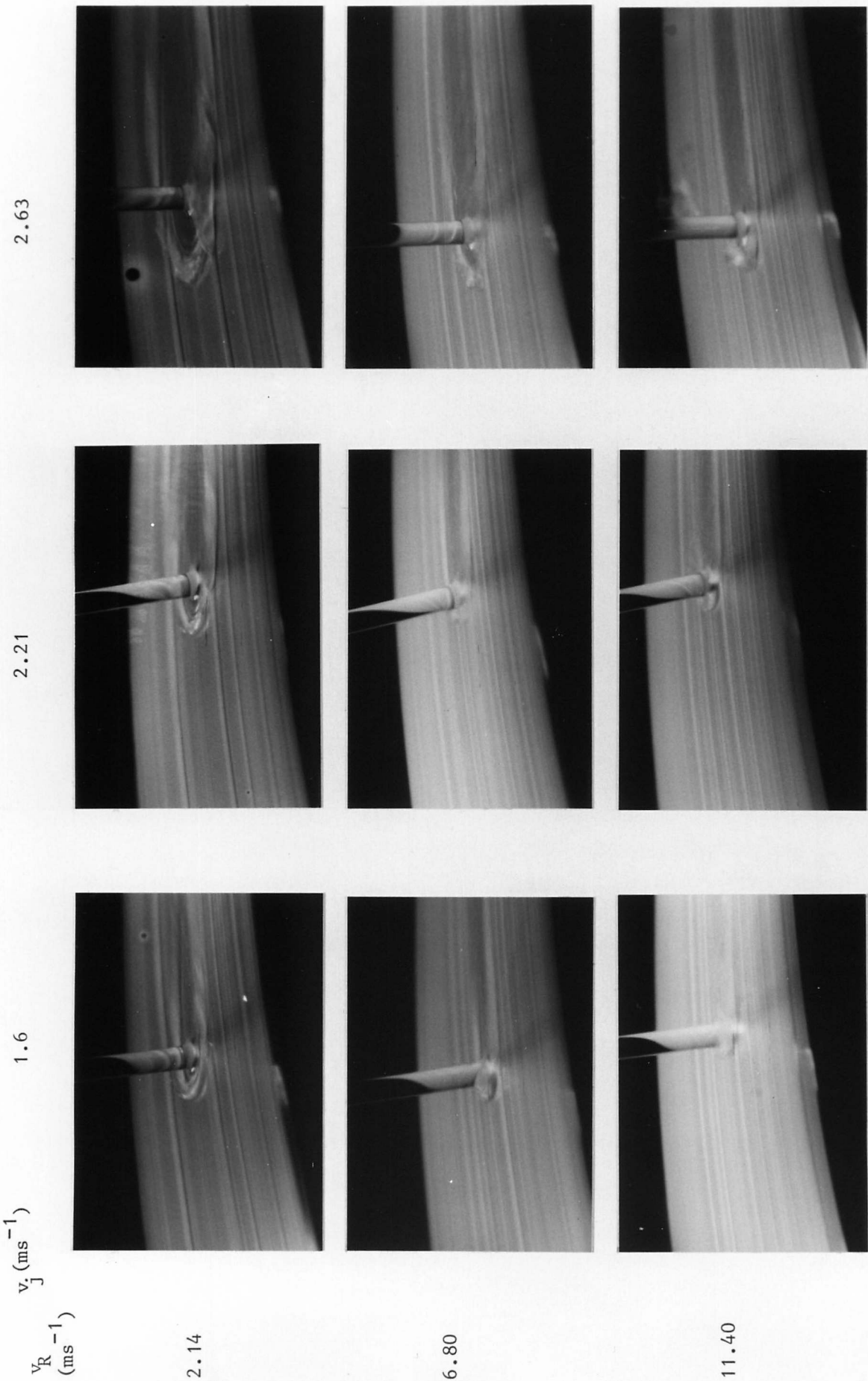
thus

$$\frac{Re_R}{Re_j} = \left[\frac{v_R}{v_j}\right]\left[\frac{w}{\phi}\right]\left[\frac{P_{amb}}{RT}\frac{\mu_\ell}{\rho_\ell}\right]\left[\frac{\overline{M}}{\mu}\right]$$ (2.42)

The dimensions of the puddle are shown in figure 2.38. Assuming the back of the puddle to be semicircular with a radius of A then

$$w = 2A \quad \text{and} \quad \phi = J$$

Substituting values of 10^5Pa, 1×10^{-3}Pa.s, 8.314 J mol^{-1}K^{-1}, 300K, 1×10^3 kgm^3 and 15.8×10^{-3}mmols for P_{amb}, μ_ℓ, R, T, ρ_ℓ and $(\overline{M}/\mu)$ respectively into equation 2.42 then:

$$Re_R = Re_j \times \left[\frac{v_R}{v_j}\right]\left[\frac{2A}{J}\right] \times 0.068$$

The tables in figure 2.39 and 2.40 show the values of v_R/v_j, $2A/J$ and Re_j, for values of v_R and v_j, from these Re_R is calculated and also shown.

The absolute values of J and A could not be measured because of the angle of observation and as can also be seen in the tables the values alter as the angle of impingement, β, is changed.

From these tables it is possible to see that as β increases from normal incidence the amount of back flow decreases and the Reynolds number for the gas boundary layer decreases because the puddle width is decreased. However for the $\phi = 0.5$mm nozzle it does look as though A goes through a minimum at about $\beta = 10^o$. In this range of v_R/v_j ratios the smaller nozzle produces a more stable melt puddle over the whole range whereas the larger orifice creates unstable melt puddles when v_R and v_j are high, although there does not seem to be a direct correlation between the product $v_R.v_j$ and Re_R. The decrease in back flow as a β increases is to be expected if the stream is considered to have both a vertical and horizontal component of momentum. As the angle of impingement shallows or β increases the contribution of the horizontal component increases proportionally to sin β while the vertical component decreases proportionally to cos β.

Figure 2.38

Dimensions of "Melt" Puddle.

$W = 2 \times A$

<u>Figure 2.39</u>

Values of Re_R calculated from experimental values of v_R, v_j, A and J for a nozzle of 1.0mm diameter.

$\dfrac{v_R}{v_j}$					Re_j		
v_j	1.60	2.21	2.63	v_j	1.60	2.21	2.63
v_R				v_R			
2.14	1.33	0.96	0.82	2.14	1600	2210	2630
6.80	4.25	3.08	2.59	6.80	1600	2210	2630
11.40	7.13	5.16	4.35	11.40	1600	2210	2630

$\dfrac{2A}{J}$					Re_R		
$\beta=0^o$							
v_j	1.6	2.21	2.63	v_j	1.6	2.21	2.63
v_R				v_R			
2.14	6.0	6.0	9.6	2.14	864	861	1416
6.80	3.4	3.6	4.8	6.80	1584	1634	2230
11.40	2.9	3.3	3.6	11.40	2224	2517	2780

$\beta=10^o$

v_j	1.6	2.21	2.63	v_j	1.6	2.21	2.63
v_R				v_R			
2.14	3.66	4.66	6.18	2.14	530	670	906
6.80	3.0	4.34	4.16	6.80	1387	1647	1927
11.40	2.4	3.20	3.34	11.40	1861	2481	2598

$\beta=20^o$

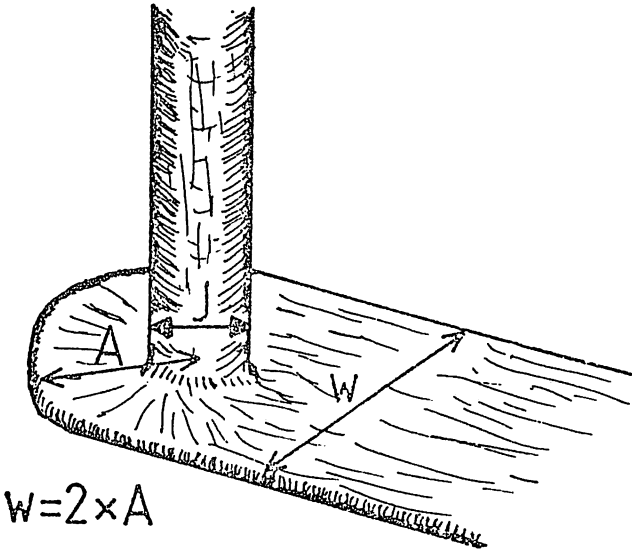| v_j	1.6	2.21	2.63	v_j	1.6	2.21	2.63
v_R				v_R			
2.14	3.2	3.66	5.2	2.14	463	528	763
6.80	2.0	2.0	3.0	6.80	925	926	1390
11.40	1.8	2.4	2.4	11.40	1396	1861	1867

Figure 2.40

Values of Re_R calculated from experimental values of v_R, v_j, A and J for a nozzle of 0.5mm diameter

v_j	$\dfrac{v_R}{v_j}$				v_j	Re_j		
	1.6	2.21	2.63			1.6	2.21	2.63
v_R					v_R			
2.14	1.33	0.96	0.82		2.14	800	1105	1315
6.80	4.25	3.08	2.59		6.80	800	1105	1315
11.40	7.13	5.16	4.35		11.40	800	1105	1315

v_j	$\dfrac{2A}{J}$				v_j	Re_R		
	1.6	2.21	2.63			1.6	2.21	2.63

$\beta = 0^{\circ}$

v_j	1.6	2.21	2.63		v_j	1.6	2.21	2.63
v_R					v_R			
2.14	3.2	3.0	5.34		2.14	232	216	392
6.80	2.5	2.0	3.34		6.80	578	462	773
11.40	2.0	2.0	3.6		11.40	776	775	1400

$\beta = 10^{\circ}$

v_j	1.6	2.21	2.63		v_j	1.6	2.21	2.63
v_R					v_R			
2.14	2.5	2.0	3.6		2.14	180	144	264
6.80	1.6	1.34	2.0		6.00	370	310	463
11.40	1.6	1.34	2.0		11.40	624	520	778

$\beta = 20^{\circ}$

v_j	1.6	2.21	2.63		v_j	1.6	2.21	2.63
v_R					v_R			
2.14	2.4	3.0	3.34		2.14	174	216	245
6.80	2.0	2.4	3.2		6.80	462	555	741
11.40	1.6	2.0	3.6		11.40	624	775	1400

2.5.2.(4) Capillary Waves

It is seen in figure 2.41 that capillary waves are obtained in this

system although only at the lowest stream speeds.   The wavelength, λ, of

the waves is about 0.3mm for the 1.0mm nozzle and 0.25mm for the 0.5mm nozzle,

and so the velocities of the waves are:

$$\phi=1\text{mm} \quad v_\lambda = \left[\frac{2\pi\ 0.072}{0.3\text{x}1.0}\right]^{\frac{1}{2}}$$

(from equation 2.31)

$$v_\lambda = 1.22\text{ms}^{-1}$$

and for $\qquad \phi=0.5\text{mm} \qquad v_\lambda = 1.36\text{ms}^{-1}$

Both these values are greater than the lowest jet velocity used and

with both nozzles less than all the other velocities, therefore such capillary waves

should only exist at the lowest jet velocity, which seems to be true.   The

waves also seem more prevalent at higher substrate velocities, and also appear to

be initiated at the impingement point.   The wavelength of the waves is far

too small for them to have been spontaneously initiated in the stream

(see equation 2.32).   These factors imply that they are the result of

some imposed vibration from the apparatus possibly related to the r.p.m.

of the wheel.   The frequencies of the waves are 4000 and 5400H$_z$ for 1 and 0.5mm

orifices respectively but there appears to be no relationship between that

frequency and the highest rotational speed of the wheel of 15H$_z$.   Such vibrations

may be initiated by harmonic resonance in the equipment.

2.5.2. (5) Instabilities in Multijet Spinning

The main aim in multijet spinning is to produce two melt pools which

interact enough to give joining but not so much as to create ridges in the

product which is preceded by the formation of a "shark's fin" (figure 2.42a).

For a particular ratio of nozzle and spacing (ϕ/d) there are optimum values

Figure 2.41

Capillary waves produced during Melt Spinning of Water $(v_j = 1.1 \mathrm{ms}^{-1})$

a) $\phi = 0.5\mathrm{mm}$
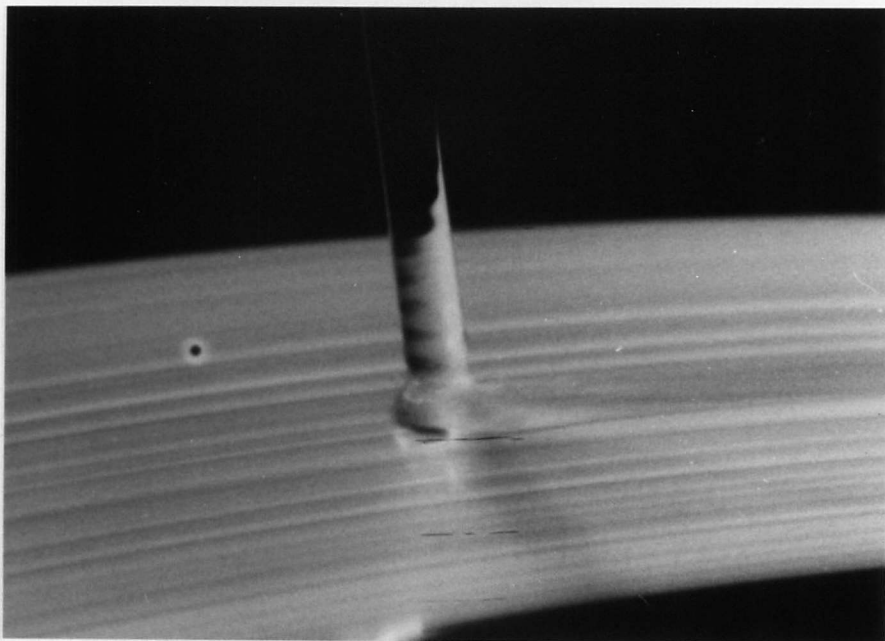
b) $\phi = 1.0\mathrm{mm}$

Figure 2.42

a)   "Shark's Fin" in Multijet Spinning of Water

b) Plot of 'h' and 'l' for "Shark's fins" against v_R for constant v_j at two

angles in multijet spinning of water.
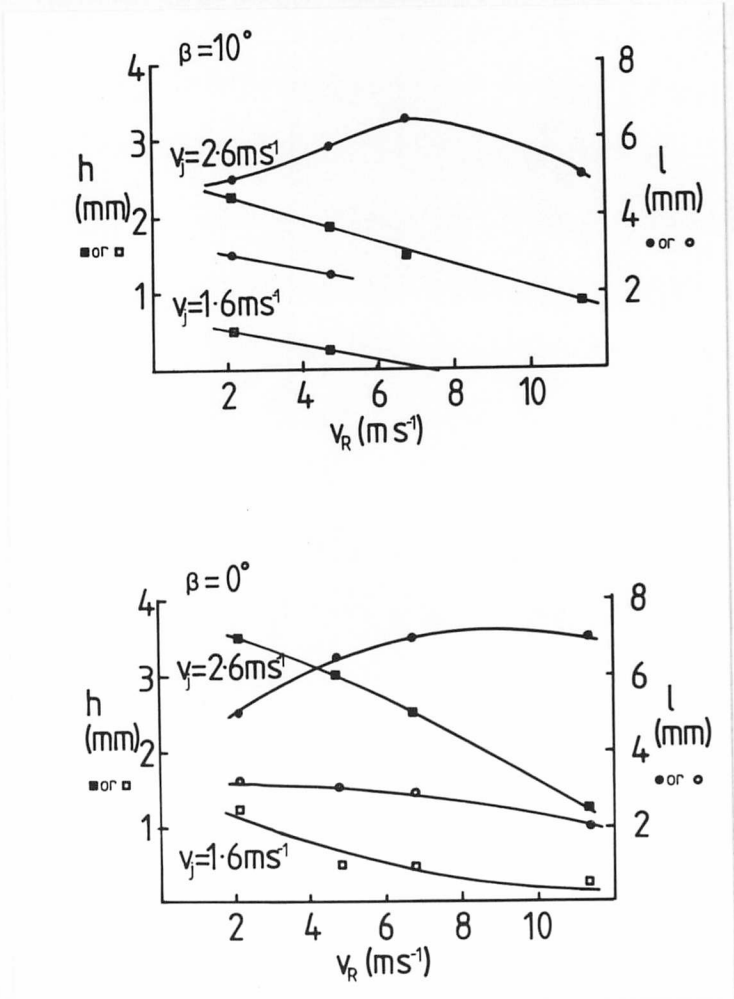
of flow rate (jet velocity) and wheel speed, to give the thickness of
ribbon required (see section 2.4.2 (4)). The width is determined by the
number and spacing of the orifices.

In the water modelling experiments only the 0.5mm nozzle was used for
multiple jet spinning as from the Re number calculations this size orifice
had better flow characteristics. The spacing, d, was 2 or 3mm, giving
ϕ^2/d ratios of 1.25×10^{-4} and 0.83×10^{-4}m respectively. The length and
height of the shark's fin were seen to be related directly to v_R, v_j, β,
ϕ and d. v_j has more effect on the height and v_R on the length.

Enough data have not been collected to make a valid assessment of the
relationships but figure 2.42b shows how height and length vary with substrate
velocity for constant jet velocity at two values of β.

2.5.3. High Speed Cine and Still Photography of the Melt Spinning of Tin

2.5.3.(1) Experimental arrangements for high speed cine and still photography

Using the melt spinning apparatus described earlier in this chapter both single and multiple nozzle spinning were observed. In the latter case an array of 9, 0.5mm holes with a 1.5mm centre-to-centre spacing, was used. In all the runs observed the circumferential speed was $15ms^{-1}$ (1250 r.p.m.). Ejection pressures were 50 and 100 kPa for the single and multiple jets respectively.

The photography was performed using a "Hadland Hyspeed" 16mm framing camera, with a framing speed of 4000 f.p.s. Kodak Ektachrome 7250 colour film, processed to 400ASA, and Ilford HP5 monochrome film, processed to 600ASA, were the recording media. The area of interest was illuminated by three 150 watt integral-reflector quartz-halogen lamps from about 100mm range.

At the framing speed used 30m of film passed through the camera in a little over one second. To accelerate to the required speed used up 9m of film at which point the ejection of molten metal was triggered by the camera via an electrically operated solenoid valve in the argon supply line.

Still photography was carried out using a $2\frac{1}{4}$ inch square format single lens reflex camera and Ilford FP4 120 monochrome film. A 150mm lens allowed an aperture of f.11 to be used giving a good depth of field. The electronically controlled flash used to illuminate the subject gave an exposure time of about 1/1500s.

The second method gave sharper pictures than the cine photography as it was recorded on a much larger negative, however the motion of the wheel was not frozen due to the longer exposure time. The second arrangement was also only used for single nozzle observation and the gas pressure and wheel speed were altered to show the effect on the melt puddle width and characteristics.

2.5.3. (2) Single jet spinning

Figure 2.43 shows two series of still photographs from single jet runs, one at constant pressure one at constant wheel speed. The series at constant pressure (fig. 2.43 a-d) show that as the substrate velocity increases from 10 to 28ms^{-1} the width of ribbon produced decreases, as expected, from 3.61 to 1.88mm. The volumetric flow rate, Q, calculated from the expression $Q = v_R w \bar{t}$ also decreases with increasing v_R suggesting that the casting conditions become more unstable at high velocities and so more spray is created. Certainly figure 2.43d shows that liquid metal is spraying out in all directions.

The second series (fig.2.43 e-h) show that as the ejection pressure increases so the width increases. Again as the pressure increases the process appears to be less stable since more spray is formed. Figure 2.43h shows the highest combination of surface velocity and ejection pressure and the amount of spray created is quite considerable.

The puddle shape has two distinct forms as observed in the water modelling. Figure 2.44 is a still photograph showing a broad flat puddle. The wheel speed was 10ms^{-1} and the ejection pressure was 208kPa, the lowest velocity and highest pressure used. It is also possible to see a ridge at the edge of the puddle. The ribbon produced was broad but very jagged as can be seen from the silhouette photograph figure 2.45. When the ratio of jet velocity to wheel velocity is decreased the puddle changes shape to become "foot" like as observed by Walter (1978) when casting amorphous alloys. Figure 2.46 shows this, the ejection pressure was 50kPa and wheel speed 15ms^{-1}.

The high speed cine photography revealed one major feature which the still photography did not capture, the formation of capillary waves on the liquid metal stream. Figure 2.46 shows these clearly but figure 2.47 is a series of frames from the cine film showing the progression of these waves.

Figure 2.43a-d   Melt Spinning of Tin (I) Constant Ejection Pressure
                                                    138kPa

a) $v_R = 10_{ms}-1$

b) $v_R = 14_{ms}-1$

c) $v_R = 24_{ms}-1$

d) $v_R = 28_{ms}-1$
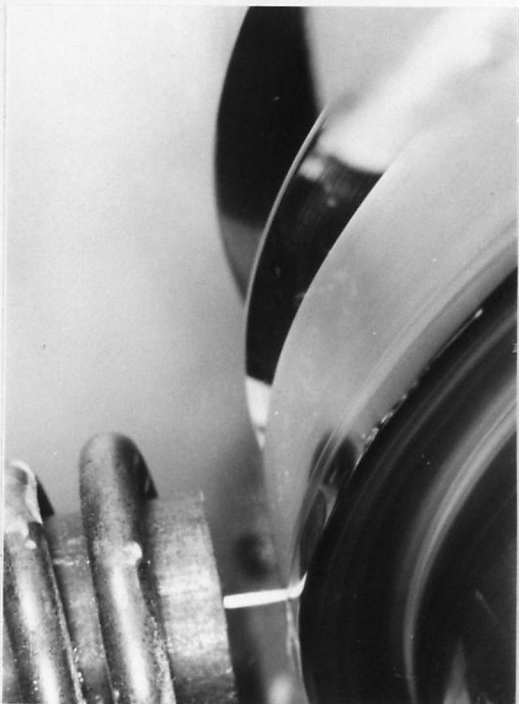
e) P = 35 kPa

f) P = 69kPa

g) P = 138 kPa

h) P = 208kPa

Figure 2.43e-h   Melt Spinning of Tin (II) Constant Velocity 28ms^{-1}

Figure 2.44   Broad Flat Melt Puddle in Melt Spinning of Tin

$v_R = 10ms^{-1}$ P = 208kPa.   (run No. 312)

Figure 2.45   Silhouette of Ribbon from run No. 312

5mm

Figure 2.46   High Speed Cine Photograph of Melt Spinning

of Tin showing Oscillations in the Jet.

$v_R = 15ms^{-1}$ P = 50kPa

Figure 2.47

High Speed Cine Photographs of Melt Spinning of Tin

showing the Progression of Capillary Waves in the Jet.

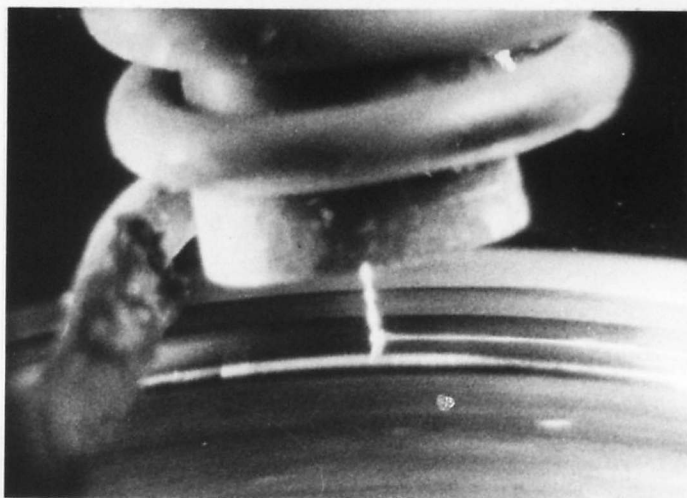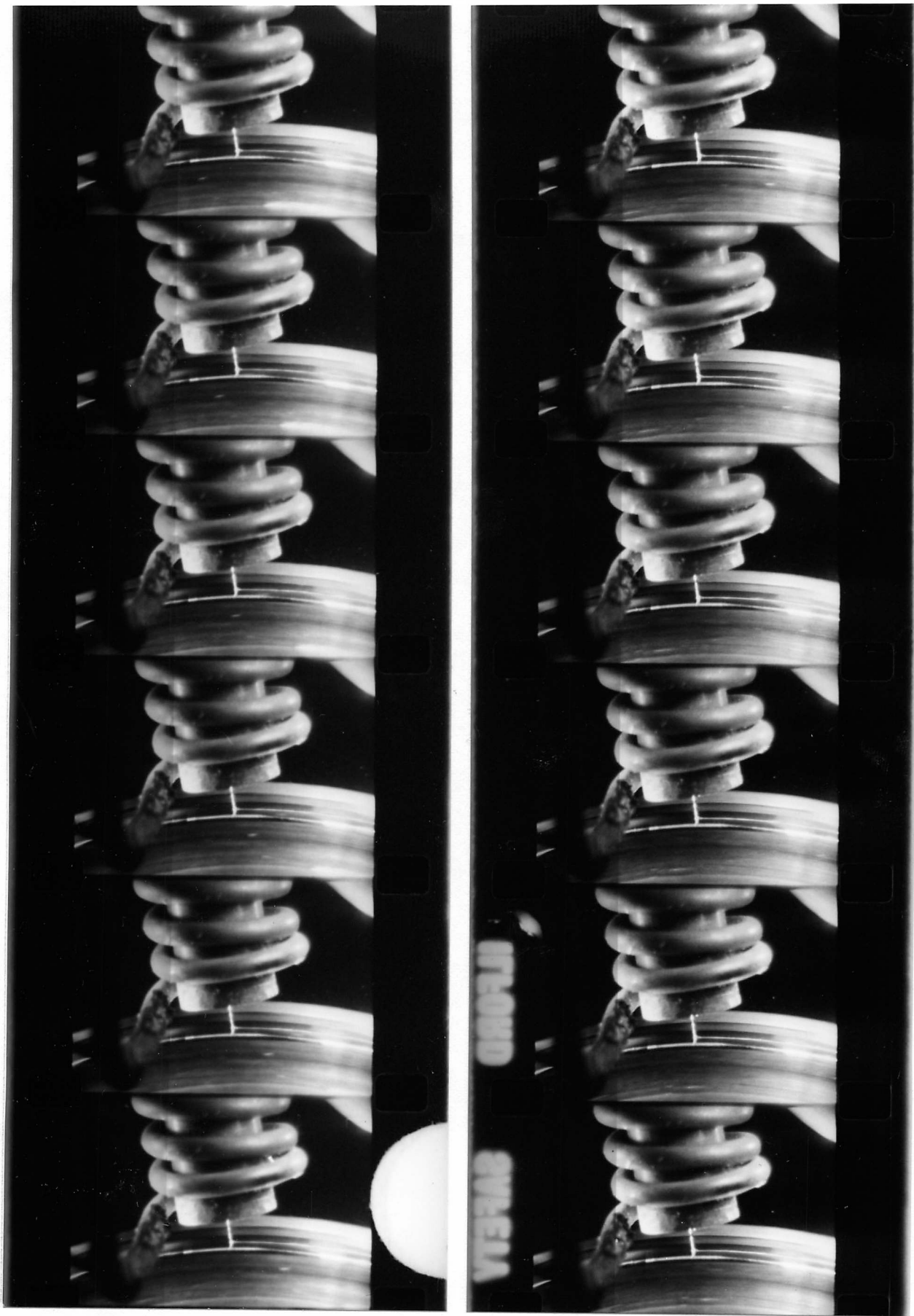The waves are obviously not the same as those observed in the water modelling as they occur along the whole length of the jet and are not confined to the region near the melt puddle. The other interesting feature is that the top or first wave is stationary whereas the others below it are continually destroyed and reformed. The wavelength of the waves is about 1.4mm, thus giving a velocity of 0.57ms^{-1} and a frequency of 400H$_z$. This wavelength is consistent with that expected of a wave formed spontaneously by surface tension effects from an orifice 0.45mm in diameter (section 2.4.2.(2)). As a certain amount of "vena contracta" would occur on ejection from the nozzle this could account for the lower effective nozzle size being experienced.

However, as the velocity of the jet can be approximated to:

$$v_j = \left[\frac{2P}{\rho}\right]^{\frac{1}{2}}$$

(2.25)

(section 2.2)

where P is the applied pressure and ρ the metal density, the jet velocity can be calculated as 3.7ms^{-1}. Waves travelling at 0.57 s^{-1} should therefore be destroyed. There is the possibility that if the surface tension forces are fairly large then it takes some time for the waves to be destroyed. If this were the case then the first wave is not destroyed because the time to its formation is very short, approximately 0.15ms, whereas for the subsequent waves there is sufficient length of stream to dissipate them. The other possible reason for the constant formation and destruction of the waves is the production of a beat note or harmonic in the apparatus due to vibration. This however is very difficult to assess.

Both still and cine photography showed that the length of the arc of contact for the ribbon was not constant for steady state conditions. During a run it can be seen that the ribbon is actually vibrating as it leaves the wheel thus changing the contact length. Figure 2.48 shows a series of high speed cine photographs demonstrating this effect. This phenomenon could be

Figure 2.48   High Speed Cine Photographs of Melt Spinning of Tin

Showing the Variation in Arc of Contact of Ribbon.

of major importance to an alloy whose final microstructure was dependent

not only on the solidification rate but also the subsequent solid state

quenching.   In tin alloys this probably does not matter too much as they

do not go through a naturally occurring solid state transformation.

## 2.5.3. (3) Melt spinning with Multiple Jets.

As has already been stated this technique is usually used for producing

wide ribbon although it could be used for the production of multiple single

ribbons. The ribbon produced in the conditions used, v_R of 15ms^{-1} and P

of 100kPa, was about 14mm wide and 50μm thick. (cf. fig.2.32).   Figure 2.49

shows a series of high speed cine photographs from the start of the run.

As the run progresses it can be seen that considerable interference develops

between adjacent melt pools leading to enhanced back flow and the formation

of a "shark's fin", as observed in the water modelling. This in turn leads

to the ejection of debris from the surface of the melt region. The material

which has experienced backward flow is subsequently accelerated forwards by

the wheel and back into the melt puddle. It would be erroneous to assume that

flow under these conditions was in anyway streamlined but surprisingly the

ribbon produced was smooth and reproducible. This run, and others like it, was

obviously inefficient as a large amount of molten metal was lost.   This

could have been reduced by lowering the jet velocity until such a time as

the melt puddles just interacted. Walter (1978) has found that a "W" jet

configuration gives more stable condition, as described in section 2.3.

Figure 2.50 shows a similar run to that in figure 2.49 but with a slightly

lower ejection pressure. The photograph has two important features. It

shows that, despite carefully machined nozzles, the liquid streams are

not all parallel and look unevenly spaced, and as a result of this the

ribbon is not always joined, the brass wheel can be seen through the slits in

the ribbon.

Figure 2.49.   Series of High Speed Cine Photographs of Multijet Melt Spinning of Tin showing build up of turbulence. ($v_R = 15ms^{-1}$ P=96kPa)

a) t=0ms
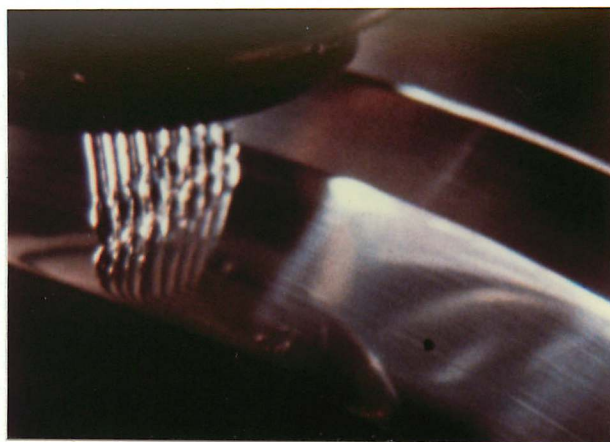
b) t=0.75ms
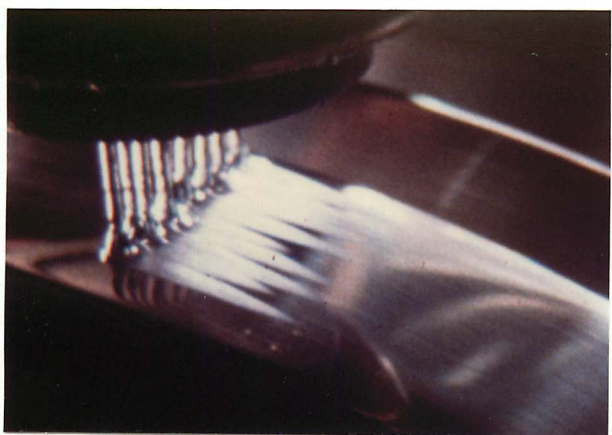
c) t=1.50ms
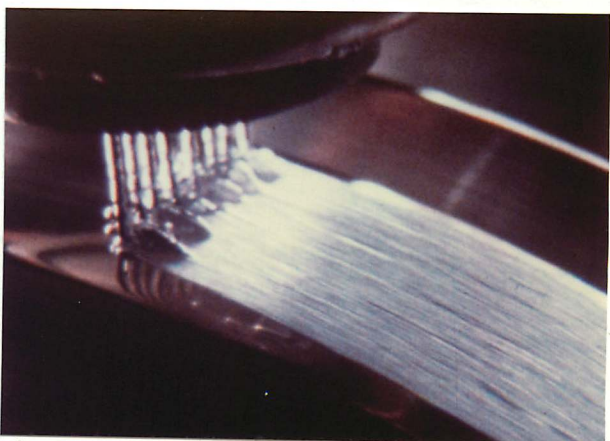
d) t=3.50ms

e) t=7.00ms

f) t=8.25ms
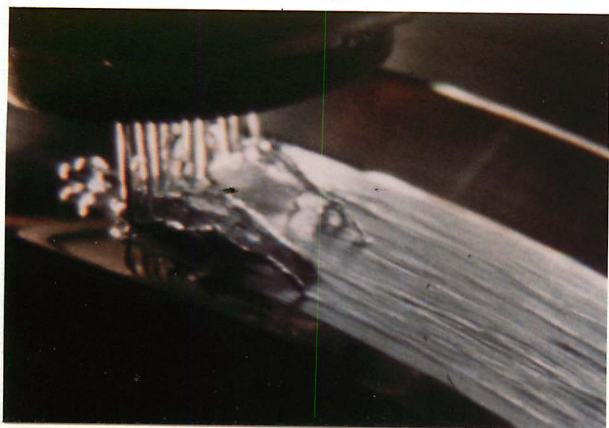
g) t=15.00ms
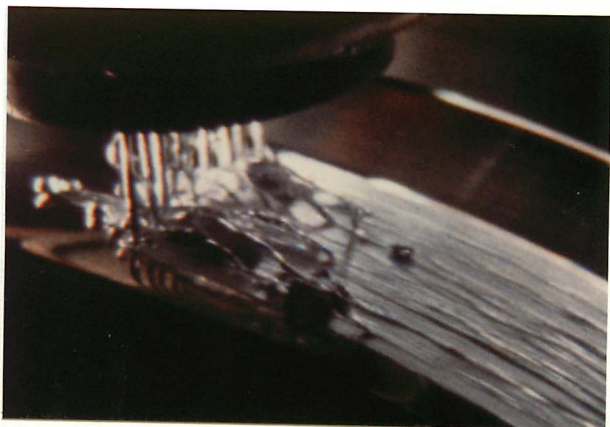
h) t=15.25ms

Figure 2.50   High Speed Cine Photography of Melt Spinning of Tin

$v_R = 15ms^{-1}$ $P = 35kPa$

Figure 2.51   Sources of Imperfections in Melt Spinning which

change the Thermal Contact Resistance.
                                                (Anthony & Cline 1979)

2.6. Control of Product Uniformity

Various methods have been developed in an attempt to stabilise the puddle during melt spinning. These have nearly all involved changing the atmosphere surrounding the melt pool thereby changing the flow characteristics.

Liebermann's calculations (1978c) show that if casting takes place in different atmospheres then turbulence in the gas boundary layer can be eradicated. Using either a low m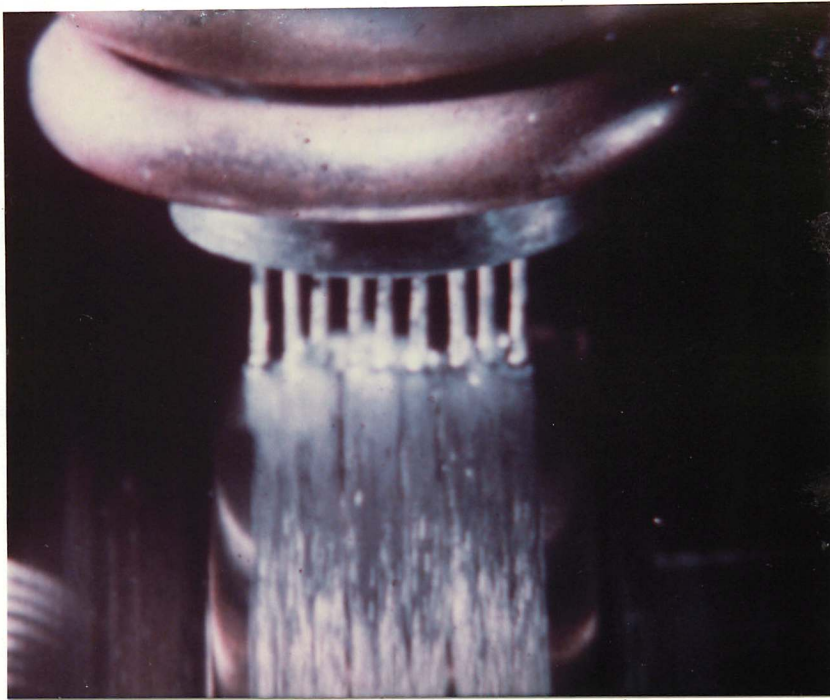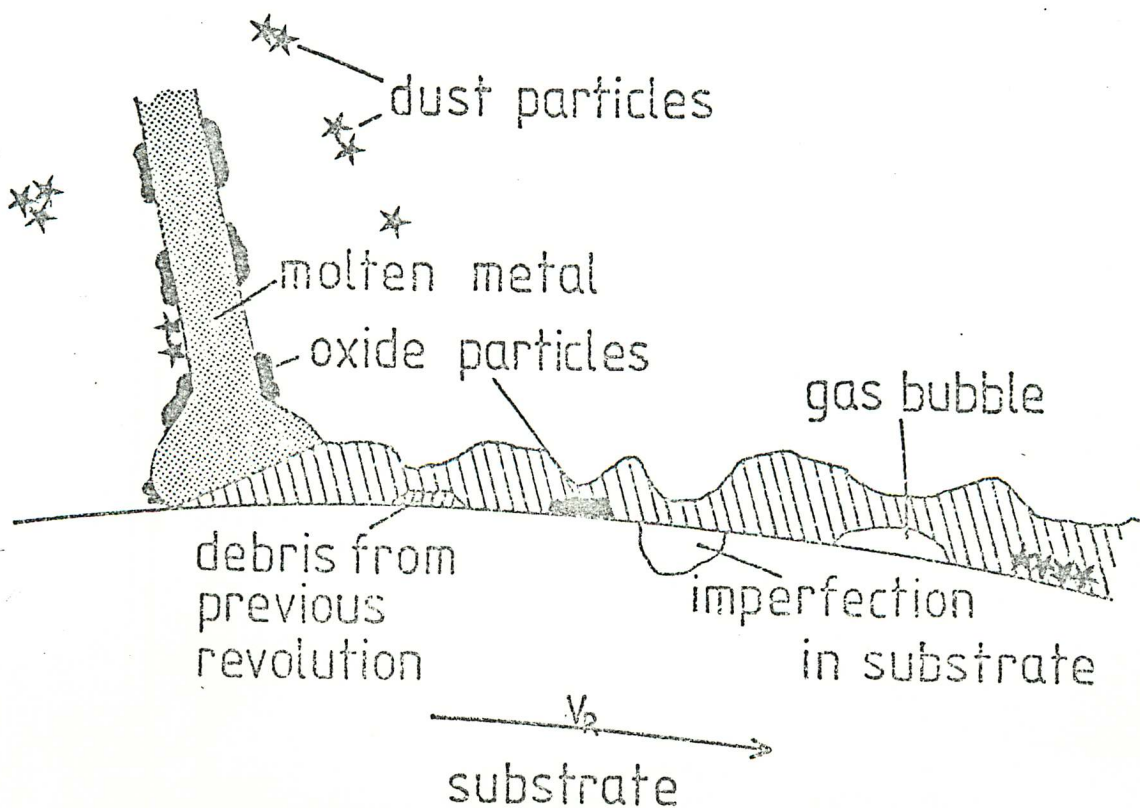olecular weight/viscosity gas or a low atmospheric pressure then the Reynolds number of the gas boundary layer can be reduced to below 2000 which is the critical value above which the ribbons become serrated.

This has been achieved by various methods one of which is the "quenching stabiliser" (Pavuna, 1980), by which a shroud of gas is introduced between the nozzle and wheel. The gas commonly used is Helium as this produces an atmosphere which not only has a low molecular weight/viscosity value but also a higher thermal conductivity than air and therefore enhances top surface cooling. It has a secondary effect of protecting the free solidification surface from oxidation. The design of Pavuna's stabiliser has changed from just a flattened tube to a jaw shaped nozzle (Pavuna, 1981) as shown in figure 1.14.

Coaxial jet melt spinning (C.J.M.S.) developed by Liebermann (1981) is another attempt to stabilise the melt pool by introducing a gas shroud via a sleeve surrounding the melting crucible, and is thus directed at the periphery of the melt puddle (fig.1.15).

Whichever stabiliser is used, if they are incorrectly operated then the shroud gas can introduce turbulence rather than control it. If the ribbons produced exceed a certain width, "shoulders" are produced at the edges, and is due to a phenomenon called the "hydraulic jump" (Olsson and Turkdogan, 1966). This could also account for the changes in puddle shape from "foot" to "broad flat" already described in section 2.5.

The fluctuations in width and length of the melt puddle caused by oscillating capillary waves and the position of the puddle on the wheel surface, all have very real effects on the shape and dimensions of the ribbon produced.   These are discussed by Anthony and Cline (1979) who also study the possible effects of inhomogeneities on the substrate surface, which cause changes of heat transfer conditions and resulting in thickness variations. Figure 2.51 shows some of the sources of imperfections which occur during melt spinning with the resulting dimensional changes.

2.7. Conclusions

In the previous sections of this chapter an attempt has been made to describe the process of melt spinning and the effects of various parameters on the dimensions and uniformity of the ribbon. Theoretical and empirical relationships of other workers have been presented and applied to the observations and data collected for tin and tin-antimony alloys, in order to allow the prediction of ribbon thickness and width for a specific set of casting conditions and alloy. The causes of instabilities arising during melt spinning have been assessed and applied to those observed in this work in an attempt to account for such phenomena.

The results obtained and presented in this chapter do not prove or disprove any theory so far proposed but hopefully they will provide more data with which other workers in the field may be able to make comparisons. These tin alloys have proved to be good model systems for melt spinning with both single and multiple jets and the information obtained has hopefully contributed to the full understanding of the melt spinning process.

Chapter 3.

PRELIMINARY STUDIES OF THE RAPIDLY SOLIDIFIED TIN AND TIN ALLOY RIBBONS

In this chapter the results of some preliminary investigations on the structure and properties of the rapidly solidified ribbons are presented. Some problems were encountered due to the inherent weakness of the materials and the product size and shape, these are discussed in the relevant sections.

3.1. Introduction

Despite its low melting point and therefore the improbability of being quenched to form a glass, tin and its alloys have been studied by a number of workers in the field of rapid solidification.

A metastable γ phase formed in alloys with a Valency Electron Concentration (V.E.C.) between 3.4 and 3.9 was observed by Kane et al (1966). The γ phase has a simple hexagonal structure and is stable in the Sn-In, Cd, and Hg systems at equilibrium between 5 and 25 atomic %. Alloys with Ag, Al, Au, Ga, Ca, Cu, Hg, Pb, Pd and Zn also form γ but those with Bi, Sb and Pt, which have a V.E.C. of greater than 4, do not.

It was therefore expected that a considerable increase of solid solubility of Sb in Sn could be achieved by rapid solidification without the creation of new metastable phases.

3.2. The Ribbon

3.2.1. Physical Description

In general it was found that the tin-antimony alloys chosen for this study were very easy to melt spin. The ribbons produced were of good quality, with relatively smooth and parallel edges and a flat top surface. The ribbons ranged from 0.67 to 4.33mm wide from a 0.5mm orifice and 12 to 100µm thick. Wider ribbon was produced from a 1.0mm nozzle, and also from multijet nozzles. The larger nozzle diameter was not generally used as

the batch mass was restricted to a maximum of 35g compared with 85g for the smaller orifice, due to surface tension considerations. Ribbons from the multijet nozzles were not used in the investigation of the effects of rapid solidification on the structure and properties of the alloys.

3.2.2. The Ribbon Surfaces

The two surfaces of the ribbon can be described as the "chill" surface, that in contact with the wheel, and the air cooled "free solidification" surface. In the alloys used in the present work they are easily distinguishable by eye, the chill surface being very reflective while the free surface gave the impression of much greater roughness.

The chill surface appeared to replicate the surface finish of the wheel in as much as there were longitudinal markings similar in size to those on the wheel surface. On examination by scanning electron microscopy (S.E.M.) (See Chapter 5 for details) it could be seen that surface replication was not the only feature of the chill surface. Figure 3.1 shows other regions which are called "non-contact" or "lift-off" areas (Wood and Honeycombe, 1974). The largest of these have widths of about 40μm while the long "scratches" are about 10μm wide.

It has been postulated that such features could arise from several causes:

(i) Gas bubble formation at the liquid/substrate interface

(ii) Solidification shrinkage

(iii) Cavitation as a result of shearing.

(iv) Liquid flow instabilities.

It would appear that the first proposal is the most likely, however work done by Mobley et al (1978) shows that the lift off regions occur probably from a combination of all the above suggestions. A correlation between the surface roughness and the size and distribution of these features is

Figures 3.1 and 3.2

Scanning Electron Micrographs of the surfaces of

Melt Spun Tin-Antimony Ribbons.

3.1   Chill Surface of Sn10%Sb Ribbon Showing

Replication of Substrate Surface and Bubbles.
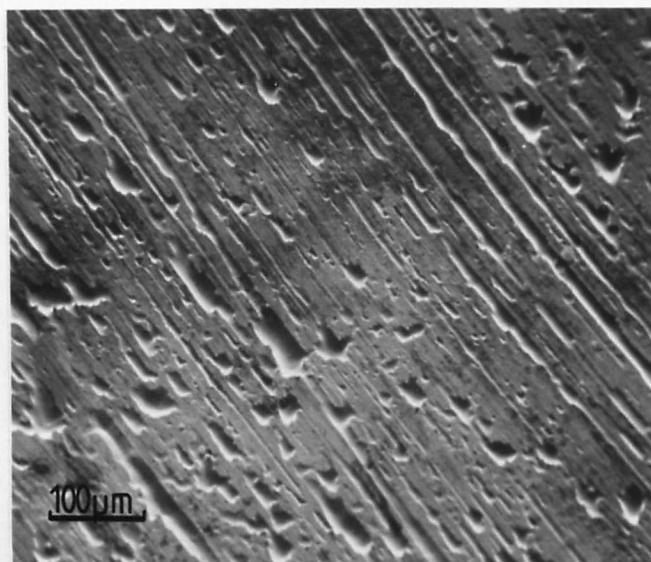
3.2   Free Solidification Surface of Alloy Ribbons showing

Rippled Surface and Shoulders.

a) 15%Sb

b) Tin

made by Huang and Fiedler (1981).

In a microcrystalline alloy the "free" surface can be expected to

show shrinkage marks (tin has a shrinkage on solidification of 2.8%,

ITRI, (1962)), and protuberances and ripples associated with dendrites

in a decanted surface. As the solidification is so rapid mass diffusion
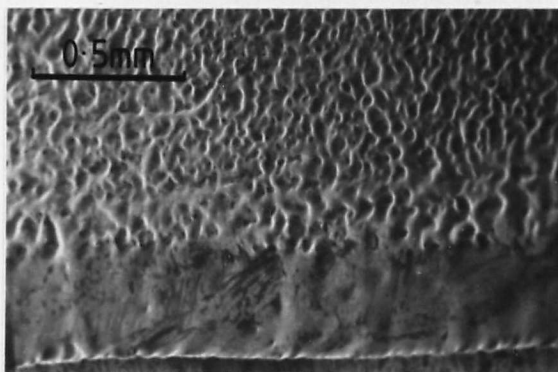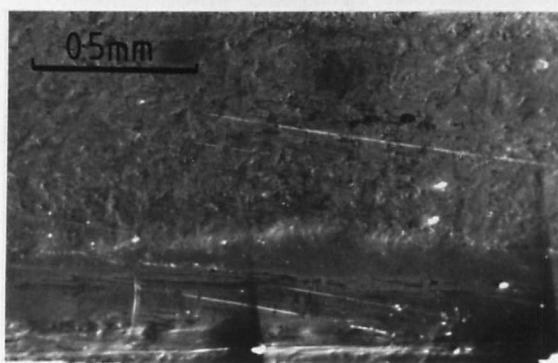
to "feed" the shrinkage voids cannot occur so interdendritic porosity

is created. Typical "free solidification" surfaces are shown in figure 3.2.

The other obvious feature is the occurrence of smooth, ripple free, edge

zones. This can total 50% of the "free" area of the ribbon. Such regions,

called shoulders have been noted by Pavuna (1981) but only in amorphous not

crystalline alloys. These could arise from two causes:

(i)   liquid flow characteristics of the puddle(hydraulic jump)

(ii)   conduction differences at the edge of the melt pool

In the first case if the melt puddle is broad with ridges at the

edge (high v_j/v_R ratio, see Chapter 2) then the cooling rate at the edges

is going to be slower than in the centre due to the greater depth of liquid.

If the cooling is very much slower, then the decanted effect may not manifest

itself if feeding is adequate. In the second case however the heat

extraction from the edge of the ribbon is faster than from the centre as

the diffusion field is greater at the edge. The edges are therefore the

first regions to solidify and the slower cooling central region acts

as a feeder for the edges which results in a decanted central region.

Again it is likely that the effect arises from a combination of both

causes although not enough work has been carried out to assess the problem

properly.

3.3. X-ray Analysis of Rapidly Solidified Tin-Antimony Alloys
3.3.1. Introduction and Method

Debye Scherrer powder camera pictures have been used by many workers

to measure accurately, changes in lattice parameter which occur in solid

solutions. Such X-ray analysis can also be used to determine the crystal structure of the material.

In the present work a 114.6mm diameter Deby-Scherrer powder camera was used. The samples were folded lengths of ribbon centred in the usual fashion. From these powder photographs parameters were calculated using a computer program and the following method.

β-tin has a body centred tetragonal structure, space group $I\frac{422}{amd}$, which makes calculations of lattice parameters marginally more difficult than in a cubic material. An iterative process has to be used to give progressively better values of the lattice parameters.

The spacing, d, between any set of like planes in a tetragonal material is given by:

$$\frac{1}{d^2} = \left(\frac{h^2 + k^2}{a^2}\right) + \left(\frac{\ell^2}{c^2}\right) \tag{3.1}$$

$$\text{where } d = \frac{\lambda}{2\sin\Theta}$$

a and c are therefore given by

$$a = d \left[(h^2 + k^2) + \left(\frac{a}{c}\right)^2 \ell^2 \right]^{\frac{1}{2}} \tag{3.1a}$$

$$c = d \left[\left(\frac{c}{a}\right)^2 (h^2 + k^2) + \ell^2 \right]^{\frac{1}{2}} \tag{3.1b}$$

Assuming a (c/a) ratio of 0.546 (ASTM card file No. 4-0669). Values of a and c were calculated for each line on the film. The program then used a linear regression analysis package to plot both a and c against a function of $\Theta(f\Theta)$, where $f(\Theta)$ was the Nelson-Riley-Taylor-Sinclair expression:

$$f(\Theta) = \tfrac{1}{2}\left\{\frac{\cos^2\Theta}{\sin\Theta} + \frac{\cos^2\Theta}{\Theta}\right\} \tag{3.2}$$

Each point was also given a sec²θ weighting to account for the higher

accuracy of high angle lines. (Cullity, 1959; Chapter 14). Extrapolation

back to f(θ) = 0 gave values of a and c which were then used to calculate

a new (^{c}/a) ratio. The process was repeated until there was no change

in the fifth decimal place of the parameters when measured in Ångström units.

An intermetallic phase, SbSn, can exist at equilibrium in alloys with

more than 5% antimony. SbSn has a rhombohedral structure, space group

I $\underline{4}$ $\bar{3}$ $\underline{2}$ with a lattice parameter of 6.138Å and an internal angle of 89.38
  m m

degrees at 52.4 atomic % Sb (ASTM card file No.1.0828). This has been

described as a slightly deformed NaCl structure, thus giving rise to its

cubic appearance on X-ray films.

3.3.2. Results and Discussion.

X-ray patterns were taken of pure tin and the following tin-antimony

alloys 5, 10, 15, 20 and 50%Sb.

The alloys containing up to 15%Sb showed the same structure as for

pure tin with a slight displacement of the lines. The 20%Sb pattern was

mixed, with both the lines from tetragonal β-Sn solid solution, and a

second apparently cubic phase present. The 50%Sb ribbon showed a single

phase which appeared cubic. From these films it was seen that immediately

after spinning the alloys of tin with up to 15%Sb were a single phase solid

solution, at 20%Sb a proportion of SbSn was present and at 50%Sb only SbSn

was formed. On ageing at room temperature however the alloy containing 15%Sb

showed faint SbSn lines after 45 days and at 443K the lines appeared after

12 hours.

Figure 3.3. shows plots of lattice parameters against composition up to

20%Sb. It can be seen that results of the present work are very close to

those of Raynor and Lee (1954) who could only produce solid solution up to

about 8%Sb by conventional chill casting. The 'a' parameter increases linearly

with composition up to just greater than 15%, then tails off as the SbSn phase

Figure 3.3

Plot of Lattice Parameters, a and c, against Sb content.
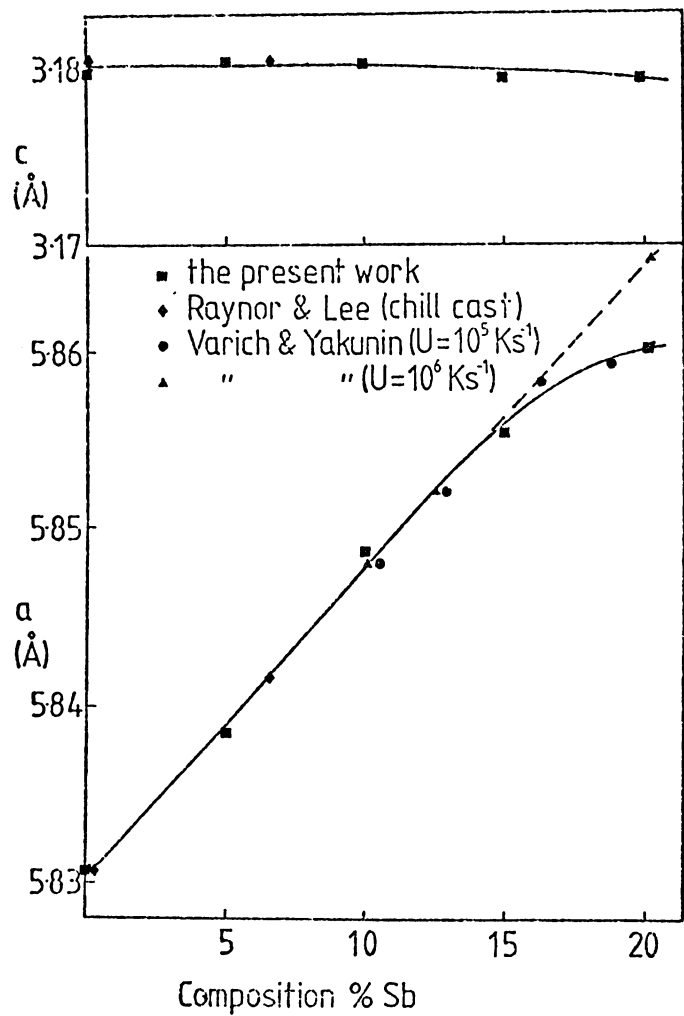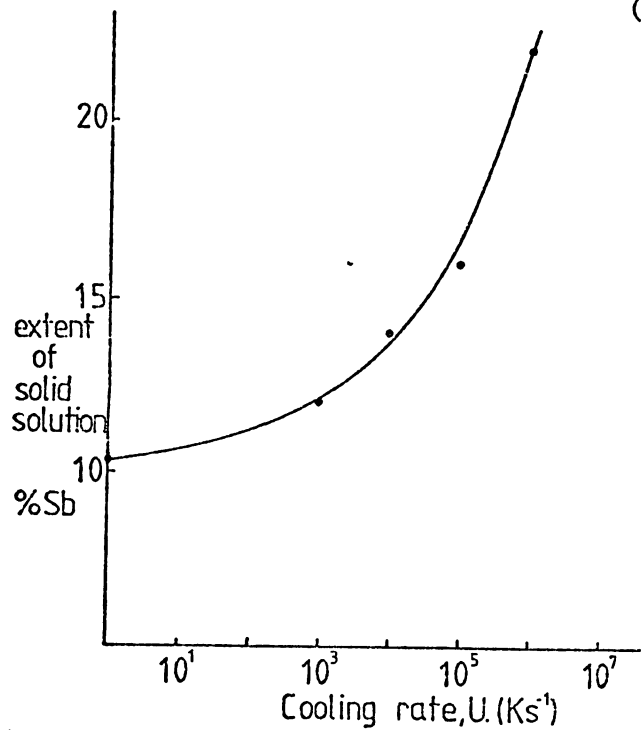

Figure 3.4   Plot of Extent of Solid Solubility against Cooling Rate.

(After Varich & Yakunin 1968)

is formed. The 'c' parameter is approximately constant but may show a slight decrease at the high antimony end. The increase in lattice parameter is a result of the substitution of the slightly bigger Sb atoms for the Sn atoms thus expanding the structure.

Varich and Yakunin (1968) managed to obtain a solid solution extension of 22%Sb in splat material with a cooling rate of $10^6 Ks^{-1}$. They plot a graph of cooling rate against extension of solid solution (fig. 3.4). From this graph it would appear that the cooling rate in the present work was between 10^5 and $10^6 Ks^{-1}$, which is to be expected from melt spinning.

Khera and Nayar (1971) report a new phase which occurs when they quench tin alloys with as little as 0.85%Sb. The phase is tetragonal with a = 5.86Å and c = 6.14Å. At 11%Sb they start producing SbSn intermetallic. They postulate that the new phase is an intermediate between β- tin structure and the SbSn structure. The results of the present work, Kane et al (1966) and Varich and Yakunin (1968) do not suggest that such a phase exists. The conclusion of Khera and Nayar could have arisen from the misinterpretation of their X-ray photographs. They may also have assumed an incorrect cooling rate and erroneously assumed that some SbSn present is a new metastable phase.

Varich and Yakunin (1968) also show in their work that in Pb-Sb and Sn-Pb alloys, decomposition commences rapidly soon after splat cooling. The incubation time in each case is of the order of 120 to 180s. but the time to 50% decomposition can vary between 600 to 1800s depending on the composition. It would be reasonable to assume that similar effects also occur in Sn-Sb alloys.

3.4. The Metallography of Tin and Tin Alloy Ribbons

3.4.1. Introduction

The metallographic examination of tin ribbons proved to be exceedingly difficult. As tin has such a low melting point (505K) it is important that if the solidification structure is to be seen it should not be heated overmuch during specimen preparation. This should avoid any recrystallisation or annealing which may be initiated by any temperature rise during mounting or polishing.

The structure of the ribbons were observed by optical metallography, scanning electron microscopy (SEM) of fractured surfaces, and a little transmission electron microscopy (TEM).

3.4.2. Optical Metallography

Specimens for optical metallography were usually copper plated to make them more durable before being mounted in Stuers' Specifix Powder cold mounting resin. Both plating process and mounting reaction raised the temperature about 30K to about 325K (0.65 T_m).Specimens were then ground and polished down to 0.05µm alumina. Figure 3.5 is a table of etchants which have been used on tin alloys with an assessment of their usefulness. The most successful were Tin Etch and $SnCl_2$/HCl.

It was found that although it was difficult to polish and produce a good surface on pure tin, the etching was straightforward. However as soon as there was any antimony in the alloy polishing became easier as the alloys were harder but etching to show grain boundaries was almost impossible.

Figure 3.6 is a micrograph of the whole width of a tin ribbon cast at 20ms^{-1}. The structure is clearly visible even at the low magnification the grain size can be seen to be of the same order as the ribbon thickness. Figure 3.7 is the same ribbon but at a higher magnification. This clearly shows some columnar grains growing with boundaries at right angles to the faces of the ribbon. The average grain width is 25µm.

Fig. 3.5.

Etchant	Comments	
	Sn	SnSb alloys
Nital 2%/5% (Rollason, 1973)	Unsatisfactory	Darkens Sn rich areas. Leaves SbSn white.
HCl 2%	Not very good but could show grain boundaries	Tendancy to pit.
HCl vapour	Possibly showed grains.	Good macroetch.
$SnCl_2$/dil HCl until $SnCl_2$ dissolved	Good grain boundary etch even when very small grains.	Unsatisfactory.
NaOH 20%	Unsatisfactory.	Unsatisfactory.
Citric Acid 50%	Unsatisfactory.	Unsatisfactory.
Acid Dichromate $\begin{bmatrix} 2\%K_2Cr_2O_7 / \\ 8\%H_2SO_4 / \\ 4\%NaCl \text{ sat soln}/ \\ 86\%C_2H_5OH \end{bmatrix}$	Unsatisfactory.	Unsatisfactory.
Tin Etch $\begin{bmatrix} 2cm^3 \ HCl / \\ 5cm^3 \ HNO_3 / \\ 100cm^3 \ H_2O \end{bmatrix}$	Grain contrast etch.	Grain contrast etch Leaves SbSn white Better for macro than micro.
Ammonium Polysulphide	Unsatisfactory.	Good for macro etch.

The ribbon shown in figure 3.8 was spun at a lower speed, $10ms^{-1}$, and was a good example of a bad run showing "fir tree" defects and ripples on the top surface.   The grain size of this ribbon is 15μm, and the grains seem to be equiaxed rather than columnar.   This difference is seen better in figure 3.9.   As the average thickness, $\bar{t}$, of the ribbon spun at $10ms^{-1}$ is greater than that of ribbon spun at $20ms^{-1}$, it would be expected that the grain size would also be bigger (see Chapter 2).   The thicker the splat, the lower the cooling rate and hence the larger the grain size.   This conclusion does not take into account the flow of the fluid in the melt puddle.   It is well known that stirring can initiate crystal growth, as the run at $10ms^{-1}$ was an unstable, turbulent run then there may well have been enough eddy currents produced in the puddle to initiate crystal nucleation.   This would suggest that a highly turbulent melt puddle could in fact produce a finer grain size than a stable puddle.   Providing the dimensional uniformity of the ribbon is not important then this could be an acceptable way of further refining the grain size.

All the grain sizes in the rapidly solidified ribbon are much smaller than expected in a cast tin alloy where the grain size could be from 500μm to 5000μm.

3.4.3 The grain morphology of a 15%Sb ribbon as revealed by an S.E.M. Study of fracture surfaces.

In order to assess the scale of microstructure obtained in rapidly solidified antimony-bearing alloy ribbons it was necessary to resort to studying fracture surfaces of the ribbons, which had failed in tension, (see section 3.5.2.) by S.E.M.

It was not possible to study pure tin ribbons by this method because the fracture surfaces produced were heavily deformed and smeared.   In the alloys containing antimony the ductility was much lower and the fracture surfaces

Optical Micrographs of Rapidly Solidified Tin Ribbon

Etched in Tin Etch.

3.6 v_R = 20ms^{-1} P = 208kPa   w = 2.45mm $\bar{t}$=20μm

Ribbon 750   500μm

3.7 v_R = 20ms^{-1} P = 208kPa   w = 2.45mm $\bar{t}$=20μm

Ribbon 750

100 μm
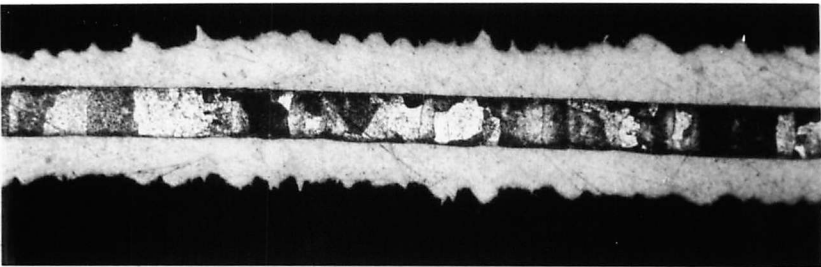
3.8 v_R = 10ms^{-1} P = 138kPa   w = 3.61mm $\bar{t}$=22.4μm

Ribbon 749

100μm
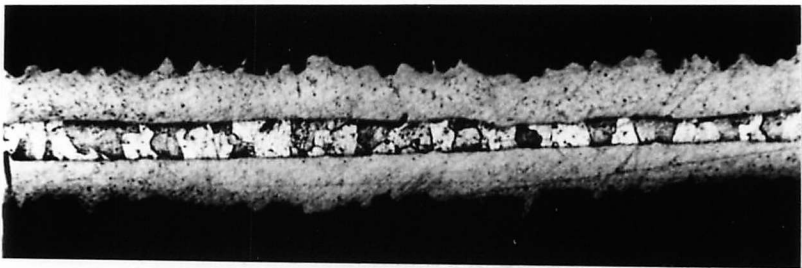
3.9

a)

Ribbon 750

b)

Ribbon 749

50 μm
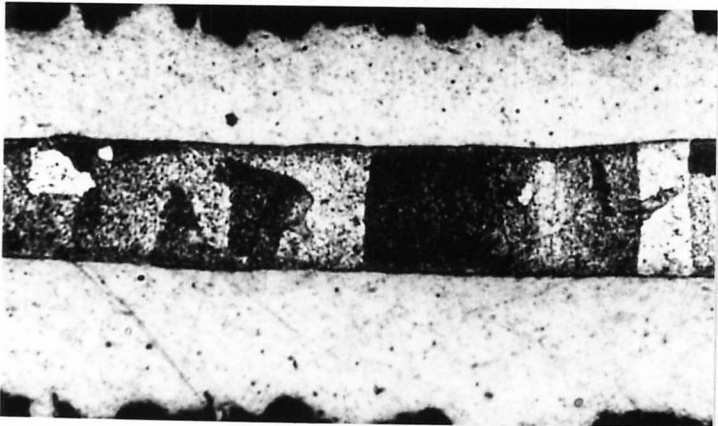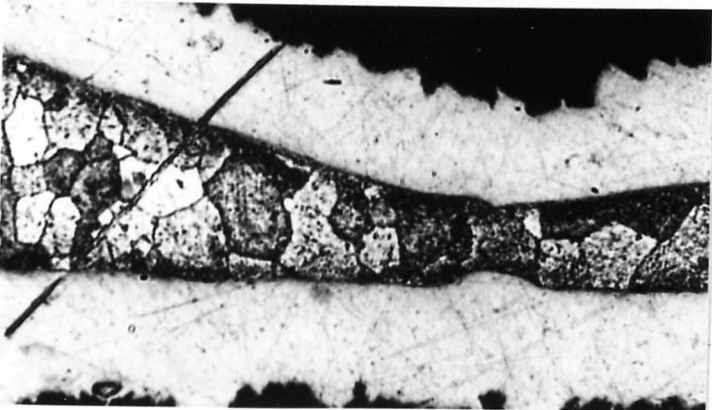
were clearly visible.

Figure 3.10 shows the fracture surface from a Sn15%Sb ribbon.   It is possible to see three distinct regions in these micrographs.

Region A.

This bounds the chill surface of the ribbon and it can be seen that the grain boundaries are perpendicular to the surfaces of the ribbon.   The grain width here is of the order of 10μm and the fracture is intergranular. This type of structure has often been described as cellular.

Region B.

At a point some half way up the thickness of the ribbon the structure changes from a cellular appearance to a rounded "dendritic" type.   There may also be some interdendritic porosity caused by poor feeding during solidification hence the decanted appearance of the structure.

Region C.

This is an area of ductile fracture.

Pure tin does not undergo brittle fracture at room temperature.   The occurrance of some regions of cleavage fracture in the rapidly solidified 15%Sb ribbon could be the result of two effects:

i) Segregation

ii) Orientation

i)   Segregation of antimony during solidification could produce regions of high and low antimony content.   Such segregation could be a result of differences in cooling rate across the ribbon.   Regions with a high antimony content will be more brittle than those deficient in antimony thus giving rise to a mixed mode fracture surface.

ii)   As tin solid solutions are body centred tetragonal in structure they have a limited number of slip planes.   There will therefore be a high possibility of anisotropic deformation occurring in the polycrystalline state.

Figure 3.10 Scanning Electron Micrograph of Fracture Surface of
Rapidly Solidified Sn 15% Sb Ribbon
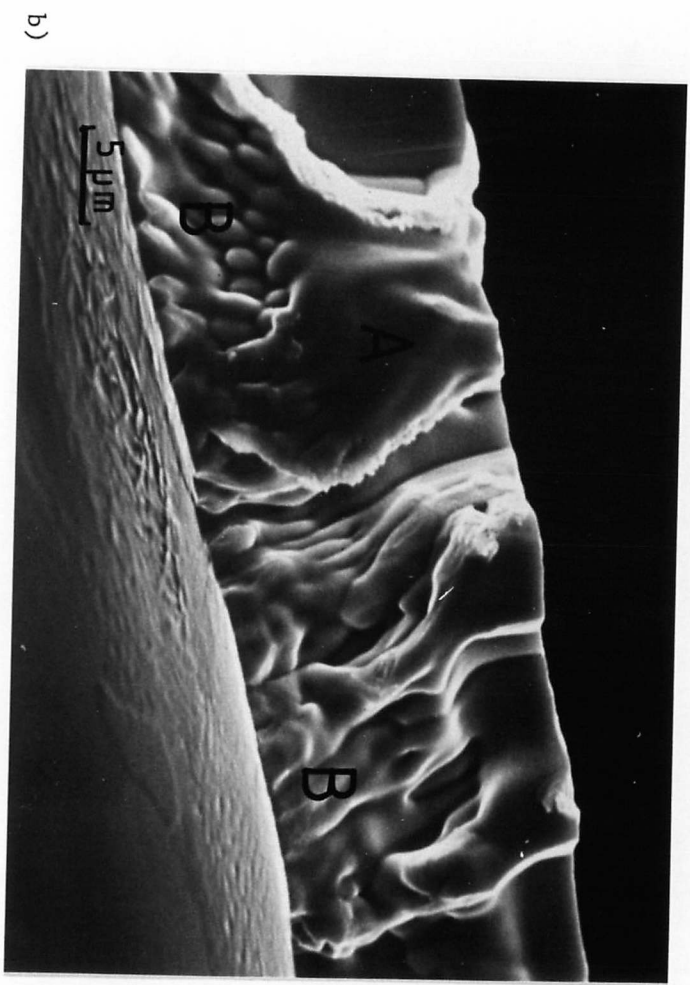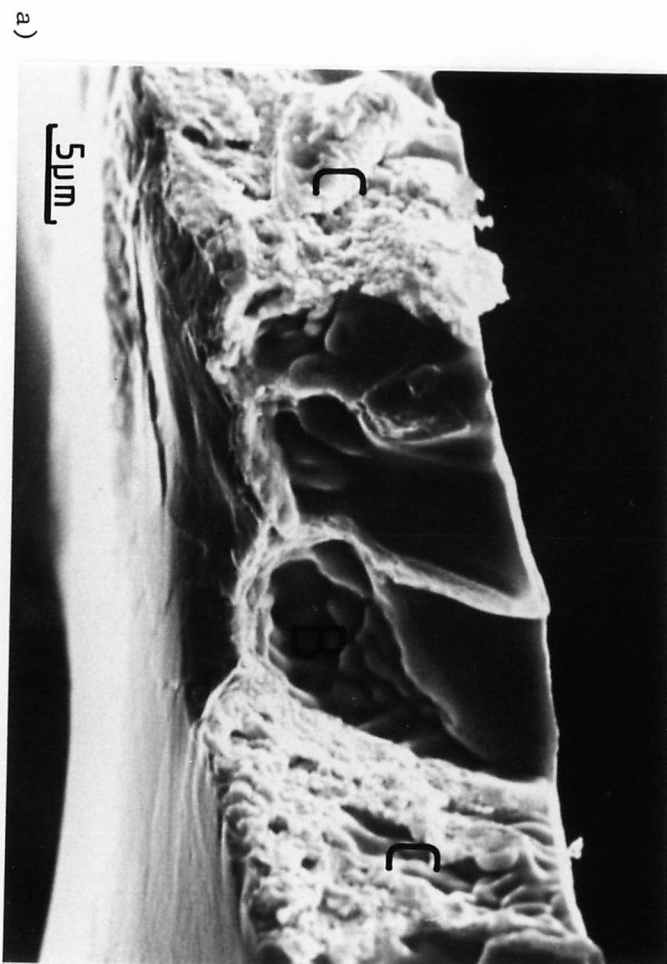
This is further enhanced by the fact that the ribbons seem to be only a single crystal thick and thus any strain is not easily accommodated by neighbouring grains. This again could give rise to the ductile/brittle fracture surface observed.

The mechanism by which the structure changes across the ribbon is dependent on the rate of heat extraction. Initially the heat flow is very much greater through the chill surface than through the liquid, thus giving rise to the cellular growth of region A (fig. 3.11a). With time the substrate surface heats up and the liquid cools down and the heat extraction through the liquid becomes significant. There is now the possibility of the remaining liquid becoming undercooled thus stabilizing any perturbation on the until now planar solidification surface (fig.3.11b,c). Dendrites can only grow into a region of negative temperature gradient so they now become stable. There may also be some contribution from constitutional undercooling.

The dendritic appearance of region B is a typical solidification structure and could even be "solidification cracking" (Davies and Garland, 1975). The interdendritic regions will not be "fed" by liquid metal in the final stage of solidification thus giving rise to a rippled surface (fig.3.12) and the possibility of internal porosity.

3.4.4. T.E.M. of a Sn10%Sb Ribbon.

Transmission electron microscopy of the alloy ribbons in this study proved, as with the optical metallography, to be rather difficult. Attempts at electropolishing any of the alloys resulted in an insoluble black precipitate on the surface of the specimen which was assumed to be a finely divided deposit of antimony.

It was therefore decided to ion-beam thin the ribbons after punching out 3.0mm discs. Even using this technique only one foil was produced which had enough thin area to take micrographs. A Phillips E.M.300 transmission

Figure 3.11

Mechanism for Occurance of Dendritic Interface in

Rapid Solidification   (Schematic)

a) $t_1 \sim 0$ Planar Interface

substrate T liquid T_s air

T_B 'splat'

b) $t_2 > t_1$ Planar Interface (perturbations dissolve in positive Temperature gradient)

T T_s

T_B—

c) $t_3 > t_2$ Dendritic Growth
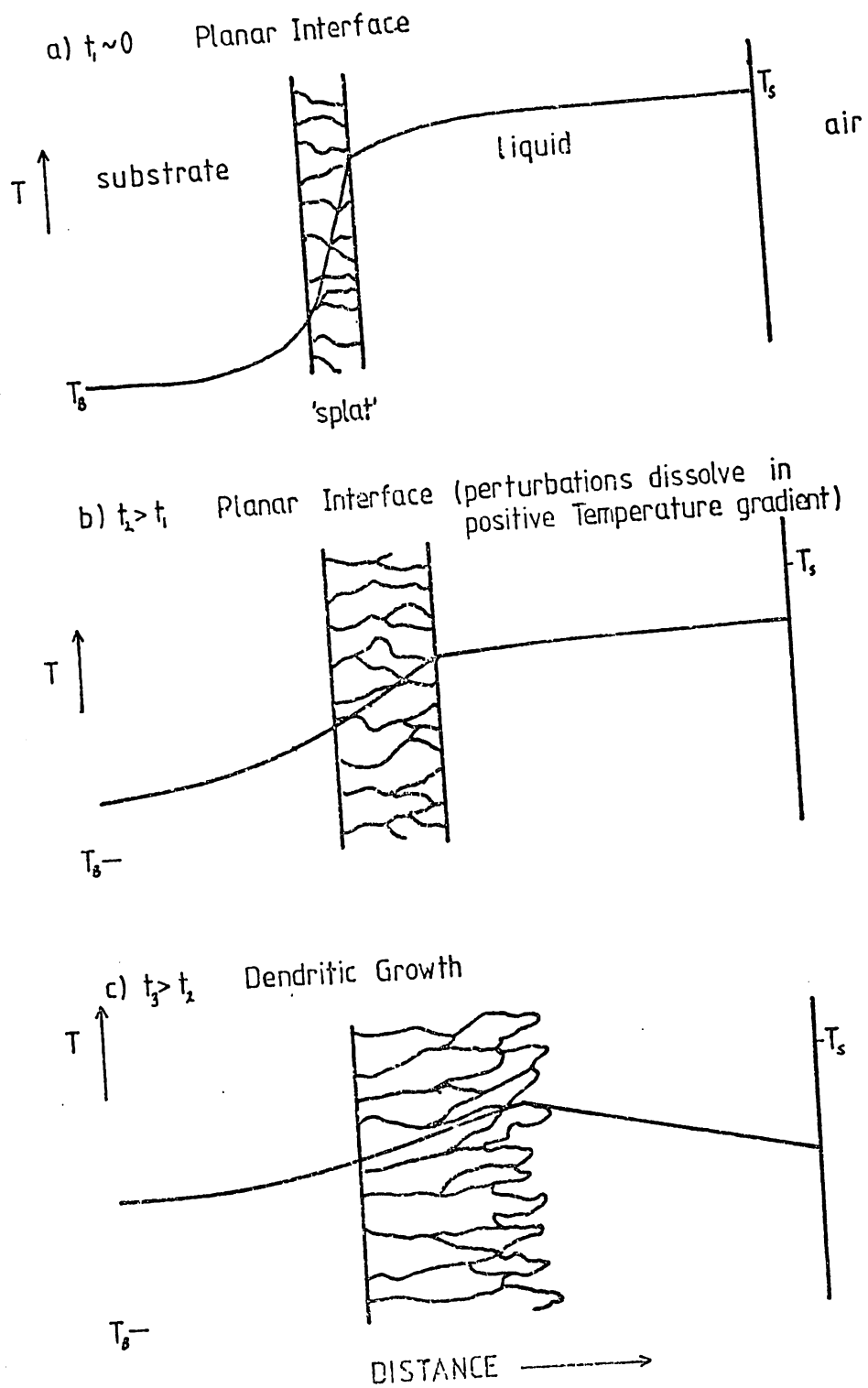
T T_s

T_B—

DISTANCE ———→

Figure 3.12

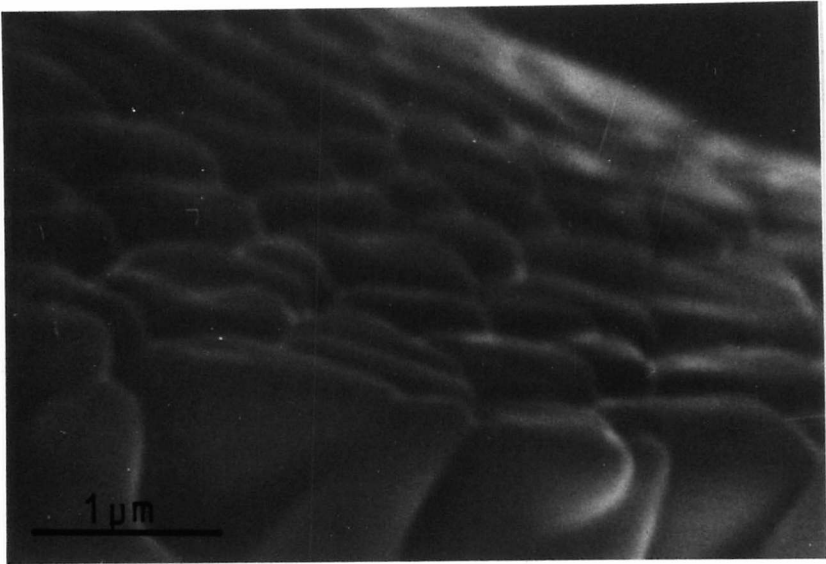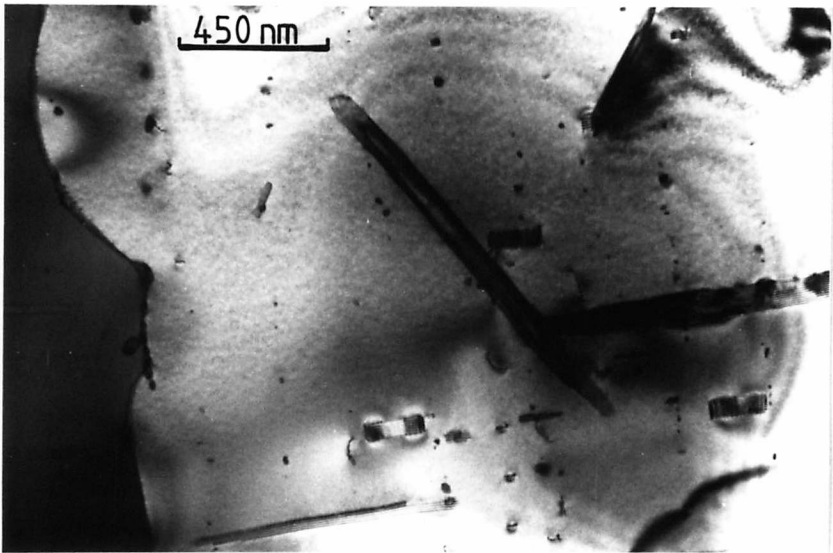Scanning Electron Micrograph of 'Free' Surface of Sn 15% Sb

Melt Spun Ribbon

Figure 3.13

Transmission Electron Micrograph of Sn 10% Sb Melt Spun Ribbon

electron microscope was used at 100kV.

Figure 3.13 shows a region of the Sn10%Sb foil in which can be seen needle like precipitates of SbSn. A bowing grain boundary, pinned by precipitates, can also be seen. The precipitates appear to be growing at angles of 60 degrees to each other and are some 25 to 75nm wide and up to 1500nm long.

Such precipitates have also been observed by Kaczorowski and Matyja (1979) in splat quenched foils of Sn10%Sb.[*] Their specimens were not thinned as the method of production gives sufficient electron transparent regions of material. Their initial foils showed only a single phase product. On heat treating at 373K for 10^4s they obtained needles of the size seen in figure 3.13. However they did observe clustering after annealing for only 300s.

Their analysis shows that the following relationship is established between the precipitate and the matrix lattices:

$$<020>_{SbSn} \parallel <020>_{Sn}$$

$$\{202\}_{SbSn} \parallel \{201\}_{Sn}$$

It was not possible to verify this relationship as not enough diffraction patterns could be taken.

It should also be noted that the SbSn particles which have precipitated in rapidly solidified alloys are a completely different shape to those obtained from conventional casting methods. Whereas the SbSn particles in conventional alloys are cuboids, in rapidly solidified alloys they are needles. This is a result of the different reactions in each case, one being a liquid state reaction, $\ell \rightarrow SbSn + \beta$ the other being a solid state reaction, $\beta' \rightarrow SbSn + \beta$, where

*Footnote: The work by Kaczorowski and Matyja (1979) was published a year after the start of the present work. Further T.E.M. work was discontinued to avoid the possibility of overlap.

β' is the solid solution of Sb in Sn. In the liquid state reaction there are no growth direction constraints as there are in the solid state reaction.

3.5. The Mechanical Properties of the Rapidly Solidified Ribbons.

Having studied the microstructure of the rapidly solidified ribbon and noted the refining effect that rapid quenching has had on the grain size of the alloy, and the amount of solid solution extension possible, it is necessary to study what changes in mechanical properties have taken place, if any.

Two tests were used to assess such changes:

      1)   Microhardness

      2)   Tensile Testing

3.5.1. Microhardness

Due to insurmountable problems as a result of a combination of effects, namely the material hardness and ribbon thickness, no microhardness results can be reported.

3.5.2. Tensile Tests

Tensile tests were performed on an Instron T.M.M. tensile testing machine using a crosshead speed of 10mm. $\min^{-1}$.

The problem of clamping such delicate ribbons immediately arose. The answer was to glue the ribbons between aluminium plates using a cyanoacryllic glue (fig.3.14).

It should be appreciated that there are significant problems related to the evaluation of results obtained in such a fashion. One major difficulty arises from the dimensional inconsistency of the ribbons due to the irregular top surface (fig.3.6). Also the specimens do not have exactly parallel edges or an increasing cross section at the clamps. Any specimen which failed near the clamps was rejected as it could have produced spurious results.

Figure 3.14

Tensile Clamps for Rapidly Solidified Ribbon

Al CLAMPS
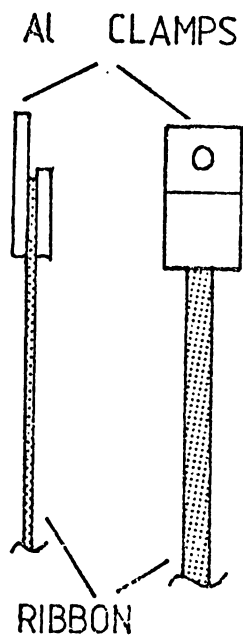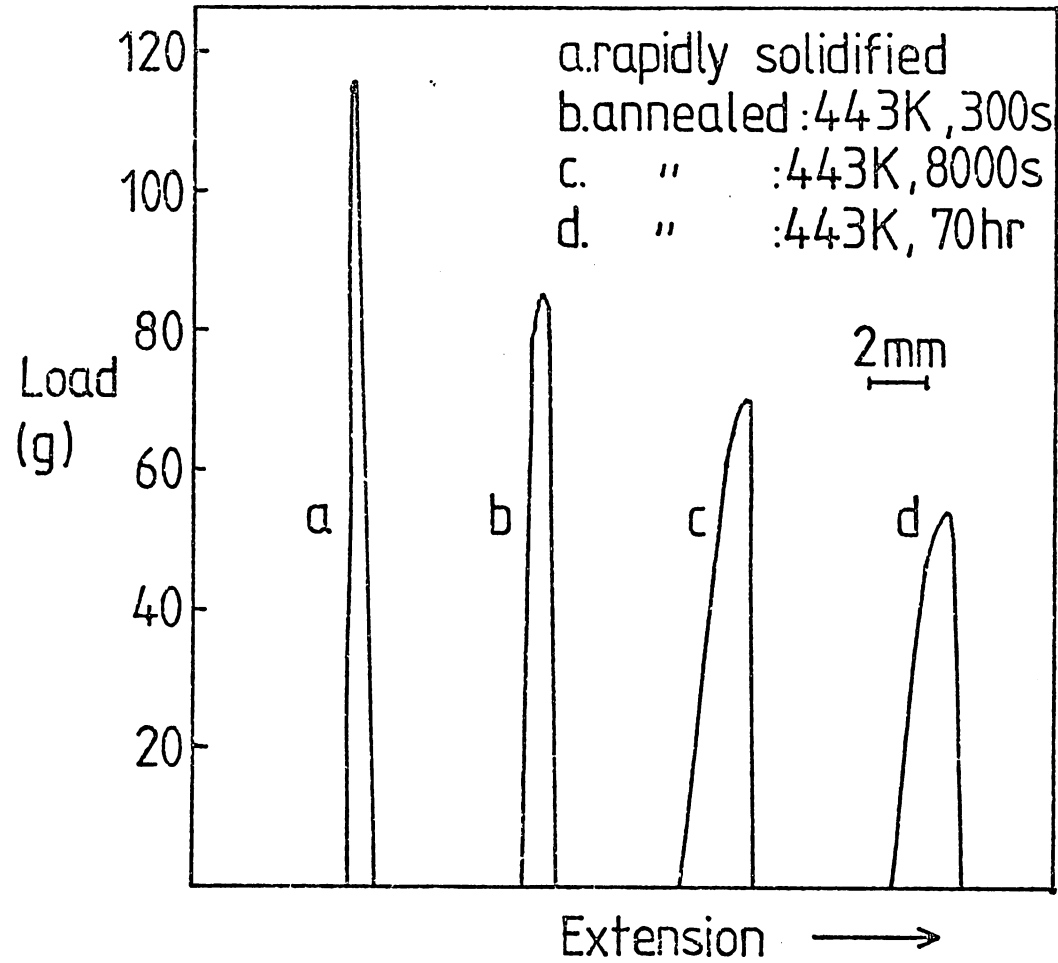
RIBBON

Figure 3.15

Tensile Curves for Rapidly Solidified Tin Ribbon

a. rapidly solidified
b. annealed : 443K, 300s
c.   "   : 443K, 8000s
d.   "   : 443K, 70hr

2mm

Load
(g)

a   b   c   d

120
100
80
60
40
20

Extension ⟶

The tensile specimens were tested to failure and the load/extension curves for pure tin are shown in figure 3.15. As the actual area of the ribbon was unknown these loads should not really be converted to stresses. However to obtain a comparison between the materials the average area of the ribbon was calculated from the density and average width of the ribbon, and a known mass of known length. (Chapter 2). This gave a Tensile Strength for pure tin of 32MPa which on ageing at 343K dropped dramatically to less than half this value after 2.5×10^5s. The ductility is also increased. The alloy containing 15%Sb gave a Tensile Strength of approximately 140MPa which after ageing at 343K for 9×10^3s had risen to 155MPa.

The drop in strength for the pure tin is almost certainly due to grain growth and this is shown again in Chapter 6. The rise in strength in the 15%Sb alloy is probably due to the precipitation of SbSn intermetallic seen in the previous section.

3.6. Conclusions.

1)   Tin-antimony alloys are easy to melt spin and produce ribbons with reasonable dimensional uniformity under correct conditions.

2)   The "chill" surface of the ribbons have a smooth appearance to the naked eye but on closer inspection contain some voids probably due to the entrapment of gas bubbles at the liquid metal/substrate interface.

3)   The "free solidification" surfaces of the ribbons have a rippled appearance associated with the growth of dendrites.

4)   The "shoulders" at the edge of the ribbons are probably due to flow characteristics of the puddle.

5)   Melt spun supersaturated alloys containing up to 15%Sb are single phase solid solutions whose major lattice parameter increases linearly with increasing antimony content.

6)   Alloys containing 20%Sb and above are two phase, as intermetallic

SbSn is formed on casting.

7)   There is an extension of solid solubility of Sb in Sn from 4.0% at equilibrium to between 15 and 20% by rapid solidification, this is consistent with results obtained by other workers.

8)   Optical metallography was difficult due to problems finding a good etchant, Tin Etch and a solution of $SnCl_2$/HCl were most successful.

9)   Considerable grain refinement has been achieved by rapid solidification but grain size may depend on casting speed and flow characteristics of the melt puddle.

10)   Three distinct regions exist in the fracture surfaces of the alloys, due to segregation of antimony and a change from planar to dendritic growth during solidification.

11)   Preparing specimens for T.E.M. examinations was difficult but ion-beam thinning was marginally successful.

12)   SbSn initially precipitates as needles from rapidly solidified solid solution compared with cuboids in conventionally cast alloys.

13)   Mechanical properties are difficult to measure by conventional tests. The tensile strength is increased by increasing the antimony content. Ageing pure tin produces a drop in strength due to grain growth whereas in 15%Sb ribbons the strength is increased probably due to the precipitation of SbSn.

Chapter 4.   <u>CONSOLIDATION OF RAPIDLY SOLIDIFIED RIBBON</u>

4.1. Introduction

In the present work the ribbon produced by melt spinning has little

or no use as an engineering material even if the mechanical properties have

been enhanced. It is therefore necessary to produce a bulk form of rapidly

solidified material while retaining the properties produced by the initial

rapid solidification.

Many workers have produced consolidated rapidly solidified materials.

Morris (1980,1982) uses a gas-gun technique to impart a shock wave to metallic

glass particles. He proposes that the particles actually melt at the surface

but that there is sufficient solid material left to "re-rapidly solidify"

the molten regions.

Morris produces bulk materials which have retained their amorphous

properties. Liebermann (1980a,b) uses warm extrusion and warm die pressing

to consolidate glassy alloy ribbons and finds the former method superior

as it introduces shear stresses into the material. He also finds it

possible to clad these amorphous alloys onto conventional engineering

materials. Cline (1982) uses both explosive forming and gas-gun techniques

to produce bulk glassy material and reports that the mechanical properties

are equivalent to those of ribbons of the same material.

Savage and Jones (1982) study the effect of consolidating, rapidly

solidified Al-Mn alloys, by extrusion. With an extrusion ratio (E.R.)

of 23:1 they report an increase of 2.4 times the tensile strength, hardness

and proof stresses with retention of the ductility found in conventionally

cast materials. Most workers do not consolidate ribbons but use either

flakes or powders and sometimes chopped ribbons. This supposedly gives

better packing prior to the application of pressure, and for hard materials

would therefore lead to increased densification, compared with ribbons.

However in the present work all the materials consolidated were extremely ductile and it was unnecessary to prepare the ribbons in any way other than to degrease the surfaces.

Previous work on the consolidation of tin powders was performed in the mid 1960s by Eastwood and Robins at the International Tin Research Institute (ITRI). The work was mainly carried out on pure tin powders although an Sn 7%Sb 3.5%Cu alloy was also compacted (ITRI, 1967). Using extrusion ratios from 20:1 to 80:1 they produced good compacts from powders of controlled particle size, thus changing the dispersion of oxides introduced by the oxide film on the surface of the powder particles. They report increases of tensile strength and hardness but a corresponding decrease in ductility (ITRI, 1965). The consolidated tin also performs better in stress-rupture tests than both chill cast tin and Sn6%Sb alloys. Their main problem was the poor ductility exhibited at right angles to the direction of extrusion.

4.2. Methods of Consolidation

Consolidation techniques can be divided into two types, Static, which includes Hot Isostatic Pressing (HIP) and conventional power metallurgical methods of cold and warm die pressing, and sintering, and Dynamic which includes, explosive or gun compaction and extrusion.

Conventional powder metallurgy involves pressing and sintering and typically materials consolidated in this way will have densities in the range 90-96% theoretical (Lawley, 1978). Hot Isostatic Pressing can produce bulk products of almost full density. Dynamic methods usually produce compacts of greater than 99% theoretical density.

The advantage of dynamic compaction over static is that often no extra heating is required for sintering the particles, especially in explosive or gas-gun compaction. It has been proposed that friction between the particles is sufficient to generate enough heat, if the shock wave moves fast enough,

to produce adequate welding and sintering at the surfaces of the particles without raising the bulk temperature too much (Morris, 1980). This is especially necessary when dealing with rapidly solidified materials. The difference between dynamic and static compaction is shown schematically in figure 4.1.

4.3. Consolidation of Tin Alloy Ribbons.

In the present work consolidation was achieved by a combination of static and dynamic processes. In order to make comparisons with conventionally cast alloys of the same composition three routes were chosen for the production of rods.

i) CC alloys

Chill casting to a slug of 40mm diameter

Indirect extrusion to a rod of 6.3mm diameter

ii) CT alloys

Chill casting to a slug of 40mm diameter

Machining to give lathe turnings

Compaction to a slug of 40mm diameter using a pressure of 230MPa

Indirect extrusion to a rod of 6.3mm diameter

iii) RS alloys

Melt spinning to give rapidly solidified ribbon

Compaction to a slug of 40mm diameter using a pressure of 230MPa

Indirect extrusion to a rod of 6.3mm diameter

Figure 4.2 shows the variation of density with pressure in compacted slugs of pure tin. This indicates that increasing the compaction pressure to a greater than 250MPa has no beneficial effect on the density of the compact hence the choice of 230MPa as the compaction pressure.

Each slug had a mass of about 250g and a density in the CT and RS alloys of between 94 and 98% theoretical. Figure 4.3 is a plot of percentage theoretical

Figure 4.1   Comparison of Dynamic and Static Compaction (Schematic)
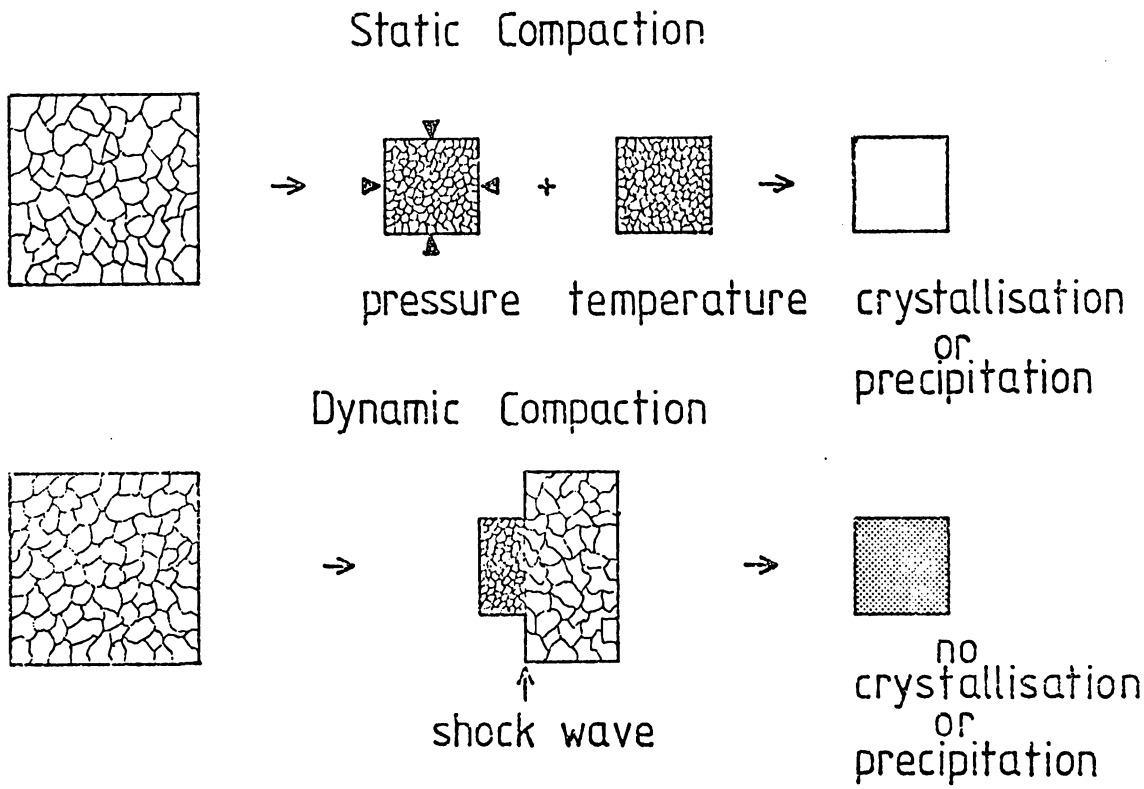
(After Morris 1980)

Static Compaction

pressure   temperature   crystallisation
or
precipitation

Dynamic Compaction

shock wave

no
crystallisation
or
precipitation

Figure 4.2

% theoretical density (%ρ_t) against compaction pressure for Sn Ribbon

%ρ_t

Compaction Pressure (MPa)
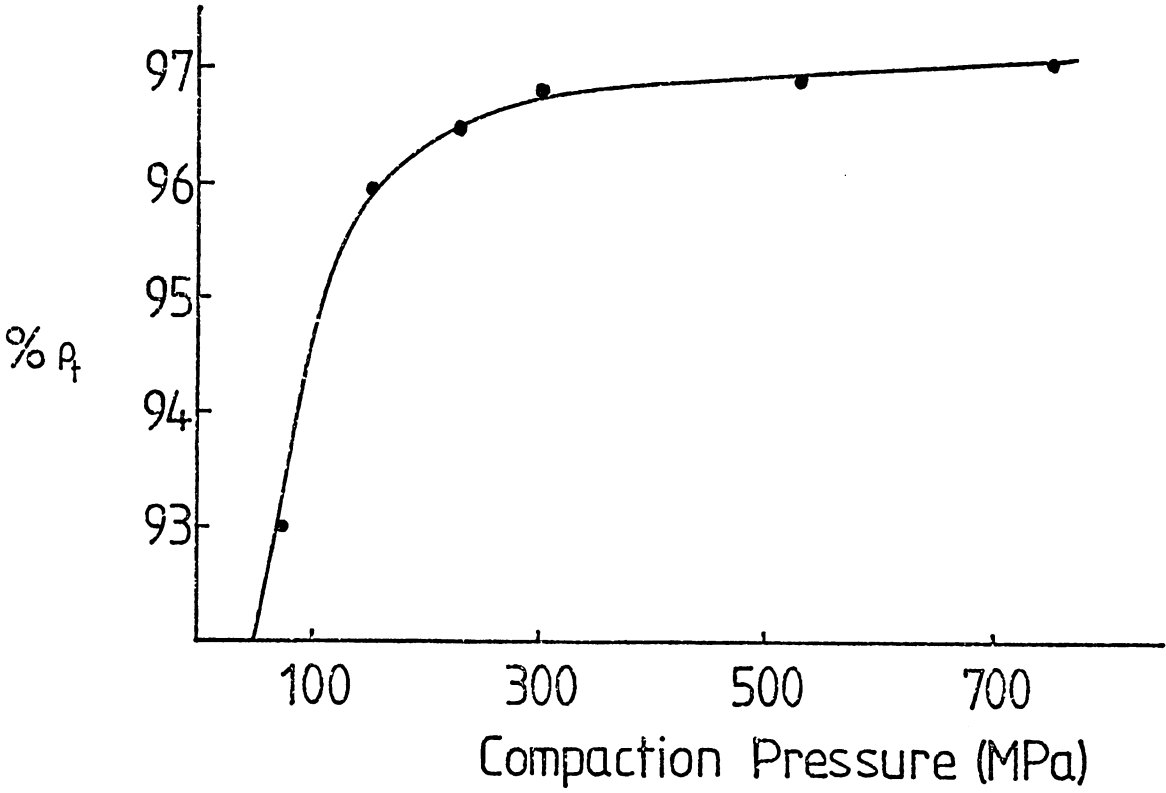
density (%ρ_t) against antimony content showing that the harder alloys

(high Sb content) densify less well than the more ductile materials.

This has also been observed by Morris (1980) during the dynamic compaction

of metallic glasses.

The indirect extrusion in each case was performed at ambient temperatures.

The extrusion ratio of 40:1 is a reduction of 97.5%.

4.4. The Extruded Rods of Tin Alloys.

4.4.1. The Extrusion Pressure.

Sound rods were produced from both the consolidated ribbons and turnings

and both types appeared to have low porosity.   The density was usually

greater than 99% theoretical and the external appearance of the rods in

no way suggested any differences in alloy content or previous history.

Figure 4.4 is a table of the maximum extrusion pressure, P, required

to produce the rods.   It can be seen that as the antimony content increases

so the extrusion pressures increase whatever the previous history, signifying

a rise in the flow stress of the alloys.   This effect tails off for the CC

and CT alloys with 10 and 15%Sb content.   The other obvious difference is that

for each alloy the extrusion pressure required is greatest for the RS alloy

and lowest for the CC alloy with the CT alloy between the two values.

The extrusion force, F, can be given by the expression:

$$F = \sigma_o A_o \ln (E.R.) \qquad \text{(Dieter, 1961)} \qquad (4.1)$$

where σ_o is the uniaxial flow stress, A_o is the initial area of the slug

and E.R. is the extrusion ratio.   This equation predicts extrusion forces

much lower than required as it ignores the frictional effects of the process.

However it does show that for a constant extrusion ratio then the flow stress

is proportional to the extrusion pressure:

$$\sigma_o \propto \frac{F}{A_o} \qquad \text{(for constant E.R.)} \qquad (4.2)$$

It is therefore reasonable to assume that comparisons are valid between

Figure 4.3 Plot of theoretical densities ($\%\rho_t$) prior to extrusion against composition (%Sb) for turnings and ribbon.

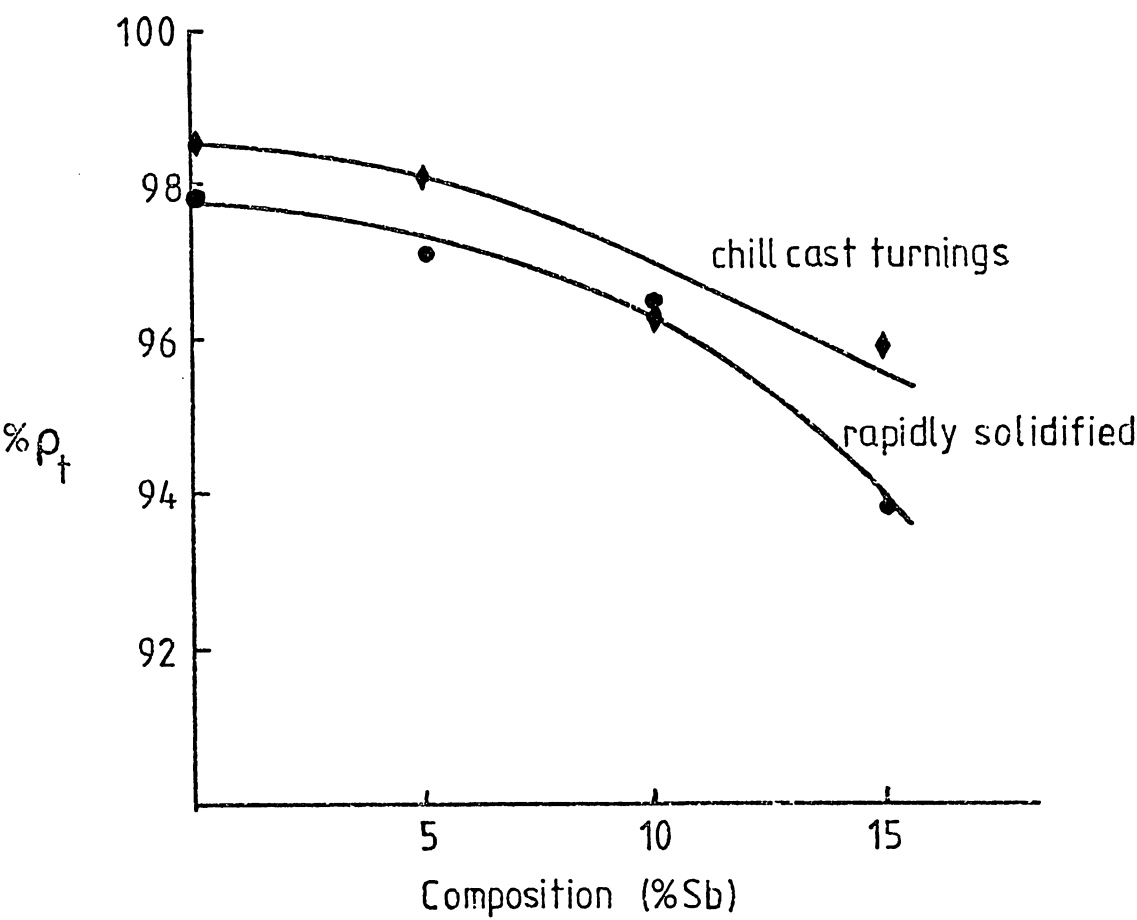**Figure 4.4**

Extrusion Pressures in MPa for Extrusion ratio for 40:1 for Tin-Antimony Alloys.

Alloy % Sb	History	CC	CT	RS
0		310	320	380
5		480	565	565
10		610	675	730
15		625	675	835

the values in figure 4.4 as the extrusion ratio is the same in each case.

The differences in the extrusion pressures could therefore be a result of two things:

1)   an increase in the flow stress of the materials due to microstructural changes.

2)   the effect of particle surface area in the consolidated materials.

1)   There are obvious microstructural differences in the alloys as the antimony content increases, hence the change in flow stress, but for those alloys of the same composition but with different production histories detailed examination of the microstructure is necessary, this is dealt with in chapter 5.

2)   Movement between particles may give rise to an increase in friction during the process as a result of the surface oxide and might have the effect of raising the flow stress of the bulk material.   The effect of ribbon thickness on the surface area of ribbon is shown below.

Consider a ribbon of surface area, SA

$$SA = 2\ell \, (t + w) \tag{4.3}$$

where: ℓ: length

t: thickness

w: width

since $\ell = \dfrac{M}{tw\rho}$ and $V = \dfrac{M}{\rho}$

where: M: mass

ρ: density

V: volume

then $\dfrac{SA}{V} = 2 \left(\dfrac{1}{t} + \dfrac{1}{w} \right)$

if t<<w

then $\dfrac{SA}{V} \approx \dfrac{2}{t}$ (4.5)

The surface area per unit volume of a ribbon is inversely proportional to its thickness. Unfortunately in this study the slugs were made up of many ribbons with a mixture of thicknesses and thus it is not possible to quantify this effect.

The increase in extrusion pressure required to produce the consolidated rapidly solidified ribbon compared with the turnings suggests that there are definite microstructural differences caused by the different production routes. It also implies that the rapidly solidified ribbon is stronger than the chill cast alloys of the same composition.

4.4.2. The Temperature Rise During Extrusion.

During the extrusion process it was noted that the temperature of the rods was increased to above ambient temperatures. Sometimes this was greater than "hand hot" ($\sim > 65°C$). The temperature rise depended on the material being extruded, the low antimony alloys were not heated as much as those with a high antimony content.

The work done (WD) during extrusion can be expressed by

$$WD = \text{Force} \times \text{Slug Depth (d)} \tag{4.6}$$

$$\text{and} \quad WD = C_p \, \Delta T \tag{4.7}$$

$$\text{therefore} \quad \Delta T = \frac{P \times A_o \times d}{C_p} \tag{4.8}$$

where ΔT: Temperature rise

P : Extrusion pressure

A_o: Initial slug area

C_p: Heat capacity of alloy

Most of the slugs were about 250g in weight and had green depths of about 30mm. The heat capacity, C_p, of tin is 0.22×10^3 J kg K^{-1} and therefore for the material C CSn (pure chill cast tin) the expected temperature rise would

be

$$\Delta T = \frac{310 \times 10^6}{0.22 \times 10^3} \quad x \quad \frac{(40 \times 10^{-3}) \times \pi \times 30 \times 10^{-3}}{4}$$

$$\Delta T \approx 53K$$

While for the material RS15%Sb, $\Delta T \approx 143K$. These temperature rises give absolute temperatures of 346K (73°C) and 436K (163°C) assuming an ambient temperature of 193K (20°C).

These are obviously very much estimates but they do seem to be of the same order of magnitude as the temperature rises observed. If it were possible to include the effects of friction and conduction from the die surface then a much more accurate result would be obtained. It has also been assumed that the heat capacity of the 15%Sb alloy is the same as that for pure tin.

4.5. Conclusions.

1) Consolidation by extrusion at ambient temperatures, of rapidly solidified ribbon and chill cast turnings of tin and tin-antimony alloys containing up to 15%Sb, produces sound rods with low porosity.

2) An increase in the antimony content of the alloy raises the pressure required to extrude the material.

3) The extrusion pressure required for rapidly solidified alloys is greater than for chill cast turnings which in turn is greater than for the bulk chill cast material. Such increases in extrusion pressure probably indicate an increase in flow stress.

4) The increases in flow stress are probably a result of differences in microstructures introduced by the different production routes.

5) The temperature rises produced during extrusion are consistent with those predicted by theory.

Chapter 5.   THE METALLOGRAPHY AND MICROSTRUCTURE OF EXTRUDED

RODS OF RAPIDLY SOLIDIFIED AND CHILL CAST ALLOYS

5.1. Preparation and Techniques

5.1.1. Introduction

A qualitative and quantative description of the microstructure of a material is invaluable in understanding its behaviour during tests on mechanical properties.

A material is most commonly defined firstly by its composition, but then it can be further described by its microstructural features.

Those most commonly used are:

    (i)   The grain size

    (ii)   The proportion of any second phase present

    (iii) The distribution and particle size of any second phase present

The term second phase is used to describe anything other than the matrix, from sub-micron precipitates to intermetallics or non-metallic inclusions of the order of millimetres in diameter.

There are problems involved in measuring the sizes of such particles for unless the particles are physically separated from the matrix by dissolution, then only a representative cross section of the particles is seen, which then has to be related to the probable size and volume fraction of particles.

5.1.2. Metallographic Preparation

In this work both longitudinal and transverse cross sections of the 6.5mm diameter rods were mounted in Struers Specifix Powder cold mounting resin. The longitudinal specimens were machined down to produce a section at the centre of the rod thus hopefully showing if there was any radial texturing.

Such specimens were ground on emery paper then polished down to 0.05μm alumina or 0.25μm diamond. As these alloys are so soft great care was taken

at all times to prevent contamination during polishing and only light
pressure was used to reduce the possibility of surface deformation.

As with the melt spun ribbons etching proved difficult but it was
found that for pure tin samples a solution of $SnCl_2$ in HCl gave a good grain
boundary etch. For antimony containing alloys and a grain contrast etch
for tin, "Tin Etch" was used. (For further information please refer to figure 3.4).

Optical metallography was carried out on a Vickers N55 light microscope
and 100 x 75mm photographic plates used to record the micrographs.

Grain sizes were measured using lineal analysis. Average grain size ($\bar{D}$)
was obtained by using the relationship

$$\bar{D} \approx 1.75\bar{d}$$

where $\bar{d}$ is the mean linear intercept. The maximum grain size expected, D_M,
can be given by

$$D_M = 1.86\bar{d}$$

This takes account of the shape of the grains assuming they are
reasonably equiaxed   (Pickering, 1976).

5.1.3. Techniques - SEM and Quantimet

A Cambridge Instruments S4 Stereoscan was used for scanning electron
microscopy (S.E.M) of the fracture surfaces of all the specimens used in
tensile testing. Such specimens were first gold coated before being subjected
to examination. It was found that due to the unevenness of these specimens
the X-ray facility for determination of composition was useless. To show
the distribution of antimony the polished optical metallographical specimens
were used. These were firstly heavily etched in Ammonium Polysulphide and
then carbon coated. Micrographs were recorded on Ilford 120 HP4 film.

A Quantimet was used to measure the volume fraction and size
distribution of intermetallic. For the former a point counting technique
was used. In the latter technique, it was assumed that the particles

were spheres and thus the cross section were all circles. The area of

each particle was measured, then the equivalent diameter, d_{eq}, calculated

using the relationship:

$$d_{eq} = \left[\frac{4 \times Area}{\pi}\right]^{\frac{1}{2}} \qquad\qquad (5.1)$$

It was found that for the smaller intermetallics observed the measured

distribution was positively skewed and so the mode was used as the

measurement of particle size.

Specimens were examined soon after extrusion and after various ageing

treatments at either 373K(100°C) or 473K(200°C) for up to 1.8 x 10^{5}s. The

following sections deal with the alloys individually, making a comparison

between the three different production routes.

5.2. Comparison of the Microstructures of Pure Tin Extruded Rods produced from Chill Cast Material, Chill Cast Turnings and Rapidly Solidified Ribbon

5.2.1. Chill Cast extruded rods in the as-extruded and aged conditions

Figure 5.1a is an optical micrograph of the chill cast extruded pure tin.

The grains have an average diameter of 47μm thus the maximum grain diameter should

be of the order of 50μm. (Pickering, 1976). The grains are smooth and un-

deformed with no directional features.

Figure 5.2 shows the microstructure of the pure tin after ageing at 473K

(200°C) for 9000s (2.5 hours). Massive grain growth has taken place, the

average grain diameter is now 1900μm.

Figure 5.3 is a table showing the grain sizes obtained for various heat

treatment times at 473K and 373K.

The specimens aged at 373K for 1.8 x 10^{5}s showed two very different

sizes of grains, the smaller ones of the order of 250μm diameter and larger

grains of about 1300μm diameter. This can be seen in figure 5.4.

These microstructres show the typical behaviour of a metal which

is subjected to ageing treatments. The first structure (figure 5.1a) is a

Figures 5.1 and 5.2.   Optical Micrographs of Extruded Pure Tin Rods

5.1a) Chill Cast Pure Tin.   (Polarised light & Quartz.   Etched $SnCl_2$/HCl)   5.1b) Compressed Turnings of Pure Tin (Etched HCl)
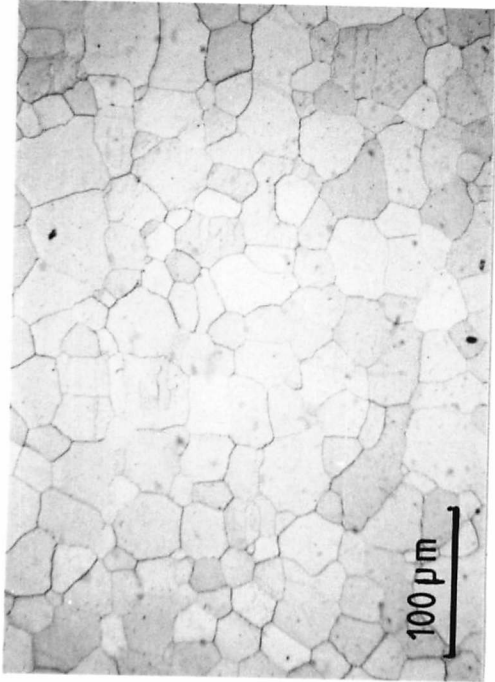
5.1c) Compressed Melt Spun Ribbon (Polarised Light & Quartz. Etched $SnCl_2$/HCl)

5.2   Chill Cast Pure Tin Aged @ 473K for 9×10^4 S (Etched Tin Etch)

Figure 5.3

Grain size ($\bar{D}$,µm) of chill cast extruded pure tin

Ageing time ($s \times 10^3$)	0	0.9	1.8	9.0	90	180
Ageing Temp.(K)						
373	47	190	186	270	/	{ 230 1300
473	47	1360	/	1930	2670	/

All the above values are the average grain size, $\bar{D}$, in micrometres, and are calculated from the mean linear intercept (m.l.i.), $\bar{d}$. The average grain size $\bar{D}$ is given by:

$$\bar{D} = 1.75\bar{d} \qquad \text{(Pickering, 1976)}$$

recrystallised structure, obtained in this case because of the amount of work and heat experienced by the chill cast alloy. The extrusion, assuming a temperature rise of some 50K, was performed at about 340K or 0.7 Tm.This is in the region of hot working and so a fully recrystallised structure would be expected.

On ageing at 473K (200°C) normal grain growth occurs very rapidly with only a few grains surviving after only 900s. However on ageing at 373K normal grain growth occurs much more slowly until after 9000s a few grains start growing faster than the others. After 1.8×10^5s (fig. 5.4) these grains are 5 x the size of the smaller grains. This is called secondary re-crystallisation due to abnormal grain growth. Cottrell (1975,p.343) suggests that this effect is due to the rate of dissolution of particles pinning the grain boundaries. At the low temperature anneal particles slowly dissolve and coarsen, thus only a few grain boundaries are released and sweep through the metal. At high temperatures the particles dissolve quickly thus releasing all the boundaries at the same time and normal grain growth results. This presumes the presence of a secondary phase pinning the grain boundaries. In this case they would be the impurities which occur in pure tin. With an annealing temperature of 0.95Tm it is safe to assume that any sub-microscopic second phase particles would dissolve fairly rapidly.

5.2.2. The microstructures of consolidated extruded chill cast turnings and consolidated extruded rapidly solidified ribbon

Figures 5.1b and 5.1c show the microstructures of the as-extruded consolidated turnings, and rapidly solidified ribbon, of pure tin. They both show similar structures with the consolidated ribbon being marginally finer. The consolidated turnings has a grain size of about 16μm and an average band width of 18μm. The consolidated ribbon has an average grain size of 11μm and a band width of about 19μm.

Figures 5.5a, b and c show microstructures of the consolidated ribbon

Figures 5.4 and 5.5

Optical Micrographs of Extruded Rods of Pure Tin

5.5a) As-extruded RS Tin. (Tin Etch)

5.5c) RS Tin Aged @ 373K for 1.8×10^5 s. (Tin Etch)

5.4 Chill Cast Pure Tin Aged @ 373K for 1.8×10^5 s. (Tin Etch)

5.5b) RS Tin Aged @ 373K for 1.8×10^4 s. (Tin Etch)

at a low magnification in the as-extruded condition, and after heat treatments at 373K for 1.8 x 10^4s and 1.8 x 10^5s respectively. One striking feature is that these microstructures are in fact all very similar, although the as-extruded structure looks slightly more deformed. On closer examination it is possible to see that the as-extruded structure looks heavily twinned and as ageing progresses these 'twins' become less in number.

The other major feature is that the banding in the longitudinal direction becomes finer towards the centre of the rod. The length of the 'grains' in the aged specimens seems to reach a maximum of 2500μm.

5.2.3. Comparison of fracture surfaces of extruded tin rods by S.E.M.

Figures 5.6a, b and c show the fracture surfaces of the as-extruded rods of pure tin produced from slugs of chill cast metal, chill cast turnings and rapidly solidified ribbon respectively.

All the structures are ductile-dimple in appearance. The chill cast material is much coarser than either of the consolidated rods, as would be expected from the optical examination. The rapidly solidified structure looks marginally finer than the chill cast turnings.

On ageing the structures obtained are those seen in figure 5.7. The chill cast material is virtually featureless. The structures of the consolidated materials are very similar, again the rapidly solidifed structure is possibly finer than the chill cast turnings but it is difficult to put any quantitative value on this observation. In all cases the structure is coarser than in the as-extruded state.

There was no evidence of particles at the bottom of the dimples in the consolidated structures but if the particles of oxide were of the order of 0.015μm a magnification of >50000 x would be required to make them easily distinguishable and this was not possible on the instrument used.

Figures 5.6 and 5.7

Scanning Electron Micrographs of Extruded Rods of Pure Tin

5.7   a   b   c
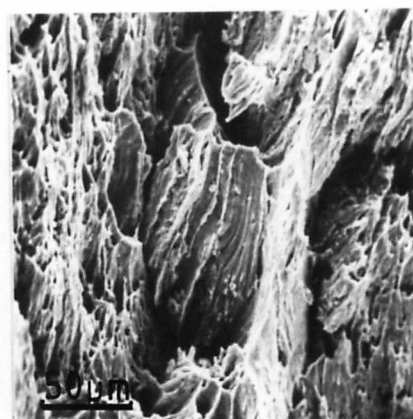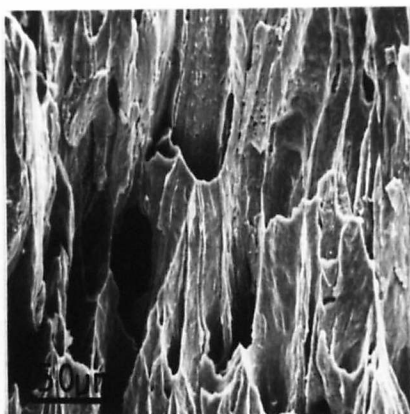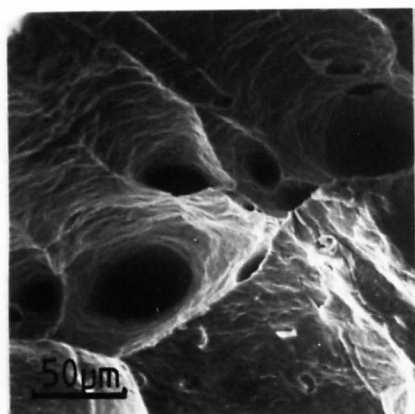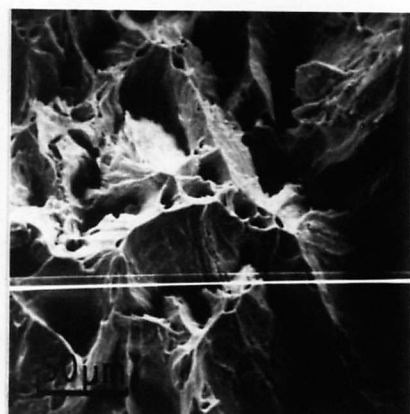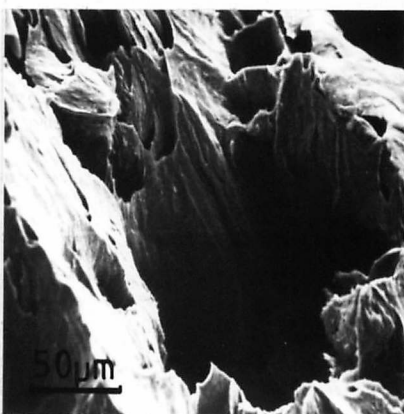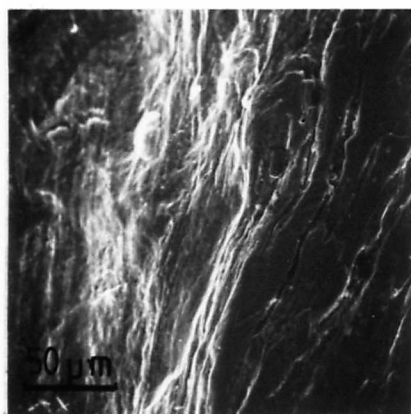

Fracture surfaces of as-extruded rods of pure tin.

a) Chill cast   b) Consolidated chill cast turnings c) Consolidated

Rapidly Solidified ribbon.

5.8   a   b   c

Fracture surfaces of aged rods of pure tin after 9×10^4 s at 473K

a) Chill cast   b) Consolidated Chill Cast Turnings

c) Consolidated Rapidly Solidified Ribbon.

5.2.4. Comparison of surface features of tensile specimen of extruded tin rods

Figure 5.8 shows the tensile specimens of the extruded chill cast and rapidly solidified rods of pure tin in the as-extruded state and, after ageing at 473K (200°C) for various times.

Both the unaged specimens have a grainy appearance but it can be seen that the rapidly solidified material is much finer. On ageing, the individual grains can clearly be observed in the chill cast material after only 15 minutes and their growth can be seen in the specimens aged for up to 25 hours. This is accentuated by the machining marks which show that deformation occurs by slip in the individual crystals rather than grain boundary sliding. The rapidly solidified material can be seen to have a much finer structure with no such surface relief features. The chill cast material also undergoes considerable necking compared to the rapidly solidified tin thus indicating that it is much more ductile.

5.2.5. Discussion

Such structures are very similar to those obtained in consolidated tin powder by Eastwood and Robins (1964) as shown by figures 5.9a and b. These are of consolidated tin powder (-53μm) containing less than 0.3% of tin oxides as surface films on the particles and extruded at a ratio of 40:1. The average grain size of the as-extruded rod can be seen to be about 4μm. The grain growth they procure on ageing is much greater than in the rapidly solidified tin in this study.

It is the presence of the oxide film on the particles which produces the increase in strength compared to chill cast material. Eastwood and Robins (ITRI, 1966) suggest that it is the dispersion rather than just the volume fraction of particles which is the most important factor. In other words finer powders give a finer dispersion and stronger material.

In their work the average size of powder was some 30μm and their oxide content was 0.3% for the strongest material they produced. Assuming all

Figure 5.8

Tensile Specimens of Extruded Rods of Chill Cast and Rapidly

Solidified Pure Tin in the As-Cast and Aged Conditions

Ageing Temperature 473K

Chill Cast Tin

Rapidly Solidified

Tin

Ageing Times
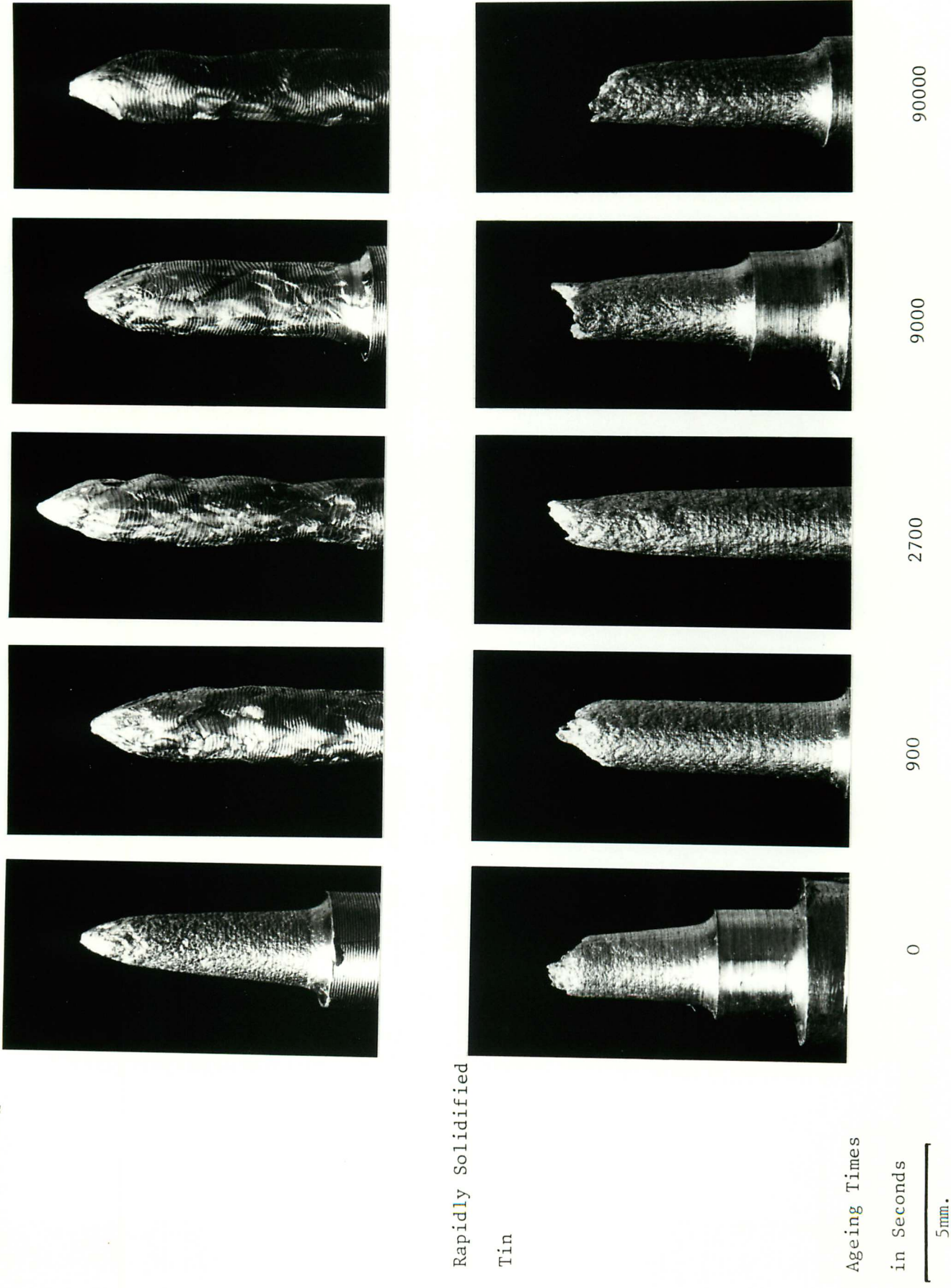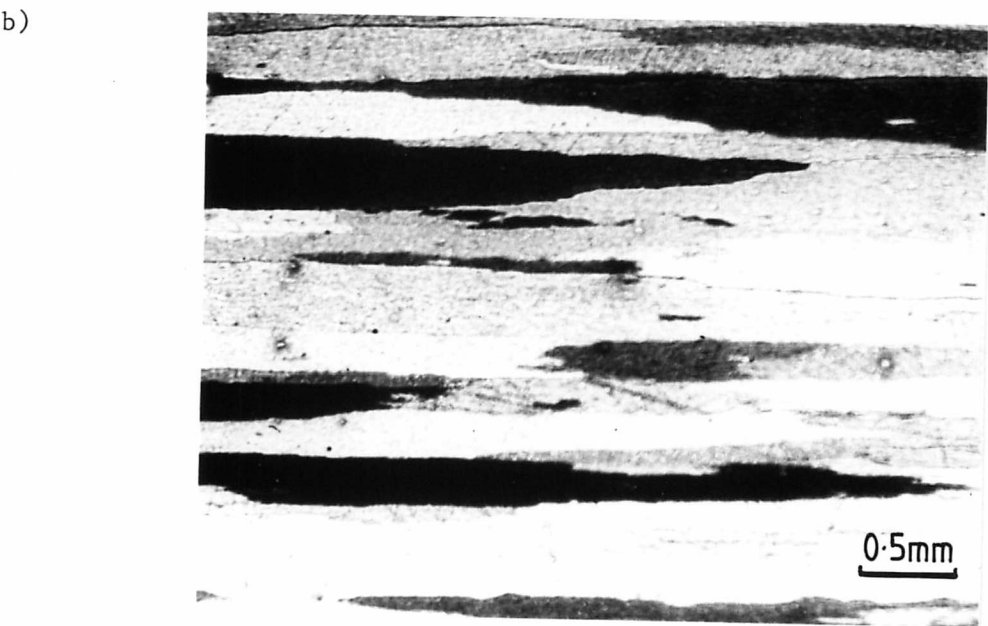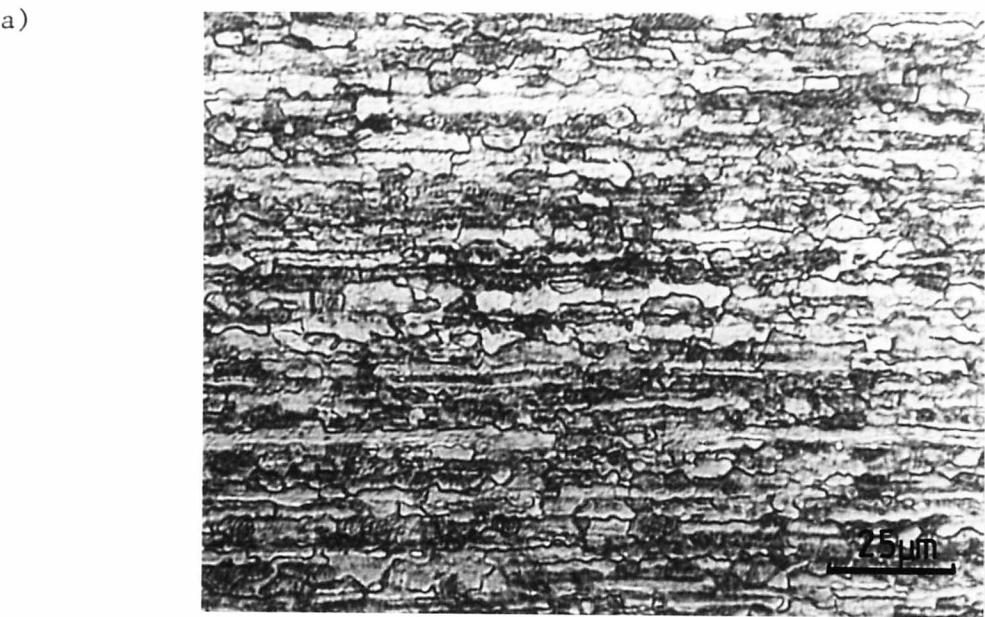
in Seconds

90000

9000

2700

900

0

5mm.

Figure 5.9

Microstructures of Consolidated, Extruded Powders of Pure Tin
in the As-Extruded State (a) and after Annealing for 1 hour at
423K (b).   (Eastwood and Robins, 1964).

a)

b)

the particles to be spherical and 30μm in diameter an oxide film thickness can be estimated.

r: radius of tin excluding oxide thickness

t: oxide film thickness

R: radius of powder.   R = r + t

$$\frac{\text{Volume of powder - Volume tin}}{\text{Volume Powder}} = 0.003. \qquad (5.2)$$

$$\frac{R^3 - r^3}{R^3} = 0.003$$

$$r = (0.997 \ R^3)^{\frac{1}{3}}$$

$$r = 14.985 \mu m$$

$$t = R-r = 0.015 \mu m \qquad (150\text{Å})$$

This gives a rough approximation of the thickness of oxide film expected on tin in air at ambient temperature.

It has previously been shown (Chapter 4.3) that for a ribbon the ratio of surface area to volume can be given by:

$$\frac{SA}{V} = \frac{2}{t_R} \qquad (4.5)$$

$$\text{for } t_R << w_R$$

Assuming an average ribbon thickness, t_R, of 25μm and an oxide film thickness of 0.015μm (150Å) then the volume oxide/volume tin is given by

$$\frac{2 \times 0.015}{25} = 0.0012$$

This small amount of oxide, 0.12%, is not easily detected by analytical methods but it obviously had some effect on the mechanical properties of the compacts (see chapter 6).

The effect of this oxide layer can be seen in both this work and the study by Eastwood and Robins. The as-extruded structure does not show the smooth recrystallised grain shape expected after "hot" working, as a result of grain boundary pinning by the oxide dispersion, thus preventing grain growth. The grain growth which occurs along the extrusion direction is a result of the banding caused by the extrusion which creates oxide "stringers" along the rods.

The S.E.M. study of the fracture surfaces is consistent with the optical metallography and shows that the structures of all the materials are changed by ageing. The slight change observed in the consolidated chill cast and rapidly solidified rods is a result of the oxide dispersion rather than some property conferred by rapid solidification. A comparison of these microstructures and those obtained in consolidated tin powders by Eastwood and Robins, suggests that the process of rapid solidification confers no special property on tin.

5.3. Comparison of the Microstructure of Sn5%Sb Extruded Rod produced from Chill Cast Material, Chill Cast Turnings and Rapidly Solidified Ribbon.

5.3.1. Chill Cast Extruded Rods.

Figure 5.10 shows a series of low magnification optical micrographs of extruded chill cast Sn5%Sb alloys in the as extruded state and after various ageing treatments at 473K.

In the as-extruded state the structure is very fine with no evidence of any second phase particles, but noticeable texturing in the direction of extrusion.

On ageing for 900s considerable normal grain growth has taken place, the grains are equiaxed with an average diameter, D, of 310µm. There is no evidence of banding thus suggesting recrystallisation has occurred.
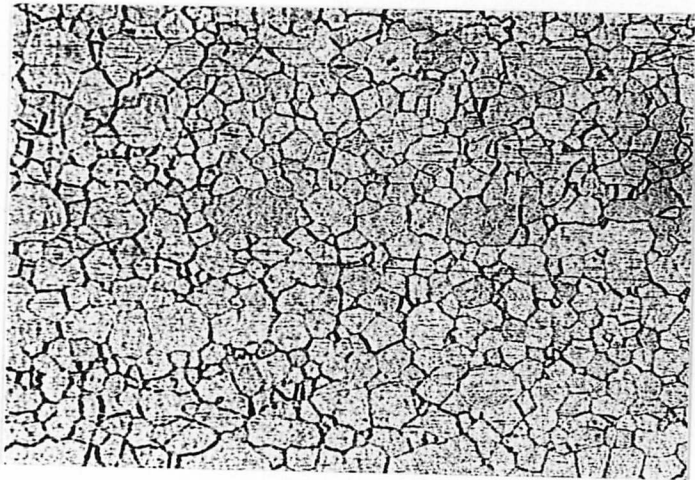
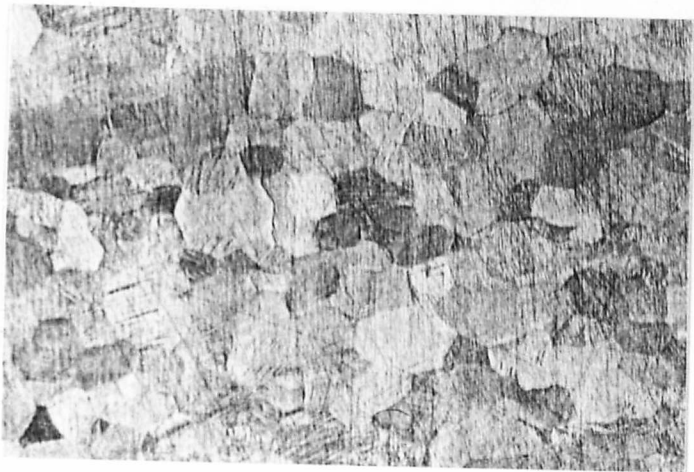Figures 5.10. Optical Micrographs of Chill Cast Sn5%Sb Extruded Rod

<u>1 mm</u>

<u>a</u> as extruded
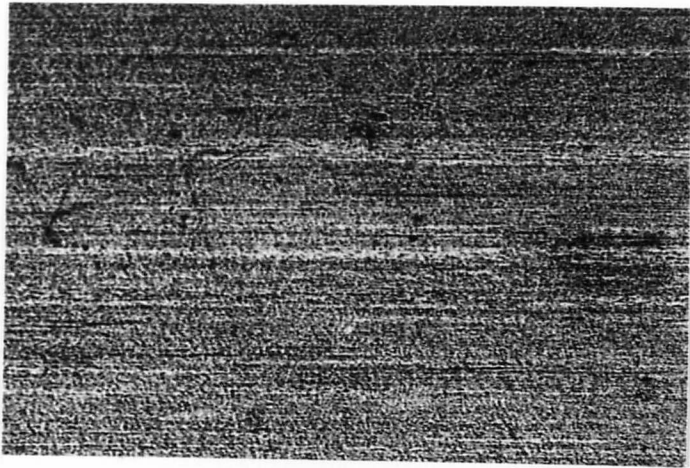
<u>b</u> aged @ 473K for 900s

<u>c</u> aged @ 473K for 9×10^4s.

After heat treatment for 9×10^4s abnormal grain growth has been initiated

due to secondary recrystallisation. There are thus two grain size

distributions, one with a mean of 565µm and one with a mean of 2600µm.

As with the pure tin this suggests that there are particles pinning the grain

boundaries which have a finite dissolution time and thus suddenly release

the grain boundaries. In the pure tin however this didn't occur at 473K

due to the speed of dissolution of the particles present. The fact that in

Sn5%Sb this secondary recrystallisation occurs suggests the presence of a

larger number of particles or that these present are bigger and thus take

longer to dissolve.

Examination at higher magnification revealed the presence of small

particles of a second phase presumably SbSn. Their average size was 2.5µm

in the as extruded rod and 2.0 in aged rods. Their volume fractions were

2.8% and 2.9% for the as-extruded and aged conditions respectively. These

microstructures are shown in figure 5.11. Using the phase diagram

(fig.1.5) and applying the lever rule the maximum volume fraction of SbSn

particles is about 4% for a 5%Sb alloy.

5.3.2. The Microstructure of consolidated chill cast turnings and consolidated

ribbons.

As with the chill cast material, complete solution of the alloy addition

would be expected prior to extrusion. With both turnings and ribbon the

rods produced contained a significant proportion of second phase SbSn particles.

Figure 5.12 shows the microstructures of the extruded consolidated turnings and

ribbon both in the as-extruded and aged slates. In both cases there is some

evidence of texturing or banding along the axis in the direction of

extrusion this is more visible at low magnifications. (fig. 513). There is

no evidence of any grain growth as with the pure tin or bulk chill cast

alloys as can be seen in the micrograph in figure 5.13. The volume fractions

of intermetallic are 4.2% and 4.0% for the consolidated turnings and ribbon

Figure 5.11   Microstructure of Sn5%Sb Chill Cast extruded rods

50µm

a) as extruded

b) aged 373K for 1.8×10^5 s

Figure 5.12   Microstructures of Consolidated Sn5%Sb alloys

50 µm   a,c and d   100 µm

a) As-extruded turnings

b) Turnings Aged @ 473K
   for 1.8×10^5 s

c) RS Ribbon as-extruded

d) RS Ribbon Aged@ 473K
   for 1.8×10^5 s.

respectively and the average particle sizes 2.8μm and 2.2μm respectively.

5.3.3. Comparison of fracture surfaces of extruded Sn5%Sb rods by S.E.M.

Figure 5.14 shows the fracture surfaces of the as-extruded rods after testing in tension. All the specimens show ductile dimple failure with the dimples of the order of 1 to 5μm. The chill cast material may be slightly finer in structure than the turnings or ribbon although this may be a feature of the different angles of viewing. In both the rapidly solidified material and chill cast turnings there is some evidence of delamination, this could possibly be along oxide stringers.

Figure 5.15 shows the structures obtained after ageing at 473K for 9×10^4s. The chill cast alloy has undergone considerable grain growth giving rise to extremely large dimples some 0.5mm across, in fact in the chill cast material aged for only 9×10^3s one dimple grew to almost the whole diameter of the specimen (fig.5.16).

With both the turnings and ribbon, the structure has coarsened with respect to the as-extruded state but to nowhere near the same extent as the chill cast alloy. Again there is evidence of delamination in both these cases. In figures 5.14 d and e it is not possible to see evidence of particles at the bottom of the dimples, thereby suggesting a mechanism of fracture initiated by decohesion of the SbSn particles from the matrix is not valid but rather that the dimples are initiated by oxide particles, possibly with some small contribution from the intermetallics and impurities. If it were the SbSn particles initiating the dimple formation then the fractures of the aged chill cast alloys would be the same as the as-extruded rods. The dimples in all the as-extruded fractures are in any case too prolific and too small to all be initiated by the SbSn particles. The reason for the fracture surface obtained in figure 5.16 is that massive ductile void coalescence has occurred due to the extreme ductility of the

Figure 5.13

Optical Micrograph of R.S. Extruded Sn5%Sb Alloy.
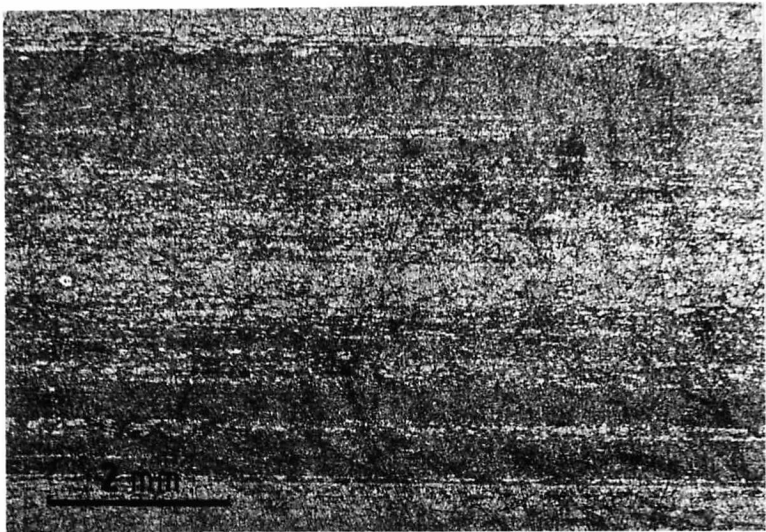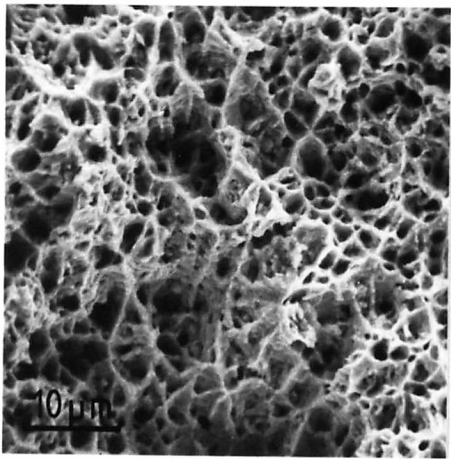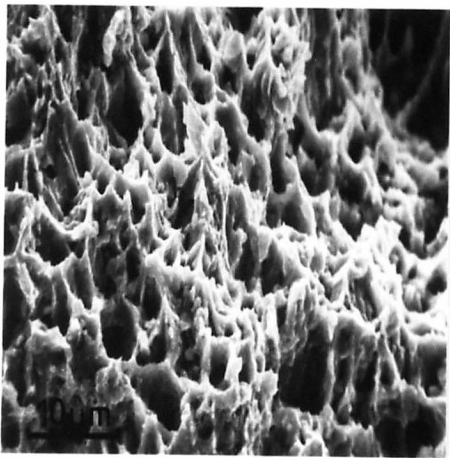
Aged @ 473K for 1.8×10^5 s.

Figure 5.14 (d and e)

Scanning Electron Micrographs of Fracture Surfaces of
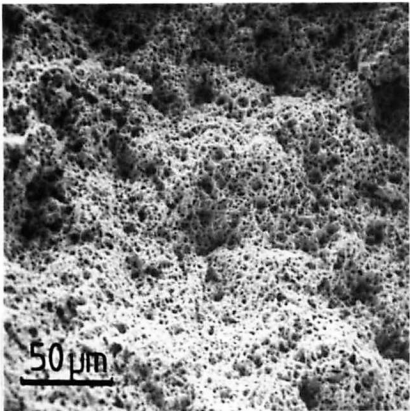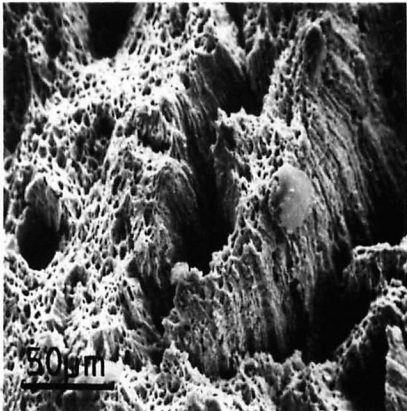Sn5%Sb As-Extruded Rods.

d) Chill Cast.

e) Rapidly Solidified

Scanning Electron Micrographs of Fracture Surfaces of Extruded Rods
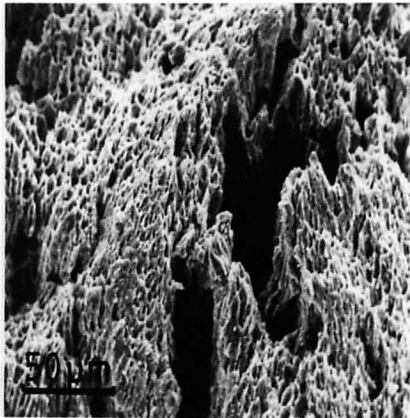of Sn5%Sb

5.14   As-extruded condition.

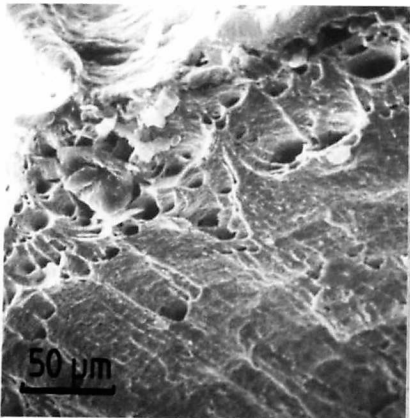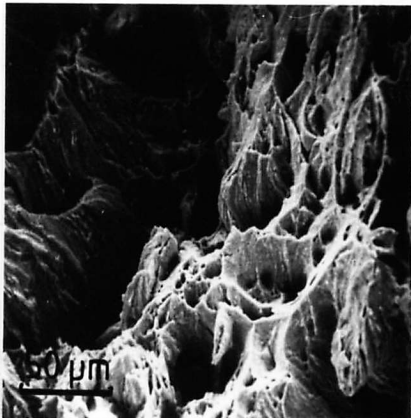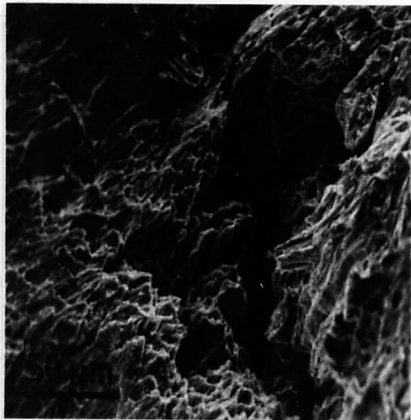a) Chill Cast   b) Turnings   c) Ribbon

5.15 Aged @ 473K for 9×10^4s
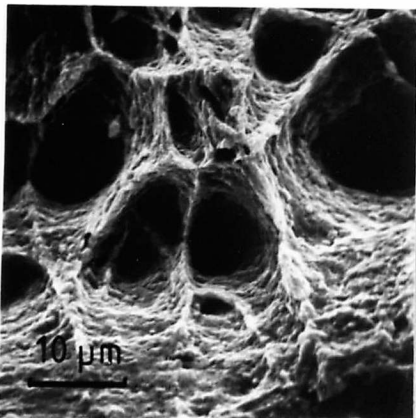

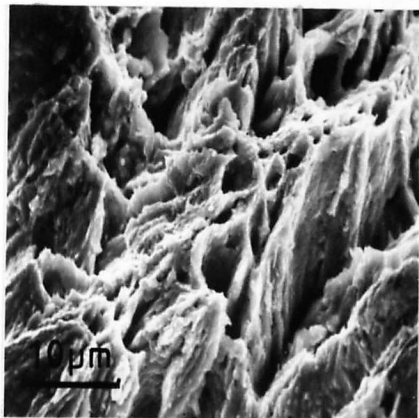a) Chill Cast   b) Turnings   c) Ribbon

d) Chill Cast   e) Ribbon

alloy. In ductile f.c.c. metals such as aluminium or copper it is not usual for the dimples produced in ductile fracture to be related to grain size as this entails the agglomeration of dislocation pile-ups to produce voids at grain boundaries. However in both the pure tin and the Sn5%Sb the dimples seem to have been related to grain size except where the grains are very large when rupture has occurred.

5.3.4. Discussion.

In a conventionally chill cast Sn5%Sb alloy, SbSn intermetallic particles would not normally be seen as it is possible by chill casting to retain up to 8%Sb in solution. The chill cast alloy in the present work has undergone considerable mechanical working and auto-annealing during the extrusion process which has caused all the excess solute, above the equilibrium value of about 4%Sb (see fig.1.5), to precipitate out as particles of SbSn. There is the possibility that some of these particles may be submicroscopic and therefore small enough to pin grain boundaries, thus providing the mechanism for secondary recrystallisation. At 473K, 5%Sb is just on the phase boundary and so at such an annealing temperature the Sb could well be in solution and thus reprecipitate on cooling so allowing grain growth to occur. As some particles will dissolve faster than others certain grain boundaries will be released earlier than others thus giving rise to abnormal grain growth.

The microstructures of the two consolidated rods are again very similar to the chill cast alloy immediately after extrusion. It can be assumed therefore that the only real difference is going to the presence of an oxide dispersion introduced from the oxide film on the surface of the turnings and the ribbon prior to consolidation. This oxide dispersion, as with the pure tin compacts, will pin grain boundaries and thus prevent grain growth, giving the much finer structure seen after ageing than in the chill cast alloys. The banding seen in figure 5.13 is representative of

the flow during extrusion and caused by the production of stringers of
oxide along the extrusion direction and this may well also have caused
the delamination observed by S.E.M.

5.4. Comparison of the Microstructure of 10%Sb and 15%Sb Extruded Rods produced
from Chill Cast Material, Chill Cast Turnings and Rapidly Solidified Ribbon.

The microstructures of these two alloys were only different in volume
fraction of intermetallic and as it was felt unnecessary to devote a separate
section to each. The word intermetallic refers to the SbSn phase.

5.4.1. Chill Cast Extruded Rods.

Figure 5.17 shows the as-extruded and aged structures of both 10% and
15%Sb chill cast extruded rods at low magnification. In the as-extruded
10%Sb alloy the intermetallics have been dragged out by the polishing thus
leaving holes which although not representative of the true size of the
intermetallic do give an idea of the distribution. It can be seen that
with the 10% Sb alloys there is considerable macrosegregation in both the
as-extruded and aged microstructures (figs 5.17a,b). This segregation
must have been present in the original slug prior to extrusion and despite the
massive deformation undergone the segregation pattern still remains, with
little, if any, intermetallic in the centre of the rod. The effect of the
intermetallic on grain growth is clearly seen by comparing the centre and
edge regions of figures 5.17a and b. Grain growth is obviously hindered
by the intermetallics even though they are extremely large, for on ageing, in
the central region the grains are considerably larger than at edge where
the SbSn occurs.

With the 15%Sb alloys however, in both the as-extruded and aged
conditions, there is a fairly even distribution of intermetallic SbSn.

This difference between the two alloys is purely due to the different
volume fraction of intermetallic produced.

Studying these alloys at a higher magnification revealed a second

Figure 5.16   Scanning Electron Micrograph of Fracture Surface of

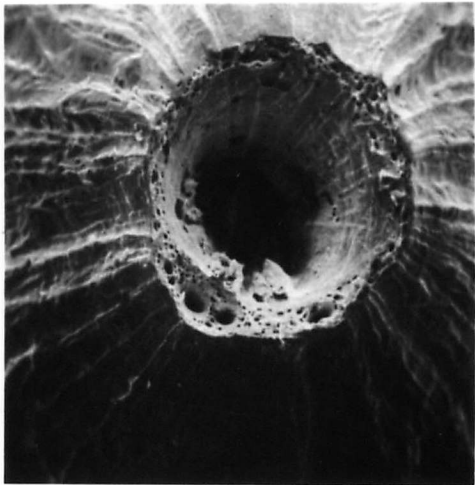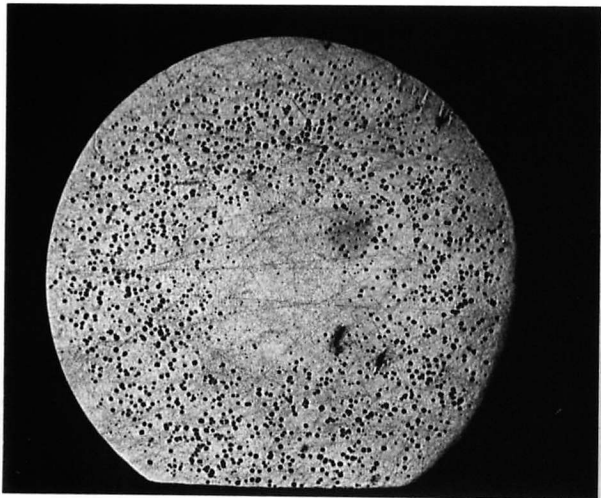Chill Cast Extruded Sn5%Sb Alloy
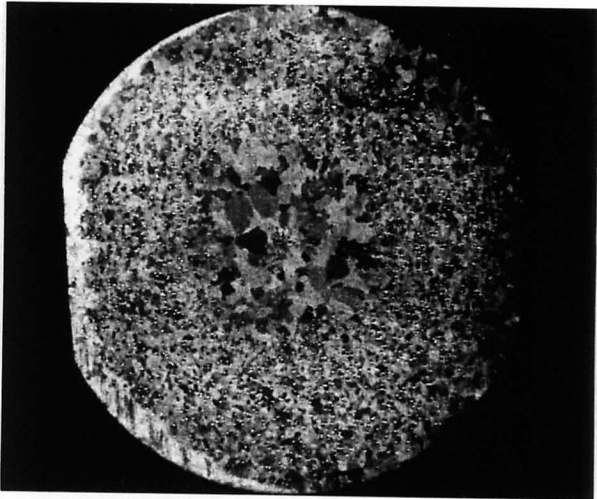
0·5 mm

Figure 5.17   Optical Micrographs of Extruded Chill Cast 10 and 15%Sb Alloys
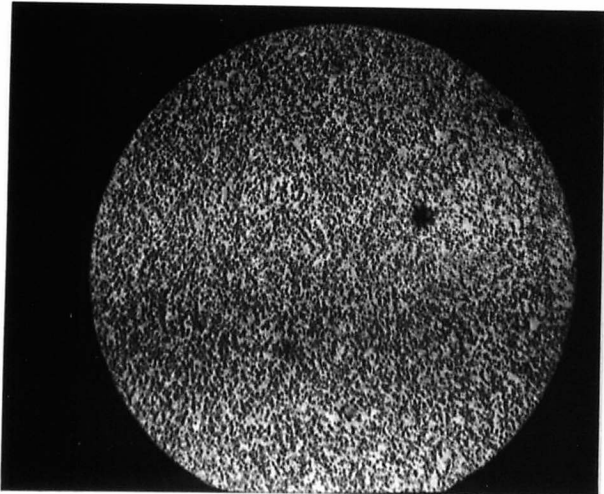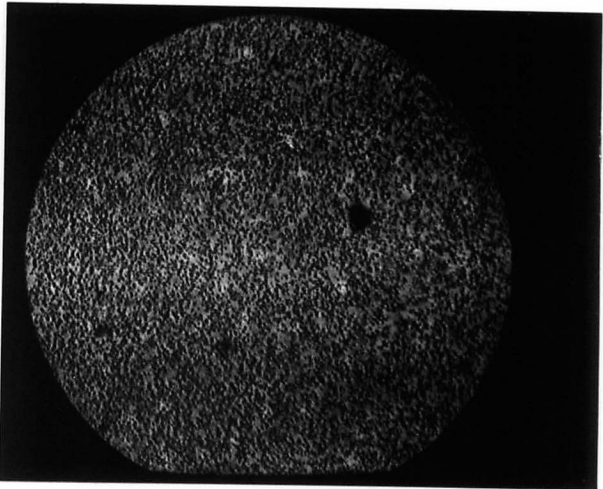
2 mm

%Sb

a) As-extruded

b) Aged 473K for 9×10^4 s

Sb

c) As extruded

d) Aged 473K for 9×10^4 s

interesting point.   Figure 5.18 shows various areas of 10%Sb and 15%Sb

alloys at a magnification of 500x, in the as-extruded and aged conditions.

In each case it is seen there is a distribution of very small SbSn

particles as well as the larger ones visible at low magnification.   The

larger particles are also not smooth edged as is normal in such chill

cast alloys but are jagged in appearance.

The size of the large particles ranges from 20 to 60μm for both

10% and 15%Sb alloys and the smaller particles averaged 1.2μm and 1.7μm

for the 10% and 15%Sb alloys respectively with no obvious effect of ageing.

The volume fraction of intermetallic was found to be 7.4% for the 10%Sb

alloy made up from a contribution of 5% large particles and 2.4% small

particles.   For the 15%Sb alloy the volume fraction was 21%, 18.5%

from the large particles and 2.5% from the smaller.   Calculations of volume

fraction of SbSn intermetallic from the SnSb phase diagram (fig.1.5)

give values of 10 and 29% for the 10 and 15%Sb alloys respectively.

However even in chill casting the amount of solute retained in solid

solution can be up to 8%Sb so using this value as the phase boundary

values of 5.8 and 20.5% SbSn were obtained for 10 and 15% Sb alloys. These

results would suggest that most of the visible particles, both large and

small, were formed in the first place on chill casting. The smaller particles

could be present as a result of two mechanisms, shearing and fracture of

larger particles and precipitation from excess solid solution. The remaining

solute unaccounted for must either be in solid solution or in a form which

is sub-optical-microscopic.

5.4.2. Consolidated Chill Cast turnings.

The microstructure of the consolidated chill cast turnings of both

10 and 15%Sb alloys looked exactly similar to those of the chill cast alloys

in section 5.4.1.   Figure 5.19 shows two micrographs at x100.   The only difference

Figure 5.18

Optical Micrographs of Chill Cast and Chill Cast Turnings of Sn10% +15%Sb
in the As-extruded and Aged conditions.

50 μm
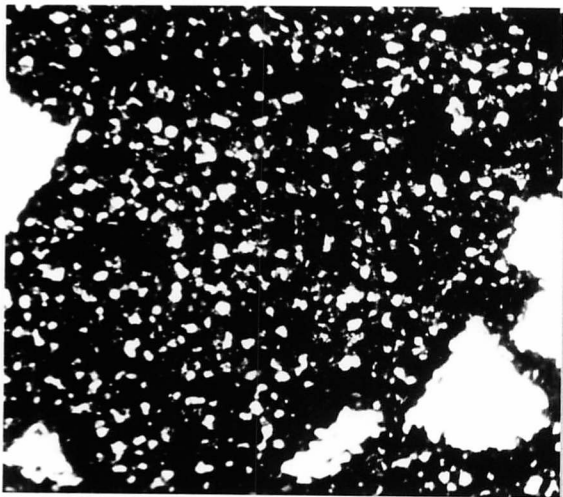
10%Sb

a) As extruded

b) Aged @ 373K for 1.8×10^5 s

15%Sb

c) As-extruded
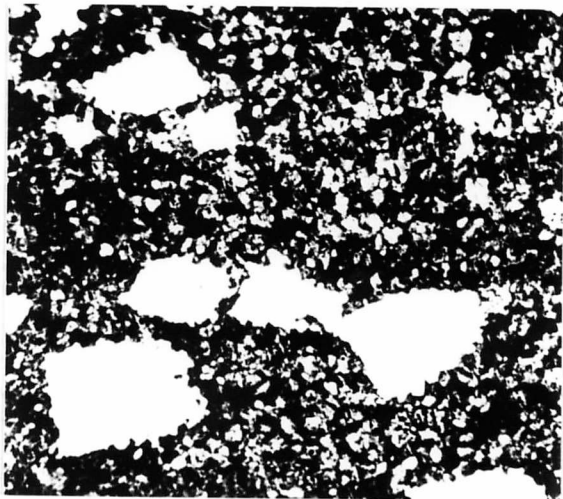
d) Aged @ 373K for 1.8×10^5 s

Figure 5.19

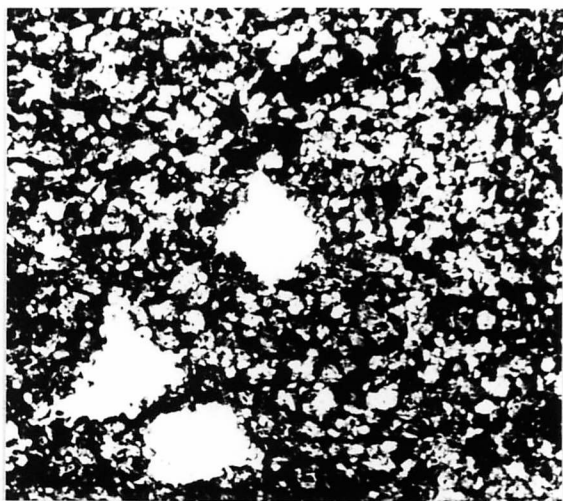Optical Micrographs of Extruded Chill Cast Turnings of 10 and 15%Sb

Alloys in the As-extruded state

$\overline{200\,\mu m}$
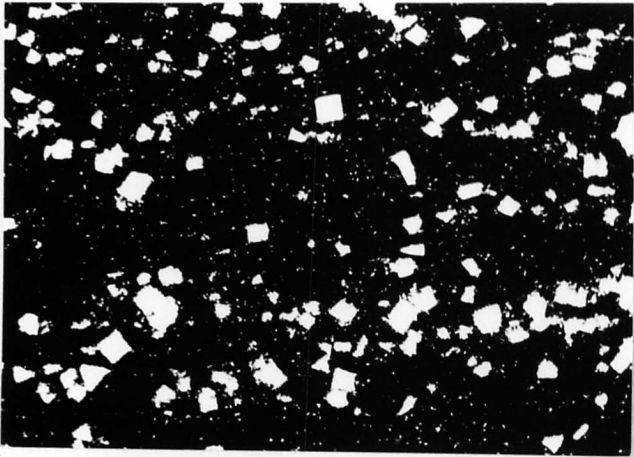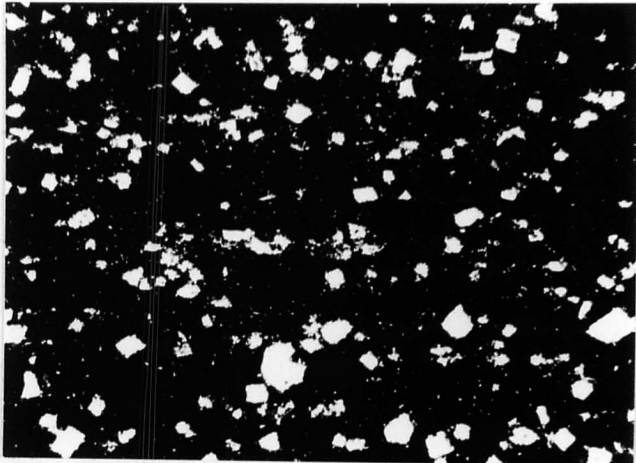
a)   10%Sb   b)   15%Sb

Figure 5.20

Optical Micrographs of Extruded Rods of Rapidly Solidified 10 and 15%Sb

Alloys in As-extruded and Aged Conditions. $\overline{50\,\mu m}$
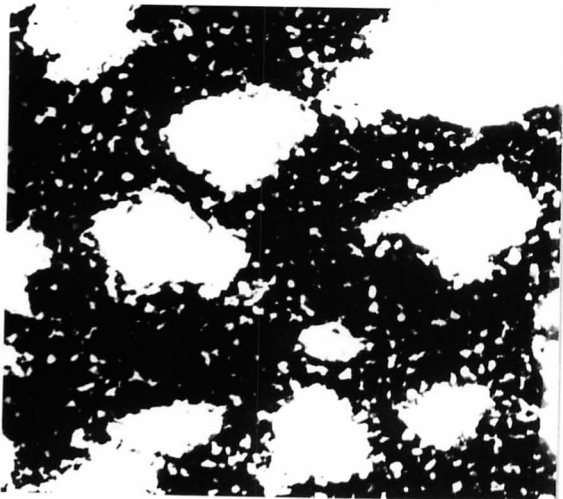

a) As-extruded   b) Aged 373 for 1.8×10^5 s

) As-extruded   d) Aged 373 for 1.8×10^5 s

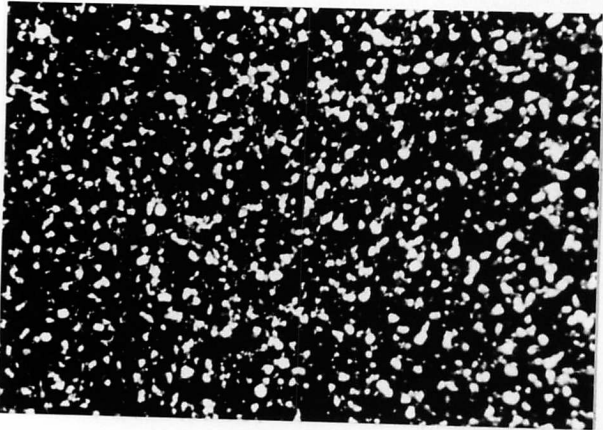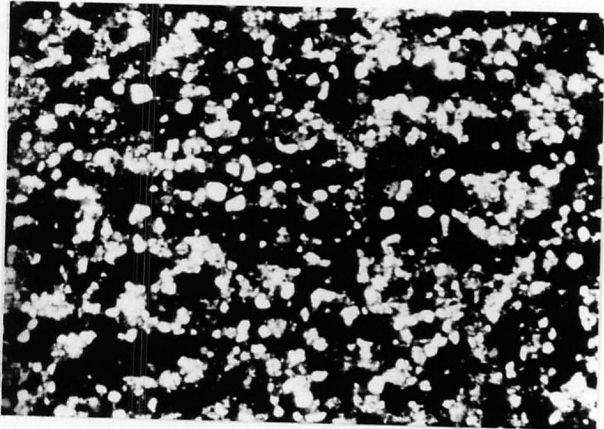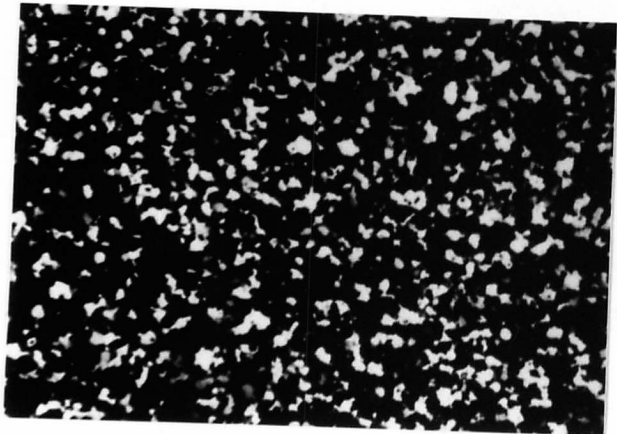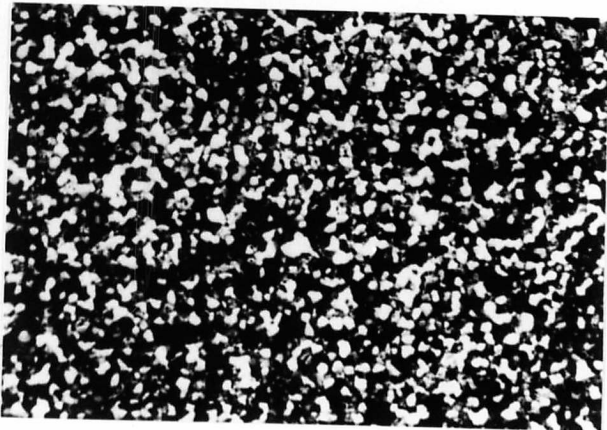there will be, but which is not visible, is the presence of an oxide

dispersion from the surface oxide film formed on the turnings.

5.4.3. Consolidated Rapidly Solidified Ribbons.

Figure 5.20 shows the microstructures of the 10 and 15%Sb consolidated

rapidly solidified ribbons in the as-extruded and aged conditions. Unlike

the chill cast materials there is only one distribution of particles with

an average size of 1.2 and 1.9μm for 10 and 15%Sb alloys respectively.

Both distributions are extremely skew suggesting that there were particles

present smaller than the resolution of the microscope would allow. Also

the volume fraction of particles in each alloy was only 8% which again

suggests a large number of sub-microscopic particles present, or massive

retention of solute which is unlikely after the amount of deformation

undergone during extrusion. The microstructure of both alloys seems

unaffected by the heat treatments. Again as with all the ribbon compacts

there must also be a dispersion of sub-microscopic oxide particles from

the surface oxide film.

5.4.4. Comparison of fracture surfaces of extruded rods of 10%Sb and

15%Sb alloys, by S.E.M.

Figure 5.21 shows the fracture surfaces from tensile specimens of chill

cast, chill cast turnings and rapidly solidified ribbons of 10 and 15%Sb

alloys in the as-extruded condition. These show similar differences

to those encountered using optical microscopy. The surface texture of

the consolidated ribbons (figs. 5.21e and f) is very fine and corresponds to

the size and distribution of the small SbSn particles. Thus ductile dimple

fracture has occurred with decohesion of the intermetallic as a crack

propagator. With the alloys produced from chill cast material there are

large regions of the fracture surface which seem to have undergone brittle

fracture these are of the same size and distribution as the large particles
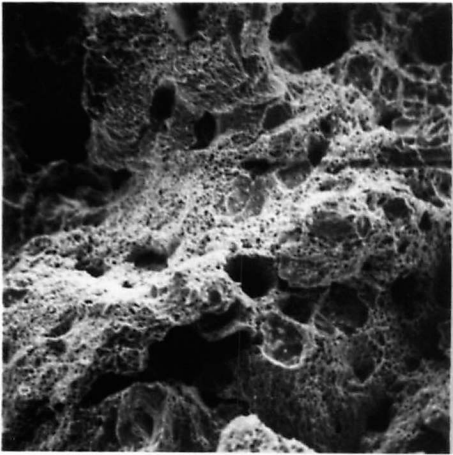
Figure 5.21 Scanning Electron Micrographs of the Fracture Surfaces of the As-extruded Rods of 10 and 15% Sb Alloys.

10%Sb   15%Sb

100 μm

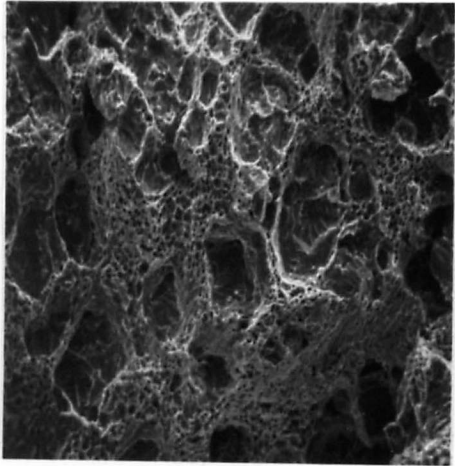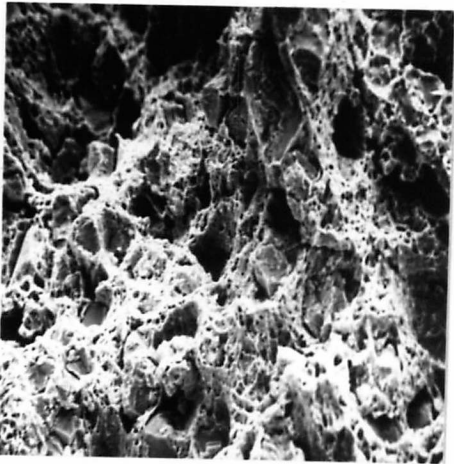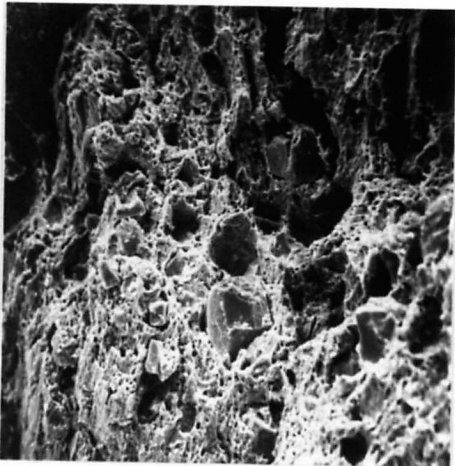a)   Chill Cast   d)   Chill Cast
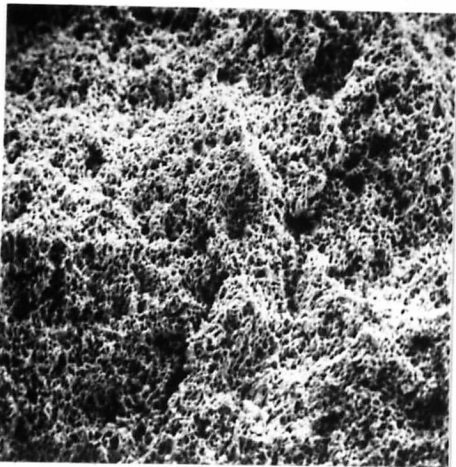
b)   Turnings   e)   Turnings

c)   Ribbon   f)   Ribbon

of SbSn seen under the optical microscope. Figure 5.22 shows one such

particle and an elemental map for Sb, showing that these regions are indeed

Sb rich. The regions between such particles (figs. 5.21a, b, d, e) also

show ductile fracture with dimples again corresponding to the size of the

smaller particles. The fracture mechanism would probably be fracture of the

larger brittle intermetallic followed by ductile dimple fracture with decohesion

of the smaller particles, so the ductility of the material as a whole would be

related to the volume fraction of the larger particles of brittle phase.

Figure 5.23 shows a similar array of micrographs as in figure 5.21

but in the aged condition, after 9×10^4s at 473K. Again the main difference

is that the consolidated rapidly solidified ribbon is much finer than the

chill cast or chill cast turnings for both 10 and 15%Sb alloys. Comparing

these fine surface structures with the unaged condition (figs. 5.21c and f)

it is possible to see that some coarsening has occurred but it is fairly slight.

The chill cast, and chill cast turnings both have similar structures but

these are slightly different from those in the as-extruded state. The

larger intermetallic SbSn particles have all fractured into very small bits,

this can possibly be more easily seen at a higher magnification (figure 5.24).

The regions between what were large intermetallics have undergone ductile

fracture but seemingly unrelated to the size of the smaller particles. It

would seem therefore that the heat treatment has caused some form of internal

stress fracture in the SbSn, a form of single cycle thermal fatigue,

releasing the internal stresses caused by deformation during extrusion.

This theory is also backed by the fact that the length of time at temperature

has no effect, the same structure results however long the ageing treatment is.

5.4.5. The Distribution of Antimony in Sn15%Sb Alloys.

Figures 5.25 are S.E.M. photographs showing the distribution of Sb in

a 15%Sb alloy of both rapidly solidified and chill cast extruded rods.

The elemental maps for antimony show that in the rapidly solidified

Figure 5.22

Scanning Electron Micrographs of As-extruded Chill Cast
Sn15%Sb Alloy showing an SbSn particle and an Elemental
Map for Antimony.
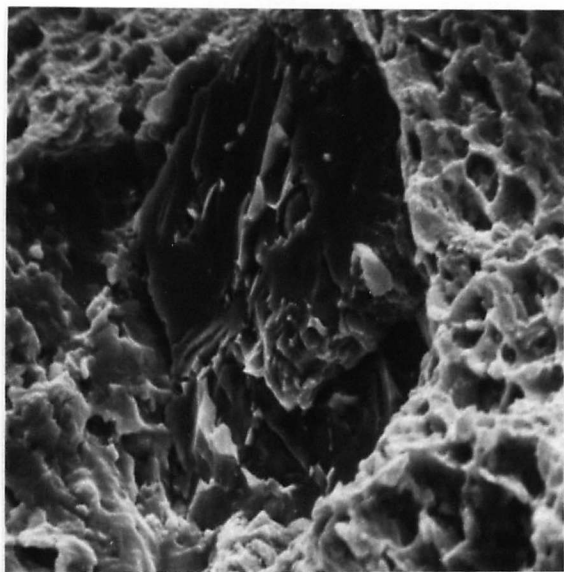
a) SbSn particle in Sn15%Sb (Chill Cast)   20μm
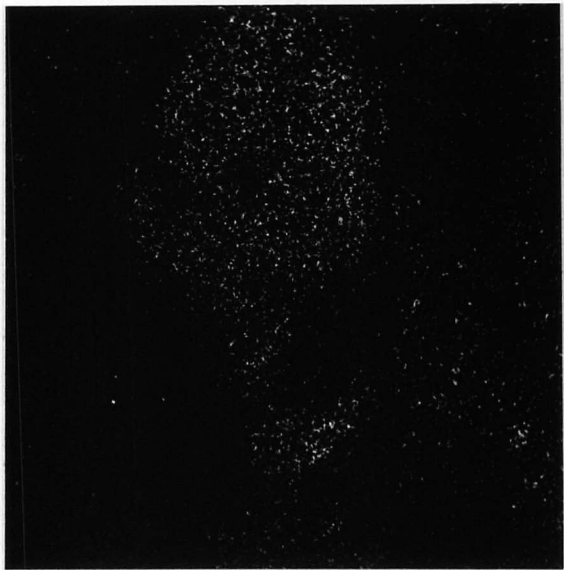
b) Elemental Map for Antimony

Figure 5.23 Scanning Electron Micrographs of the Fracture Surfaces of the
Extruded Rods of 10 and 15%Sb after ageing at 473K for 9×10^4 s

10%Sb $\underline{\ \ 100\,\mu m\ \ }$ 15%Sb
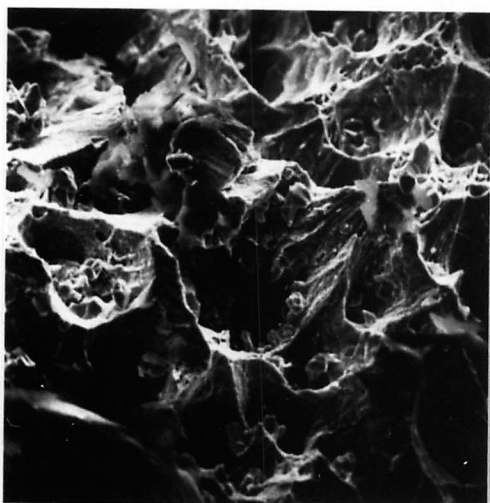
a)   Chill Cast
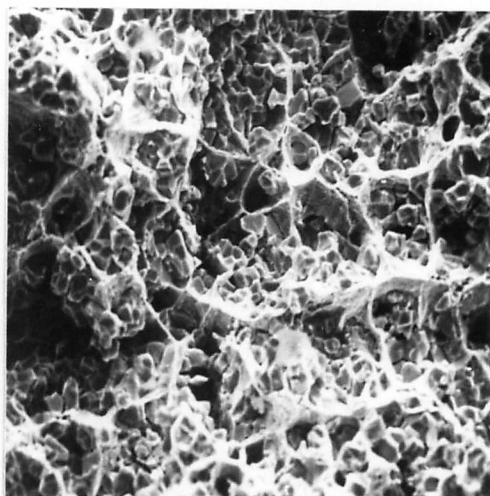
d)   Chill Cast
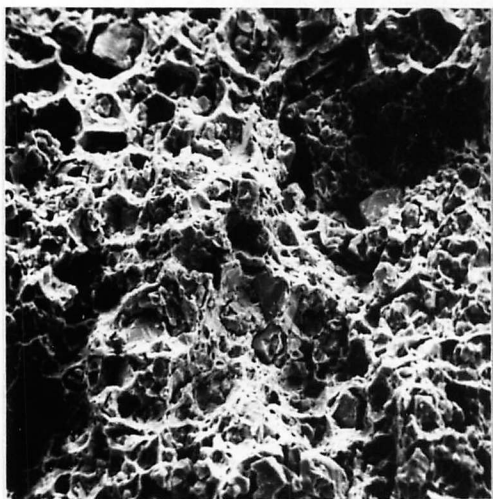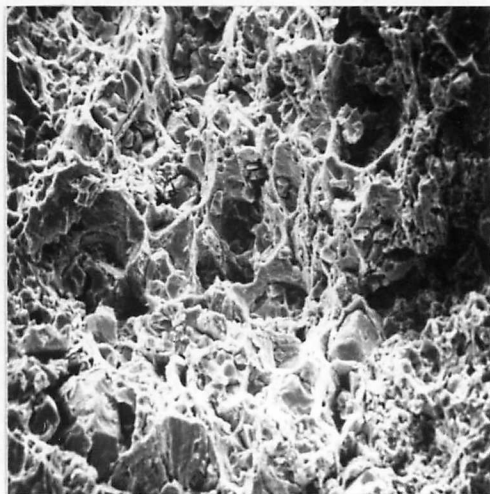
b)   Turnings

e)   Turnings
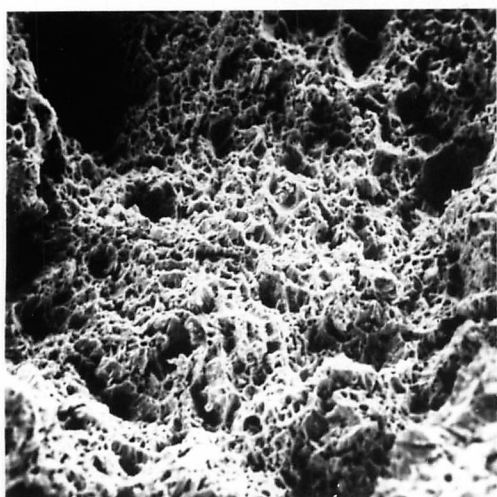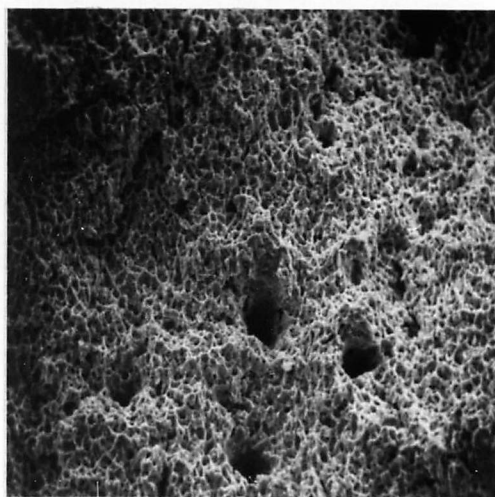
c)   Ribbon

f)   Ribbon

material there is an even distribution of Sb due to the smaller particle size. In the chill cast alloy there is segregation due to the large particle size. In the rapidly solidified alloy the particles are all of the order of 1 to 3μm. In the chill cast material there are two particle size distributions, the larger being of the order of 20μm and the smaller, some 1 to 3μm.

Both these values are very similar to those obtained from the analysis of the optical specimens by Quantimet.

5.4.6. Discussion.

Conventionally cast alloys of 10 and 15%Sb would contain primary cuboids of SbSn intermetallic and a matrix with up to 8%Sb retained in solid solution. Extrusion of this structure has resulted in limited deformation of the large intermetallics and also some fracture but where there was macro-segregation this has remained. The extrusion process has probably also initiated the precipitation of some of the Sb retained in solid solution if not all of it. Such precipitation may also have contributed to the roughened appearance of the primary SbSn cuboids whose surfaces would have provided ideal nucleation sites for the excess antimony in solid solution, during the extrusion process.

Rapidly solidified ribbons containing up to 15%Sb retain all the Sb in solid solution. This is not precipitated unless held for long times at temperature or, in this case, during extrusion when the deformation and heating due to warm working initiate precipitation. The morphology of the precipitates thus formed is different, they appear as spheroids rather than cuboids.

A change in shape of these second phase particles is not surprising as is seen in section 3.4.4, but those precipitates are needle shaped. The change from needle shaped precipitates to spheres must occur when the surface energy of the precipitates becomes an important factor. The nucleation and primary growth phase of the SbSn intermetallic relies on

Figure 5.24   Scanning Electron Micrograph of Fracture Surface of
                Extruded Chill Cast Sn10%Sb Alloy in the Aged Condition
                showing a fractured SbSn particle.
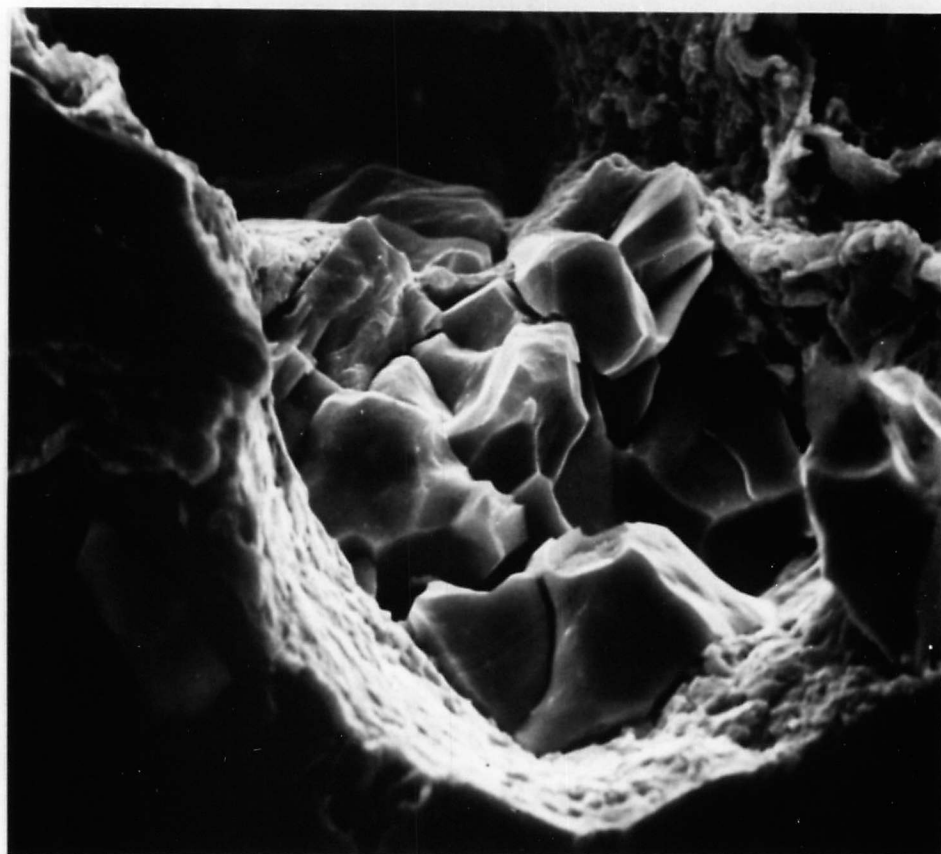
growth along directions with a low mismatch. In this case the <202> of the needles grows along the <201> of the matrix giving a mismatch of 0.6%. The {020} of the SbSn lie parallel to the {020} of the matrix with a mismatch of 5.3%. The needles are therefore semi-coherent with the matrix. The needles have a very high surface area to volume ratio and so as they grow there must come a point when the energy required to form new surfaces is too great and so spherodisation occurs to lower the surface area to volume ratio. If this is the case then heating of conventional alloys for long times should also cause spherodisation of cuboids. This has been found to occur by work completed at the International Tin Research Institute.

As the percentage of Sb in the alloy has increased the volume fraction of SbSn has also increased, except in the case of the 15%Sb alloy. This is probably due to a hidden volume fraction of a significant proportion of very small particles which have remained undetected probably due to the low resolution of an optical microscope. Transmission electron microscopy with thin foils or replicas might have been able to show this but it was found impossible to produce either.

5.5. General Discussion, Summary and Conclusions.

Figure 5.26 is a table summarising the microstructures of all the tin-antimony alloys studied in the present work. The structures of the 5%Sb alloy rods of rapidly solidified ribbon and chill cast turnings are most similar and should therefore behave similarly in the tests on mechanical properties (Chapter 6). These two alloys are only different from the chill cast extruded 5%Sb alloy by the presence of the oxide dispersion, and so any differences in properties can be assigned to the "oxide effect".

As the antimony content increases there is some evidence that some particles of SbSn are pinning the grain boundaries as the grain growth decreases as the antimony content increases in the chill cast extruded alloys (figs.5.2, 5.10a, 5.17b and d). This could be due to the "hidden" volume

Figure 5.25

Scanning Electron Micrographs of Extruded Rods of Chill Cast and Rapidly Solidified Sn15%Sb alloys after Polishing and Heavy Etching in Ammonium Polysulphide

Rapidly solidified.
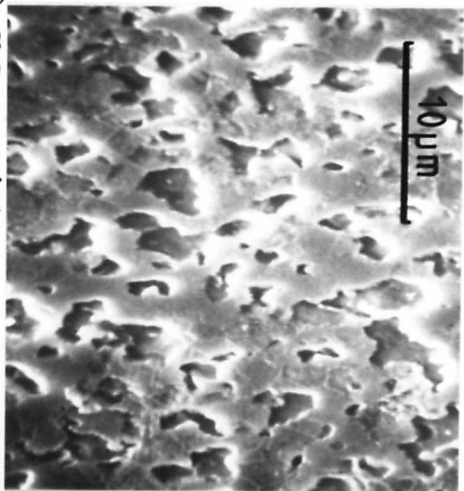
a) SbSn particles

b) Sb Elemental Map
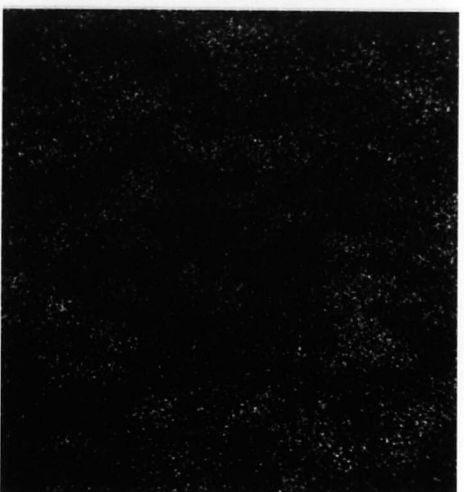
c) SbSn particles

d) Sb Elemental Map
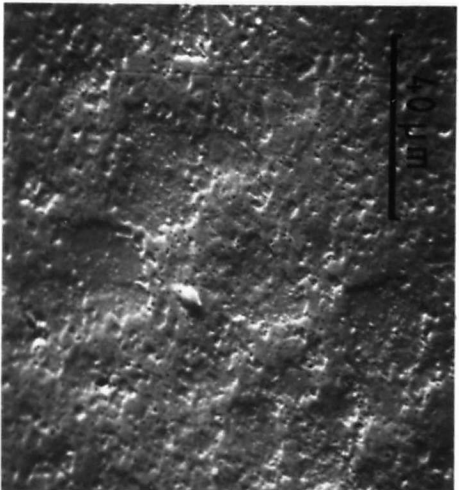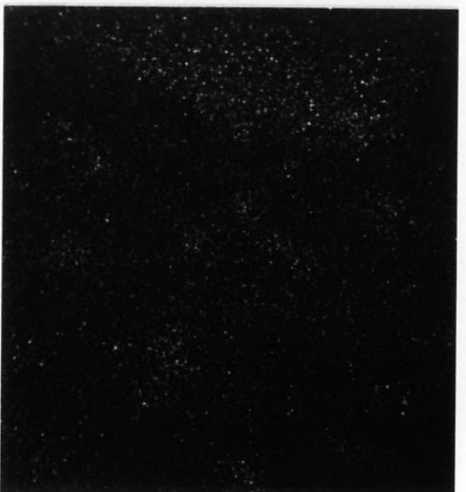
Chill Cast

e) SbSn particles

f) Sb Elemental Map

Alloy/Property		Chill Cast	Consolidated Turnings	Rapidly Solidified
a) as extruded grain size		47μm	16μm	11μm
Sn b) 2nd Phase		none	Oxides	Oxides
c) Effect of Ageing		Grain growth to 2670μm for most stringent treatment.	Elongation of grains along extrusion direction to a maximum of 2500μm.	Elongation of grains along extrusion direction to a maximum of about 2500μm.
Sn5%Sb	b)	2.8% of SbSn, 2.5μm	4.2% of SbSn, 1.8μm Oxides	4.0% of SbSn, 2.2μm Oxides
	c)	Abnormal grain growth, grains from 565μm to 2600μm.	Some coarsening visible in S.E.M.	Some coarsening visible in S.E.M.
Sn10%Sb	b)	Heavily segregated SbSn of two size distributions. 5.0% of 10-60μm. 2.4% of 1.2μm	Not so segregated SbSn of two size distributions. 4.5% of 10-60μm. 3.0% of 1.2μm. Oxides	Evenly distributed SbSn of only one size distribution. 8% of 1.2μm Oxides
	c)	Fracture of larger SbSn particles.	Fracture of larger SbSn particles.	Some coarsening but not much.
Sn15%Sb	b)	Evenly distributed SbSn of two size distributions. 18.5% of 10μ60μm 2.5% of 1.7μm	Evenly distributed SbSn of two size distributions. Oxides 16.5% of 10-60μm 4.0% of 2.9μm	Evenly distributed SbSn of one size distribution Oxides 8% of 1.9μm
	c)	Fracture of larger SbSn particles	Fracture of larger SbSn particles.	Some coarsening but only small amount.

Figure 5.26   Summary of Microstructures obtained in Extruded rods of Tin and Tin Antimony Alloys.

fraction precipitated from the small amount of excess solid solution obtained by chill casting. This pinning is not very successful until the antimony content reaches 15%. This is because pinning is favoured by small particles, a high volume fraction and large matrix grains. The high volume fraction is not achieved until there is a high antimony content. It is unlikely that the large SbSn particles have any pinning effect although in fig.5.17b it appears that the grain size is smaller where there are larger numbers of SbSn cuboids. This is probably due to the fact that there is also a higher excess solute present which precipitates out on extrusion.

The equivalent diameter assumption may have introduced errors into the calculation of size distribution. For the small particles this effect would not have been too great as they were on average spherical in shape. The larger particles however were nowhere near spherical in shape but were slightly elongated cuboids. Other errors may have been introduced by sectioning especially in heavily segregated alloys but care was taken to ensure that the areas used for analysis looked representative of the whole microstructure.

The conclusions that can be drawn from this microstructural study are:

1) The process of extrusion refines the grain size of chill cast alloys but on ageing both normal and discontinuous grain growth occurs depending on the temperature of the treatment.

2) The large SbSn particles present in the chill cast and chill cast turnings are slightly deformed during the extrusion process.

3) There is retention of some Sb in solution in the chill cast and chill cast turnings which probably precipitates on extrusion.

4) The roughened appearance of the primary SbSn phase in the rods of chill chast and chill cast turnings may be the result of either, fracture of the SbSn cuboids,or precipitation of the excess antimony in solid solution on the surfaces of the cuboids, both processes could occur during extrusion.

5)   All the antimony in the rapidly solidified alloys is contained in solid solution prior to extrusion but the excess antimony is precipitated as small SbSn particles on extrusion.

6)   The rapid solidification process does not change the microstructure of the pure tin or 5%Sb alloy.

7)   The rapid solidification process significantly reduces the size and segregation of SbSn in the 10 and 15%Sb alloys.

8)   The process of consolidation from particulate stock, whether of rapidly solidified ribbon or turnings of chill cast alloy, introduces a dispersion of oxide into the extruded rod which stabilizes the microstructure on ageing by pinning grain boundaries.

Chapter 6.   THE MECHANICAL PROPERTIES OF EXTRUDED RODS OF CHILL CAST,

CHILL CAST TURNINGS AND RAPIDLY SOLIDIFIED MATERIAL

6.1. Introduction

The mechanical properties of specimens of pure tin and alloys of 5, 10

and 15%Sb prepared from extruded rods of chill cast material consolidated chill

cast turnings and rapidly solidified ribbon were assessed using four types of test,

      i)   Hardness

      ii)   Tensile Testing

      iii) Compression Testing

      iv)   Stress-Rupture Testing

Hardness testing was used as a preliminary test to indicate relative strengths

of the alloys.   Tensile testing gave measurements of tensile strength and ductility.

Compression testing was used to give the yield point, and, along with the stress-

rupture testing, subjected the alloys to conditions similar to those found in

bearing applications.

All the alloys were also subjected to an extensive period of time at 253K

(−20°C) to ascertain whether any low temperature allotropic changes occurred.

The following five sections give the results and describe the techniques for

each test, section 6.7 is a discussion based on the results of this chapter and

chapter 5.

6.2. Hardness Testing.

6.2.1. Technique

Hardness testing is one of the most convenient and simple ways of indicating

the relative strengths of alloys.   In this study a Vickers Diamond Pyramid

indenter was used with a load of 2.5kg.   Specimens were prepared by grinding

longitudinally along lengths of the extruded rods until a flat of approximately

3mm width was obtained, these were then polished to a 6μm diamond finish.

Specimens were aged at 473, 423, 373K and room temperature (approximately 300K)

for up to 6 months depending on the temperature.

6.2.2. Hardness Results

The indentations obtained were extremely good with little barreling or pincushion effect in most cases. The indentation diagonal measurements ranged from 410μm to 960μm. The smaller indentations tended to be a better shape than the larger, which were obtained in the very soft pure tin. Each hardness value reported is the average of at least six measurements. The maximum error, ascertained by the calculation of one standard deviation, σ, was found to be ±0.7Hv.

6.2.2.(1) As-extruded hardness.

Figure 6.1 shows a plot of the as-extruded hardness values against the antimony content of the alloy. As was expected the hardness values increased with antimony content in line with published data (Greenfield and Forrester, 1947).

The unexpected result is that apart from the pure tin all the chill cast extruded materials are harder than the rapidly solidified materials with the compacted turnings having hardnesses in between these two extremes.

6.2.2.(2) The effect of ageing on hardness.

Only the chill cast and rapidly solidified materials were subjected to ageing treatments. The results of such ageing treatments are shown in figure 6.2 as plots of hardness against ageing time for each alloy, at various temperatures.

These curves show no dramatic increase or decrease with ageing time at any temperature, and do not indicate any typical precipitation hardening reaction. There is however a general increase in hardness for the chill cast materials aged at 473K. Figure 6.3 shows a plot of extrapolated hardness values after ageing at 473K for 10^6s against antimony content. It is interesting to note that the values for the chill cast materials are now very similar to those reported by Greenfield and Forrester (1947) for

Figure 6.1   Plot of As-extruded Hardness (Hv) against Composition (%Sb)
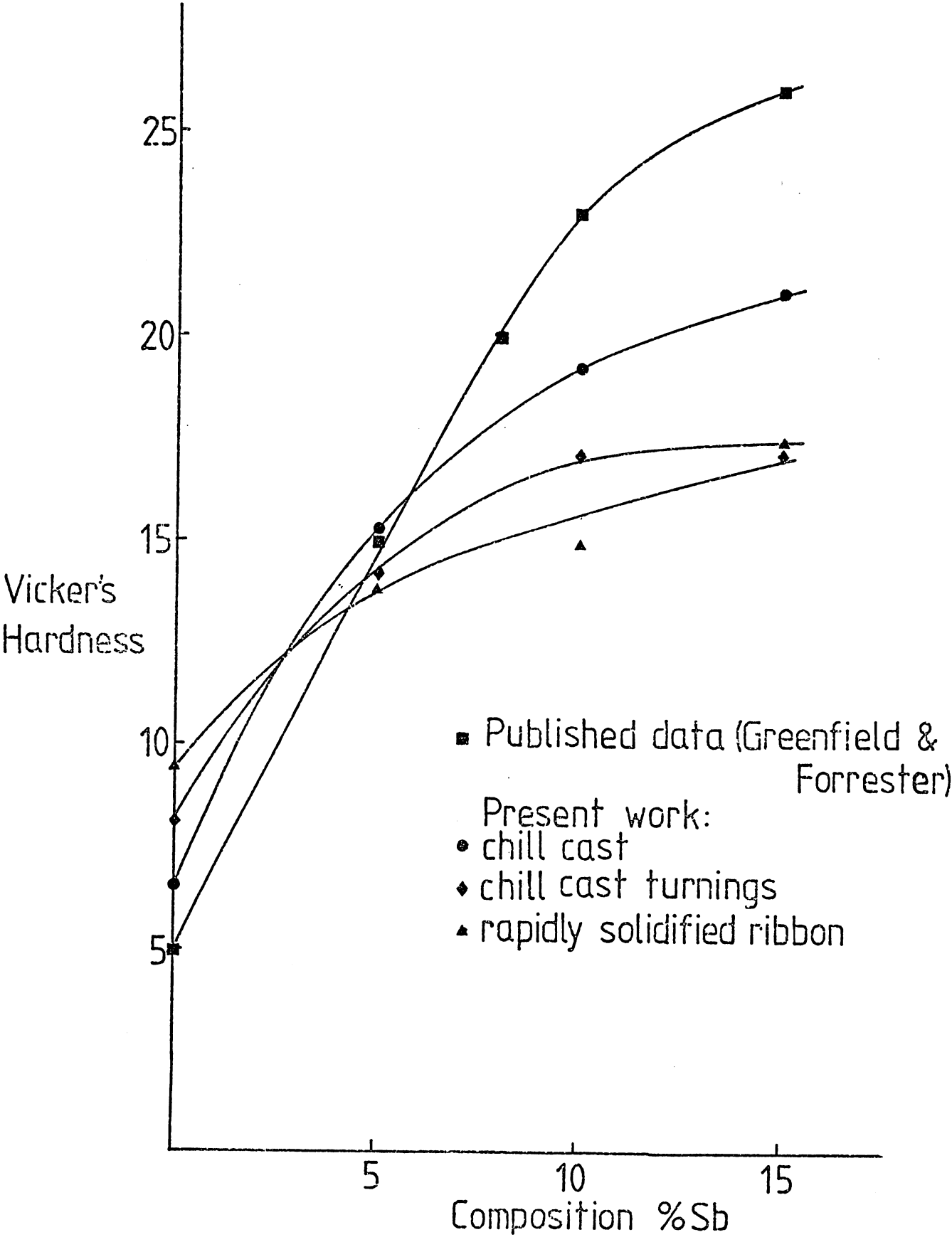
Figure 6.2

Plots of Hardness (Hv) against Ageing Time (t) at Various Temperatures (T)

a) T=473K

b) T=423K

c) T=373K

d) T=300K (Room temperature)

• rapidly solidified

σ=07
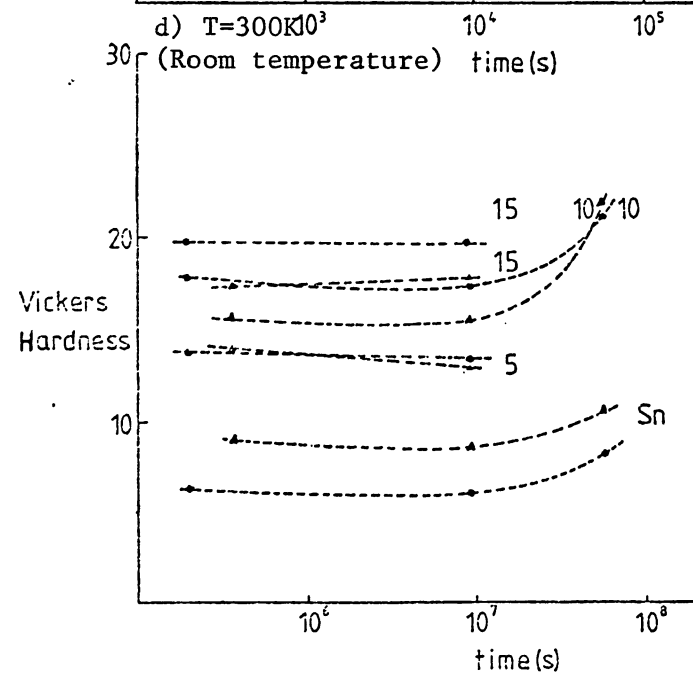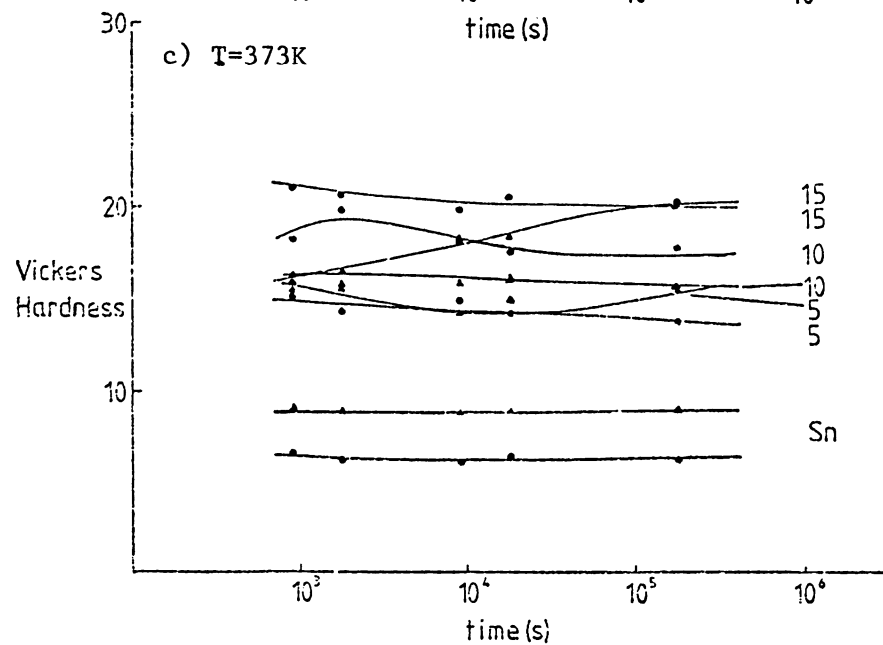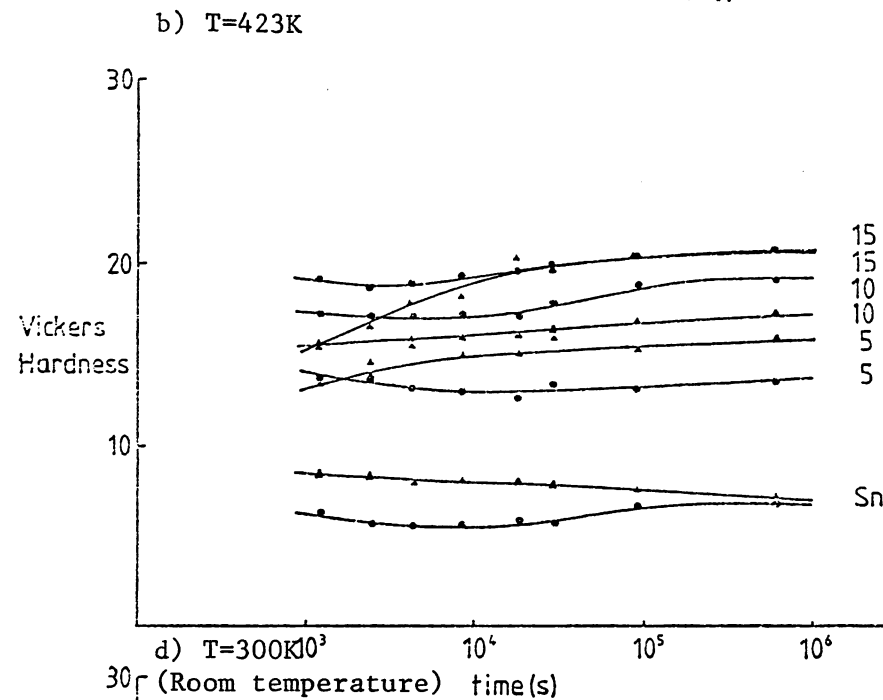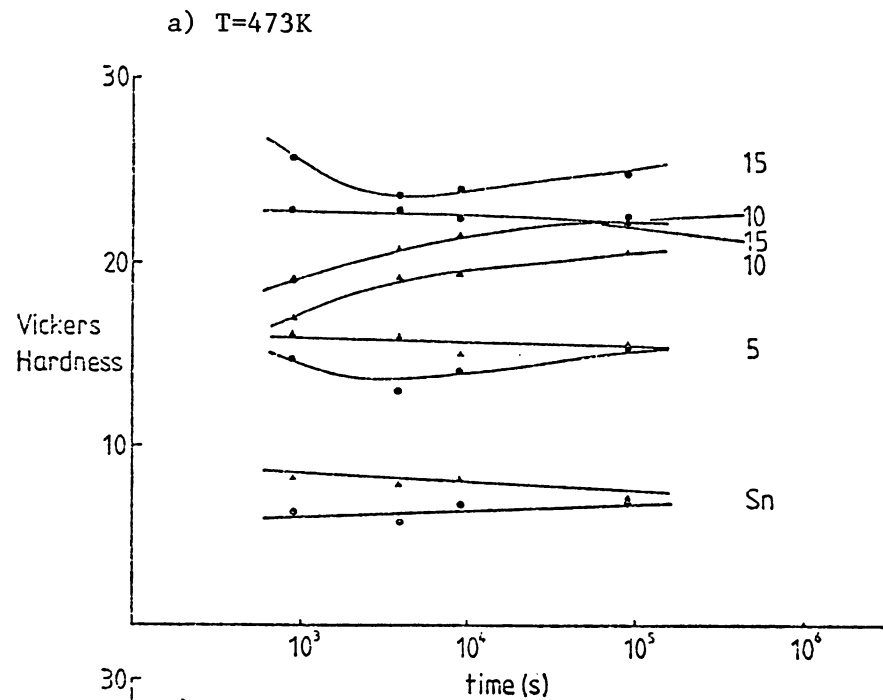
Figure 6.3

Plot of Hardness (Hv) after ageing at 473K for 10^6s against

Composition (%Sb)
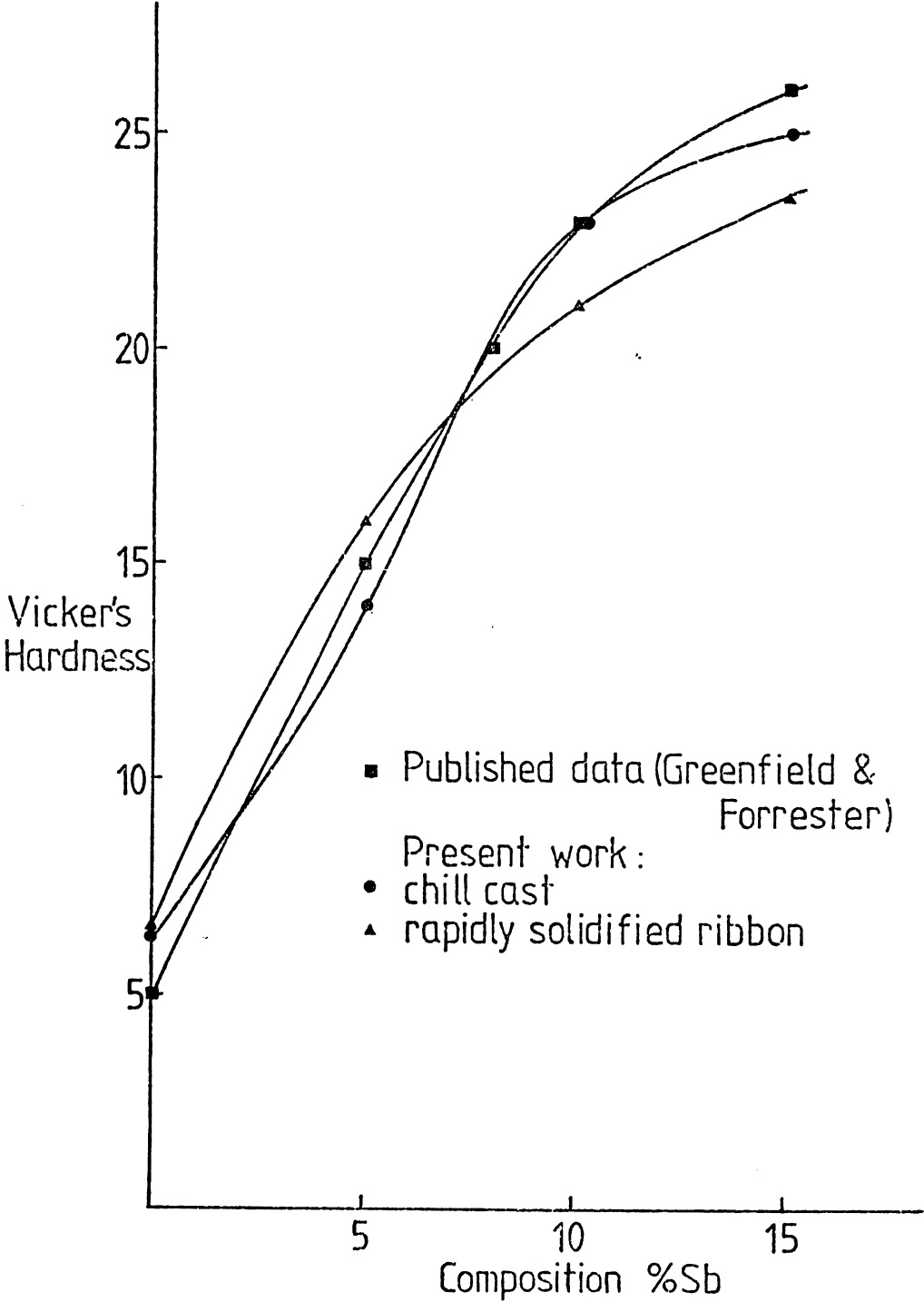
chill cast specimens.

The increases hardness observed in both C.C. and R.S. pure tin and 10%Sb rods may be an artefact due to the use of a different testing machine but not enough data was collected to draw any significant conclusion from this.

6.2.3. Analysis for the prediction of long term properties.

An attempt was made to rationalise all the above hardness results. From the assumption that hardness is related to grain size, and that grain size is in some way related to ageing time and temperature, a parameter was devised similar to that proposed by Larson and Miller (1952) for creep testing and used by Underwood (1959) for hot hardness testing.

It was proposed that the hardness Hv was directly proportional to such a parameter, H,

$$Hv \propto H$$

where

$$H = T \left[K + \ln(t)\right]$$

T is the absolute ageing temperature, t the ageing time in seconds, and K the best fit constant.

Unfortunately the results from this analysis tended just to show three separate lines, one for each ageing temperature, except in the case of the rapidly solidified pure tin where a continuous line was shown. This suggests that whatever changes in structure there are, which affect the hardness, are different when there are intermetallics of SbSn present and not just simply related to any grain growth which may occur.

6.3. Tensile Testing

6.3.1. Technique.

All the tensile tests were carried out on Hounsfield Number 11 specimens which are double shouldered and useful for ductile materials. Some initial

tests were performed on a large Instron T.M.M. tensile testing machine but the results reported here were mainly obtained from a J.J. Instruments T5000 table-top tensile testing machine using an X-Y plotter to record the results.

All the alloys were tested in the as-extruded state. The chill cast and rapidly solidified alloys were also tested after various ageing times at 473K while the compressed turnings were only aged for 9×10^4s at 473K and then tested.

In an ideal situation the yield point, σ_y, is the best value to report from a tensile test, in the present work this was difficult to detect due to the softness of the machine used and the high ductility of the materials tested. Instead four other values are reported to give an indication of the strength and ductility of the materials.

     i)   Tensile Strength (T.S. or $\sigma_{T.S.}$)

     ii)   Strain to maximum load ($\%e_{T.S.}$)

     iii) Reduction of area at failure ($\%R.A.$)

     (iv) Elongation to failure ($\%e_F$)

From such values a comparison can be made for each alloy in order to assess the effect of

     i)   process route

     ii)   ageing treatment

The choice of strain rate was influenced by the length of time the tests took. One initial test at a strain rate of $0.73 \times 10^{-3}s^{-1}$ produced an elongation of 250% which took almost an hour to complete, this was obviously not feasible and so the strain rate was varied up to $1.46s^{-1}$, and it was eventually decided that a strain rate of $0.73 \times 10^{-1}s^{-1}$ gave reasonable test times. Published data by Greenfield and Forrester (1947) used strain rates of $0.25 \times 10^{-2}s^{-1}$. It was noted that all the measurements to be made were very strain rate dependent and therefore it would be difficult to compare

with published data. This can be seen in figure 6.4, which shows the variation of tensile strength with initial strain rate for a rapidly solidified Sn10%Sb alloy. This variation is linear if a log plot is made of T.S. $\alpha \ln (\dot{e})$. This type of variation has been observed before, for example in copper (Nadai and Manjoine, 1941). It is often possible to measure a parameter called the strain rate sensitivity, m, but this requires measurements of yield point which in the present work were not observed.

6.3.2. Tensile Results.

Figure 6.5 shows examples of tensile test curves from all the alloys studied in the present work in the as-extruded and aged conditions. The ageing treatments were all carried out at 473K and the curves shown are for a time of 9×10^4s. Figure 6.6 is a table summarising the four measurements of TS, $\%e_{TS}$, %RA and $\%e_F$, for such tests. Each value in the table is the average from at least three tensile tests.

From the above data the following observations can be made. For the chill cast materials in both as-extruded and aged conditions as the antimony content increases so the tensile strength increases but the ductility decreases. Except for the 5%Sb alloy the aged specimens have much reduced ductility and a decrease in tensile strength relative to the unaged state. The 5%Sb alloy shows an increase in ductility. The as-extruded pure tin is very ductile and the testing machine was too soft to show any elastic deformation. In the aged condition the pure tin shows a series of yield drops until maximum load is reached, thereafter the curve is smooth.

The compressed turnings of chill cast alloys (fig.6.5c,d) show similar changes in the as-extruded state as the chill cast materials. As the percentage of antimony increases so does the tensile strength and the ductility drops. The ductility changes are not as great, in as much as the CT pure tin is less ductile than the CC pure tin but for the 15%Sb alloy the CT material is more ductile than the CC alloy. The tensile strengths in the

Figure 6.4

Plot of Tensile Strength (σ_{TS}) against Strain Rate ($\dot{e}$) for a Consolidated

Rapidly Solidifed Sn10%Sb Alloy.
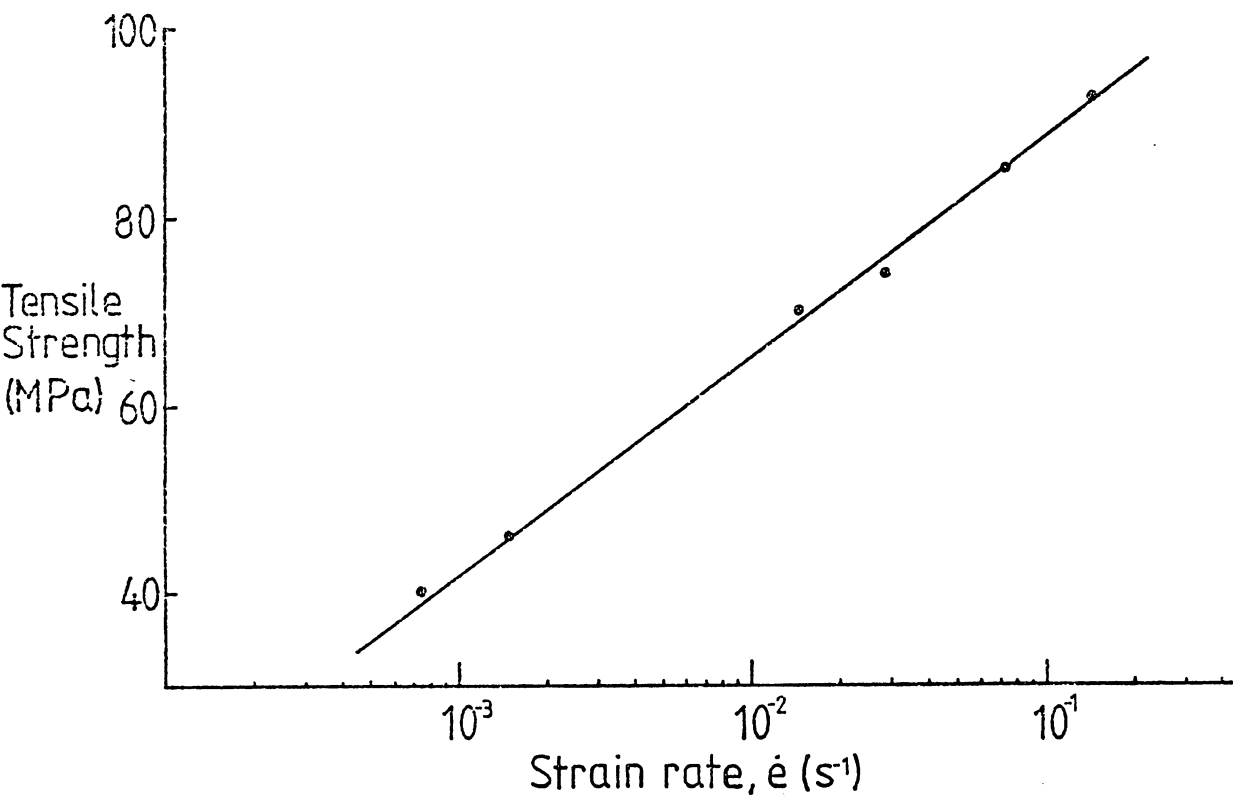
Figure 6.5 a and b

Tensile Test Curves for As-Extruded and Aged (@ 473K for 9×10^4s) Rods of Chill Cast Alloys.

a) As-extruded
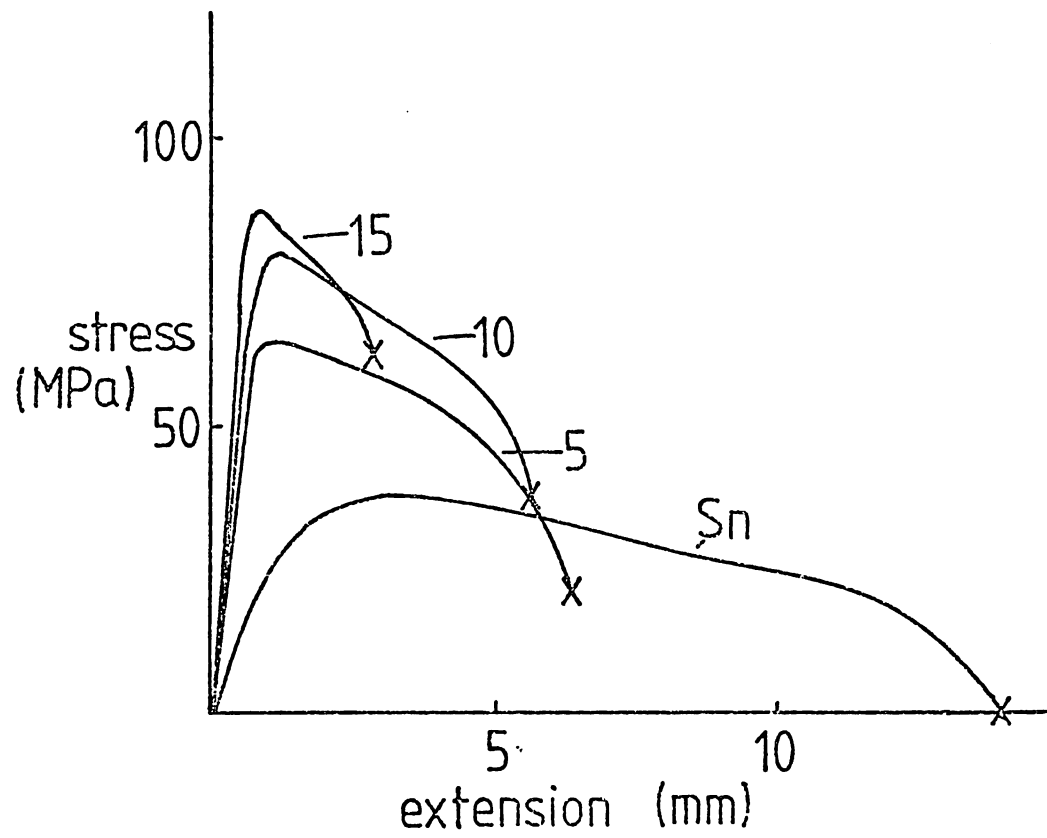
b) Aged
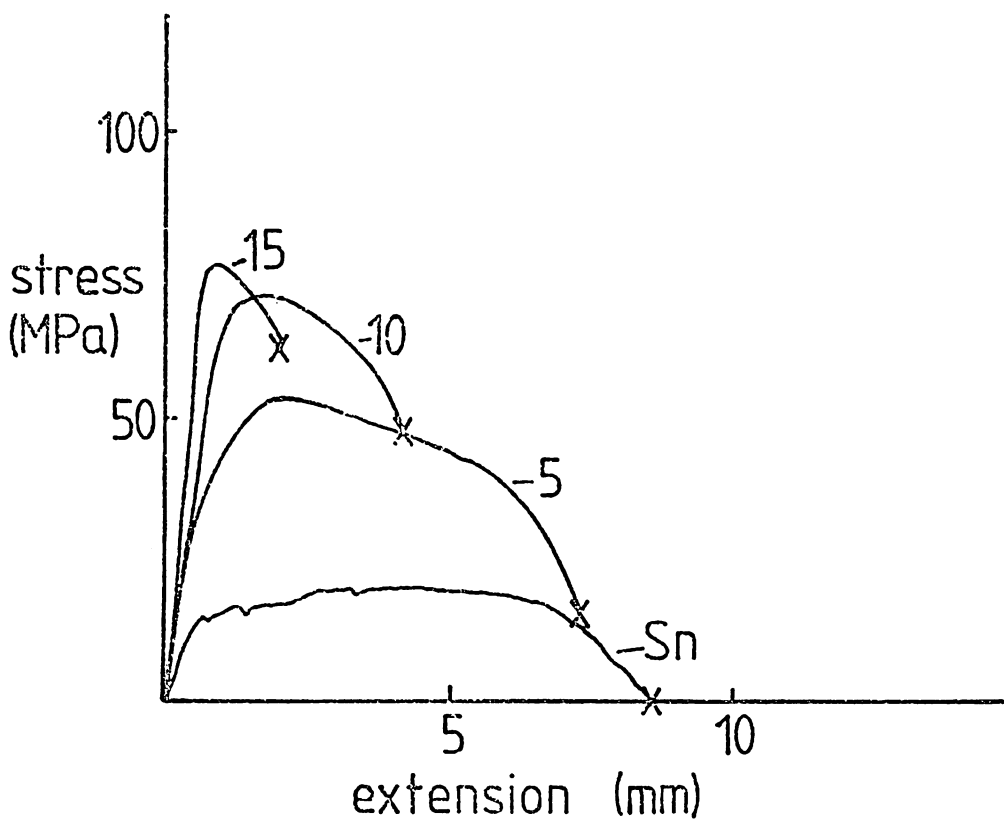
Figure 6.5 c and d.

Tensile Test Curves for As-Extruded and Aged (@ 473K for 9×10^4 s) Rods of Chill Cast Consolidated Turnings.

c) As-extruded
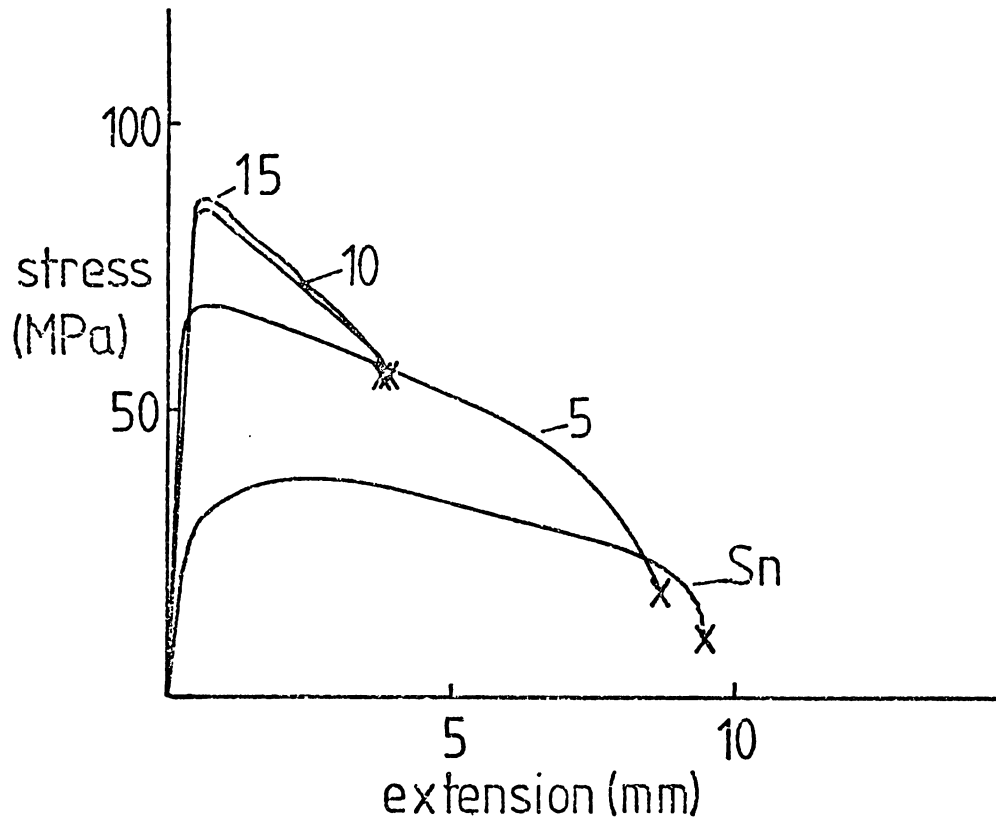
d) Aged
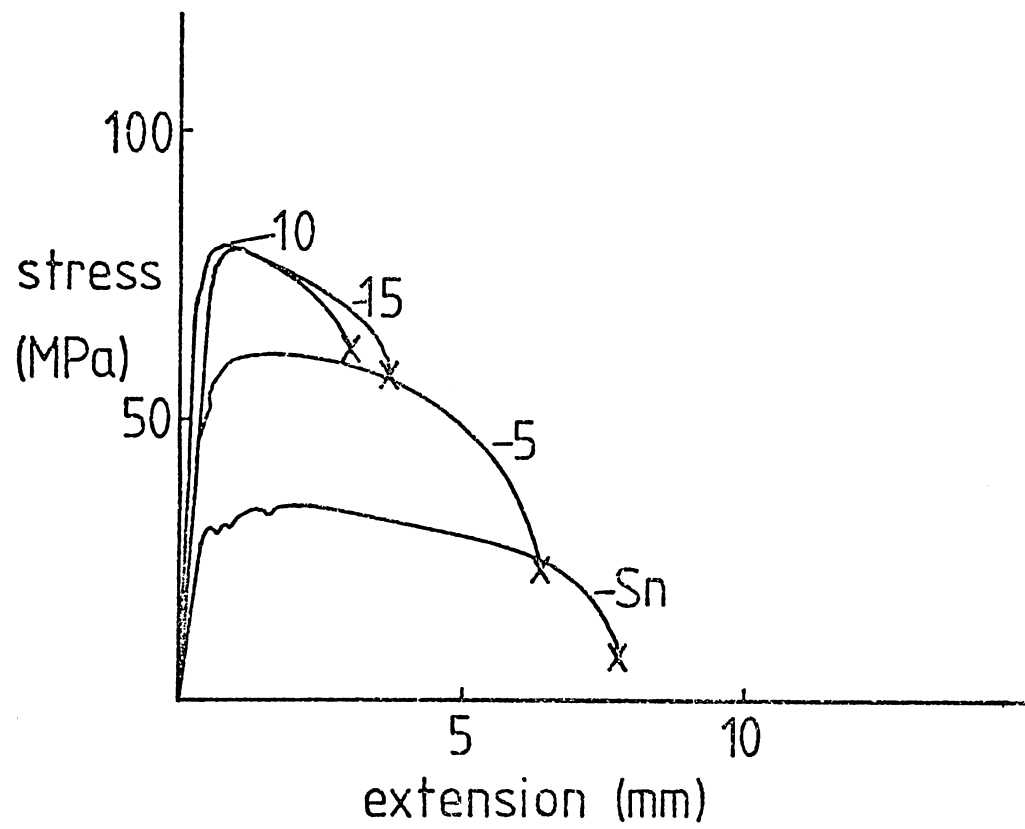
Figure 6.5 e and f

Tensile Test Curves for the As-Extruded and Aged (@ 473K for 9×10^4 s) Rods of Consolidated Rapidly Solidifed Ribbon.

e) As-extruded
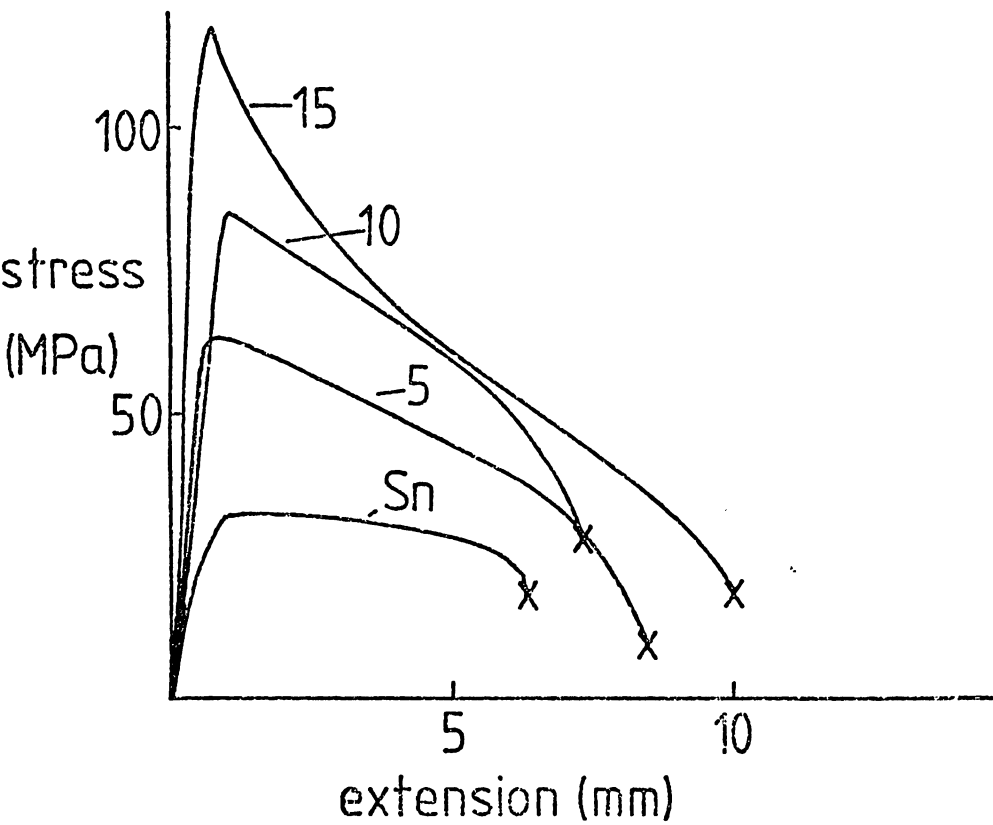
f) Aged
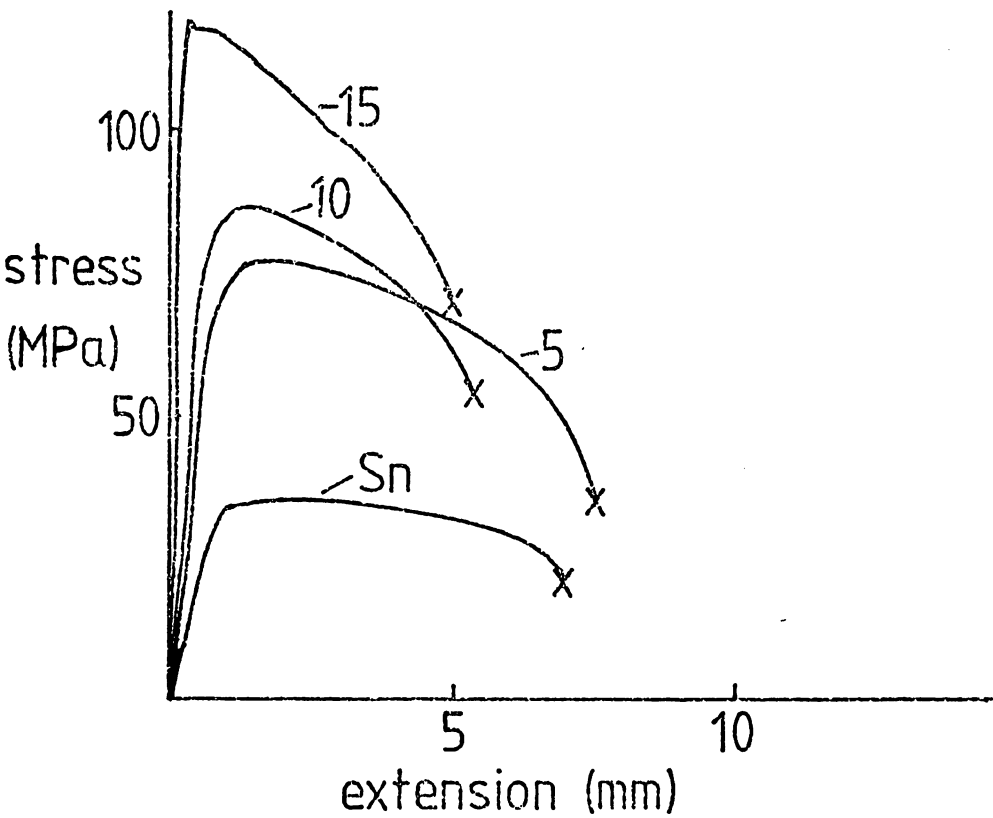
Figure 6.6.

Summary of Tensile Results

Condition	%Sb	Process Property	0			5			10			15		
			R S	C C	CT	RS	CC	CT	RS	CC	CT	RS	CC	CT
as extruded		TS(MPa)	36.9	36.7	38.7	62.9	64.4	66.7	84.3	79.8	83.3	116.3	87.3	83.8
		$\rho_{TS}\%$	10.5	23.0	20.3	4.5	11.0	7.3	3.7	8.0	6.0	4.1	5.0	6.3
		$RA\%_F$	60.0	>99	64.0	85.8	82.4	82.0	75.0	55.6	31.0	75.2	22.6	30.0
		$\rho_F\%$	51.0	118.0	74.6	68.7	54.0	74.3	57.0	47.0	33.7	76.4	14.5	31.7
Aged @ 200°C for 1500 mins.		TS(MPa)	34.9	19.0	34.9	79.6	52.9	62.4	85.3	76.1	81.0	117.8	76.0	78.3
		$\rho_{TS}\%$	17.4	34.0	16.6	12.8	15.0	15.5	8.5	13.0	7.6	2.0	4.6	9.0
		$RA\%_F$	55.0	>99	/	66.1	98.9	74.0	42.0	56.5	25.0	48.6	16.5	27.0
		$\rho_F\%$	55.0	75.0	53.8	64.0	63.0	54.5	46.0	38.1	24.6	41.1	14.1	30.0

RS: Rapidly Solidified Ribbon, Compacted and Extruded at 40:1

CC: Chill Cast alloys extruded at 40:1

CT: Compacted turnings of chill cast alloy extruded at 40:1

ensile tests at Room temperature on a JJ.T5000 machine, using a crosshead speed

f 50mm/min. or an initial strain rate of $0.073s^{-1}$

TS: Tensile Strength.

1 MPa= $1Nmm^{-2}$=0.065Tsi.

$\rho_{TS}\%$: Elongation % to TS

$RA\%_F$: Reduction of Area % to failure

$\rho_F\%$: Elongation % to failure

All the values reported are the average from at least three tests.

a) As extruded

b) Aged 473K for 9×10^4 s

Tensile Strength (MPa)

Composition %Sb

- chill cast
- chill cast turnings
- rapidly solidified

Figure 6.7 a and b.

Plots of Tensile Strength (σ_{TS}) against Composition (%Sb) in the As-extruded and Aged (@ 473K for 9×10^4 s) conditions.
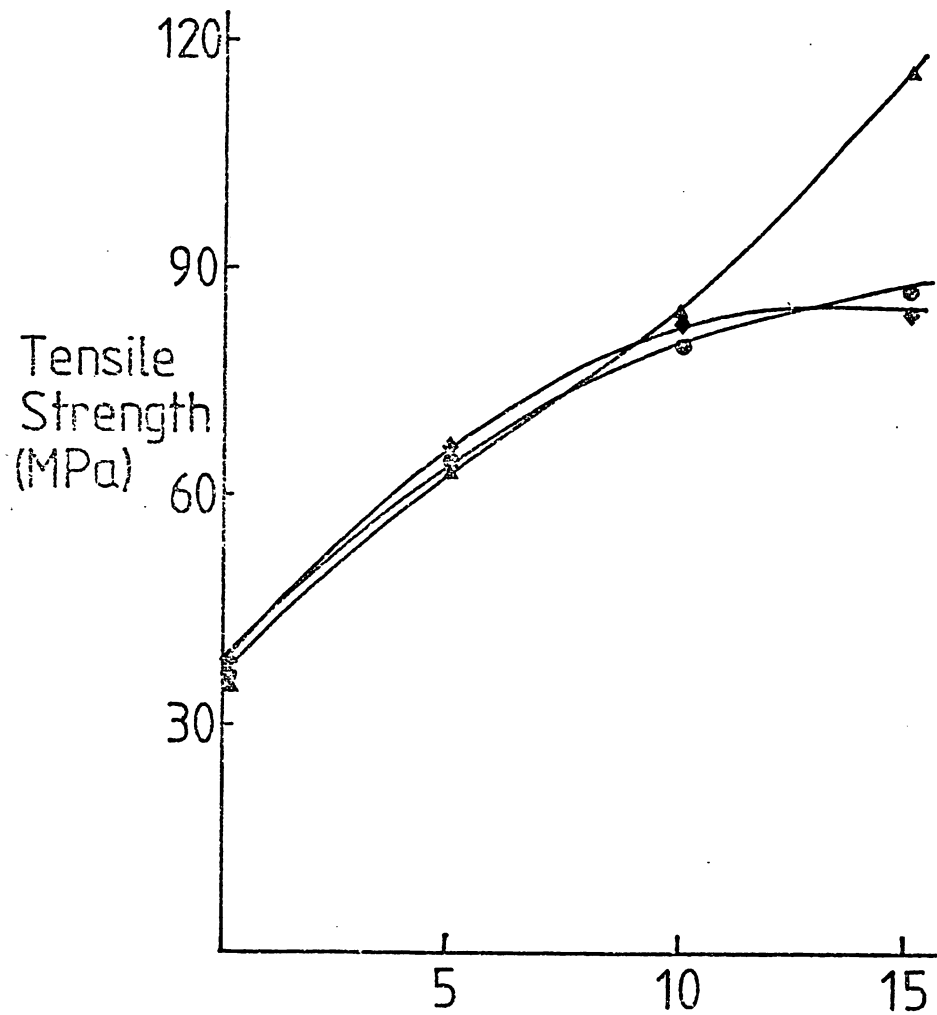
c) As-extruded

d) Aged 473K for 9×10^4 s

- chill cast
- chill cast turnings
- rapidly solidified

Composition %Sb

Figures 6.7 e and f

Plots of Perecentage Reduction of Area at Failure (%RA) against Composition

(%Sb) in the As-Extruded and Aged (@ 473K for 9x10^4 s) Conditions.
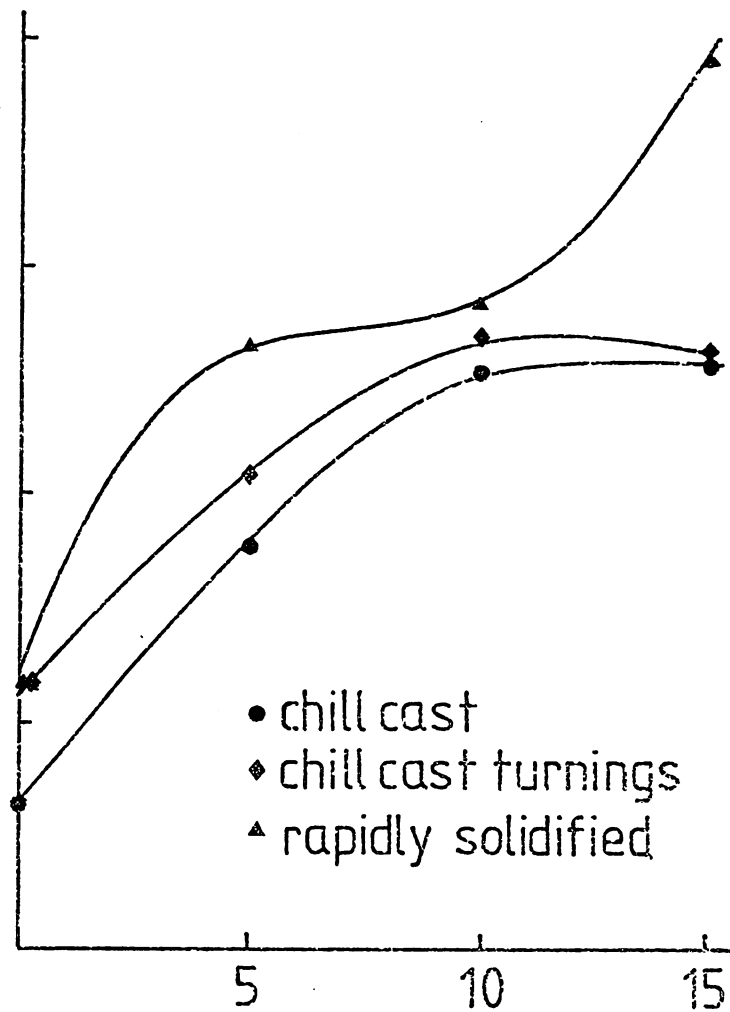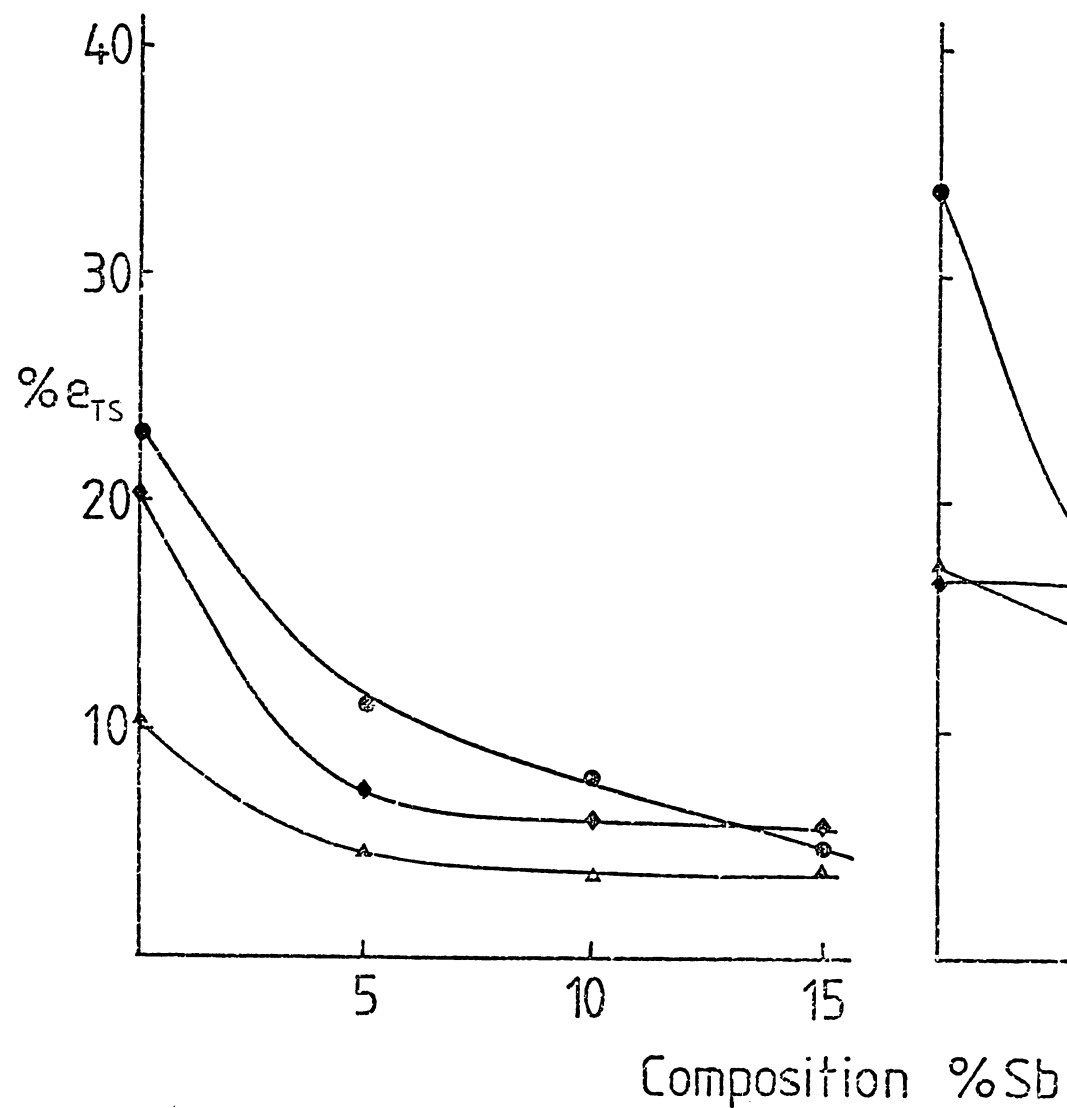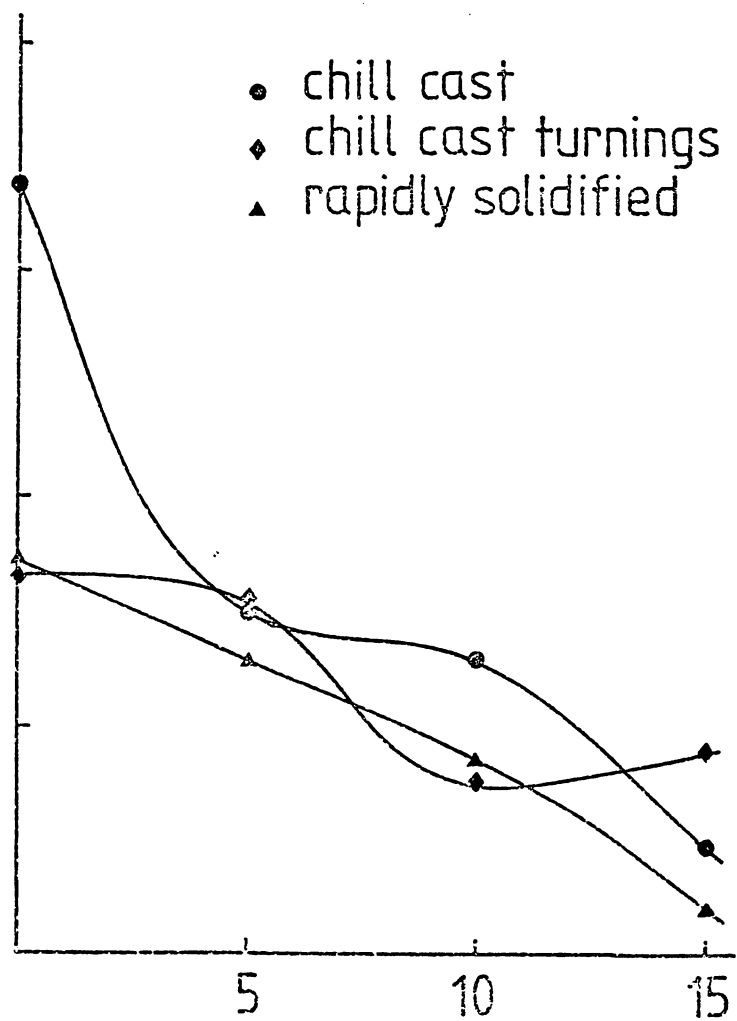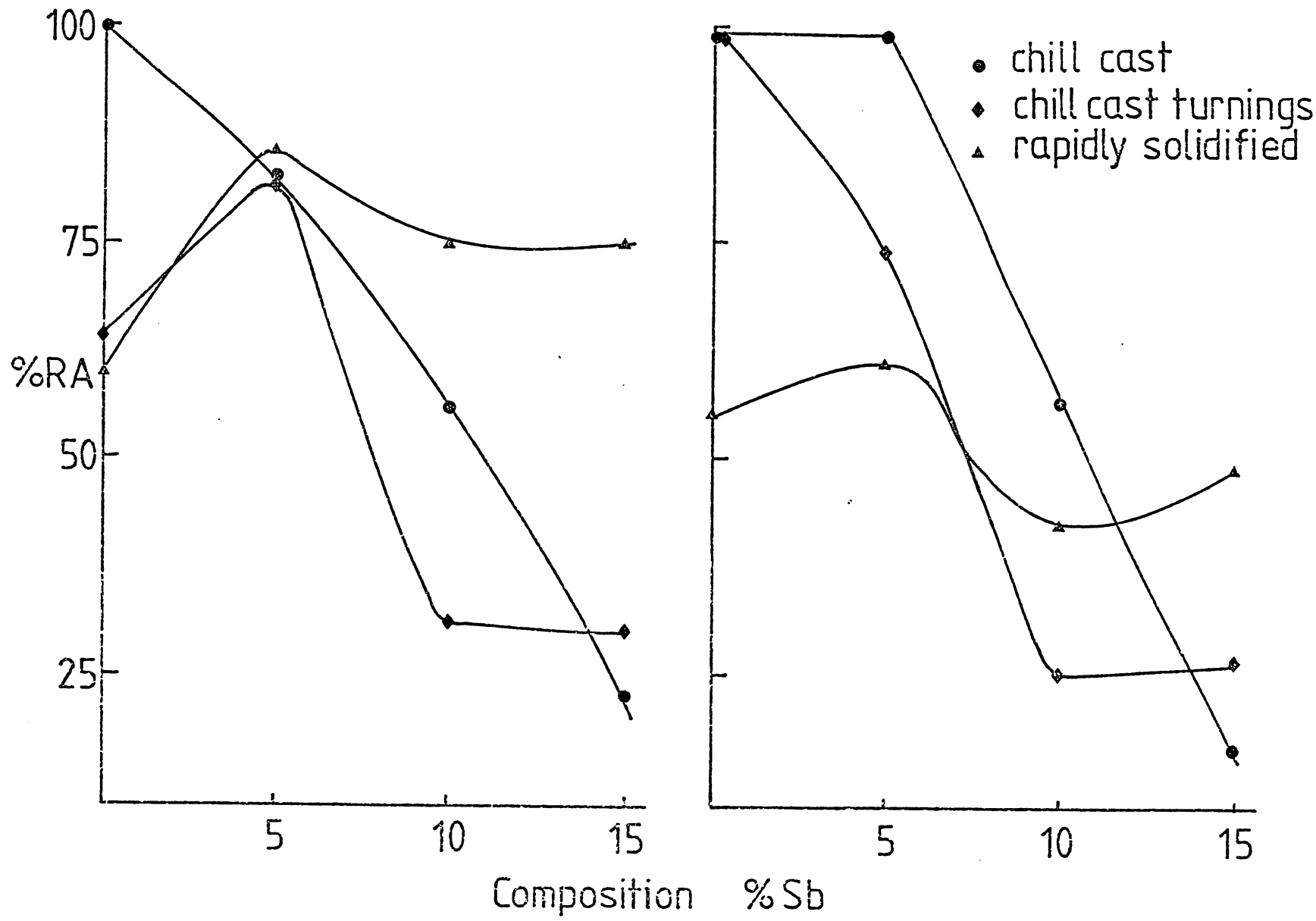
Figure 6.8

Values of Tensile Strength, TS, Percentage Elongation to Maximum Load, $\%\rho_{TS}$, and Percentage Reduction of Area at Failure, %RA, at Intermediate Ageing times for Chill Cast (CC) and Rapidly Solidified (RS) Rods.

Alloy(%Sb)		0		5		10		15
State		CC	RS	CC	RS	CC	RS	CC	TS

Ageing time (s)	Property	CC	RS	CC	RS	CC	RS	CC	TS
0	TS	36.7	35.9	64.4	62.9	79.8	84.3	87.3	116.3
	$\%\rho_{TS}$	23.0	10.5	11.0	4.5	8.0	3.7	5.0	4.1
	%RA	/	60	82	86	56	75	23	75
900	TS	23.0	29.9	56.4	70.1	81.3	84.8	89.8	108.8
	$\%\rho_{TS}$	22.0	13.5	15	12.3	10	5.4	7.2	3.4
	%RA	/	62	94	74	63	70	29	58
2700	TS	28.2	36.4	60.1	66.9	88.3	91.8	96.3	114.8
	$\%\rho_{TS}$	19.2	15.7	14.0	14.9	11.4	10.5	5.2	5.7
	%RA	/	72	96	70	75	58	24	58
9×10^3	TS	21.0	36.9	51.9	65.1	80.6	87.8	79.6	109.8
	$\%\rho_{TS}$	26.0	16.2	14.0	12.6	11.5	8.4	5.9	3.8
	%RA	/	59	95	65	54	67	21	54
9×10^4	TS	19	34.9	52.9	79.6	76.1	85.3	76.8	117.8
	$\%\rho_{TS}$	34.0	17.4	15.0	12.8	13.0	8.5	4.6	2.0
	%RA	/	55	99	66	56	42	17	49

as-extruded condition are very similar for both the CT and CC materials. In the aged condition a significant loss of ductility is seen for all the alloys with little reduction in tensile strength, even for the pure tin.

For the rods produced from rapidly solidified material the trends in ductility in the as-extruded condition are completely reversed. As the antimony content is increased so the ductility and tensile strengths are increased. It is also worth noting the concavity of the curve for the 15%Sb alloy after the point of maximum loading. Comparing these curves with the chill cast and compressed turnings results it can be seen that the RS pure Sn is much less ductile but has a similar tensile strength. The 5%Sb alloys all show approximately the same behaviour, the RS 10%Sb alloy is more ductile than both CC and CT alloys but has the same tensile strength while the RS 15%Sb is more-ductile and has a much higher strength than the other two types of rod. The effect of ageing on all the rapidly solidified alloys is to lower the ductility except for the pure tin which stays approximately the same. The tensile strength also stays the same except for the Sn5%Sb alloy in which there is a marked increase. The aged 15%Sb curves all showed a small sharp drop in load after maximum loading and thereafter a smooth decrease.

Figure 6.7 shows graphical summaries of the behaviour of the materials in tensile testing, by way of plotting T.S., $\%e_{TS}$ and %RA against antimony content for the as-extruded and aged conditions. The results for the ageing times for less than 9×10^4s are shown in figure 6.8 for the rapidly solidified and chill cast materials.

6.4. Compression Testing

6.4.1. Technique.

Using a cage and table-top Instron Tensile Testing machine (fig.6.9) the resistance to homogeneous deformation in compression, of tin and tin-antimony alloys was studied.

Figure 6.9   The Compression Rig.

Figure 6.10   Compression Specimens after Various Strains showing the
                small amount of Barreling obtained during the Tests.

$\dot{e}_i = 0.09s^{-1}$ $\dfrac{d_o}{h_o} = 0.667$

% e   0   11   54   74
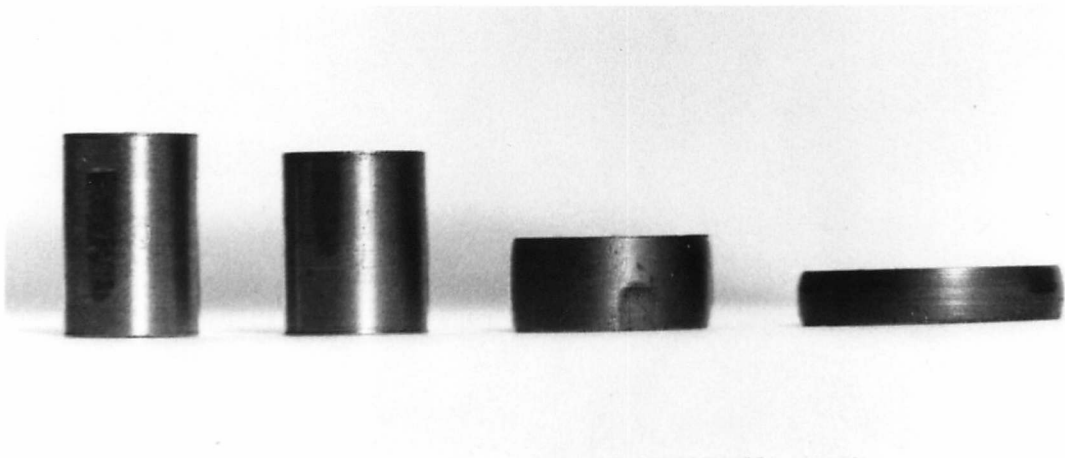
Cylindrical compression test specimens, 6mm in diameter and 6, 7.5 and

12mm in height were machined from the 6.5mm diameter as-extruded rods.

Tests were initially performed using a cross head speed of 50mm min^{-1}.

As there were four different height cylinders being compressed this gave

initial strain rates of $6.9x10^{-2}$, $9.2x10^{-2}$, $1.1x10^{-1}$ and $1.4x10^{-1}s^{-1}$ for

the 12, 9, 7.5 and 6mm specimens respectively.

A series of tests was performed to see how strain rate sensitive the

materials were in compression. It was found that for a change of strain

rate of two orders of magnitude the yield point changed by a factor of

six. However the difference in initial strain rates is only a factor of

two and so it was assumed that the resultant compression curves from

different height specimens could be compared. Throughout the tests the tool

faces were kept liberally lubricated with Vaseline.

6.4.2. Compression Results.

Figure 6.10 is a photograph showing the progression of a compression

test using a specimen with an initial height, h, of 9mm. As the initial

diameter, d_o, is 6mm then (d_o/h_o) is 0.667. In this series it can be

seen there is very little barreling even after 74% deformation. Figures 6.11

show the stress-reduction of height curves for specimens with a (d_o/h_o) of 0.8.

As with the tensile tests, increasing the antimony content increases the

stress required to deform the material. In all cases except the 5%Sb alloy the

rapidly solidified material had a higher yield point than the compressed

turnings which in turn were stronger than the chill cast rods. However in

5%Sb alloy the turnings and rapidly solidified material have similar yield

points with the chill cast material being weaker.

The yield points were measured as the point where the compression stress-

reduction of height curve deviates from a linear relationship. Stress

measurements were also taken from the curves after a 25% reduction of height.

a) Chill Cast (CC) b) Chill Cast Turnings (CT) c) Rapidly Solidified (RS)

Figure 6.11

Compression Test Curves for Alloys in the As-extruded condition.
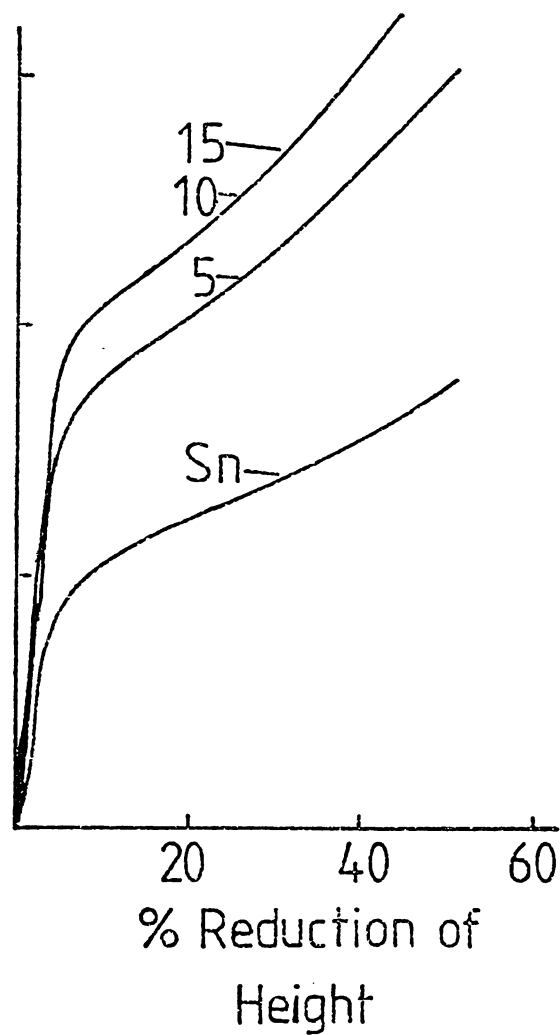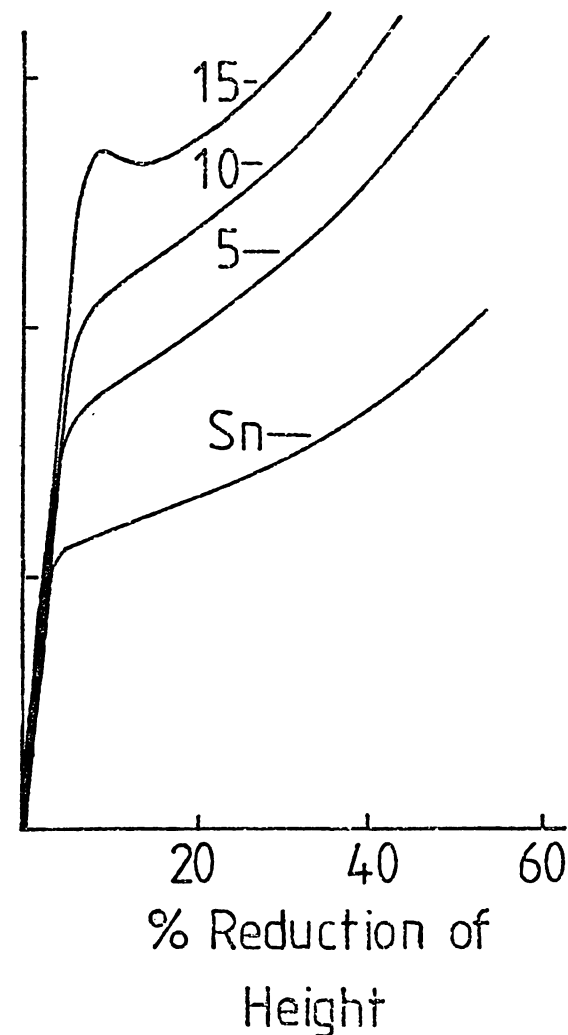
Adapting the method of Cook and Larke (1941) who studied the effect of specimen heights on the compression stress for copper and copper alloys, plots were made of compression stress against the ratio d_o/h_o (Figure 6.12). Extrapolating these plots back to $(d_o/h_o) = 0$ gave values of the compression stress which, it is postulated by Cook and Larke, are free from end effects (Figure 6.13). Most of the tests performed on the 12mm specimens were not used as they tended to become unstable and sideways shear occurred (Cottrell p.431, 1975).

Figure 6.14 shows a graphical representation of figure 13 with a plot of stress against antimony content, and illustrates clearly that at 25% strain only the 15%Sb rapidly solidified alloy has a higher strength than the specimens of either chill cast or compacted turnings. All the other alloys have similar strengths whatever the production route (cf. Tensile strengths, Fig.6.6).

The appearance of a yield drop in the rapidly solidified 15%Sb alloy can be seen in figure 6.11. A series of tests was carried out on specimens of rapidly solidified 15%Sb rod with a (d_o/h_o) of 0.667 to try to obtain some more information so that the cause of this phenomenon might be found.

Figure 6.15 shows a series of tests performed by an Instron machine in which the load was applied until the yield point was reached, then the load was removed then reapplied immediately. This procedure was carried out several times. As can be seen from the curves the yield drop was present in each case. Figure 6.16 shows a second series of tests on the rapidly solidified 15%Sb alloy in which the initial strain rate of the test is reduced. Only with a strain rate of $9.25 \times 10^{-2} s^{-1}$ is the yield drop present, at the lower strain rates no such drop occurs.

6.5. Stress-Rupture Testing.

6.5.1. Introduction and Method.

The stress-rupture test is really a simplified form of creep test in which the applied load is always big enough to cause failure of the specimen

Figure 6.12

Plots of Stress (σ) against do/ho ratios in Compression Tests for all the Alloys.

At Yield Point   At 25% Strain
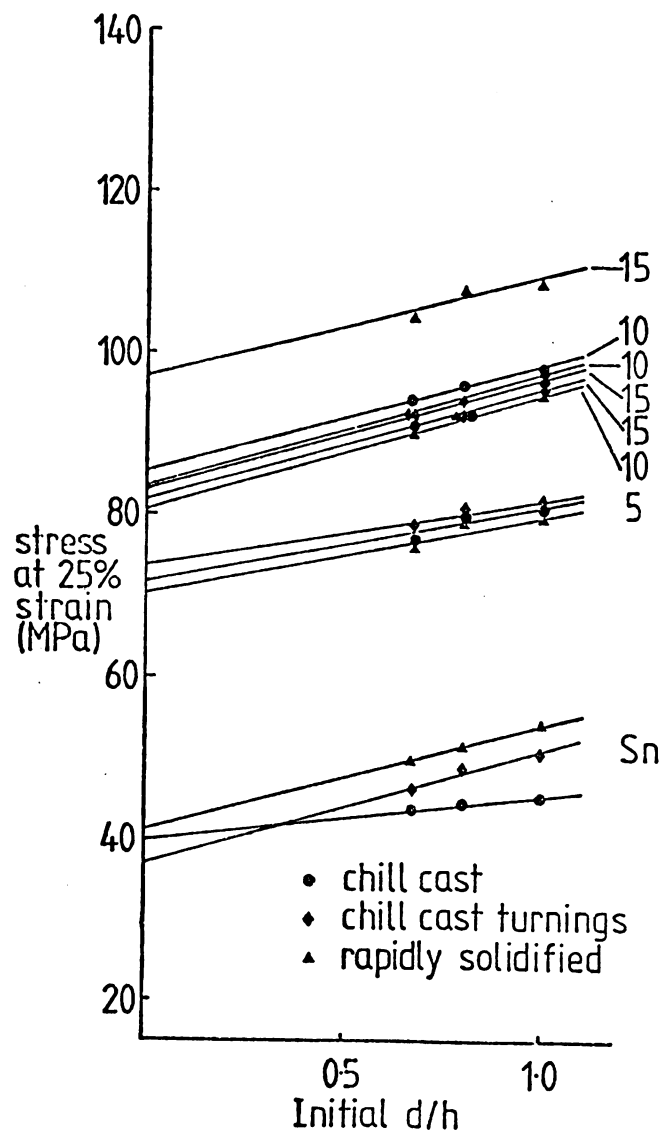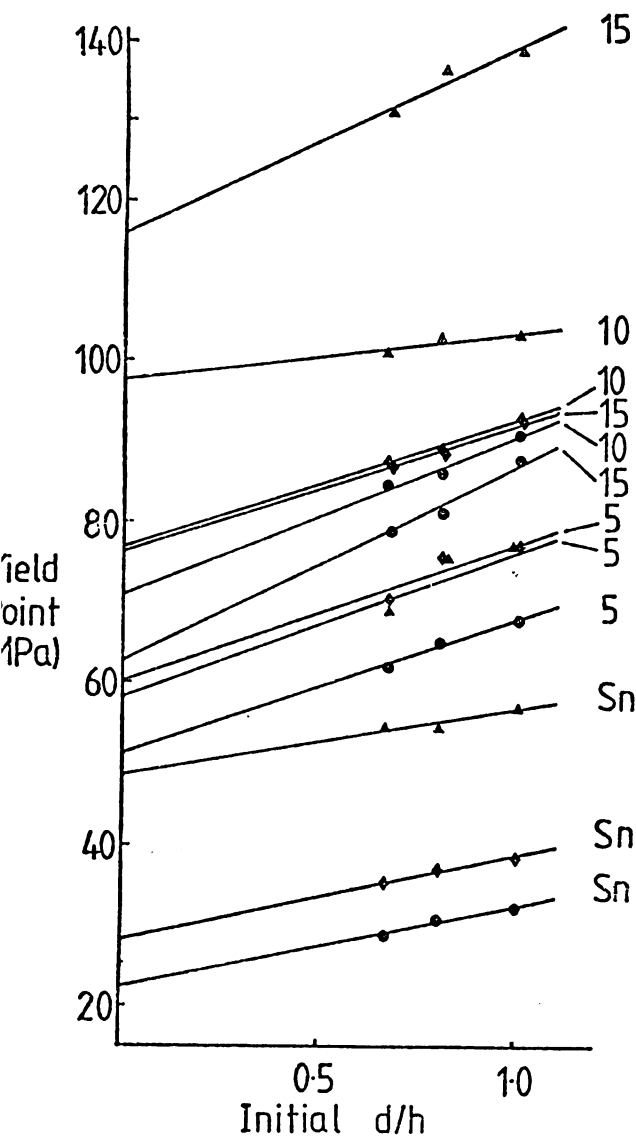
Figure 6.13

Values of $d_o/h_o = 0$ for Yield Stress (σ_y) and Stress at 25% Strain (σ_{25}) in Compression for Sn-Sb alloys in the as-extruded condition.

Crosshead speed 50mm min^{-1}

All tests at room temperature ($\sim$300K)

Stresses in MPa

Alloy (%Sb)		Chill Cast	Chill Cast Turnings	Rapidly Solidified Ribbon
Sn	σ_y	24	28	49
	σ_{25}	40	37	41
5	σ_y	51	60	58
	σ_{25}	72	74	70
10	σ_y	71	77	98
	σ_{25}	86	83	79
15	σ_y	62	77	117
	σ_{25}	82	83	97

Figure 6.14

Plots of σ_y and σ_{25} in Compression against Composition (%Sb) for SnSb
Alloys in the As-Extruded condition.

a) σ_y v. %Sb
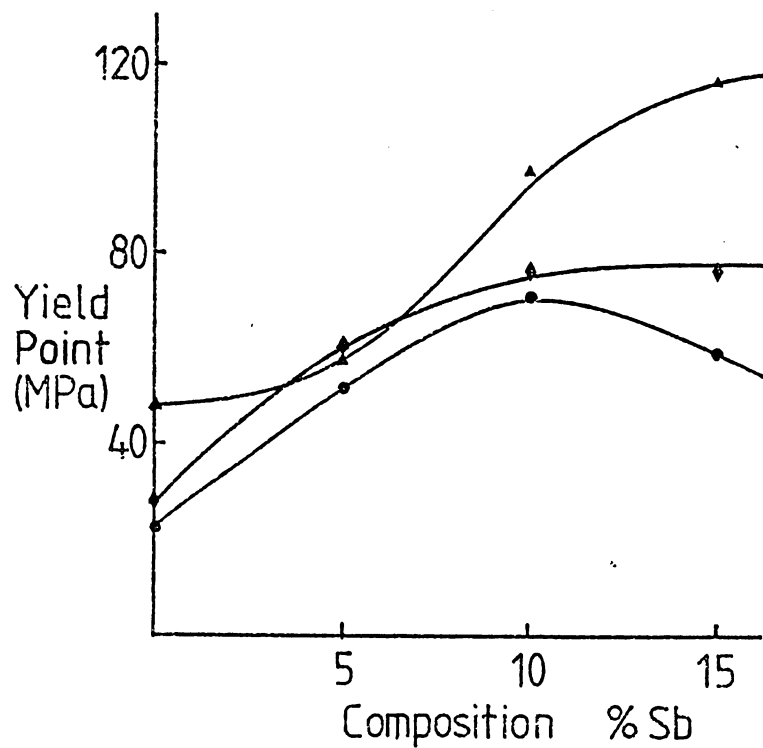
b) σ_{25} v. %Sb
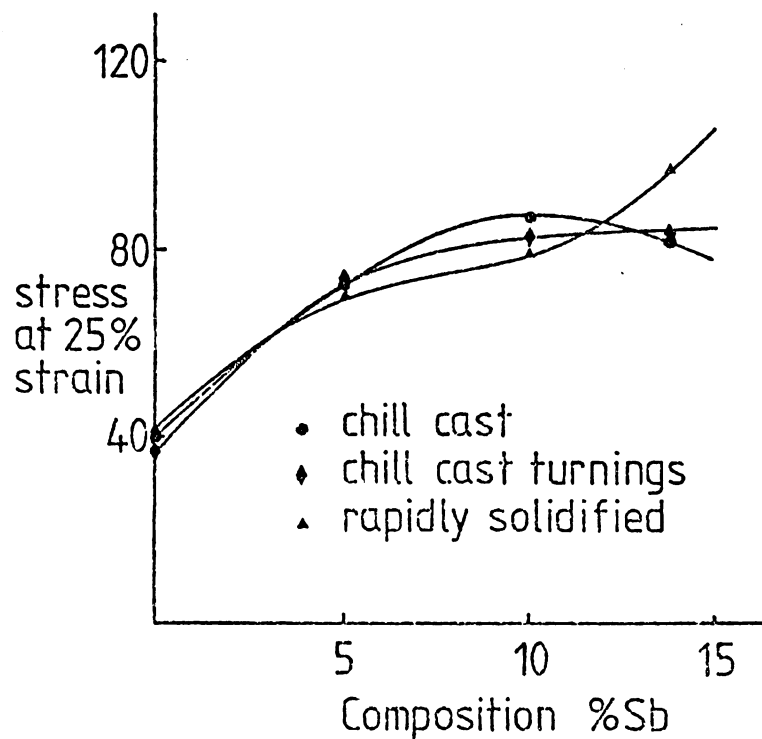
Figure 6.15

Compression Curves from RS.15 Alloy showing the Yield Drop Phenomenon after loading, unloading and immediate reloading.
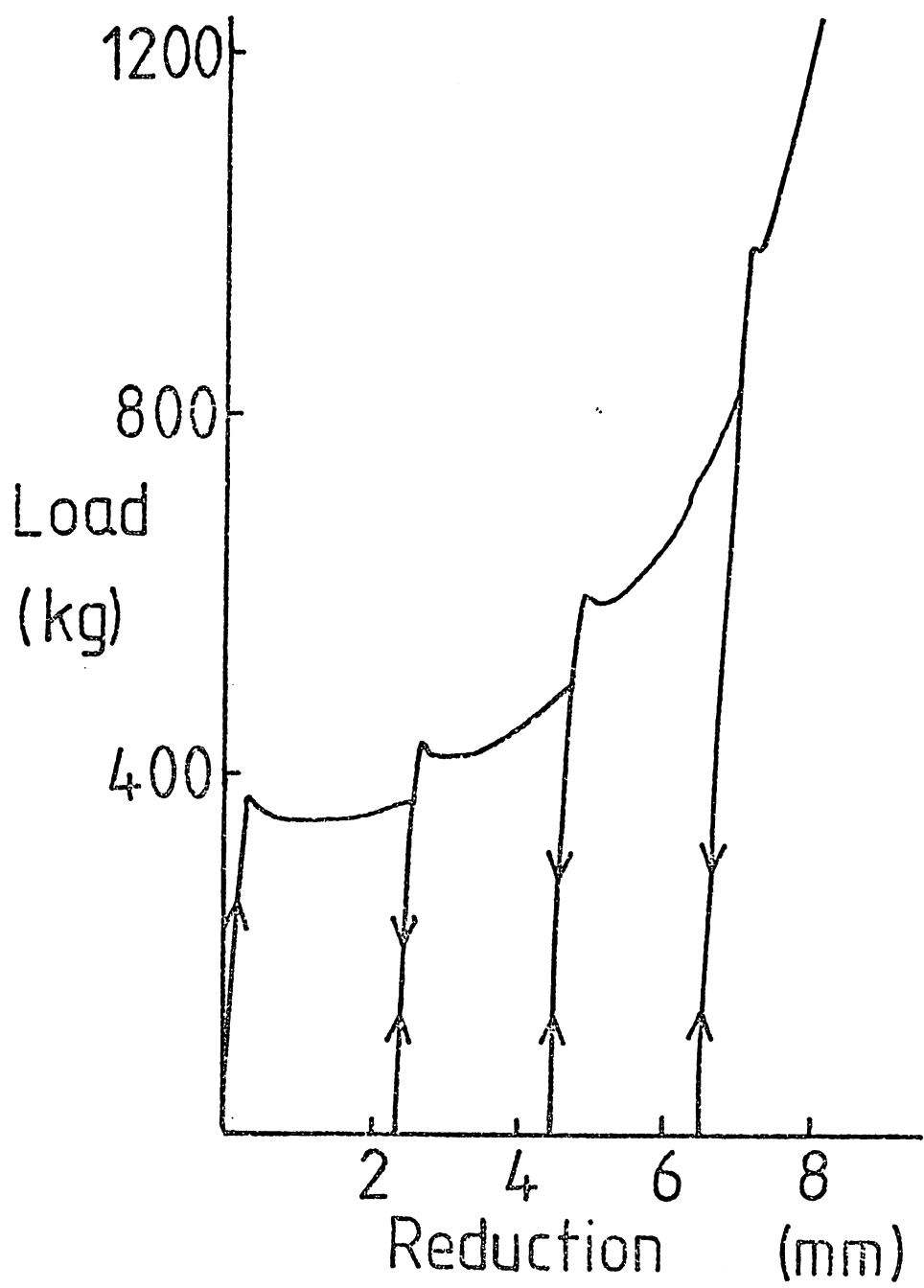
Figure 6.16 Compression Curves for RS15 Alloy Showing the Dependence of the Yield Drop Phenomenon on Strain Rate. (Values in parentheses are Crosshead Speeds)
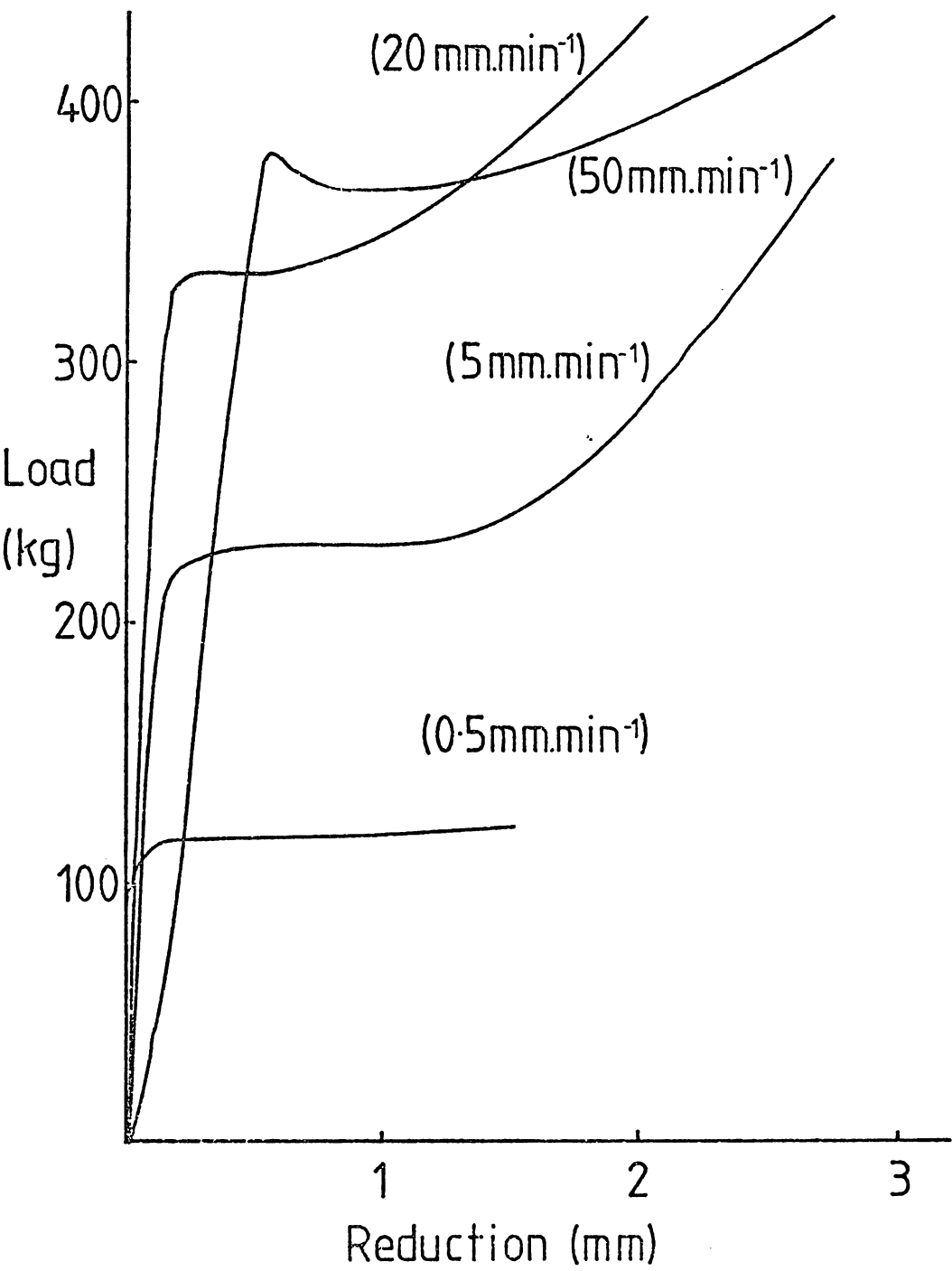
after about 4×10^6 s.   As the applied stress is higher than in creep tests

the strain rate is also higher.   As the accurate measurement of elongation

is not performed in stress-rupture testing, the equipment required is very simple.

In the present work the apparatus used can be seen in figure 6.17.

The tests were performed on Hounsfield Number 11 tensile test specimens at

room temperature (0.55 - 0.60 Tm depending on alloy) on the chill cast and

rapidly solidified material in the as-extruded state only.   Initial stresses

ranged from 28.3 to 4.5MPa to give tests lasting 9min. to several thousand hours.

$(0.5 \times 10^3$ to 10^7 s).

6.5.2. Stress-Rupture Results.

Figure 6.18 shows plots of initial stress against rupture time for all the

alloys tested.   From these plots table 6.19 was constructed to give a comparison

of these curves.   From these two figures it can be seen that at all stresses

the rapidly solidified pure tin is far superior to the chill cast pure tin.

At long times (greater than 1000hrs.) the rapidly solidified material can

withstand twice the stresses that the chill cast tin can take.

The results for the alloys are slightly more complicated.   At high loads

the chill cast materials appear to perform much better, but at stresses which

give a rupture life of greater than 100hrs. the rapidly solidified alloys are

superior in performance although the improvements are not very much Extrapolated

and interpolated results for 2000 hrs. give increases of 25, 26 and 6% for the

5, 10 and 15%Sb alloys respectively.   The rapidly solidified alloys also

gave much greater elongations to failure.   The rapidly solidified 5%Sb, for

example, stressed at 8.9MPa failed with an elongation of 250%.

The other major result can be seen by comparing the rupture strengths

of the alloys with the pure tin.   It appears that adding antimony to the

rapidly solidified tin actually decreases the creep resistance of the alloy.

Not until the addition of 15%Sb are the creep properties better in the rapidly

solidified alloy than in the pure metal.

Figure 6.17

Diagram of Stress-Rupture Apparatus

a) Pure Tin

b) Sn5%Sb

• chill cast
▲ rapidly solidified
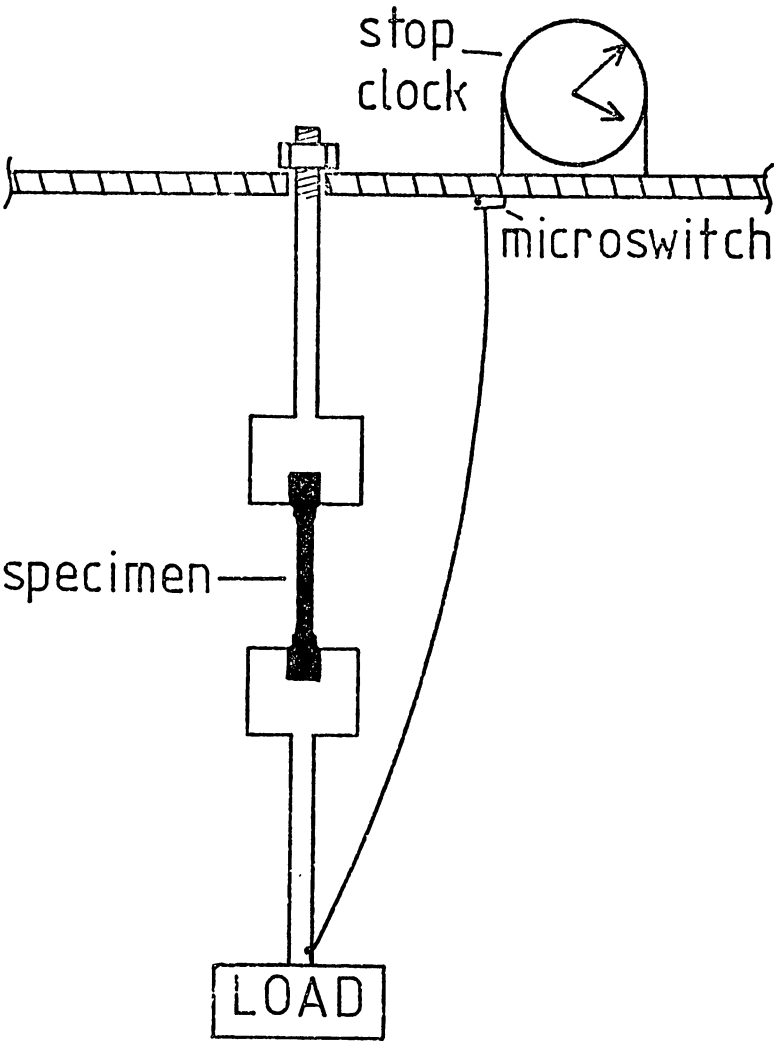
c) Sn10%Sb

d) Sn15%Sb

Figure 6.18   Stress-Rupture Curves for Chill Cast and Rapidly Solidifed Alloys in the As-extruded condition.
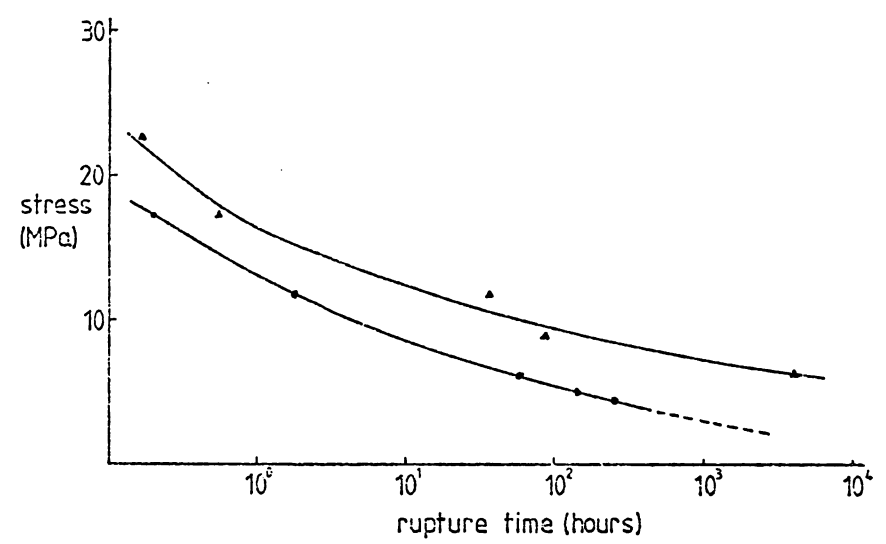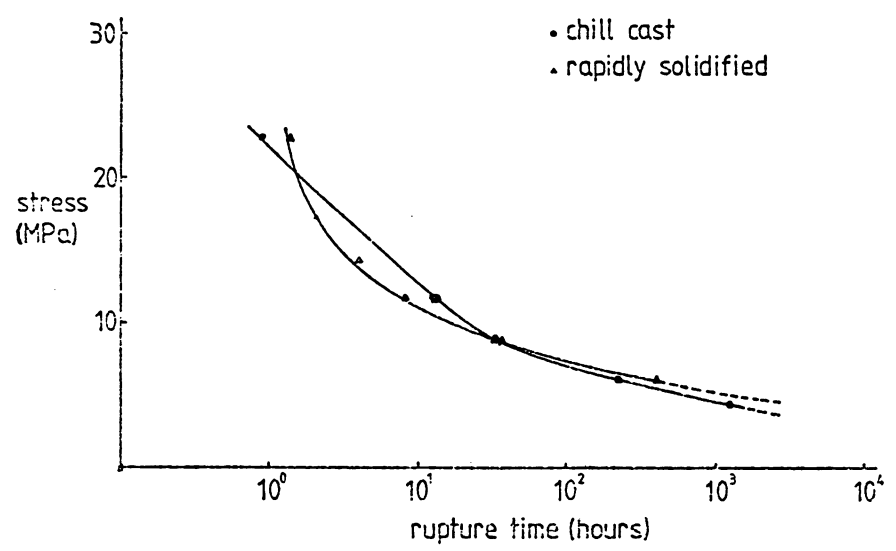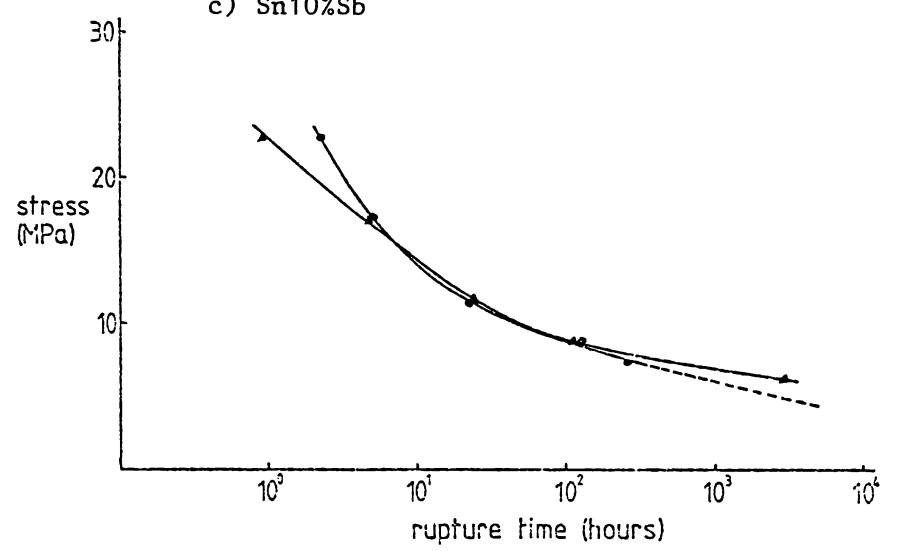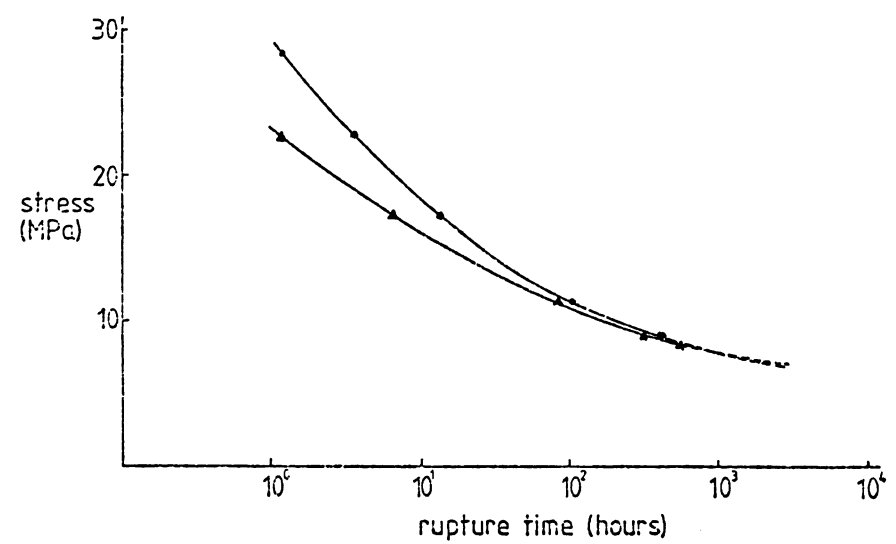
Figure 6.19

Stress to Rupture Results for Rapidly Solidified SnSb alloys and Chill Cast SnSb alloys.   Extruded at 40:1 and machined to Hounsfield 11 specimens.   All tests at Room temperature.

Alloy	Initial σ(M.Pa)		Rupture	%e / hr.	
	Rap.Solid.	Chill Cast	time (hrs)	RS	CC
Pure Sn.	10.5	6.3	50	0.55	4.0
	9.5	5.5	100	0.20	1.45
	7.0	3.1*	1000	0.012	0.064
	6.5	2.4*	2000	0.007	0.027
Sn5%Sb	8.5	8.5	50	2.2	4.0
	7.5	7.25	100	1.3	1.75
	5.6*	4.5	1000	0.3	0.12
	5.0*	4.0*	2000	0.17	0.064
Sn10%Sb	9.75	9.75	50	2.2	2.2
	8.8	8.7	100	1.2	1.4
	7.2	6.0*	1000	0.32	0.46
	6.7	5.3*	2000	0.21	0.35
Sn15%Sb	12.4	13.1	50	2.7	1.5
	11.0	11.5	100	1.3	0.55
	7.7*	7.46*	1000	0.13	0.12
	6.8*	6.5*	2000	0.062	0.066

* Extrapolated values

6.6. The "Ice box" Test.

Pure tin undergoes an allotropic transformation from β to α at 286K (13°C). The high temperature form, β, or white tin, has a body centred tetragonal structure (Space Group I $\frac{422}{amd}$) with a c/a ratio of 0.546 and a density of 7.28 x $10^3 kgm^{-3}$.

The low temperature form, α, or grey tin, has a diamond cubic structure (Space Group F d3m) with a lattice parameter of 6.491Å and a density of 5.77 x 10^3 Kgm^{-3}. The transformation, β→α which is suppressed by very small amounts of impurities, especially Sb, is therefore accompanied by a volume increase of some 26%. This large volume change cannot be accommodated by the material by elastic or plastic strain and the result is that the metal disintegrates.

60mm lengths of all the alloys tested in this work were subjected to an ageing treatment at 253K (-20°C). Figure 6.20 shows a photograph of the rapidly solidified pure tin. It can be seen that the rod has fallen to pieces by fracturing along the length of the rod although there is some circumferential cracking. This failure occurred after only a few days of the treatment, all the other rods stayed intact even after treatments of up to one year.

Figure 6.20

Consolidated and Extruded Rapidly Solidified

Ribbon after Ageing at 253K (-20°C)

10 mm
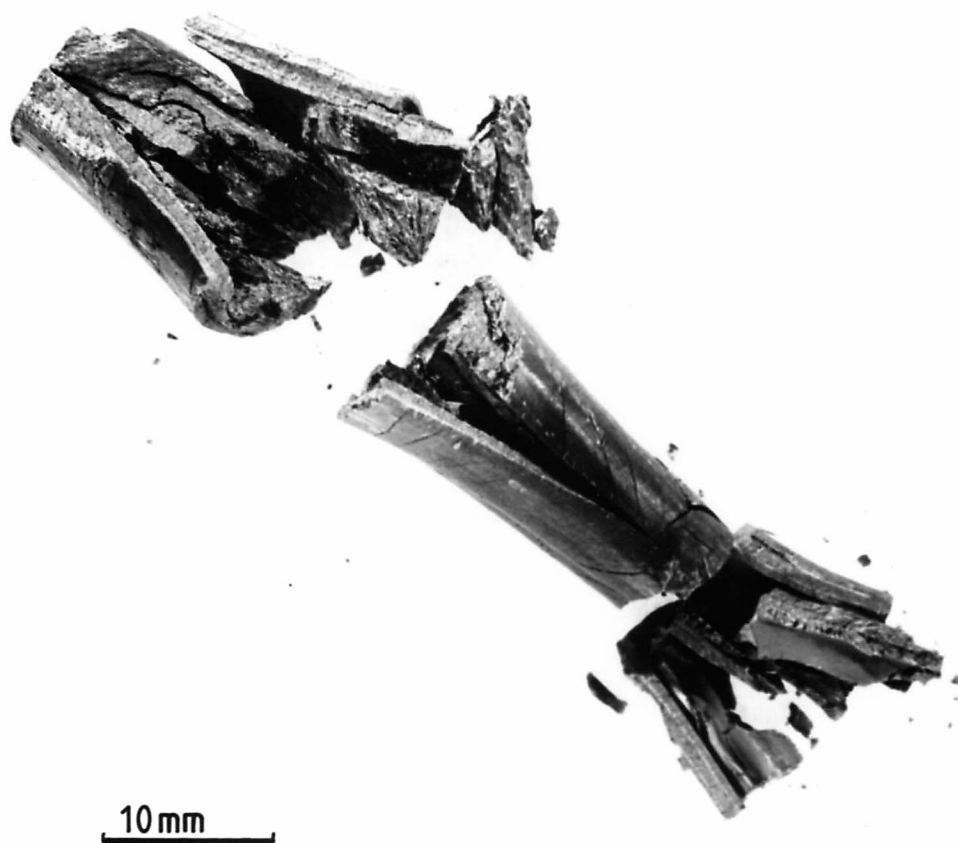
6.7. Discussion.

6.7.1. Introduction

The strength of a material may be increased in the following ways:

   i)   reduction of grain size.

   ii) introduction of dislocations (e.g. by working)

   iii) addition of alloying elements to produce either solid

       solution strengthening or precipitation hardening.

   iv) introduction of a dispersion of a stable phase.

In general tin-based alloys have a coarse grain size and, as room

temperature is $\sim$0.6 of their absolute melting temperature, they tend to be

weak.   Any process which refines the microstructure must therefore be

advantageous.

The majority of work to investigate the mechanical properties of tin

alloys was carried out in the 1930's on chill cast material. Brinell

hardness tests and tensile tests were performed by Hanson and Pell-Walpole

(1938) on as-cast and rolled tin-antimony alloys. At the low values of

hardness obtained these may be compared with the Vickers hardness results

of the present work (Greenfield and Forrester, 1947). The tensile tests

may not be compared as the strain rates used were very much lower than

those in the present work. Their conclusion that working actually softened

the alloys followed the ideas of Hill (1928) and Hargreaves and Hill (1928, 1929),

who proposed that work softening occurs in two phase alloys when both

constituents have the property of spontaneous annealing at room temperature.

It is difficult to see how this condition can be applied to the intermetallic

SbSn particles in the tin-antimony system.

Hanson and Pell-Walpole also report little improvement of mechanical

properties with additions of more than 9%Sb due to the appearance of primary

cuboids of SbSn, and that antimony additions generally refine the grain size.

They suggest that annealing worked alloys has no other effect than to increase the grain size and during the process restore the material to its original chill cast strength.

Such a statement appears to contradict the Hall-Petch relationship

$$\sigma_y = \sigma_i + kd^{-\frac{1}{2}}$$ (1.1)

but in a previous work, Hanson and Sandford (1936), in which they acknowledge the usefulness of such "quick" tests to measure the hardness and tensile properties, state that such results must be treated with care, for at normal (room) temperatures tin is well within the range where pronounced creep must be anticipated.

Creep resistance may be improved by

    i)   reducing diffusivity by alloying

   ii) increasing the grain size

  iii) changing the grain shape

   iv) opposing grain boundary sliding

    v) opposing recrystallisation

   vi) decreasing the effectiveness of grain boundaries as

        sinks and sources for vacancies.

Obviously then, any grain refinements, whether produced by working, additions of antimony or by rapid solidification must reduce the creep resistance.

An estimation of the stresses involved in the hardness tests performed in the present work can be made using the equation:

$$H_V = \frac{1.854P}{L^2}$$ (Dieter, 1961) (6.1)

where H_V: Vickers Hardness

P : Load in kg.

L : Indentation diagonal in mm.

From this it can be seen that the approximate pressure at the indenter/
metal interface can be calculated by using the relationship:

$$\sigma = \frac{Hv}{1.854} \times g \qquad (6.2)$$

This gives a minimum σ of 30MPa for the softest material,chill cast pure
tin,and 136MPa for the hardest material,chill cast Sn15%Sb.   At such high
stresses the creep resistance of all the rapidly solidified antimony-bearing
alloys is much lower than the chill cast alloys of the same composition.   The
rapidly solidified pure tin by contrast shows much greater creep resistance
than the chill cast equivalent and thus performs better in the hardness test.
The stresses involved are of the same order of magnitude as the tensile strengths
of the materials tested (fig. 6.8) and so creep in all the alloys would be
extreme.   Such considerations led to the choice of the extremely rapid strain
rate during both tensile testing and compression testing in the present work.

A rough calculation using the Ashby deformation parameters of $\ln(\sigma/\mu)$
and T/T_m, where μ is the shear modulus and T and T_m are on the absolute scale,
indicates that even at such strain rates the tensile and compression tests
in the present work are operating in the creep regime.   Increasing the strain
rate to a very high value might push the tests into the "hot" working regime,
but only by low temperature testing would the values be comparable with normal
tensile test conditions.

Despite the obvious problem of interpretation of the tests performed
on these materials it is possible to recognise several factors influencing
their behaviour under such stringent conditions.

    i)   the oxide effect

    ii)   the solid solution effect

    iii) the grain size effect

    iv) the effect of SbSn phase

6.7.2. The Effects of Four Recognisable Microstructural Features on the

Mechanical Properties of Tin-Antimony alloys.

6.7.2. (1) The Oxide Effect.

A dispersion of oxide is introduced into all the consolidated materials by the oxide film formed at normal temperatures on the turnings and ribbon. The oxide is a mixture of Tin (II) and Tin (IV) oxides (Eastwood and Robins, 1964) and has a volume fraction of about 0.12% and a thickness of about 15nm (Section 5.2.).

The oxide has little effect, if any, on the tensile strengths of the alloys, as can be seen comparing the values of T.S. for the rods of chill cast and consolidated turnings, where the only microstructural difference is the presence of oxide in the latter. This is because in the as-extruded state the oxides are only at the grain boundaries not interspersed in the grains as with precipitates. Dislocations are therefore free to move as easily in the grains of materials with an oxide dispersion as those without, they are only hindered by impingement on grain boundaries. Due to its presence at grain boundaries the oxide does influence the growth of grains by grain boundary pinning. Thus on heat treatment the growth of grains is limited to a size dictated by the dispersion of the oxide particles. This is clearly seen in the ageing behaviour of the pure tin specimens where the chill cast grains grow very rapidly on annealing at 473K and so the tensile strength drops as opposed to the stable behaviour of the consolidated rods. Although it is not possible to link the tensile strength directly with grain size there is a definite influence. The ductility should also be reduced by the presence of oxide for as the volume fraction of a hard second phase increases so the ductility drops. This can only be seen directly in the pure tin rods where there is no influence from intermetallic compounds.

Comparison of the compressive yield strengths for the extruded pure tin rods shows that the rapidly solidified material is twice as strong as either of the other two materials in the as-extruded condition. This could be due to three factors:

i)   the grain size

ii) the presence of defects

iii) the oxide dispersion

The grain size of the rapidly solidified material does not appear too much smaller than the chill cast turnings or the chill cast material (fig.5.1) and so it is unlikely that this has a major contribution to the yield point difference.

The density of defects has not been measured in any of the materials although Wood and Honeycombe (1974) suggest that rapid solidification introduces a large number of defects into the solid metal.

The oxide dispersion in the consolidated rapidly solidified material may be finer than in the chill cast material as the turnings were thicker than the ribbon.

There is no evidence to suggest which of the latter two explanations is correct and it is reasonable to assume that there is a contribution from both.

As the oxide pins the grain boundaries during ageing it will also hinder grain boundary movement during creep. This is demonstrated by the better creep properties exhibited by the rapidly solidified material when compared with the chill cast rods of pure tin. This was also observed by Eastwood and Robins (ITRI, 1967) whose values for the creep life of pure tin rods produced from tin powder are very similar to those obtained in rapidly solidified pure tin in the present work (fig.6.21).

The oxide particles may also serve to decrease the effectiveness of the grain boundaries as sources and sinks for vacancies thereby improving

Figure 6.21

The Creep Life of Consolidated, Extruded Pure Tin.

Rupture Time (hrs)	Jolly	σi (MPa) Eastwood and Robins
50	10.5	9.7
100	9.5	9.0
1000	7.0	6.9

Jolly: Consolidated Rapidly Solidified Ribbon

Eastwood and Robins: Consolidated Conventionally Produced Powders.

Figure 6.22

Points showing %RA against %SbSn
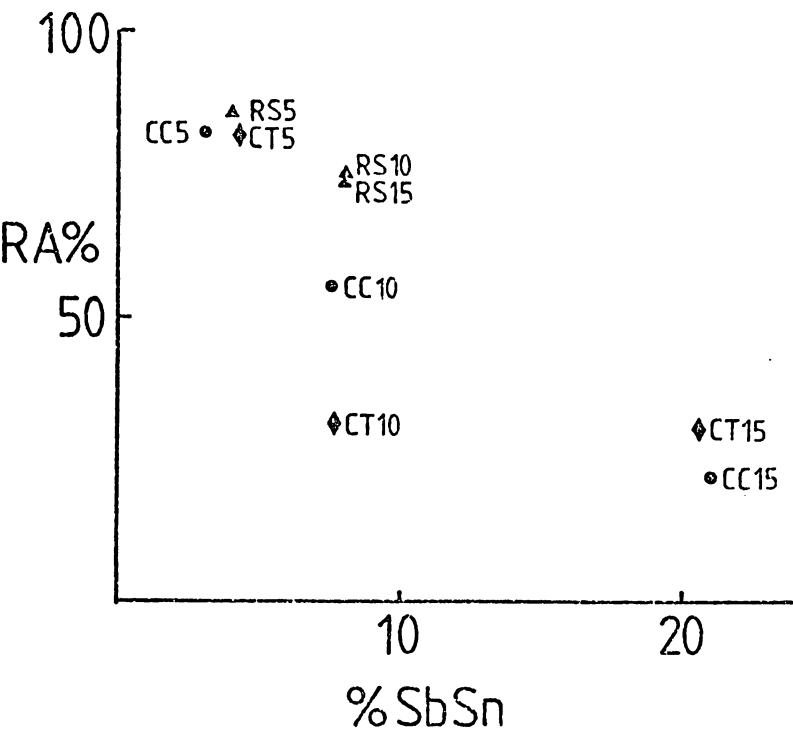
the creep resistance.

The oxide dispersion does not then directly strengthen the extruded consolidated rods as it is only present at grain boundaries but it contributes to the stability of the alloys by pinning grain boundaries on ageing thus suppressing grain growth.

6.7.2.(2) The Solid Solution Effect.

Antimony has a limit of solid solubility in tin of about 4% at room temperature equilibrium. This is increased to about 8% in chill casting and between 15 and 20% on melt spinning. Alloys with excess antimony in solid solution are reasonably stable at room temperature but working and heating the alloys have the effect of stimulating precipitation of the SbSn intermetallic.

The antimony in solid solution in tin has two main effects, it increases the strength and produces a refinement of the grain size.

The increase in strength produced by the solute antimony is shown by the increase in tensile strength and the compressive yield point between the pure tin and 5%Sb alloys. There is the presence of a small volume fraction of SbSn precipitate (approximately 3%) but prior to extrusion this would have been in solid solution, and the marked increase in extrusion pressure required by the Sn5%Sb alloy compared with the pure tin is an effect of the solid solution strengthening not precipitation hardening. Additions of 10 and 15%Sb do not increase the amount of solid solution in the chill cast extruded alloys as all the excess antimony is precipitated on extrusion.

The refinement of grain size and the solid solution strengthening imparted by the addition of antimony oppose each other during creep testing.

The increase in creep resistance imparted by solid solution strengthening is clearly shown by the difference between the creep lines for chill cast pure tin and Sn5%Sb. However the benefits gained from grain boundary pinning of oxide in the rapidly solidified material are not shown in the RS5%Sb due to further grain refinement and increase in grain boundaries not pinned by oxide particles. There is thus a drop in the creep resistance of the RS5%Sb alloy coincidently to that of CC5%Sb alloy.

6.7.2.(3) The Grain Size Effect.

It has already been stated that finer grains improve the strength of a metal except where creep resistance is required. An attempt has been made to cut down the creep effects in the tensile and compression tests by increasing the strain rate, but this was not possible in the hardness tests.

The effect of grain size on the strength of extruded pure tin has been shown already. Grain growth is also shown in both the chill cast 5 and 10%SbCC alloys.

There is also a contribution to the increase in strength as the antimony content increases, which is directly due to the refination of grain size (Hanson and Pell-Walpole, 1938).

Small grain sizes should also give higher ductility. This effect is competing with the pinning of grain boundaries by oxide particles in the consolidated materials.

6.7.2.(4) The effect of the SbSn phase

The SbSn exists in two different forms in these alloys

      i)   Primary SbSn from the solidification reaction.

     ii)   A precipitate of SbSn from a solid state reaction.

The former particles exist as cuboids and range from 10 to 60μm in size. They are produced as primary SbSn from the melt reaction L $\rightarrow$ L+SbSn.

These appear in the CT and CC alloys containing 10 and 15%Sb.

The latter particles are less than 5μm in size and appear in all the alloys. They arise due to the solid state reaction β'→β+SbSn where β is a solid solution of antimony in tin, and β' is a supersaturated solid solution of antimony in tin. The SbSn phase has a hardness ten times that of pure tin and is very brittle. Not surprisingly then as the volume fraction of the intermetallic rises the ductility of the alloy drops (fig.6.22). There is not a direct relationship as it also depends on the distribution and size of the particles. The difference in values between the CT and CC 10%Sb alloy is almost certainly due to the segregation of the SbSn in the extruded rod of chill cast material (figs.5.17a,b), which has left the centre of the rod almost entirely free of large SbSn particles. Whereas the higher ductility of the RS10%Sb alloy compared with its corresponding CC and CT alloys is due to the much smaller size of the particles of SbSn, as well as a contribution due to grain size refinement.

The larger particles of SbSn do not have a beneficial effect on the tensile strength, in fact they are probably detrimental. The difference in strength between the RS15 and the CC and CT15%Sb alloys is almost certainly due to a large volume fraction of very small SbSn precipitates of the order of size similar to those seen in section 3.4. The compressive yield point is again not benefited by the large particles of SbSn but is by the very small particles.

The small particles of SbSn created by the fracture of primary SbSn during extrusion have as much influence over the mechanical properties as those of a similar size but created by the precipition and growth from solid solution during extrusion.

The ageing treatments have two effects on the SbSn

      i) thermal fracture

     ii) particle coarsening.

Thermal fracture can be seen in the larger particles of SbSn after
all ageing treatments at 473K (figure 5.24). This could be a result of
the release of internal stresses originally created by the extrusion process.

The coarsening of the smaller SbSn particles is not observed optically
but can easily be seen in the SEM pictures of the fracture surfaces of
tensile specimens (figure 6.23).

The first effect seems not to affect the tensile strength of either
the CC or CT alloys, thus suggesting that the large particles play no part
in strengthening the alloys. There is a slight decrease in ductility but
this could be due to the coarsening of the smaller particles and general
grain growth.

6.7.3. The Yield Point Behaviour of Rapidly Solidified 15%Sb Alloy.

The appearance of a yield drop in the RS15%Sb alloy is the result of
the presence of a high number of foreign atoms, in solution, capable of
pinning dislocations. In chapter 5 it was seen that the volume fraction of
intermetallic SbSn particles was only 8% rather than the 29% predicted by
theory. Allowing for the fact that some particles will be submicroscopic
there must still be a considerable proportion of Sb in solid solution or
as particles small enough to pin dislocations.

In metals where yield points are usually observed, immediate reloading,
after removal of the load, produces a tensile curve with no yield drop present.
The yield drop only reappears after a low temperature anneal during which
the pinning atoms segregate once again to the dislocations. In the RS15%Sb
alloy this was not the case as the yield drop did not disappear on immediate
reloading. However as room temperature is $\sim0.6T_m$ for these alloys, auto-
annealing was probably occurring throughout the test.

The yield behaviour of these alloys is highly strain-rate dependant
(see fig.6.4). As the strain-rate is lowered the upper yield point τ_u
decreases and so must the dislocation density, ρ_u.

Figure 6.23

Scanning Electron Micrographs Showing Coarsening of SbSn Particles on Ageing at 473K for 9×10^4 s in Consolidated RS10 and RS15 alloys.

RS10
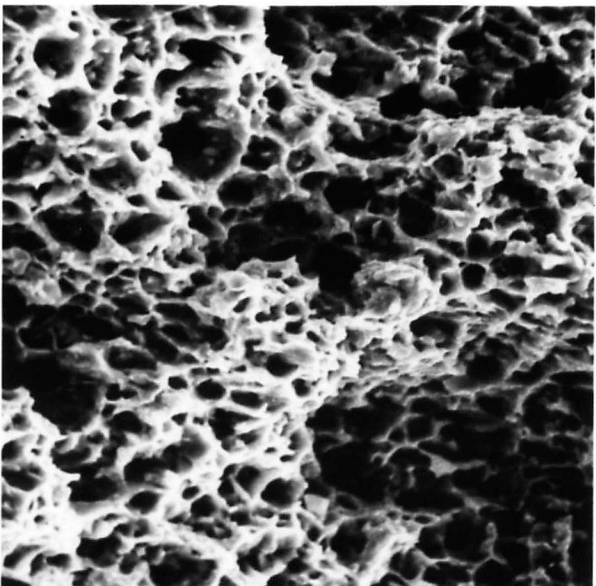
a) As-extruded
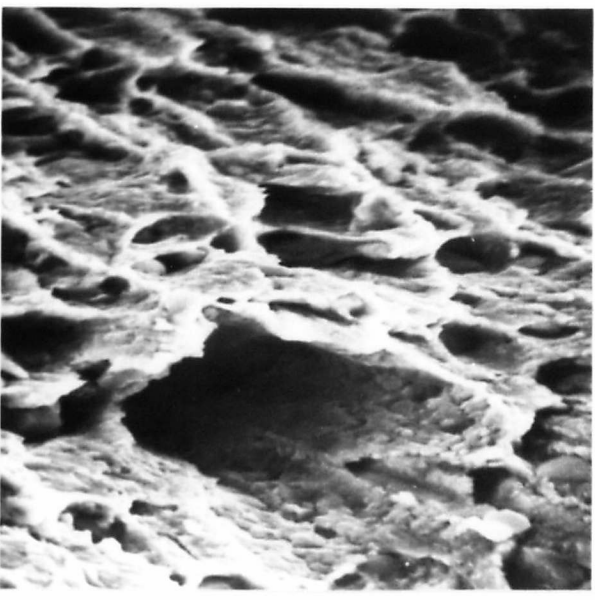
b) Aged

RS15
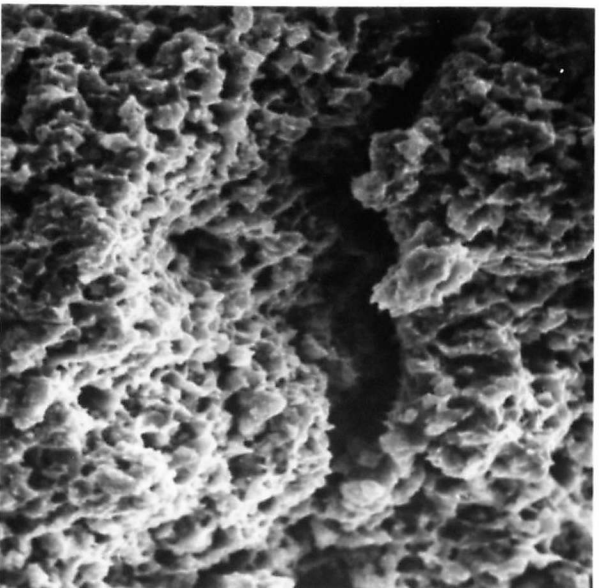
c) As-extruded
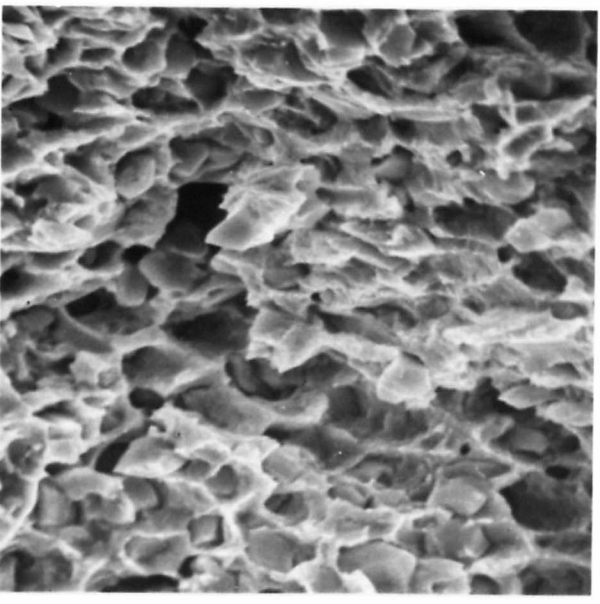
d) Aged

20μm

It has been shown that

$$\frac{\tau_u}{\tau_L} = \left(\frac{\rho_L}{\rho_u}\right)^{1/m} \qquad \text{(Honeycombe, 1968, p.153)} \quad 6.3$$

where τ_L and ρ_L are the lower yield point and dislocation density respectively. The values of m and ρ_u are the criteria for the magnitude of the yield drop. As m is a material parameter ρ_u becomes the controlling factor in the present case and so as the dislocation density drops so does the ratio τ_u/τ_L.

There may also be an effect of machine softness which could change the extent of the yield drop at different strain-rates, however no work has been performed to assess this in the present work.

6.8. Conclusions.

1) Although hardness testing is quick and easy to perform, under the conditions of the present work the creep rate of the alloys tested was so high that the results obtained have to be assessed with this in mind.

2) The act of consolidation introduces a dispersion of oxide into the alloys which, although does not directly increase the strengths of such materials, inhibits grain growth above a certain size on annealing.

3) The tensile strength and yield point in compression of the rapidly solidified materials are both increased by the addition of antimony.

4) The tensile strength and yield point in compression of the rods of chill cast and chill cast turnings are increased by the addition of up to 10% antimony, further additions do not increase the strength due to the formation of primary SbSn in the melt.

5) The increases in tensile strength and yield point in compression in all cases, are due to a complex pattern of contributions from solid solution strengthening, grain refinement and precipitation hardening.

6) The ductility of the alloys is affected by the complex interaction between grain size, grain boundary pinning by oxide and/or SbSn precipitates,

dislocation pinning by SbSn precipitates and grain boundaries, and the volume fraction of large, brittle, primary SbSn particles.

7) Decreases in ductility on ageing are as a result of grain growth, precipitation of SbSn or particle coarsening, depending on the alloy and its history.

8) Extrusion of the rapidly solidified 10 and 15% antimony alloys may not cause precipitations of all the excess antimony in the supersaturated solid solutions caused by the rapid solidification. Thus the possibility of age hardening these materials arises to produce increase strength and better creep resistance.

9) Rapidly solidified tin had improved strength and creep resistance compared with the control materials. Such improvements were similar to those found by other workers using consolidated tin powders.

10) Of the alloys only the rapidly solidified 15%Sb had significantly better mechanical properties than the comparable rods of chill cast or chill cast turnings. Tensile strength, compressive yield strength, ductility and creep strength were all improved. The alloy was also extremely stable to ageing and was the only alloy to show the yield drop phenomenon.

Chapter 7.   GENERAL CONCLUSIONS

Throughout the thesis discussion has been included in the relevant

chapter or section.   This last chapter serves to summarise the main conclusions

of the thesis.

Chapter 1 attempts to show the effects of rapid solidification on the

microstructure of a material and to indicate the many methods for producing

rapidly solidified material.   It concludes that for the present work the

process of melt spinning would be the most convenient to use.   The choice

of the tin-antimony system as a model is influenced by the fact that it is

the basis of White metal bearing alloys, which would benefit from improved

mechanical properties.

Chapter 2 provides data for the melt spinning of the tin-antimony

system, providing new information for the analysis of the melt spinning of

crystalline alloys.   Observations show that when the multijet technique

is used to produce wide ribbon the process can be extremely inefficient as

a result of interactions between adjacent streams.   An analysis is made to

understand the changes which occur in the shape of the melt puddle and to

predict when instabilities arise.   It was found that the critical Reynold's

Number for gas boundary layer instabilities to arise, increases with increasing

substrate velocity.

Chapter 3 shows that between 15 and 20%Sb can be retained in tin in a

supersaturated solid solution by rapid solidification.   This compares with

4%Sb at equilibrium and 8%Sb by chill casting.   The grain sizes in the

rapidly solidified material are of the order of the thickness of the ribbon.

The grain size may also be influenced by instabilities in the melt puddle

region.   The grain sizes obtained were much smaller than those achieved

by conventional casting methods.   The metallography of these alloys proved

extremely difficult due to problems with finding a suitable etchant.   It

was shown that the decomposition of the supersaturated solid solution of

Sn10%Sb took place over a matter of months at room temperature.   The

precipitates formed were semicoherent SbSn needles which were approximately

1500Å by 7.5Å at a maximum.   This is consistent with work done on the same

alloy by Kaczorowski and Matyja (1979) however further T.E.M. work is

necessary on the other alloys of the system.

Chapter 4 describes the differences between static and dynamic

consolidation.   Extrusion is chosen as a convenient method for consolidation.

Comparisons made with two control materials indicate that rapid solidification

imparts some increase in flow stress to all the alloys studied.

Chapter 5 describes each alloy by its microstructural features

observed by optical and scanning electron, microscopy.   Extrusion is

shown to refine the grain size and initiate the precipitation of excess

antimony retained in solid solution above the equilibrium value. Assumptions

were made that some of these precipitates were too small to be observed by

the methods used, and that an oxide dispersion was also present in the

consolidated material due to the formation of an oxide layer on the

chill cast turnings and the rapidly solidified ribbon.   The precipitated

particles have a different morphology from the primary SbSn formed from

the melt and the rapid solidification process reduces the amount of segregation

and the SbSn particle size.   Further work is necessary to determine the

nature of the oxide particles and the grain sizes of the alloys.   This could

possibly involve the use of extraction replicas for transmission electron

microscopy.

In chapter 6 it is suggested that the hardness results obtained are

not very reliable as a result of the high creep rates experienced at room

temperature.   It is shown that additions of antimony increase the tensile

strength and compressive yield strength and reduce the ductility of the

rapidly solidified materials as it does with the chill cast alloys.   The

presence of the oxide dispersion decreases   ductility by grain boundary

pinning which also stabilises the effect of ageing on the consolidated alloys,

as little or no grain growth occurs.   The finer particles of SbSn improves

the ductility of the 10 and 15%Sb alloys when rapidly solidified.   The

presence of a yield drop in the rapidly solidified 15%Sb alloy is attributed

to the high proportion of solute atoms and submicroscopic particles of SbSn

capable of pinning dislocations.   This could be further assessed by T.E.M.

work.   Further work should also be performed on the rapidly solidified

materials to ascertain whether they could be superplastic.   From the results

of the present work it can be concluded that tin-antimony alloys are readily

melt spun and easily consolidated.   The benefits of so doing are not great

in the lower antimony alloys but with an addition of 15%Sb the tensile

strength, compressive strength and ductility are all improved.   Further work

is required to assess the performance under fatigue conditions as this is of

great importance in the bearing field.   Other work should be carried out on

the feasibility of bonding the rapidly solidified material to backing

materials by such methods as roll bonding.   Some work of this nature has

been carried out by the International Tin Research Institute but not using

rapidly solidified material.   The possibilities of using rapidly solidified

flake rather than ribbon should also be assessed and the effect of texturing

that arises from consolidation needs to be studied.

It is clear that other tin alloys are also easily rapidly solidified

(see Appendix) and a thorough investigation should be made as to which alloys

will best benefit from the process.   Such work is currently being performed

at the International Tin Research Institute.

Appendix

MELT SPINNING OF OTHER TIN ALLOY SYSTEMS

1. Introduction

During the course of the present work various other alloys than those in the tin-antimony system were melt spun, primarily to assess the ease with which ribbon could be produced. In some cases however a minimal amount of research was performed to study the microstructure or mechanical properties.

2. The Melt Spinning of an Sn10%Sb2%Cu Alloy.

This alloy is very similar to the composition of plain bearing alloys and was spun with the aim of comparing the properties with the simple Sn-Sb system.

Using an ejection pressure of 35kPa and a wheel speed of $12ms^{-1}$ enough ribbon was made to produce a compact for extrusion. X-ray work showed that the ribbon was not a complete solid solution but that there was a second phase present, probably the Cu_6Sn_5 intermetallic.

Extrusion was performed in the same manner as that used in chapter 4 and a pressure of 560MPa was required for an extrusion ratio of 40:1. Tensile specimens were made from the rods and tested at the same strain rate as those in the SnSb system. A tensile strength of 118MPa, with a failure ductility (RA%) of 47%, was obtained in the as-extruded state. The rapidly solidified 15%Sb alloy gave a tensile strength of 117MPa but had a ductility of 75%. It would appear from this that small additions of Cu increases the strength of the SnSb system but even on rapidly solidifying the ductility is poor.

3. The Melt Spinning of Aluminium-Tin Alloys.

Aluminium-tin alloys are often now used in high speed small bearings instead of the traditional white metal. The system has a eutectic at 0.6%Al but the alloys used have either 6 or 20%Sn in them. Both alloys were melt spun and preliminary X-ray work showed that the alloys were both two phased as is the case when conventionally cast. No other work was performed.

4. The melt spinning of two Copper-Tin alloys.

Two alloys of the Cu-Sn system were spun using an ejection pressure of 104kPa and a wheel speed of $12ms^{-1}$. The compositions were Sn10 and Sn20%Cu which at equilibrium contain significant proportions of the η phase (Cu_6Sn_5) which is very brittle. The resultant ribbon was very ductile and is being used by the Electrical, Magnetic and Superconductivity group in the University of Cambridge,Department of Metallurgy and Materials Science for tests involving superconductivity.

5. The Melt Spinning of Eutectic Tin-Bismuth.

Eutectic tin-bismuth has the composition 43%Sn-57%Bi, and is extremely brittle due to the presence of the Bi rich solid solution phase. It is often used to make solder preforms in the electronics industry and requires an enormous amount of hot working to produce thin tape 10mm wide.

The alloy was spun using a 9 holed nozzle to produce tape some 13mm wide with a gas pressure of 104kPa and a wheel speed of $12ms^{-1}$. X-ray analysis showed the ribbon was two phased but simple tensile tests indicated that the rapidly solidified material was extremely ductile. This increase in ductility must be assumed to be due to a decrease in lamellar spacing in the absence of any other evidence. Samples of this ribbon are at present undergoing tests with the Israeli Atomic Energy Authority.

References

The following abbreviations have been used for the 6 major conferences on Rapid Solidification.

RQ1   Proc. of International Conference on Metastable Metallic Alloys. Brela, Yugoslavia, 1970. Fizika, IUPAP. 2(2) (1970).

RQ2   Proc. of 2nd International Conference on Rapidly Quenched Metals. M.I.T. Cambridge U.S.A. 1975. Eds. Grant, N.J. and Giessen, B.C. Mat. Sci. Eng. 23 (1976) 81-324. or M.I.T. Press. Massachusetts, U.S.A. (1976).

RQ3   Proc. of 3rd International Conference on Rapidly Quenched Metals. Brighton, U.K. 1978. Ed. Cantor B.,Metals Society, London, (1978).

RQ4   Proc. of 4th International Conference on Rapidly Quenched Metals. Sendai, Japan, 1981. Eds. Masumoto, T. and Suzuki, K., Japan Institute of Metals, Sendai, Japan (1982).

Reston 1   Proc. of Conference on Rapid Solidification Processing: Principles and Technologies. Reston, Virginia, USA, 1977. Eds. Mehrabian, R., Kear, B.H. and Cohen, M. Claitors Pub. Div., Baton Rouge, La., USA. (1978).

Reston 2   Proc. of 2nd Conference on Rapid Solidification Processing: Principles and Technologies. Reston, Virginia, USA, 1980. Eds. Mehrabian, R., Kear, B.H. and Cohen, M. Claitors Pub. Div., Baton Rouge, La., USA.(1980).

Anantharaman, T.R. and Suryanarayana, C., J. Mat. Sci. 6 (1971) 1111

Anthony, T.R. and Cline, H.E., J. Appl. Phys. 49 (1978) 829

Anthony T.R. and Cline H.E., J. Appl. Phys. 50 (1979) 245.(G.E. Tech.
        Information Series. Rpt. 78CRD067 (1978))

Aptekar, I.L. and Kemenetskaya, D.S., Fiz. Metal. i Metalloved 14 (1962) 358

Babbitt,I., U.S. Pat. No. 1252 (1839)

Babić, E., Girt, E., Krsnik, R. and Leontić, B., J. Phys. E. Sci. Int. 3 (1970a)
        1014

Babić, E., Girt, E., Krsnik, R., Leontić, B. and Zorić, I., RQ1 (1970b) 1

Baker, J.C. and Cahn, J.W., Acta. Met. 17 (1969) 575

Baker, J.C. and Cahn, J.W., "Solidification". Am. Soc. for Metals Seminar.
        A.S.M., Metals Park, Ohio, USA, (1971) 23

Baralis, G., J. Cryst. Growth 3-4, (1968) 627

Batchelor, G.K., "Fluid Dynamics", 1st Ed. C.U.P., Cambridge, U.K.(1967)

Bedell, J.R., U.S. Pat. No. 3,862,658 Jan (1975)

Bierlein, J.C., Sci. Amer. 233(1) (1975) 50

Booth, A.R. and Charles, J.A., Nature (Lond) 212 (1966) 750

Borisov, V.T., Sov. Phys. "Doklady" 7 (1960) 50

Boswell, P.G. and Chadwick, G.A., Scr. Met. 11 (1977) 459

Brown, A.R.G., Jepson, K.S. and Heavens, J., J.I.M. 93 (1965) 542

Burden, M.H. and Jones, H., J.I.M., 98 (1970) 249

Cahn, R.W., Krishnanand, K.D., Laridsani, M., Greenholz, M. and Hill, R.,
        RQ2 (1970) 83

Carbonara, R.S., Raman, R.V., and Clauer, A.H., RQ4 (I) (1982)

Chadwick, G.A., J.I.M. 91 (1963) 169

Charter, S.J.B., Mooney, D.R., Cheese, R., and Cantor, B., J. Mat. Sci. 15
        (1980) 2658

Chen, H.S. and Miller, C.E., Rev. Sci. Inst. 41 (1970) 1237

Christian, J.W., "Theory of Transformations in Metals and Alloys" pt.1.
2nd Ed. p.182, Pergamon Press, Oxford, U.K. (1975)

Cline, C.F., RQ4 (I) (1982) 129

Cline, H.E. and Anthony, T.R., G.E. Tech. Inf.Series Rpt. No. 78CRD066 (1978)

Cook, M. and Larke, E.C., J.I.M. 71 (1945) 371

Cottrell, A.H. "An Introduction to Metallurgy" Edward Arnold, London (1975)

Coulson, J.M. and Richardson, J.F. "Chemical Engineering" Pt.1. 2nd Ed. Ch.9.
Pergamon Press, Oxford, U.K. (1964)

Cullity, B.D., "Elements of X-ray Diffraction", Addison Wesley Pub. Co. Inc.,
Reading, Mass. U.S.A. (1959)

Dantzig, J.A. and Davis, S.H., Mat. Sci. Eng., 32(3) (1978) 199

Davies, G. and Garland, J., Intl. Met. Rev. 196 (20) (1975) 83

Davies, H.A. and Hull, J.B., Scripta Met. 6. (1972) 241

Davies, H.A. and Hull, J.B., J. Mat. Sci. 9 (1974) 707

Davies, H.A. and Lewis, B.G., Met. Trans. A. 7A(2) (1976) 310

Davies, H.A., Lewis, B.G. and Donald, I.W., Reston 1 (1978) 78

Dayton, R.W., Metals and Alloys 9 (1938) 323

Dieter, G.E., "Mechanical Metallurgy", 2nd Ed. McGraw-Hill, New York (1961)

Duwez, P., Prog. Sol. State Chem. 3(8) (1966) 377

Duwez, P., Trans. A.S.M. 60 (1967) 607

Duwez, P., Willens, R.H. and Klement, W. Jr., J. App. Phys. 31 (1960a) 1136

Duwez, P., Willens, R.H. and Klement, W. Jr., J. App. Phys. 31 (1960b) 1137

Duwez, P. and Willens, R.H., Trans. AIME. 227 (1963) 362

Eastwood, B.J. and Robins, D.A. Pow. Met. 7 (1964) 99

Falkenhagen, G. and Hofmann, W., Z. Met. 43 (1952) 69

Giessen, B.C., Z. Met. 59 (1968) 805

Giessen, B.C., "Advances in X-ray Analysis". Vol.12. Eds. Barrett, C.S.,
Mallett, G.R. and Newkirk, J.B. Plenum Press, New York (1969)

Giessen, B.C. and Vitek, J.M., Met. Trans. 3(9) (1972) 2449

Grant, N.J. and Duwez, P., J. Met. 17 (1965) 1167

Greenfield, L.T. and Forrester, P.G.,"Properties of Tin Alloys",

       International Tin Research Institute, Publication No. 155 (1947)

Hall, O.E., Proc. Phys. Soc. (Lond.) 64B (1951) 747

Hanson, D. and Pell-Walpole, W.T., J.I.M. 63 (1938) 87

Hanson, D. and Sandford, E.J., J.I.M. 59 (1936) 159

Harbur, D.R., Anderson, J.W. and Maraman, W.J., Trans. Met. Soc. AIME.

      245 (1969) 1055

Hargreaves, F., J.I.M. 39 (1928) 301

Hargreaves, F. and Hills, R.J., J.I.M. 40 (1928) 41

Hargreaves, F. and Hills, R.J., J.I.M. 41 (1929) 257

Hiller, W., La Metallurgie 100 (1968) 35

Hillman, H. and Hilzinger, H.R., RQ3 1 (1978) 22

Hinesley, C.D. and Morris, J.G., Met. Trans. 1 (1970) 1476

Honeycombe, R.W.K., J. Council for Sci. and Ind. Res. Australia Dec (1946)

Honeycombe, R.W.K.,"Plastic Deformation of Metals", Edward Arnold, London (1968)

Honeycombe, R.W.K., RQ3 1 (1978) 73

Huang, Shyh-Chin, and Fiedler, H.C., Met. Trans. 12A (1981) 1107

Ishihara, J. and Ikuta, I., RQ4 I (1982) 19

Ishii,H., Naka, M. and Masumoto, T., RQ4 I (1982) 35

I.T.R.I., International Tin Research Institute, Yearly Reports from 1962 to

      1968 inc.

Jindal, B.K. and Tiller, W.A., J. Chem.Phys. 49 (1968) 4632

Joly, R.A. and Mehrabian, R., J. Mat. Sci. 9 (1974) 1446

Jones, H., Mat. Sci. Eng. 5 (1969) 1

Jones, H., Rep. Prog. Phys. 36(11) (1973) 1425

Jones, H., Met. Soc. Conf. Proc. on Vacancies. 1976,Brighton, U.K.

      Eds. Smallman, R.E. and Harris, J.E., Met. Soc. London. (1977) 175

Jones, H., Reston 1 (1978) 28

Jones, H. and Burden, M.H., J. Phys. E. Sci. Inst. $\underline{4}$ (1971) 671

Jones, H. and Suryanarayana, C., J. Mat. Sci. $\underline{8}$ (1973) 705

Kaczorowski, M, and Matyja, H., J. Mat. Sci. $\underline{14}$ (1979) 2887

Kamal, M. and Pieri, J.C., J. Mat. Sci. $\underline{15}$ (1980) 525

Kane, R.H., Giessen, B.C. and Grant, N.J., Acta. Met. $\underline{14}$ (1966) 605

Kaneko, H. and Ikeuchi, J., 1st Int. Conf. on Electrodischarge Machining
        Tokyo, Japan E.D.M. Soc. (1965) 23

Kaufmann, A.R. and Muller, W., U.S.E.A.C. Report. N.H.I. 1262 (1964)

Kavesh, S., "Metallic Glasses", A.S.M. Metals Park, Cleveland, Ohio (1978) 36
        Reston 1 (1978) 165

Khera, S.K. and Nayar, P.K., Proc. Symp. on Mat. Sci. Res. in India 1970 $\underline{2}$
        (1971) 345

Kim, M.H. and Jones, H. RQ4 $\underline{I}$ (1982) 85

Kirin, A. and Bonefačić,A.,Scripta Met. $\underline{4}$ (1970) 525

Klement, W. Jr. Can. J. Phys. $\underline{40}$ (1962) 1397

Klement, W. Jr., Willens, R.H. and Duwez, P., Nature $\underline{187}$ (1960) 869

Kumar, R. and Sinha, A.N., Trans. Ind. Met. $\underline{21}$ (1968) 9

Laine, E., Lähteenmäki, I. and Lehtoranta, I., J. Mat. Sci. $\underline{13(1)}$ (1978) 108

Larson, F.R. and Miller, J., Trans. AIME $\underline{74}$ (1952) 765

Lawley, A., Reston 1 (1978) 306

Leontić, B., Lukatela, J., Babić, E. and Ocko, H., RQ3 $\underline{I}$ (1978) 41

Lewis, B.G., Donald, I.W. and Davies, H.A., Proc. Conf. on Solidification and
        Casting of Metals, Sheffield, England 1977. Met. Soc. London (1979) 490

Liard, M., Müller, M., Ackermann, K.P., Delley, B., Agyemann, K., Künzi, H.U.,
        Rudin, H. and Güntherodt, H-J., RQ3 $\underline{II}$ (1978) 29

Liebermann, H.H., RQ3 $\underline{I}$ (1978) 34, G.E. Tech. Inf. Series Rpt. No. 78CRD028 (1978)

Liebermann, H.H., IEEE Trans. Mag. $\underline{Mag15}$ (1979a) 1393, G.E. Tech. Inf. Series Rpt.
        No. 79CRD183 (1979a)

Liebermann, H.H., J. App. Phys. 50(11) (1979b) 6773

Liebermann, H.H. G.E. Tech. Inf. Series Rpt. No. 79CRD254 (1979c).
Mat. Sci. Eng. 43 (1980a) 203

Liebermann, H.H., G.E. Tech. Inf. Series Rpt. No. 80CDR029 (1980b),
Reston 2 (1980b) 393.

Liebermann, H.H., J. Mat. Sci. 15 (1981) 2772

Liebermann, H.H. and Graham, C.D.Jr., I.E.E.E. Trans. Mag. Mag12 (1976)

Lunn, G.H., Nature 291 (1981) 617

Luo, H.L. and Duwez, P., Can. J. Phys. 41 (1963) 758

Maringer, R.E., U.S. Pat. No. 4215084 (1980)

Maringer, R.E. and Mobley, C.E., J. Vac. Sci. Tech. 11(6) (1974) 1067

Maringer, R.E., and Mobley, C.E. RQ3 I (1978) 49

Maringer, R.E., Rudnik, A and Mobley, C.E., U.S. Pat. No. 3838185 (1974)

Masumoto, T., RQ4 I (1982) 5

Masumoto, T., Inoue, A., Hagiwara, M., Ohnaka, I, and Fukusako, T., RQ4 I
(1982) 47

Masur, L.J. and Flemings, M.C., RQ4 II (1982) 1557

Matyja, H., Giessen, B.C. and Grant, N.J., J.I.M. 96 (1968) 30

Midson, S.P., Buckley, R.A. and Jones, H., RQ4 II (1982) 1521

Midson, S.P. and Jones, H., RQ4 II (1982) 1539

Miura, H., Isa, S. and Omuro, K., RQ4 I (1982) 43

Miyazawa, K-I, Choh, T. and Inouye, M., RQ4 I (1982) 75

Miyazawa, K-I. and Szekely, J., Met. Trans. 12A (1981) 1047

Mobley, C.E. and Maringer, R.E., U.S. Pat. No. 3861450 (1975)

Mobley, C.E., Maringer, R.E. and Dillinger, L., Reston (1978) 222

Morris, D.G., Reston 2 (1980) 372

Morris, D.G., RQ4 I (1982) 145

Moss, M., Smith, D.L. and Lefever, R.A., App. Phys. Letters. 5 (1964) 120

Mutsuzaki, K., Suzuki, M. and Kawai, E., J. Jap. Inst. Met. 27 (1963) 424

Nadai, A. and Manjoine, M.J., J. App. Mech. 8 (1941) A77

Narasiman, M.C., U.S. Pat.No.4142571 (1979)

Ohnaka, I. and Fukusako, T., J.Jap. Inst. Met. 42 (1978) 415

Ohnaka, I., Fukusako, T. and Ohmichi, T.,J.Jap. Inst. Met. 45 (1981) 751

Ohnaka, I., Fukusako, T., Ohmichi, T., Masumoto, T., Inoue, I and

       Hagiwara, M. RQ4 I (1982) 31

Olsen, W.T. and Hultgren, R., Trans. A.I.M.E. 188 (1950) 1323

Olsson, R.G. and Turkdogan, E.T., Nature, 211 (1966) 813

Patterson, J.P., PhD. Thesis, University of Cambridge (1979)

Pavuna, D., J. Non-Cryst. Sol. 37 (1980) 133

Pavuna, D., J. Mat. Sci. 16 (1981) 2419

Pavuna, D., RQ4 I (1982) 81

Pavuna, D. and Hainsworth, D., J. Non-Cryst. Sol. 37 (1980) 417

Petch, N.J., J.I.S.I. (Lond) 174 (1953) 25

Pickering, F.B., "The Basis of Quantitative Metallography" Metals and

       Metallurgy Trust for Inst. of Met. Tech. London. Monograph No.1 (1976)

Pietrowsky, P.,Rev. Sci. Instr. 34 (1963) 445

Pond, R.B., U.S. Pat.No.2825108 (1958)

Pond, R.B., U.S. Pat.No.2976590 (1961)

Pond, R.B.Jr. and Madden, R., Trans. A.I.M.E. 245 (1969) 2475

Pond, R.B.Sr. and Winter, J.M.,RQ2 (1976) 87

Predecki, P. Mullendore, A.W. and Grant, N.J., Trans. A.I.M.E. 233 (1965) 1581

Ramachandrarao, P. Garg, P.K., and Anantharaman, T.R., Ind. J. of Tech.

       8 (1970) 263

Ramachandrarao, P., Scott, M.G. and Chadwick, G.A., Phil. Mag. 25 (1972) 961

Rayleigh, Lord, Proc. Roy. Soc. 29 (1879) 71

Raynor, G.V. and Lee, J.A., Acta. Met. 2 (1954) 616

Reti, L., Sci. American 224(2) (1971) 101

Robins, D.A. "Tin" International Tin Research Institute Publication No.582 (1980)

Rollason, E.C. "Metallurgy for Engineers" 4th Ed. Edward Arnold. London (1973)

Ruhl, R.C., Mat. Sci. Eng. 1 (1967) 313

Ruhl, W., Z. Phys. 138 (1954) 136

Sakata, M. and Ishibachi, T.,RQ4 I (1982) 39

Sarin, V.K. and Grant, N.J.,Met. Trans. 3 (1972) 875

Savage, S.J. and Jones, H.,RQ4 I (1982) 159

Savitsky, E.M. Revyakin, A.V., Efimov, Y.V., Glyuzitsku, B.D. and
        Sumarokov, U.N., Dokl. Akad. Nauk SSSR 210 (1973) 405

Shimanuki, S., Yoshino, H. and Inomata, K.,RQ4 I (1982) 15

Shingu, P.H. and Ozaki, R., Met. Trans. 6A (1975) 33

Shohoji, N., Davies, H.A. and Warrington, D.H.,RQ4 I (1982) 69

Srivastava, P.K., Giessen, B.C. and Grant, N.J., Acta Met 16 (1968) 1199

Strange, E.H. and Pim, C.A., U.S. Pat. No. 905758 (1908)

Stewart, O.M., Maringer, R.E., and Mobley, C.E.,U.S. Pat.No. 3812901 (1974)

Suryanarayana, C. and Anantharaman, T.R.,J. Mat. Sci. 5 (1970) 992

Takayama, S., J. Mat. Sci. 11 (1976) 164

Tonejc, A.M., Kirin, A. and Bonefačić, A.,Fizika (Yug) 8 (1976) 87

Thomas, G. and Willens, R.H.,Acta Met. 12 (1964) 191

Thursfield, G. and Jones, H., J. Phys. E. 4 (1971) 675

Underwood, E.E., J.I.M. 88 (1959) 266

Varich, N.I. and Yakunin, A.A.,Russ. Met. No.2 (1968) 148

Vincent, J.H. and Davies, H.A., Proc. Conf. Solid. Tech. in Foundry and
        Casthouse Warwick (1980)

Vincent, J.H., Herbertson, J.G. and Davies, H.A., RQ4 I (1982) 77

Vinci, L.da., Codex Madrid I (c.1495)

Walter, J.L., RQ3 1 (1978) 30

Walter, J.L., G.E. Tech. Inf. Series. Rep. No. 79CRD235 (1979)

Warrington, D.H., Private Communication (1982)

Weber, V.C., Z. Angewandte Math. u. Mech. 11(2) (1931) 136

Willens, R.H. and Buehler, E., Trans. AIME <u>236</u> (1966) 171

Williams, C.A. and Jones, H., Mat. Sci. Eng. 19(2) (1975) 293

Wood, J.V. and Honeycombe, R.W.K., J. Mat. Sci. <u>9</u> (1974) 1183

Yoshimura, M. and Somiya, S., RQ4 <u>I</u> (1982) 23

Young, K.P. and Kirkwood, D.H., Met. Trans. <u>6A</u> (1975) 197

Bibliography

Batchelor, G.K. — "Fluid Dynamics"
1st Ed. C.U.P.,Cambridge UK. (1967)

Christian, J.W. — "Theory of Transformations in Metals and Alloys".
2nd Ed. Pergamon Press, Oxford,UK (1975)

Cottrell, A.H. — "An Introduction to Metallurgy"
2nd Ed. Edward Arnold, London (1975)

Coulson, J.M. and Richardson, J.F. — "Chemical Engineering"
2nd Ed. Pergamon Press, Oxford, UK (1964)

Cullity, B.D. — "Elements of X-ray Diffraction"
Addison Wesley Pub.Co.Inc., Reading, Mass., U.S.A. (1959)

Dieter, G.E. — "Mechanical Metallurgy"
McGraw-Hill, New York (1961)

Gilman, J.J. and Leamy, H.J. Eds: — "Metallic Glasses"
ASM. Metals Park, Ohio, USA (1978)

Hansen, M. — "Constitution of Binary Alloys"
2nd Ed. McGraw-Hill Book Co., New York USA (1958)

Honeycombe, R.W.K. — "Plastic Deformation of Metals"
Edward Arnold, London (1968)

Ilersic, A.R. and Pluck, R.A. — "Statistics"
14th Ed. H.F.L. (Publishers) Ltd.London (1979)

Int. Tin Research Institute. — "Properties of Tin"
ITRI, Perivale, London (1962)

Pearson, W.B. — "Handbook of Lattice Spacings of Metals and Alloys"
Pergamon Press, Oxford (1967)

Pickering, F.B. — "The Basis of Quantitative Metallography"
Metals and Metallurgy Trust for Inst. of Met. Tech., London. Monograph No.1. (1976)

Tegart, W.J. McG. — "Electrolytic and Chemical Polishing of Metals in Research and Industry"
Pergamon Press Oxford,UK (1956)